

AD _____

Award Number: DAMD17-02-1-0461

TITLE: A High Resolution Clinical PET with Breast and Whole Body
Transfigurations

PRINCIPAL INVESTIGATOR: Wai-Hoi Wong, Ph.D.

CONTRACTING ORGANIZATION: University of Texas
M. D. Anderson Cancer Center
Houston, Texas 77030

REPORT DATE: April 2003

TYPE OF REPORT: Annual

PREPARED FOR: U.S. Army Medical Research and Materiel Command
Fort Detrick, Maryland 21702-5012

DISTRIBUTION STATEMENT: Approved for Public Release;
Distribution Unlimited

The views, opinions and/or findings contained in this report are those of the author(s) and should not be construed as an official Department of the Army position, policy or decision unless so designated by other documentation.

20030923 094

REPORT DOCUMENTATION PAGE

Form Approved
OMB No. 074-0188

Public reporting burden for this collection of information is estimated to average 1 hour per response, including the time for reviewing instructions, searching existing data sources, gathering and maintaining the data needed, and completing and reviewing this collection of information. Send comments regarding this burden estimate or any other aspect of this collection of information, including suggestions for reducing this burden to Washington Headquarters Services, Directorate for Information Operations and Reports, 1215 Jefferson Davis Highway, Suite 1204, Arlington, VA 22202-4302, and to the Office of Management and Budget, Paperwork Reduction Project (0704-0188), Washington, DC 20503

1. AGENCY USE ONLY (Leave blank)		2. REPORT DATE April 2003	3. REPORT TYPE AND DATES COVERED Annual (1 Apr 02 - 31 Mar 03)	
4. TITLE AND SUBTITLE A High Resolution Clinical PET with Breast and Whole Body Transfigurations			5. FUNDING NUMBERS DAMD17-02-1-0461	
6. AUTHOR(S) Wai-Hoi Wong, Ph.D.				
7. PERFORMING ORGANIZATION NAME(S) AND ADDRESS(ES) University of Texas M. D. Anderson Cancer Center Houston, Texas 77030 E-Mail: gwong@di.mdacc.tmc.edu			8. PERFORMING ORGANIZATION REPORT NUMBER	
9. SPONSORING / MONITORING AGENCY NAME(S) AND ADDRESS(ES) U.S. Army Medical Research and Materiel Command Fort Detrick, Maryland 21702-5012			10. SPONSORING / MONITORING AGENCY REPORT NUMBER	
11. SUPPLEMENTARY NOTES				
12a. DISTRIBUTION / AVAILABILITY STATEMENT Approved for Public Release; Distribution Unlimited			12b. DISTRIBUTION CODE	
13. Abstract (<i>Maximum 200 Words</i>) (<i>abstract should contain no proprietary or confidential information</i>) Despite advances in the last decade, the radiographic diagnosis of breast cancer remains uncertain. Of the annual 600,000 cases referred for biopsy by mammograms each year, 400,000 are unnecessary, costing \$2 billion annually. The diagnosis of breast cancer in young women and women with silicone implants continues to be difficult. Accurate detection of small breast tumors (2-3 mm) is still to be achieved. Positron emission tomography (PET) has the potential to reduce this high healthcare cost, unnecessary painful anxiety, and to improve diagnosis and survivability for women of all ages. We have developed the detector and electronic technology for building an ultrahigh resolution PET camera. We propose to use such technology to construct an ultrahigh resolution PET that has a dedicated breast-diagnosis mode that has 13-26 times higher detection sensitivity than regular PET and an ultrahigh image resolution of 2.5mm compared to the 4.5-6 mm in today's PET cameras. We have already developed a scaled-down engineering prototype PET to confirm the feasibility that 2-3 mm tumor can be detected accurately. We propose to construct a scaled-up clinical version of the design so that it can be used for clinical human trials to confirm the clinical utility.				
14. SUBJECT TERMS: imaging, high resolution, PET			15. NUMBER OF PAGES 111	
			16. PRICE CODE	
17. SECURITY CLASSIFICATION OF REPORT Unclassified	18. SECURITY CLASSIFICATION OF THIS PAGE Unclassified	19. SECURITY CLASSIFICATION OF ABSTRACT Unclassified	20. LIMITATION OF ABSTRACT Unlimited	

NSN 7540-01-280-5500

Standard Form 298 (Rev. 2-89)
Prescribed by ANSI Std. Z39-18
298-102

BEST AVAILABLE COPY

Table of Contents

Cover.....	1
SF 298.....	2
Table of Contents.....	3
Introduction.....	4
Body.....	4
Key Research Accomplishments.....	9
Reportable Outcomes.....	9
Conclusions.....	11
References.....	11
Appendices	13

INTRODUCTION

Despite advances in the last decade, the radiographic diagnosis of breast cancer remains uncertain. Also, the diagnosis of breast cancer in dense breasts continues to be difficult, whether the density is a result of fibrocystic diseases or young age. Accurate detection of very small breast tumors (2-3 mm) and small metastases, which is essential for survival and breast conservation, is still to be achieved. Positron emission tomography (PET) has the potential to improve in these areas as PET images physiologic differences between tumor and normal tissue, providing > 90% sensitivity and >95% specificity in many recent studies. It also eliminates imaging difficulties for women who have silicone implants and dense breasts, which have negligible effect in PET; hence, PET is useful for high-risk young women and patients with implants.

However, for breast cancer diagnosis, there are technical limitations in current PET cameras which are designed for whole-body tumor staging instead of breast imaging. This goal of this project is to help the development of an ultrahigh resolution convertible-PET design that minimizes the limitations:

- (1) A convertible gantry with a dedicated breast mode that has 10-15 times higher detection sensitivity for breast-tumor activities than a whole-body PET
- (2) An intrinsic image resolution of 2.5-3.0 mm

BODY

The statement of work or task for this period is as follows:

- TASK 1.** Developing a PET camera gantry that can be transformed between the whole-body mode and the breast mode (Months 1-30): Design the transformation concept and develop the mechanical engineering design for the gantry (Month 1-12).
- TASK 2.** Fabricating and testing 40,000 small scintillation detectors, and building the detection system (Month 1-24):
 - a. Develop the mass-production tooling and production equipment for making the large number of scintillation detectors (Month 1-6).
 - b. Produce the scintillation detectors (Month 7-15).
- TASK 3.** Developing the high-speed electronic system, 169 circuit boards (Month 1-30): Design, build and test the front-end modular electronics, 48 circuit boards (Month 1-12).
- TASK 5.** Developing the software system (Month 1-30): Develop the image reconstruction and image processing software (Month 1-18).

We have been very productive since the funding of this US Army grant that started one year ago. All the tasks have been accomplished. A lot of progress has been made in developing this ultrahigh resolution transformable PET camera. In this one year, our research effort have resulted in the submission of 17 peer-reviewed scientific papers; 11 of these 17 papers is already in print or accepted to be published, with the other 6 still in the peer-review process.

For **TASK 1**: Design the transformation concept and develop the mechanical engineering design for the gantry (Month 1-12)

The basic mechanical transformation concept and gantry-related physics/engineering have been developed and published [1-2] during this period. The transformation design concept developed greatly reduces the detection gaps between detector modules as described in [1]. We have also researched the septa design of the gantry to reduce scatter-radiation noise to derive an optimal septa system for the gantry [2]. The detail mechanical design for the detector module that facilitates the precision of transformation (in detector positions) has been another major piece of the mechanical engineering project. The complex detector-module design is also designed for ease of maintenance and effective cooling of the detectors. The mechanical design (actual mechanical drawing) of the detector module with body-to-breast conversion is shown in fig.1-4 (in 3-D). We will start the mechanical construction of the detector modules in the next period.

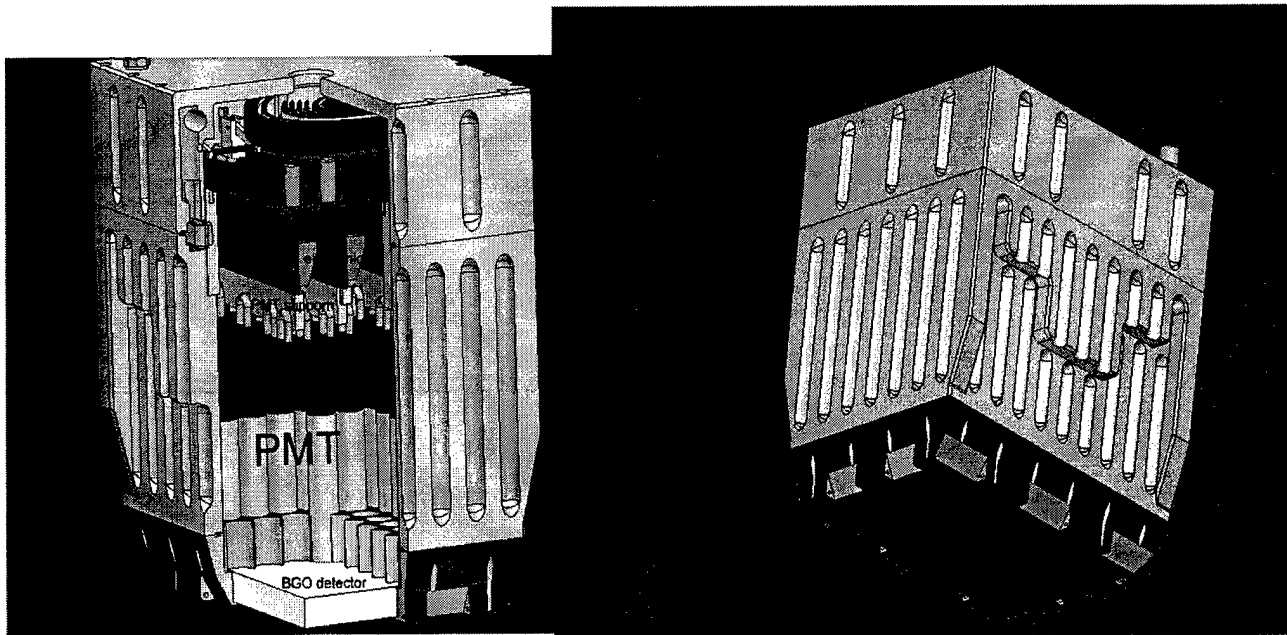


Fig. 1. LEFT: Cut-away view of one of the 12 detector modules to show its 77 photomultiplier tubes, 3200, BGO crystals and front-end electronics.

RIGHT: External view of the modules that is rectangular to facilitate the transformation between whole-body PET and breast PET.

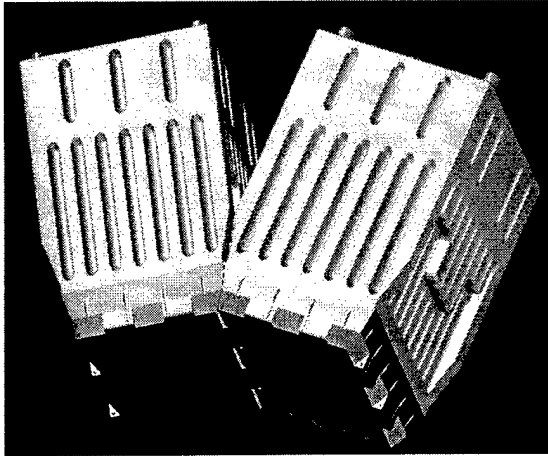


FIG. 2. Detector modules in breast mode (shows only 2 modules on the detector ring with 12 modules)

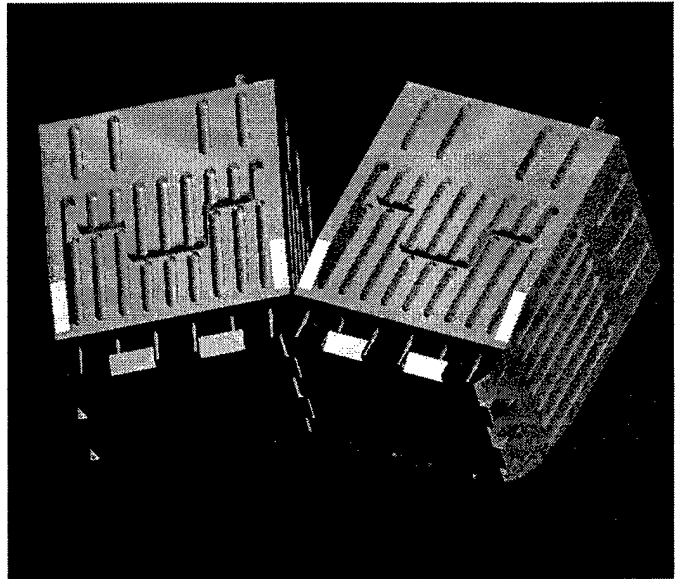


FIG. 3. Detector modules in whole-body mode (only 2 of the 12 modules on the detector ring is shown)

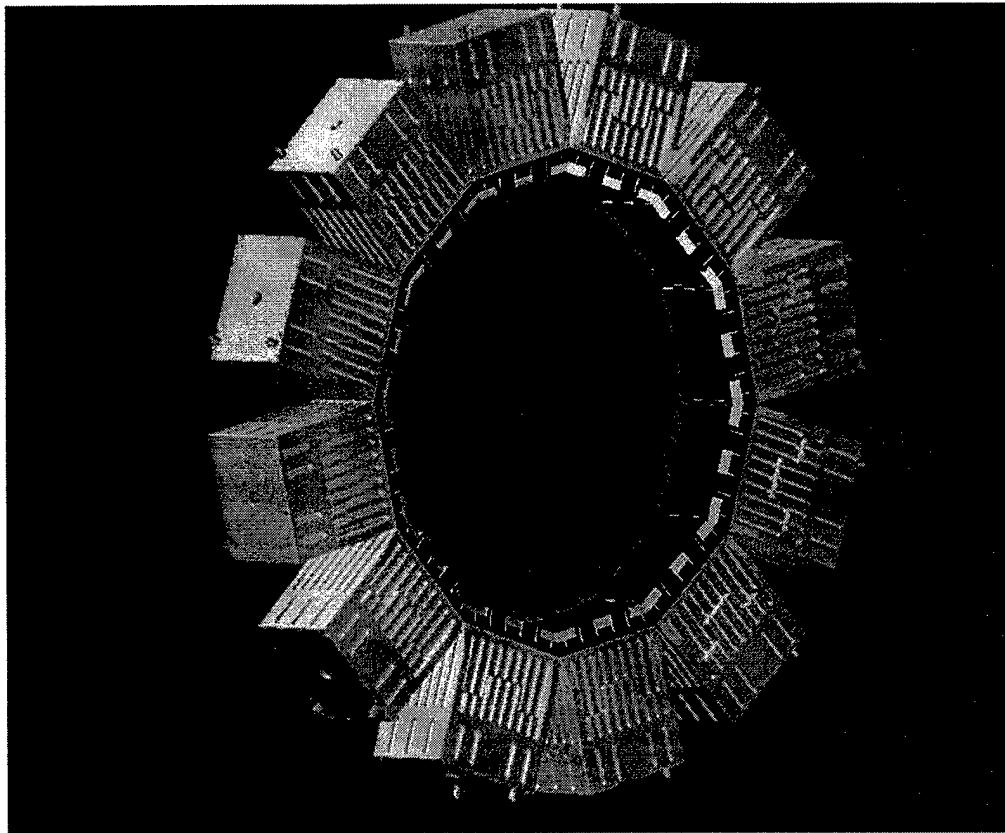


FIG. 5. The modules are locked together to form the detector ring of the PET

For **TASK 2**. Fabricating and testing 40,000 small scintillation detectors, and building the detection system (Month 1-24):

- a. Develop the mass-production tooling and production equipment for making the large number of scintillation detectors (Month 1-6).
- b. Produce the scintillation detectors and study the detector characteristics (Month 7-15).

The mass production technique and the production tooling have been developed and published [7]. We in the process of producing the 40,000 detectors; 25,000 detectors has been produced and are now being tested. Some detector characteristics and calibration methods have been measured, studied, and developed [3, 4, 5, 6, 8]. Some of the produced detectors are shown in fig.5.

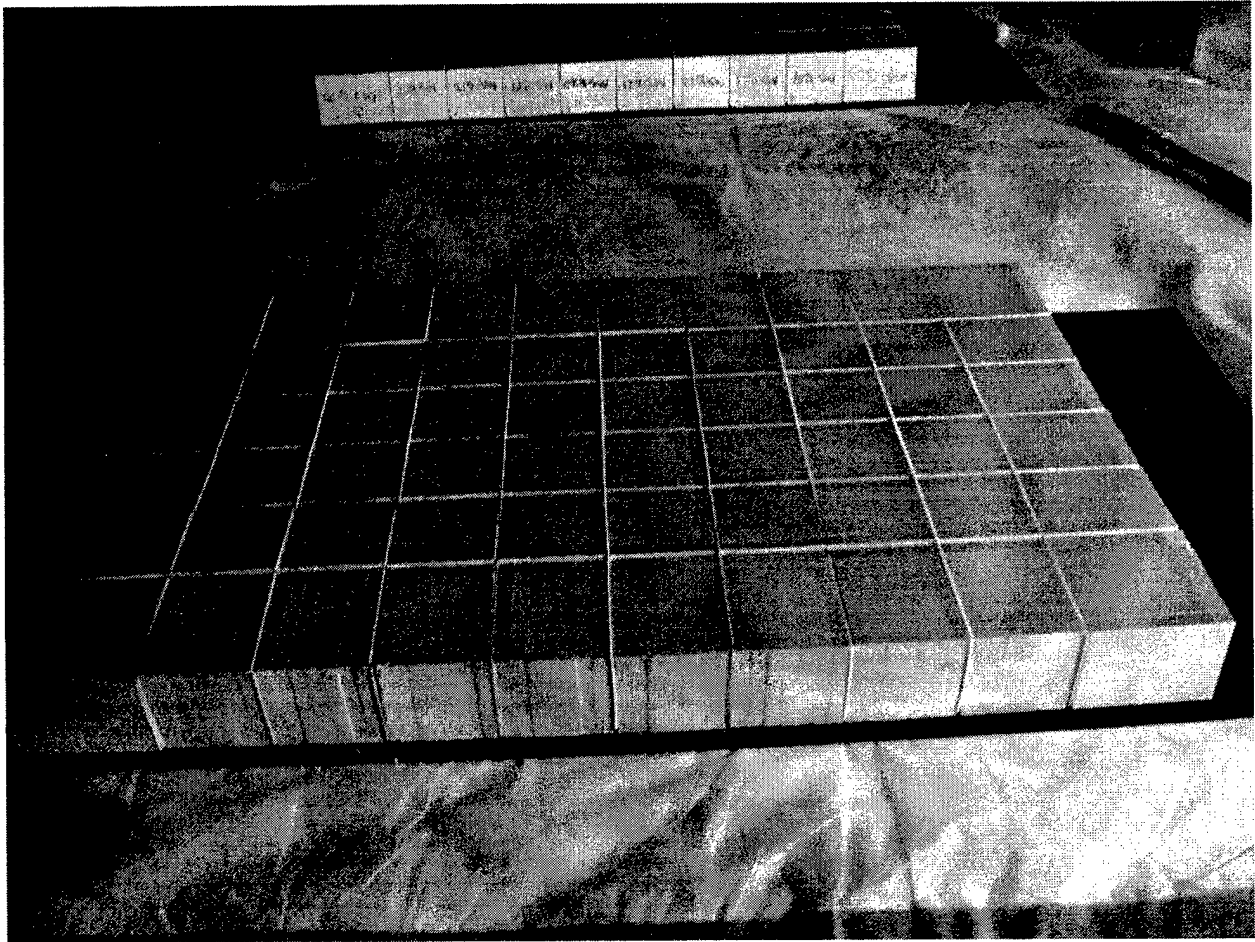


FIG. 5. 3200 BGO detectors (for one detector module) manufactured by our laboratory is shown. Each small BGO crystals is 2.6 x 2.6 mm (18 mm deep); each crystal shared a precise amount of light (as controlled by a painted optical window between each 2 crystals) to the neighboring crystals for decoding the position of each crystal. Detectors for 8 of the 12 modules have been produced.

TASK 3. Developing the high-speed electronic system, 169 circuit boards (Month 1-30): Design, build and test the front-end modular electronics, 48 circuit boards (Month 1-12).

The 48 circuit boards that were designated to be developed in the first year have been designed, constructed and are being tested. The results have been published [9, 10, 11, 12, 13]. Some of the circuit boards are shown in fig.6.

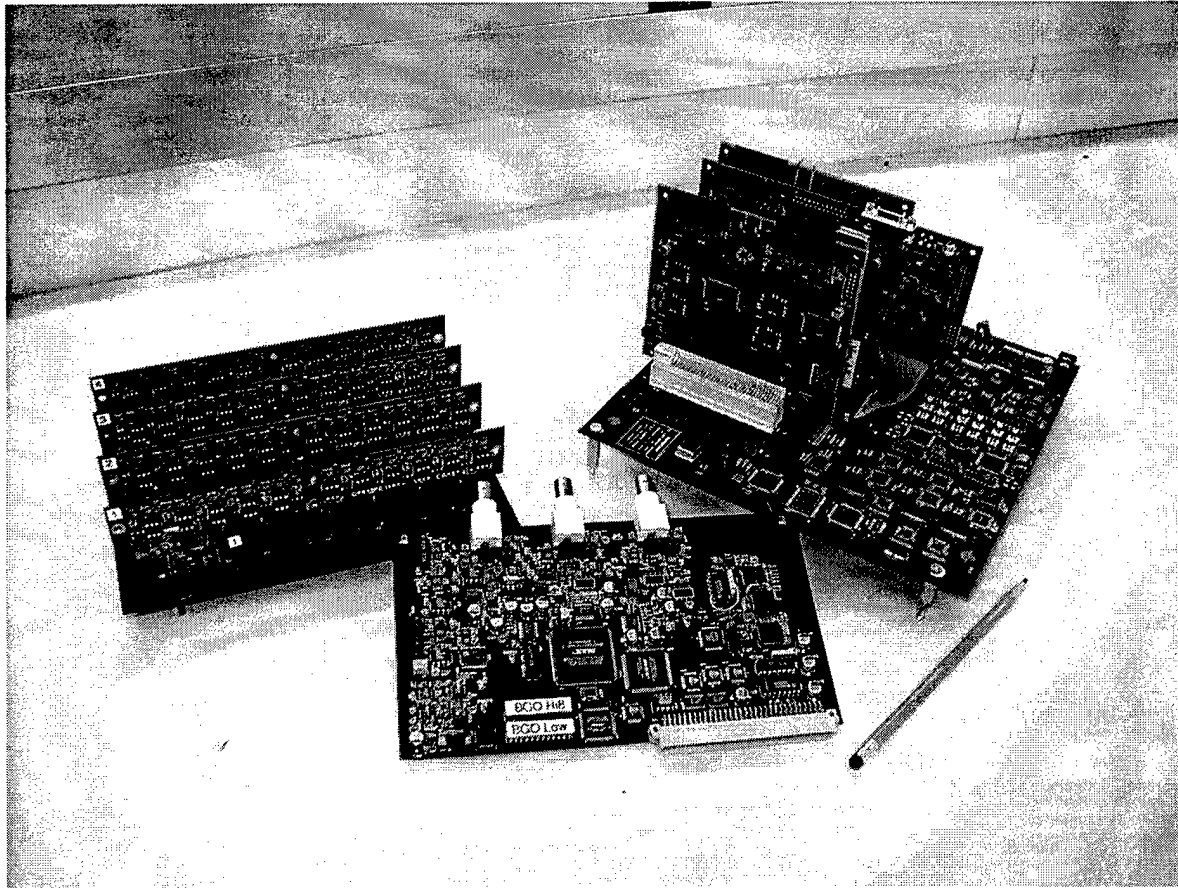


FIG. 6. LEFT: the front-end amplifier board, MIDDLE: the HYPER signal processing board, RIGHT: the coincidence board. 48 HYPER signal processing boards have been produced and tested.

TASK 5. Developing the software system (Month 1-30): Develop the image reconstruction and image processing software (Month 1-18).

Some of the image reconstruction and processing has been studied and developed. These include the digital filters used in two different image reconstruction algorithms (the OSEM and 3DRP). The results of these optimal filters have been published [14, 15]. The optimal software for attenuation correction for the system has also been studied and published [16]. The lesion detectability of the software and hardware was examined and the result has been submitted for publication [17].

KEY RESEARCH ACCOMPLISHMENTS

- The basic mechanical transformation concept and gantry-related physics/engineering have been developed and published [1-2] during this period.
- The mass production technique and the production tooling have been developed and published [7].
- The 48 circuit boards that were designated to be developed in the first year have been designed, constructed and are being tested. The results have been published [9, 10, 11, 12, 13]. Some of the circuit boards are shown in fig.6.
- The image reconstruction and processing softwares designated for the first year have been studied, developed and published [14, 15, 16, 17].

REPORTABLE OUTCOMES (Peer-reviewed papers listed below):

- 1 Wong, W-H., **Uribe, J.**, Li, H., Baghaei, H., Wang, Y., Aykac, M., Liu, Y., Xing, T., Bilgen, D., Farrel, R. The Design of a High Resolution Transformable Wholebody PET Camera. *IEEE Transactions on Nuclear Science*, 49(5), 2079-2084, October 2002.
- 2 Aykac, M., **Uribe, J.**, Baghaei, H., Li, H., Wang, Y., Liu, Y., Xing, T., Wong, W-H. Septa Design Study for Volumetric Imaging in Positron Emission Tomography. *IEEE Transactions on Nuclear Science*, 49(5), 2097-2102, October, 2002.
- 3 **Uribe, J.**, Li, H., Baghaei, H., Aykac, M., Wang, Y., Liu, Y., Xing, T., Wong, W-H. Effect of Photomultiplier Gain Drift and Radiation Exposure in Position Sensitive Detectors of Dedicated PET Cameras. Submitted for publication to *IEEE Transactions on Nuclear Science*.
- 4 Aykac, M., Li, H., **Uribe, J.**, Wang, Y., Baghaei, H., Liu, Y., Xing, T., Wong, W-H. A Study of Coincidence Line Spread Function (CLS F) Estimation for Small Scintillators Using Quadrant Sharing Technique. Submitted for publication to *IEEE Transactions on Nuclear Science*.
- 5 **Uribe, J.**, Aykac, M., Baghaei, H., Li, H., Wang, Y., Liu, Y., Xing, T., Wong, W-H. Inexpensive Position Sensitive Detector Block for Dedicated PET Cameras Using 40 mm Diameter PMT in Quadrant Sharing Configuration. Accepted and to be published in *IEEE Transactions on Nuclear Science*, June 2003.
- 6 **Uribe, J.**, Wong, W-H., Li, H., Baghaei, H., Wang, Y., Liu, Y., Xing, T., Farrell, R. Signal Characteristics of Individual Crystals in a High Resolution BGO Detector Design Using PMT-Quadrant Sharing. Accepted and to be published in *IEEE Transactions on Nuclear Science*, June 2003.
- 7 **Uribe, J.**, Wong, W-H., Li, H., Baghaei, H., Wang, Y., Liu, Y., Xing, T., Farrell, R. An

Efficient Detector Production Method for Position-Sensitive Scintillation Detector Arrays with 98% Detector Packing Fraction. Submitted for publication to IEEE Transactions on Nuclear Science.

- 8 Wang, Y., Wong, W-H., Aykac, M., **Uribe, J.**, Li, H., Baghaei, H., Liu, Y., Xing, Tao. An Iterative Energy-Centroid Method for Recalibration of PMT Gain in PET or Gamma Camera. IEEE Transactions on Nuclear Science, 49(5), 2047-2050, October, 2002.
- 9 Li, H., Wong, W-H., **Uribe, J.**, Baghaei, H., Liu, Y., Wang, Y., Xing, T., Aykac, M. A New Pileup-Prevention Front-End Electronic Design for High Resolution PET and Gamma Cameras. IEEE Transactions on Nuclear Science, 49(5), 2051-2056, October, 2002.
- 10 Liu, Y., Li, H., Wang, Y., Xing, T., **Uribe, J.**, Baghaei, H., Wong, W-H. A Programmable High-Resolution Ultra Fast Delay Generator. Accepted and to be published in IEEE Transactions on Nuclear Science, June 2003.
- 11 Li, H., Xing, T., Liu, Y., Wang, Y., Baghaei, H., **Uribe, J.**, Wong, W-H. A Hotlink/Network PC Data Acquisition and Image Reconstruction System for a High Resolution Whole-Body PET with Breath and ECG-Gated Performance. Accepted and to be published in IEEE Transactions on Nuclear Science, June 2003.
- 12 Li, H., Wong, W-H., Wang, Y., Liu, Y., Xing, T., **Uribe, J.**, Baghaei, H. Front-End Electronic Design Based on High-Yield-Pileup-Event-Recovery Method for a High-Resolution PET Camera with PMT-Quadrant-Sharing Detector Modules. Submitted to IEEE Transactions on Nuclear Science.
- 13 Wang, Y., Li, H., Liu, Y., Xing, T., **Uribe, J.**, Baghaei, H., Wong, W-H. A Modular Low Dead-Time Coincidence System for High Resolution PET Cameras. Accepted and to be published in IEEE Transactions on Nuclear Science, June 2003.
- 14 Baghaei, H., **Uribe, J.**, Li, H., Wang, Y., Aykac, M., Liu, Y., Xing, T., Wong, W-H. An Evaluation of the Effect of Filtering in 3D-OSEM Reconstruction by Using Data from A High Resolution PET Scanner. IEEE Transactions on Nuclear Science, 49(5), 2381-2386, October, 2002.
- 15 Baghaei, H., Wong, W-H., Li, H., **Uribe, J.**, Wang, Y., Aykac, M., Liu, Y., Xing, T. Evaluation of the Effect of Filter Apodization for Volume PET Imaging Using the 3DRP Algorithm, IEEE Transactions on Nuclear Science, 50(1), 3-9, Feb 2003.
- 16 Baghaei, H., **Uribe, J.**, Li, H., Aykac, M., Wang, Y., Liu, Y., Xing, T., Wong, W-H. Effects of Attenuation Correction and 3D-Reconstruction Algorithms on Brain Lesions Detectability. Submitted for publication to IEEE Transactions on Nuclear Science.
- 17 Baghaei, H., Wong, W-H., Aykac, M., **Uribe, J.**, Li, H., Wang, Y., Liu, Y., Xing, T: Brain Lesions Detectability Studies with a High Resolution PET Operating in No-Septa and Partial-Septa Configurations. Submitted for publication to IEEE Transactions on Nuclear Science.

CONCLUSION

We have been very productive since the funding of this US Army grant that started one year ago. All the tasks have been accomplished. We have accomplished much more than the statements of work that we have planned in the proposal. A lot of progress has been made in developing this ultrahigh resolution transformable PET camera. In this one year, our research effort have resulted in the submission of 17 peer-reviewed scientific papers; 11 of these 17 papers is already in print or accepted to be published, with the other 6 still in the peer-review process.

REFERENCES

- 1 Wong, W-H., **Uribe, J.**, Li, H., Baghaei, H., Wang, Y., Aykac, M., Liu, Y., Xing, T., Bilgen, D., Farrel, R. The Design of a High Resolution Transformable Wholebody PET Camera. *IEEE Transactions on Nuclear Science*, 49(5), 2079-2084, October 2002.
- 2 Aykac, M., **Uribe, J.**, Baghaei, H., Li, H., Wang, Y., Liu, Y., Xing, T., Wong, W-H. Septa Design Study for Volumetric Imaging in Positron Emission Tomography. *IEEE Transactions on Nuclear Science*, 49(5), 2097-2102, October, 2002.
- 3 **Uribe, J.**, Li, H., Baghaei, H., Aykac, M., Wang, Y., Liu, Y., Xing, T., Wong, W-H. Effect of Photomultiplier Gain Drift and Radiation Exposure in Position Sensitive Detectors of Dedicated PET Cameras. Submitted for publication to *IEEE Transactions on Nuclear Science*.
- 4 Aykac, M., Li, H., **Uribe, J.**, Wang, Y., Baghaei, H., Liu, Y., Xing, T., Wong, W-H. A Study of Coincidence Line Spread Function (CLS F) Estimation for Small Scintillators Using Quadrant Sharing Technique. Submitted for publication to *IEEE Transactions on Nuclear Science*.
- 5 **Uribe, J.**, Aykac, M., Baghaei, H., Li, H., Wang, Y., Liu, Y., Xing, T., Wong, W-H. Inexpensive Position Sensitive Detector Block for Dedicated PET Cameras Using 40 mm Diameter PMT in Quadrant Sharing Configuration. Accepted and to be published in *IEEE Transactions on Nuclear Science*, June 2003.
- 6 **Uribe, J.**, Wong, W-H., Li, H., Baghaei, H., Wang, Y., Liu, Y., Xing, T., Farrell, R. Signal Characteristics of Individual Crystals in a High Resolution BGO Detector Design Using PMT-Quadrant Sharing. Accepted and to be published in *IEEE Transactions on Nuclear Science*, June 2003.
- 7 **Uribe, J.**, Wong, W-H., Li, H., Baghaei, H., Wang, Y., Liu, Y., Xing, T., Farrell, R. An Efficient Detector Production Method for Position-Sensitive Scintillation Detector Arrays with 98% Detector Packing Fraction. Submitted for publication to *IEEE Transactions on Nuclear Science*.

- 8 Wang, Y., Wong, W-H., Aykac, M., **Uribe, J.**, Li, H., Baghaei, H., Liu, Y., Xing, Tao. An Iterative Energy-Centroid Method for Recalibration of PMT Gain in PET or Gamma Camera. *IEEE Transactions on Nuclear Science*, 49(5), 2047-2050, October, 2002.
- 9 Li, H., Wong, W-H., **Uribe, J.**, Baghaei, H., Liu, Y., Wang, Y., Xing, T., Aykac, M. A New Pileup-Prevention Front-End Electronic Design for High Resolution PET and Gamma Cameras. *IEEE Transactions on Nuclear Science*, 49(5), 2051-2056, October, 2002.
- 10 Liu, Y., Li, H., Wang, Y., Xing, T., **Uribe, J.**, Baghaei, H., Wong, W-H. A Programmable High-Resolution Ultra Fast Delay Generator. Accepted and to be published in *IEEE Transactions on Nuclear Science*, June 2003.
- 11 Li, H., Xing, T., Liu, Y., Wang, Y., Baghaei, H., **Uribe, J.**, Wong, W-H. A Hotlink/Network PC Data Acquisition and Image Reconstruction System for a High Resolution Whole-Body PET with Breath and ECG-Gated Performance. Accepted and to be published in *IEEE Transactions on Nuclear Science*, June 2003.
- 12 Li, H., Wong, W-H., Wang, Y., Liu, Y., Xing, T., **Uribe, J.**, Baghaei, H. Front-End Electronic Design Based on High-Yield-Pileup-Event-Recovery Method for a High-Resolution PET Camera with PMT-Quadrant-Sharing Detector Modules. Submitted to *IEEE Transactions on Nuclear Science*.
- 13 Wang, Y., Li, H., Liu, Y., Xing, T., **Uribe, J.**, Baghaei, H., Wong, W-H. A Modular Low Dead-Time Coincidence System for High Resolution PET Cameras. Accepted and to be published in *IEEE Transactions on Nuclear Science*, June 2003.
- 14 Baghaei, H., **Uribe, J.**, Li, H., Wang, Y., Aykac, M., Liu, Y., Xing, T., Wong, W-H. An Evaluation of the Effect of Filtering in 3D-OSEM Reconstruction by Using Data from A High Resolution PET Scanner. *IEEE Transactions on Nuclear Science*, 49(5), 2381-2386, October, 2002.
- 15 Baghaei, H., Wong, W-H., Li, H., **Uribe, J.**, Wang, Y., Aykac, M., Liu, Y., Xing, T. Evaluation of the Effect of Filter Apodization for Volume PET Imaging Using the 3DRP Algorithm, *IEEE Transactions on Nuclear Science*, 50(1), 3-9, Feb 2003.
- 16 Baghaei, H., **Uribe, J.**, Li, H., Aykac, M., Wang, Y., Liu, Y., Xing, T., Wong, W-H. Effects of Attenuation Correction and 3D-Reconstruction Algorithms on Brain Lesions Detectability. Submitted for publication to *IEEE Transactions on Nuclear Science*.
- 17 Baghaei, H., Wong, W-H., Aykac, M., **Uribe, J.**, Li, H., Wang, Y., Liu, Y., Xing, T. Brain Lesions Detectability Studies with a High Resolution PET Operating in No-Septa and Partial-Septa Configurations. Submitted for publication to *IEEE Transactions on Nuclear Science*.

The Design of a High-Resolution Transformable Wholebody PET Camera

Wai-Hoi Wong, *Member, IEEE*, Jorge Uribe, *Member, IEEE*, Hongdi Li, *Member, IEEE*,
Hossain Baghaei, *Member, IEEE*, Yu Wang, *Member, IEEE*, Mehmet Aykac,
Yaqiang Liu, Tao Xing, Deniz Bilgen, and Rossio Farrell

Abstract—The conceptual design of a high-resolution positron emission tomography (PET) camera is presented. This PET has a transformable transaxial and axial fields of view to facilitate oncology applications. The photomultiplier-quadrant-sharing (PQS) detector design is used to achieve very high resolution with lower cost. It has 38 016 small bismuth germanate crystals ($2.68 \times 2.68 \times 18 \text{ mm}^3$, $2.68 \times 3.06 \times 18 \text{ mm}^3$) and 924 photomultipliers (PMTs). The second-generation PQS detectors will be used for this high-resolution-oncologic-transformable PET (HOTPET). Monte Carlo simulations showed that image resolution would vary from 1.8 to 3.0 mm depending on the operating mode (detector ring diameter). The detector ring is made of 12 detector modules. Inside each module, the detector packing fraction is very high, 98.5% in both axial and transaxial dimensions to increase coincidence sensitivity to compensate for the loss from its narrower 13 cm wholebody axial field of view (AFOV) designed to reduce production cost and scatter and accidentals in 3-D imaging. The detector-ring diameter can change from 24 to 83 cm with no gaps between modules. For radiotherapy treatment planning, the ring expands to 100 cm creating an 80 cm patient port (17% detection gap). In the body modes, HOTPET has 44 detector rings (87 image planes). In the brain/breast modes, the detector diameter becomes 53 cm with a large AFOV (21 cm) with 72 detector rings (143 image planes). In the 24-cm mouse mode, coincidence nonlinearity may be reduced to yield a resolution of 1.8–2.2 mm for mouse/rat; it would have 21 cm AFOV providing a 3–7 \times higher geometrical coincidence sensitivity over a similar mouse-PET with 8 cm AFOV (no septa). The front-end electronics use the high-yield-pileup-event-recovery electronics to increase the count-rate performance and an automatic PMT gain-equalization for quality control.

Index Terms—Imaging, positron emission tomography (PET).

I. INTRODUCTION

A very-high-resolution positron emission tomography (PET) camera has been designed. This system was designed to provide high versatility for both clinical and research applications. The camera can be transformed into different operating modes: 1) a regular human wholebody PET; 2) an extra-large radiotherapy treatment planning system; 3) a high-sensitivity dedicated brain system; 4) a high-sensitivity dedicated breast

Manuscript received November 21, 2001; revised May 1, 2002. This work was supported in part by National Institutes of Health (NIH) Grant RO1 CA58980, NIH Grant RO1 CA61880, NIH Grant RO1 CA76246, NIH Grant RO1 CA58980S1, a U.S. Army Breast Cancer Grant, a Texas Higher Education Grant, a John S. Dunn Foundation Research Grant, and the Cobb Foundation for Cancer Research.

The authors are with the M.D. Anderson Cancer Center, University of Texas, Houston, TX 77030 USA (e-mail: gwong@di.mdacc.tmc.edu).

Digital Object Identifier 10.1109/TNS.2002.803777

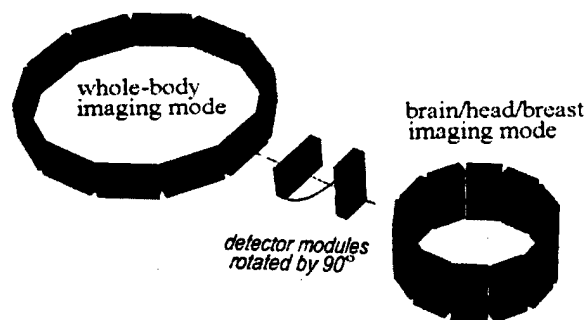


Fig. 1. Basic transformation design.

PET; and 5) a high-sensitivity small-animal PET. The expected intrinsic image resolution would be 2.6 mm for regular wholebody cancer staging and 2.2 mm for murine imaging. The PET is designed for the purpose of testing the usefulness of an ultrahigh-resolution PET for different dedicated applications in research and clinical settings. It is also designed to minimize the high production cost of very-high-resolution PETs.

II. SYSTEM CONFIGURATION DESIGN

The system uses a modular design to provide the necessary flexibility to facilitate a transformable architecture. A high-resolution-oncologic-transformable PET (HOTPET) utilizes a novel transformable geometry that can alter the detector-ring diameter from 24 to 100 cm. The detector ring is made of 12 detector modules. Each detector module is independent and has a rectangular detection area ($13 \times 21 \text{ cm}^2$). In the regular wholebody-scanning PET mode, the detector-ring diameter is 83 cm with no gap between detector modules and an axial field of view (AFOV) of 13 cm. In this regular wholebody mode, the camera has 44 detector rings imaging 87 planes/slices with a slice-to-slice separation of 1.37 mm. This imaging mode is used for wholebody cancer staging and cardiac applications as in regular commercial PET.

Secondly, the modules can rotate 90° about their individual axis, so a transaxial row of detectors becomes an axial column (Fig. 1). After this rotation and a radial displacement inward, the detector-ring diameter becomes 53 cm with a very large AFOV of 21 cm. This small-diameter mode can change the camera into a dedicated brain and breast PET with very high resolution and sensitivity. This brain/breast mode has 72 detector rings imaging 143 planes/slices simultaneously. The three-dimensional (3-D) coincidence sensitivity in this mode increases by four times from that of the regular wholebody mode (83 cm) because of

a 62% increase in AFOV and a 57% decrease in ring diameter [1], [6]. The intrinsic resolution would also improve from 2.6 to 2.2 mm by reducing annihilation noncollinearity effect [2]. This high-resolution and high-sensitivity design is beneficial for brain imaging. For breast imaging, without the body to attenuate the signal, there is another five times increase in sensitivity [3], for a total of 20 times higher sensitivity over a regular clinical PET, which when coupling to a 2.2-mm intrinsic resolution, would potentially allow very small breast lesions with lower tracer uptake to be detected.

The ring can be expanded from 83 to 100 cm by displacing the modules radially outward, thereby creating an 80-cm patient port so that the system can be used as a radiotherapy treatment-planning PET. This creates small detection gaps between detector modules (ratio of total detector gap to detector-ring circumference = 17%), which is acceptable without causing image artifacts, if the gantry can rotate 15° – 30° [4]. The system is designed to rotate 30° . In this radiotherapy treatment-planning mode, the system also has 44 detector rings imaging 87 planes/slices with a slice-to-slice separation of 1.37 mm.

The camera can also be transformed into a small-animal PET with detector diameters of 41 and 24 cm, by using only six or four of the detector modules. In the 24-cm mode (six modules), coincidence noncollinearity is minimized to yield an intrinsic resolution of 1.8–2.0 mm for imaging mice and rats from our Monte Carlo simulation [5]. Since the animal mode has 21-cm AFOV, it has seven times higher coincidence sensitivity over a similar mouse-PET with 8-cm AFOV in 3-D acquisition [1], [6].

Inside each detector module, each scintillation crystal is separated from its neighboring crystal by a very small gap of only 0.06 mm. This small inter-crystal spacing provides a very high detector-packing fraction of 98.5% for both the axial and transaxial dimensions. For a point source near the FOV center, the coincidence sensitivity is proportional to the (area packing fraction)² or (linear packing fraction)⁴ [1]. Hence, relative to a regular detector design with a typical packing fraction of 90% (the CTI detectors have 0.4-mm saw gap or spacing on a 4.5-mm crystal pitch), the present detector has a $(98.5/90)^4 = 1.43$ times increase in the geometrical coincidence sensitivity. This allows the AFOV to be decreased from 15 cm in the regular commercial bismuth germanate (BGO) PET to our 13 cm without sacrificing coincidence-detection sensitivity. In 3-D imaging acquisition, the geometrical coincidence sensitivity is proportional to (AFOV)² for a cylindrical source [1], [6]. Hence, the 1.43 times higher sensitivity coming from the very high detector-packing fraction allows us to decrease the AFOV from the regular 15 cm in the dedicated clinical BGO PET to 12.5 cm with no loss in sensitivity. Currently, we choose the AFOV to be 13 cm. Decreasing the AFOV by 2 cm in our design reduces the number of PMT, BGO, and electronics by 1/8 or 12.5%, which would lower the production cost of the camera without sacrificing detection sensitivity. Furthermore, the narrower wholebody AFOV of 13 cm in this design also allows the lead shields (on either sides of the detector ring) to block scatter and accidental events more effectively than a regular 15-cm AFOV, thereby improving image quality and noise-equivalent sensitivity in septa-less 3-D imaging. Hence, the high detector-packing fraction design would lower production cost and improve image quality at the same time.

III. DETECTOR MODULE DESIGN

Inside each detector module, we apply the high-resolution detector design that we developed in the last few years. This detector design, the photomultiplier-quadrant-sharing (PQS) design, has been demonstrated to achieve very high resolution with lower cost [7]–[9]. Each detector module has 32 BGO arrays/blocks with $2.68 \times 2.68 \times 18$ mm³ elements, 24 arrays with $2.68 \times 3.06 \times 18$ mm³ elements and 4 arrays with $3.06 \times 3.06 \times 18$ mm³ elements, and 77 PMT (19 mm). Hence, the whole system, with 12 detector modules, has 38 016 BGO crystals, and 924 PMT.

A second-generation PQS detector design will be used in this camera, instead of the first-generation PQS design in our prototype M. D. Anderson Cancer Center PET (MDAPET) [7]–[9] that achieved 2.8×3.4 mm image resolution (transaxial x axial) using 19-mm PMT. In the first-generation PQS development, we tested two light-distribution design methods: 1) the sawed grooves technique [10], [16] and 2) a painted mask technique. We built 128 BGO detector blocks/arrays where all the arrays along one dimension were saw-cut while along the other dimension, painted masks were used. The arrays were installed into our MDAPET prototype platform with all the sawed grooves along the axial direction for defining the axial resolution and with the painted masks for defining the transaxial resolution. The image resolution on the prototype was measured. The painted-mask direction (transaxial) were found to have 2.8-mm image resolution while that of the sawed-groove direction (axial) had an average resolution of 3.4 mm [7]. Since these resolution measurements were the combined effect of 128 detector arrays (6272 crystals), this finding conclusively determined that the painted-mask method was superior to the sawed-groove method for achieving higher image resolution.

The painted-mask method has two additional important advantages.

- 1) The saw-grooved method has high production breakage in a very-high-resolution detector design where the detector cutting pitches are closely spaced (2–3 mm apart). The small amount of crystal material left at the saw grooves is rather fragile. A lot of breakage was experienced during cutting and afterwards (due to the growth of micro-cracks). If one crystal element broke, the whole block/array (49 elements) was wasted. The painted-mask technique has virtually no breakage.
- 2) The sawed grooves remove detector material because of the finite saw-blade thickness and blade vibration (0.4–0.5-mm gap in a 2.7-mm detector pitch), which lowers the detection sensitivity of each array. If both the transaxial and axial dimensions were cut and even if a sawed gap of 0.35 mm can be achieved with better cutting, the detection-area packing efficiency is only $\{(2.7-0.35)/2.7\}^2$ or 75% for each detector module. This 75% packing efficiency would yield a point-source geometrical coincidence efficiency of only 56%. The thickness of a painted mask is only 0.04–0.06 mm, yielding an area-packing efficiency of $\{(2.7-0.04)/2.7\}^2$ or 97% that, in turn, yields a geometrical coincidence-detection efficiency of 94%. Hence, the painted-mask

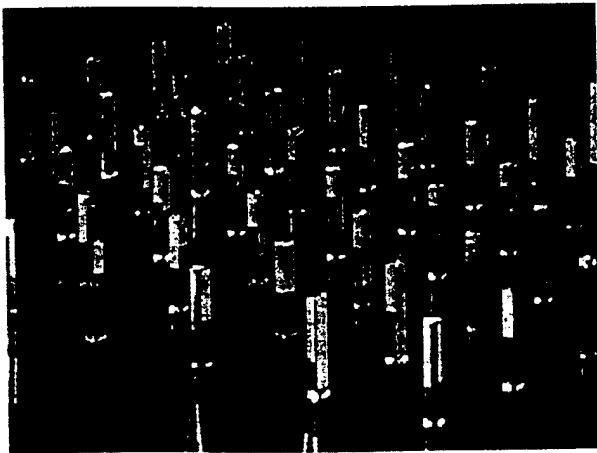


Fig. 2. PQS crystal array with white-painted masks.

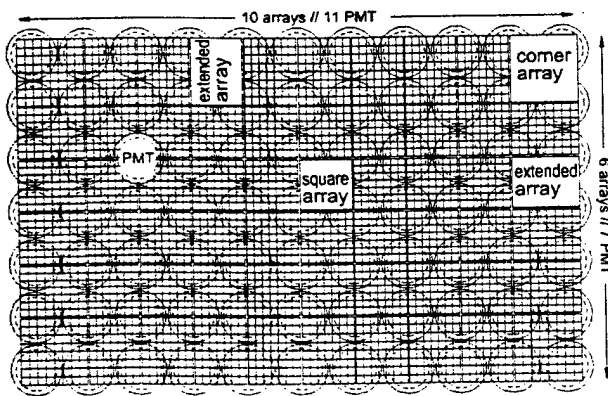


Fig. 3. Detector module design with PQS asymmetric edge and corner arrays.

technique would provide a sensitivity improvement of 94/56 or 1.7 times over the saw-groove method for our very-high-resolution detector design. In a regular commercial PET, the detector gap is 0.45 mm for a detector pitch of 4.5 mm, yielding an area-packing fraction of 90% and a coincidence-detection efficiency of 66%. Hence, the painted-mask design would provide a 94/66 or 1.42 times increase in coincidence-detection efficiency.

This increase in coincidence-detection efficiency derived from the painted mask is used to our advantage in lowering the production cost of the camera and reducing the scatter and accidental coincidence noise by decreasing the AFOV from the typical 15 to 13 cm. This decreases the detector components by one PMT ring (saving 132 PMT and 6048 BGO crystals) as discussed in the last section.

In the painted-mask design, the scintillation crystal elements are physically independent units, unlike the sawed-groove array. Each crystal has a white mask painted on each of its four cylindrical surfaces. The white mask partially covers each surface, as shown in Fig. 2. The painted crystals are optically coupled and glued to the neighboring crystals by a two-part optically transparent glue (Saint Gobain/Bicron BC-600). This design is also very robust mechanically.

The detector module design is shown in Fig. 3. In addition to using regular PQS detector design, the detector module

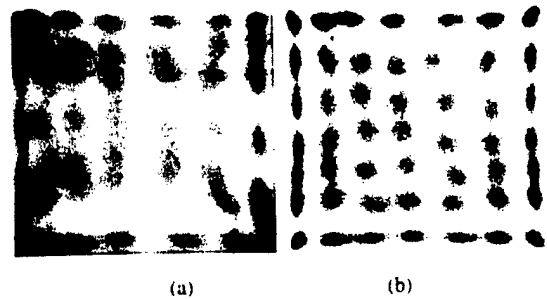


Fig. 4. Crystal decoding maps. (a) First-generation production PQS array with saw cut in one dimension. (b) Second-generation PQS array with crystals optically glued together with a thin layer of paint and glue (0.04 mm) between crystals.

also uses the elongated asymmetric PQS-arrays design along the edges and corners of each detector module to increase the usable crystal/detector areas of the PQS detector modules [11]. Without the elongated asymmetric PQS-array design, half a row of PMT would be wasted on each of the four edges of a detector module. A set of asymmetrically placed masks will be used for the edge and corner arrays [11].

The second-generation PQS detectors using the painted-mask technique also improve on the position decoding of the individual BGO crystals in the detector array (Fig. 4).

IV. SEPTA AND SHIELDING DESIGNS

Current PET cameras either operate in a two-dimensional (2-D) image acquisition mode with a full set of inter-slice septa (lead of tungsten) or operate in a 3-D imaging mode with no septa in the AFOV. In the brain/breast/animal configurations, the system will be operated in the 3-D septa-less mode. In the wholebody configuration, an intermediate septa system will be used. The intermediate septa system allows 3-D data to be acquired while reducing the scatter and accidental coincidence noise. From our Monte Carlo simulation studies, the intermediate septa system will have 5–7 septa spanning the 13-cm AFOV with a septum spacing of 2 cm [12], because it would provide the highest noise-equivalent sensitivity in the typical clinical dose and operating conditions. Since the detection system is divided into 12 modules, the intermediate septa unit for each module weight less than 3 lbs that can easily be manually inserted or removed individually, depending on imaging conditions and modes of operation.

The preliminary design of the thick lead shields on either sides of the detector ring is semi-adjustable. The thick lead shield on the back side of the detector annulus will be a fixed lead annulus fixed at the wholebody mode. The front lead shield (patient-entry side) has four opposing radially movable (sliding) sections (Q, R, S, T in Fig. 5) that can be continuously positioned between the body opening and the brain/breast opening. The four lead pieces between Q, R, S, T are fixed and these four fixed pieces are also the support for the radially sliding Q, R, S, T pieces and the flipping pieces W, X, Y, Z. In the brain/breast mode, most of the patient's body (radiation) is outside the front shield, thus, only the front shield needs to be adjustable and the back shield can be fixed to simplify the mechanics. This sliding front shield can also benefit body imaging because the patient body cross section

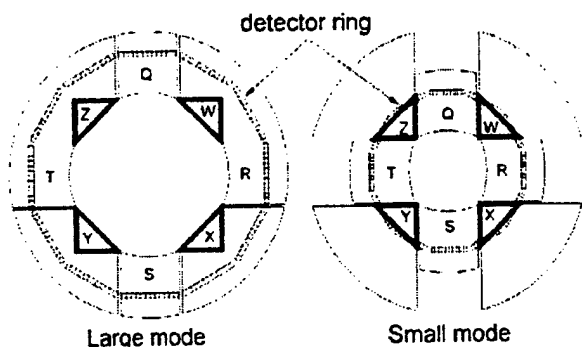


Fig. 5. Adjustable shielding design with sliding sections (Q, R, S, T). Sections (W, X, Y, Z) can be flipped or placed manually for the small mode.

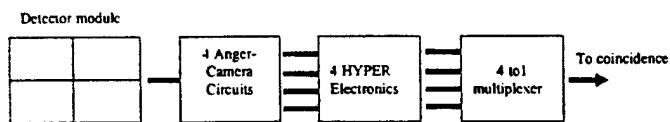


Fig. 6. Front-end electronic architecture for each detector module.

comes in different sizes and shapes. In the front shield, the four movable sections Q, R, S, T can slide to optimal positions, that is, as close to the patient as possible to block scatter/accidentals, depending on the section to be scanned and the size of the patient. Hence, optimal shielding tailored to the individual patient and study would be possible with this simple four-section sliding front shield.

V. ELECTRONIC DESIGN

The high-yield-pileup-event-recovery (HYPER) electronics that we recently developed to increase the count-rate performance of scintillation detectors will be incorporated into the front-end electronics of the camera [13]–[15]. The HYPER electronics have been demonstrated to increase the count-rate or imaging rate of NaI(Tl) by ten times [14] and that of BGO by six to eight times [12], [15].

The electronic design is also modular like the detector system. The front-end electronics design for one detector module is shown in Fig. 6. All the crystal arrays in a detector module are divided into four Anger-camera zones by Anger weighting the PMT signals according to their physical locations. There is no crystal overlap between each Anger-camera zone, but the row of PMT bordering any two zones are used by both zones. Each Anger-camera zone has one HYPER electronic board to do the real time data acquisition, thus, a total of 48 HYPER circuits are used in the system. Since each HYPER circuit allows its BGO detectors to operate at 800 000 singles/s [13], [15], the system with 48 HYPER circuits can process 30–40 million singles/s. This high-count-rate high-speed electronic design is also very low cost because only 144 ADCs are used for the 48 HYPER circuits in the whole camera that has 38 016 crystals, 924 PMT, and 720 crystal arrays. Fewer ADCs also means fewer other affiliated electronics and smaller real estate. In a regular design, there may be one ADC for each PMT (a total of 924 ADCs), or three ADCs per array (X, Y, E) for a total of 2160 ADCs.

The four-Anger-camera circuit board included in Fig. 6 consists of the amplifier for each PMT, the computer-controlled

auto-gain adjustment for each amplifier (with a PC parallel port interface to a monitoring PC), the PMT-position weighting circuit and the high-voltage distribution for the PMT. It also contains a control system for a set of pulsing light-emitting diodes (LEDs) for auto-equalization of PMT gains. Our preliminary LED equalization circuit demonstrated that all the 924 PMT can be equalized in just 30 s instead of several hours in current cameras. The four-Anger-camera circuit is a small board 12 × 20 cm placed inside each detector module.

The four-HYPER circuit in Fig. 6 consists of four HYPER daughter boards plugged into a multiplexer (4-to-1) mother board to generate one signal output for this detector module. The output signal consists of the scintillation position (before energy normalization), the energy, the zone identification, and the timing-gate pulse for coincidence matching. The output signal is synchronized (but delayed by 1.5 μ s) with the arrival of the event. The outputs of the detector modules are sent to a modular coincidence board for coincidence testing.

The coincidence matching of events coming from different detector modules is performed by an AND logic on the time of arrival of the timing gate in the module output signal. The use of the timing-AND logic for coincidence matching instead of using a time-stamp comparison is for minimizing the dead time in coincidence-matching. In the prototype MDAPET, we used the time-stamp matching design that has a dead time that is longer than desirable (80 ns). The coincidence-match dead time of the new coincidence circuit is about 22 ns for an event pair. The coincidence-timing window is adjustable between 8–16 ns. Both true and accidental coincidences are collected; the accidental timing shift is 200 ns relative to the true events. All multiple coincidences (triple, etc.) are rejected. There are 42 module pairs of coincident combinations derived from the 12 detector modules. Each of the 42 module pairs is independently processed. The coincidence circuit itself has a timing accuracy of 0.5 ns.

Since the coincidence matching is performed by timing-AND logic for the arrival of the detector-module signal, the detector-module signal for each event (single) has to be synchronized to the triggering time (arrival time) of the event. However, the HYPER pileup-prevention circuit requires a dynamic integration of the scintillation charge (the integration stops at the random time of arrival of the next event). Hence, the arrival time of an event is not synchronized to its charge-integration-stopping time; this is unlike the current PET system that has a fixed integration period. This nonsynchronization between the event-arrival time and the integration-stopping time would not normally allow the use of the timing-AND logic for coincidence matching. Hence, we have developed a technique to recover this synchronization [15] to resolve the incompatibility of HYPER and coincidence electronics.

The new HYPER pileup-prevention electronics have been tailored for BGO scintillation detectors to improve the resolution of the circuit. The improvements include a nonlinear filter for the timing trigger circuit, a multiple sampling of the raw/total energy, and position signals (including pileup signals) and a signal-distortion-compensated integration method [15].

The data-acquisition electronic architecture would provide cardiac and breath-motion gating to realize the high resolution capability for lung cancer and heart imaging.

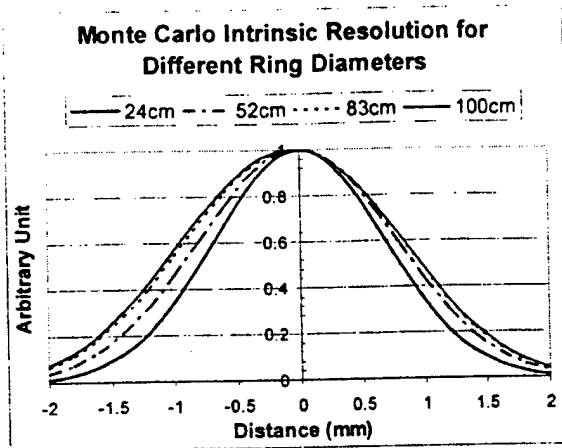


Fig. 7. Monte Carlo simulations of intrinsic spatial resolution.

TABLE I
MONTE CARLO SPATIAL RESOLUTION RESULTS

DETECTOR RING DIAMETER	24 CM	53 CM	83 CM	100 CM
INTRINSIC SPATIAL RESOLUTION	1.5 MM	1.8 MM	2.3 MM	2.6 MM
POTENTIAL IMAGE RESOLUTION	1.8 MM	2.1 MM	2.6 MM	3.0 MM

VI. MONTE CARLO SIMULATIONS

Monte Carlo simulation studies were performed to gauge the potential performance of this transformable PET camera. The simulation results included the effect of inter-crystal Compton scatters, photopeak-photpeak events, coincidence noncollinearity, light-sharing Anger-position decoding errors, and the positron range of ^{18}F isotope [2], [5]. Excluding the effect of reconstruction blurring, the intrinsic spatial resolutions were simulated for the regular body mode (83-cm detector ring), the brain/breast mode (53-cm detector ring), the radiotherapy mode (100-cm detector ring), and the murine mode (24-cm detector ring). The results are shown in Fig. 7 and Table I.

Assuming that the reconstruction processes degrade the intrinsic spatial resolution by 15%, the expected image resolutions are also estimated in Table I.

The potential image resolutions in Table I are for the central region of the transaxial field of view. For points away from the central region, the radial-resolution degradation due to the depth of interaction in detectors has not been studied. The simulation result showed a potential image resolution of 2.6 mm at 83-cm detector ring diameter, which compared reasonably well with the measured 2.9-mm transaxial resolution on the MDAPET camera that used the first-generation PQS detector design [7]. The difference in resolution results between computer simulation and that of a real camera (MDAPET) would most likely be from engineering factors such as detector-manufacturing discrepancies, detector positioning errors, and gantry mechanical tolerance errors. The actual image resolution is always worse than the potential theoretical resolution because of

engineering implementation uncertainties. The resolution blurring due to mechanical error and electronic errors cannot be adequately evaluated until the system is built.

VII. CONCLUSION AND DISCUSSION

The conceptual design of a very-high-resolution lower cost dedicated BGO PET camera with a transformable geometry has been presented. This camera has a transformable transaxial and AFOV to facilitate oncology applications and to enhance detection sensitivity for brain/breast imaging. The very-high-resolution (2.6 mm) human-body imaging mode with breath-motion gating would be more useful for detecting smaller metastatic lesions than current clinical PET cameras for more accurate cancer staging. For brain imaging, the large 21-cm AFOV, the smaller detector ring, and the 98.5% detector packing fraction would provide a total of four times higher geometrical coincidence-detection sensitivity (in 3-D) than a regular BGO clinical wholebody PET, which, when coupled to a potential 2.1-mm spatial resolution, would be a very useful brain imaging device, especially for receptor studies and for the detection of recurrent brain tumors. For the breast imaging mode, very small breast lesions can be detected with the projected resolution and an effective increase in coincidence-detection sensitivity by 20 times compared to a wholebody PET; the imaging time would be very short (1–2 min) due to its 20 times sensitivity enhancement, which would reduce patient movement artifacts and increase patient throughput. For murine imaging, the 2-mm resolution and a large 21-cm AFOV would be useful for receptor studies as it can provide a seven times higher sensitivity (3-D) compared to a similar mouse-PET with 8-cm AFOV.

Electronically, this PET camera can process 30–40 million singles/s and has a small coincidence dead time of 22 ns. Only 144 ADCs are used for the whole camera. All the PMT gains in the system can be equalized in 30 s without using radiation and human intervention, which allows the whole system to be tuned for each patient to optimize image quality at all time.

Since this is a conceptual design study, we have not discussed many outstanding detailed issues. Such outstanding issues include both engineering-implementation issues, imaging, and image-processing issues.

The detector-production engineering is the most important issue. Can such a large quantity of position-sensitive detectors (40 000) be realistically or economically produced with high manufacturing tolerance, especially with such small 2.68×2.68 mm detectors? Hence, a highly efficient and highly accurate detector-production engineering method has to be developed to make the design usable. Secondly, the mechanical engineering design will be challenging. It involves rotating the detector modules by 90° , translating the module radially, and rotating the whole system axially by 30° . Since the detectors are very small, 2.68×2.68 mm, the mechanical tolerances for all the detector related components has to be very small so that the resolution degradation due to mechanical errors is small compared to 2.68-mm detectors. Hence, an ingenious mechanical design has to be developed to realize the design. The many degrees of mechanical freedom also impact the electronic/electrical architectural design because of the complex signal and power routing

issues in the PET; the tens of thousands of detection channels coupling with coincidence detection and the fast nanosecond timing generate a very complex routing structure of signal, power, and cables, even for the regular motionless PET.

The optimal design and the form of the transmission source have not been decided. The optimal attenuation correction has not been chosen. The optimal reconstruction algorithm has not been decided; ideally, 3-D ordered subset expectation maximization (OSEM) will be used. These are just some of the outstanding issues. There are many more.

The optimal solutions for such outstanding issues will depend not only on the physics of the conceptual design, but they are also greatly dependent on the engineering paths and compromises chosen. Designing/developing a large high-resolution PET camera, especially one incorporating many new technologies, is a very complex issue. The ultimate performance of a PET camera depends partly on the design concepts based on physics and partly on the art of engineering and engineering compromises. A novel PET design concept has been proposed, which is the easy part and relatively free of constraints. Our next step is to develop the engineering and production engineering to realize the potential capability of the concept, which is a much harder undertaking because of inevitable reality constraints such as budget, material, and manpower.

ACKNOWLEDGMENT

The PET Development Laboratory would like to thank L. Easley for the help, useful discussions, and consultation in mechanical design issues and the Radiation Physics Machine Shop at the M. D. Anderson Cancer Center and its Director, M. Bushman, for mechanical fabrications and designs.

REFERENCES

- [1] R. A. Brooks, V. J. Sank, D. C. Giovanni, W. S. Friauf, and S. B. Leighton, "Design of a high resolution positron emission tomography: The Neuro-PET," *J. Comput. Assisted Tomography*, vol. 4, no. 1, pp. 5-13, 1980.
- [2] W. W. Moses and S. E. Derenzo, "Empirical observation of resolution degradation in positron emission tomographs utilizing block detectors," *J. Nucl. Med.*, vol. 34, no. 5, p. 101, 1993.
- [3] W. W. Moses, T. F. Budinger, R. H. Huesman, and S. E. Derenzo, "PET camera designs for imaging breast cancer and axillary node involvement," *J. Nucl. Med.*, vol. 36, no. 5, p. 69, 1995.
- [4] H. Baghaei, H. Li, J. Uribe, Y. Wang, and W.-H. Wong, "Compensation of missing projection data for MDAPET camera," in *Conf. Rec. 2000 IEEE Nuclear Science Symp. Medical Imaging Conf.*, vol. 3, pp. 17/41-17/45.
- [5] M. Aykac, H. Li, B. Uribe, Y. Wang, H. Baghaei, Y. Liu, T. Xing, and W.-H. Wong, "A study of Coincidence Line Spread Function (CLSF) estimation for small scintillator blocks," in *Conf. Rec. 2001 IEEE Nuclear Science Symp. Medical Imaging Conf.*
- [6] S. E. Derenzo, H. Zakled, and T. F. Budinger, "Analytical study of a high resolution positron ring detector system for transaxial reconstruction tomography," *J. Nucl. Med.*, vol. 12, pp. 1116-1173, 1975.
- [7] J. Uribe, *et al.*, "Basic imaging performance characteristics of a variable field of view PET using quadrant sharing detectors," *IEEE Trans. Nucl. Sci.*, vol. 46, pp. 491-497, Dec. 1999.
- [8] W.-H. Wong, "A positron camera detector design with cross coupled scintillators and quadrant sharing photomultipliers," *IEEE Trans. Nucl. Sci.*, vol. 40, pp. 962-966, Aug. 1993.
- [9] W.-H. Wong, J. Uribe, K. Hicks, M. Zambelli, and G. Hu, "A 2-dimensional detector decoding study on BGO array with quadrant-sharing photomultipliers," *IEEE Trans. Nucl. Sci.*, vol. 41, pp. 1453-1457, Aug. 1994.
- [10] M. P. Tornai, G. Germano, and E. J. Hoffman, "Position and energy response of PET block detectors with different light sharing schemes," *IEEE Trans. Nucl. Sci.*, vol. 41, pp. 1458-1463, Aug. 1994.
- [11] W.-H. Wong, *et al.*, "An elongated position sensitive block detector design using the PMT quadrant sharing detector array," *IEEE Trans. Nucl. Sci.*, vol. 46, pp. 542-545, June 1999.
- [12] M. Aykac, J. Uribe, H. Baghaei, H. Li, Y. Wang, Y. Liu, T. Xing, and W. H. Wong, "Septa design study for volumetric imaging in positron emission tomography," in *Conf. Rec. 2001 IEEE Nuclear Science Symp.*, vol. 3, pp. 1251-1254.
- [13] H. Li, *et al.*, "A high speed position-decoding electronics for BGO block detectors in PET," *IEEE Trans. Nucl. Sci.*, vol. 47, pp. 1006-1010, June 2000.
- [14] W.-H. Wong, *et al.*, "Feasibility of a high speed gamma camera using the high-yield-pileup-event-recovery (HYPER) method," *J. Nucl. Med.*, vol. 42, no. 4, pp. 624-632, 2001.
- [15] H. Li, *et al.*, "A new pileup prevention front-end electronic design for high resolution PET and gamma cameras," in *Conf. Rec. 2001 IEEE Nuclear Science Symp.*, vol. 4, pp. 1969-1973.
- [16] M. E. Casey and R. Nutt, "A multicrystal two dimensional BGO detector system for positron emission tomography," *IEEE Trans. Nucl. Sci.*, vol. 33, Feb. 1986.

Septa Design Study for Volumetric Imaging in Positron Emission Tomography

Mehmet Aykac, *Member, IEEE*, Jorge Uribe, *Member, IEEE*, Hossain Baghaei, *Member, IEEE*, Hongdi Li, *Member, IEEE*, Yu Wang, Yaqiang Liu, Tao Xing, and Wai-Hoi Wong, *Member, IEEE*

Abstract—Positron emission tomography (PET) has become an essential imaging tool to localize tumors in diagnostic radiology and to monitor the size of a lesion before and during the treatment in oncology. Currently, commercial PET cameras operate only in two extreme modes: i) no-septa: three-dimensional (3-D) acquisition mode, also called volumetric imaging; and ii) all-septa-in: two-dimensional (2-D) acquisition mode, also called multislice imaging. In this paper, intermediate septa designs in the brain mode have been sought to minimize the scatter and accidental coincidences with acceptable sensitivity loss. To achieve this goal, Monte Carlo simulations were performed to evaluate possible septa designs. Information about septal penetration, absorption and scattering components from simulations guided us to modify the thickness and total number of septa in the new configurations. Count rate performances of three septa configurations were measured on our experimental high resolution PET camera with 3.85-cm axial field-of-view (AFOV); the measurements were compared with the simulation results. No-septa configuration had lower noise equivalent count (NEC) compared the other two configurations because of small AFOV. Monte Carlo simulations were performed to predict the count rate performances of seven septa configurations for 13.1-cm AFOV. In the large AFOV, because of increased number of line of responses, NEC rate for no-septa case peaked rapidly at $0.07 \mu\text{Ci/cc}$. No-septa configuration is not recommended for high count rate studies. In this case where activity density is $0.3 \mu\text{Ci/cc}$ or more, 10-septa and 15-septa configurations performed better than the other configurations. Intermediate 5-septa designs with variable septum length performed better between $0.07\text{-}\mu\text{Ci/cc}$ and $0.3\text{-}\mu\text{Ci/cc}$ range which represents the clinical activity level for ^{18}F -FDG brain studies.

Index Terms—Deadtime model, Monte Carlo simulation, noise equivalent curve, positron emission tomography (PET), scatter fraction, septa.

I. INTRODUCTION

MOST of the conventional positron emission tomography (PET) cameras usually operate in two-dimensional (2-D) acquisition mode to obtain a significant decrease in the scattered coincidences and accidentals by placing septa extending all the way to the detector modules. In the last decade, manufacturers have started to design PET cameras with retractable septa to increase the system sensitivity [1]. Three-dimensional (3-D) ac-

quisition mode with no septa can be utilized in brain and animal imaging where low-level activity is present in the FOV [2], [3]. Data acquired in 3-D mode with high-level activity have very high accidentals and scatter events. At high activity in the FOV, the system electronics in 3-D acquisition mode might start to fail due to signal pile-up in the detectors and increased deadtime for true events. Increased deadtime and high accidental rate will cause significant degradation on the scanner performance. In brain studies, using whole body scanner (~ 90 cm ring diameter) with 3-D acquisition mode has been suggested to improve NEC rates [4]. Recently, a hybrid PET design was proposed to acquire projection data in both 2- and 3-D mode simultaneously by using rotating partial septa [5]. Several investigators studied optimal septal spacing in gamma cameras for PET imaging [6], [7].

This paper is a preliminary study of an optimal septa design to minimize the accidentals and scatter components for PET systems by sacrificing the system sensitivity. With the new stationary designs, 3-D acquisition mode will be utilized and, yet, accidentals, scatters, and deadtime in the detectors will diminish significantly. Differences in septa configurations will be shown in NEC rates [8]. With the addition of deadtime model, Monte Carlo simulation program becomes a useful tool to predict the count rate performance for various septa designs.

II. MONTE CARLO SIMULATION

Several investigators [9]–[11] have studied the effect of all-septa-in and no-septa cases on the scatter fraction. Thompson [9] simulated septa for multislice PET systems. Adam [10] reported the effect of various scatter components in coincidence imaging. Lecomte [11] modeled animal PET scanner in his analytical model where septa were assumed to be opaque.

Monte Carlo simulation program models the photoelectric absorption, Coherent and Compton scatterings. The interaction probabilities were calculated based on the tabulated values of interaction cross sections for lead, BGO (Bismuth Germanate), and water. Klein–Nishina formulation was used to estimate the scattering angles for Compton interactions. Coherent scattering angles were estimated based on the tabulated scattering amplitudes in Evaluated Photon Data Library. Blurring due to positron motion was defined as a Gaussian function with 0.25 mm FWHM value. A pair of photons was created for each positron decay. The angle between the annihilation photons was 180° and a small angle was chosen from a Gaussian function with FWHM value 0.5° to account for the noncolinearity [12]. Rectangular and tapered objects were modeled. In the simulation program, interactions of low energy scintillation photons were not modeled.

Manuscript received November 20, 2001. This work was supported by NIH Grants RO1 CA76246, RO1 CA61880, and RO1 CA58980, the J. S. Dunn Research Foundation, and the Cobb Endowment for Cancer Research.

M. Aykac was with the M. D. Anderson Cancer Center, University of Texas, Houston, TX 77030 USA. He is now with CPS Innovations, Rockford, TN 37853 USA (e-mail: aykac2000@yahoo.com).

J. Uribe, H. Baghaei, H. Li, Y. Wang, Y. Liu, T. Xing, and W.-H. Wong are with the M. D. Anderson Cancer Center, University of Texas, Houston, TX 77030 USA.

Digital Object Identifier 10.1109/TNS.2002.803812

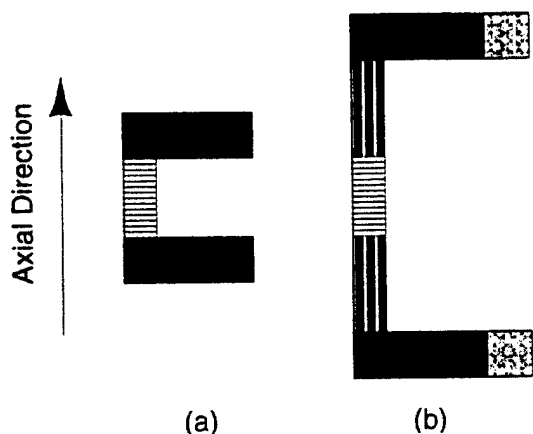


Fig. 1. (a) Original axial view of a detector module in MDAPET. (b) Axial view of modified detector module in MDAPET.

III. SCANNER MODIFICATION

The original axial dimension of our prototype PET scanner MDAPET [13] was 3.85 cm shown in Fig. 1(a). Eight detector modules were modified axially to extend from 3.85 cm to 13.1 cm. Extended parts on both sides of the modules were replaced with three layers of lead (3 mm thick) + aluminum (1.5 mm thick) sandwiches as BGO substitute to take into account for intercrystal scattering [see Fig. 1(b)]. End-shields were extended from 6 cm to 8.5 cm to reduce the radiation coming from out-of-FOV.

IV. SCATTER FRACTION MEASUREMENTS

Scatter Fraction (SF) measurements were performed based on the specifications in NEMA (National Electrical Manufacturers Association) standards [14] for PET. Line source with 6.35 mm diameter was placed in a cylindrical water phantom with 21 cm diameter and 18 cm height at three radii locations: $R = 0$ (at the center), $R = 4.5$ cm, and $R = 9$ cm. The phantom was centered both axially and transaxially in the FOV. Very low activity of ^{68}Ga was used in the line source so that the accidentals were only 1–2% of true coincidences. Five short acquisitions with at least 500 000 total true counts were performed in the brain mode and sinograms were summed. SF measurements were repeated for three septa configurations shown in Fig. 2. SF values were calculated as described in NEMA standard [see (1)].

$$SF = \frac{[F_s(R=0) + 8 * F_s(R=4.5) + 10.75 * F_s(R=9)]}{[F_{tot}(R=0) + 8 * F_{tot}(R=4.5) + 10.75 * F_{tot}(R=9)]} \quad (1)$$

where F_s and F_{tot} are the count rate per unit activity of scattered events and total events (at $R = 0, 4.5,$ and 9 cm), respectively. Results were compared to Monte Carlo simulation results.

Simulation results were found to be in agreement with the experimental measurements for SF values shown in Table I. Energy threshold was set to 350 KeV.

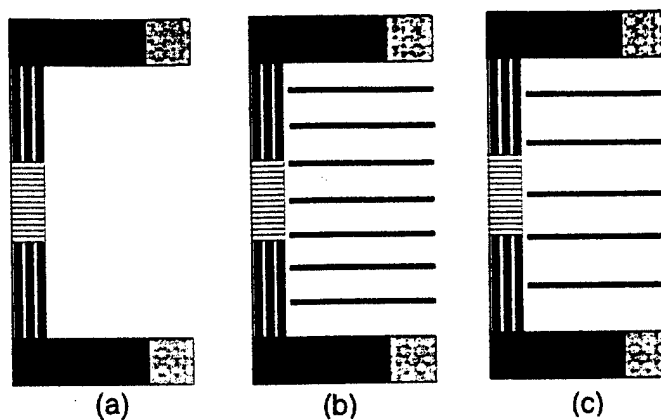


Fig. 2. Axial view of the modified version of MDAPET detector module for three septa configurations. (a) No-Septa. (b) Design-1: 7-septa-in (intergap between septa is 1.45 cm). (c) Design-2: 5-septa-in (intergap between septa is 2 cm). Septa thickness was chosen to be 2 mm in all designs.

TABLE I
COMPARISON OF EXPERIMENTAL AND MONTE CARLO SIMULATION SF RESULTS IN PERCENT FOR MODIFIED MDAPET IN BRAIN MODE

	R=0cm	R=4.5cm	R=9cm	SF(%)
No Septa (Experiment)	38.8	39.5	36.6	37.9
No Septa (Simulation)	35.7	37.4	33.2	35.0
Design-1 (Experiment)	25.6	27.0	22.6	24.5
Design-1 (Simulation)	21.9	24.2	19.9	21.7
Design-2 (Experiment)	27.6	29.2	25.3	27.0
Design-2 (Simulation)	24.1	26.5	21.1	23.4

V. DEADTIME MODEL AND COUNT RATE MEASUREMENTS

In this paper, deadtime model was established based on several earlier studies [15], [16] with slight modifications. A non-paralyzable model shown in (2) was used to describe the singles count rate (S) performance of a module:

$$S = \frac{S_{MC}}{(1 + S_{MC}\tau_{module})} \quad (2)$$

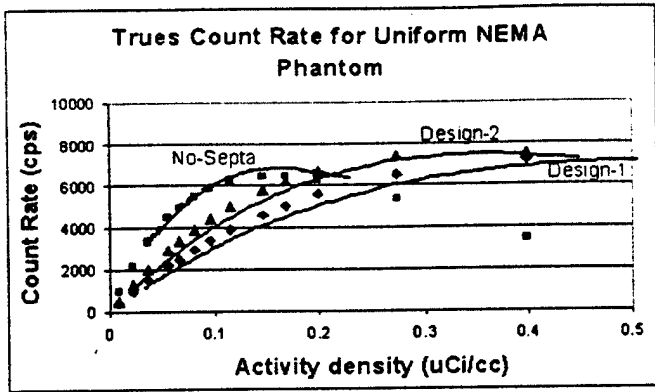
where S_{MC} is singles count rate per module obtained from the Monte Carlo simulation, τ_{module} is the module deadtime constant.

Equations (3) and (4) were used in the model to estimate the trues (T , unscattered and scattered coincidences) and randoms (R) count rate:

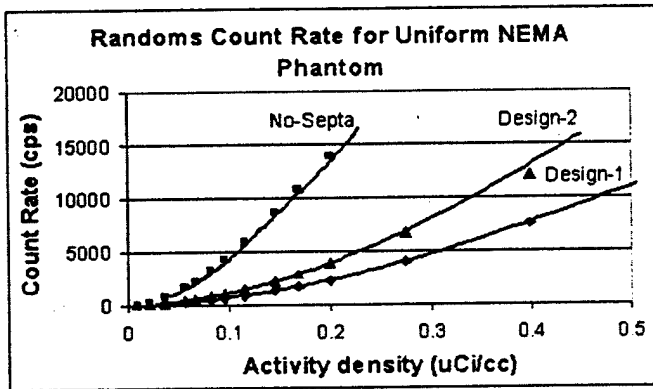
$$T = t_c T_{MC} e^{-2T_{MC}\tau_c} \quad (3)$$

$$R = \tau_c n_p \Delta T \left(k \frac{S_{MC}}{(1 + S_{MC}\tau_{module})} \right)^2 \quad (4)$$

where T_{MC} is coincidence count rate obtained from Monte Carlo simulation, τ_c is the coincidence deadtime constant. t_c (a scaling factor) is estimated by fitting the trues obtained from simulation results with the experimental values. n_p in (4) represents the total number of module pairs producing accidental coincidence and is equal to 28. ΔT (20 ns) is the



(a)



(b)

Fig. 3. Comparison of measured (solid lines) and simulated (dots: ■: No-septa, ◆: Design-1, ▲: Design-2) count rates for three detector configurations. (a) True. (b) Accidental rates.

TABLE II
ESTIMATED PARAMETERS USED IN THE DEADTIME MODEL

τ_{scat}	τ_c	t	τ
0.96 μsec	1.94 μsec	0.685	0.395

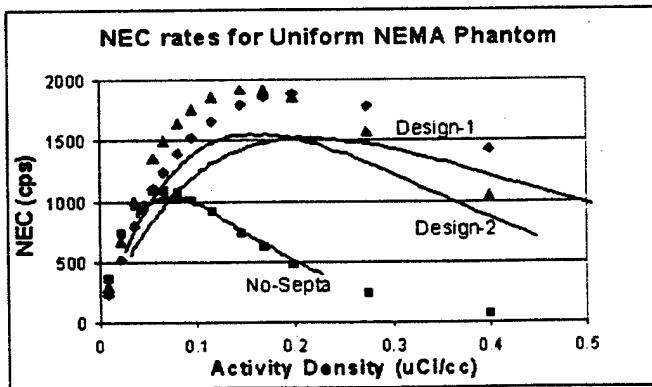
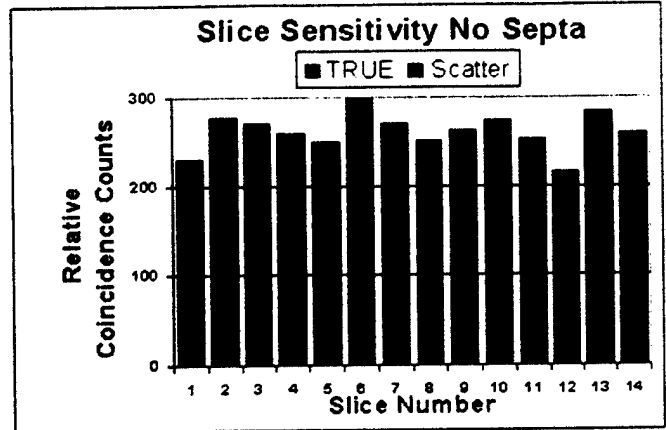
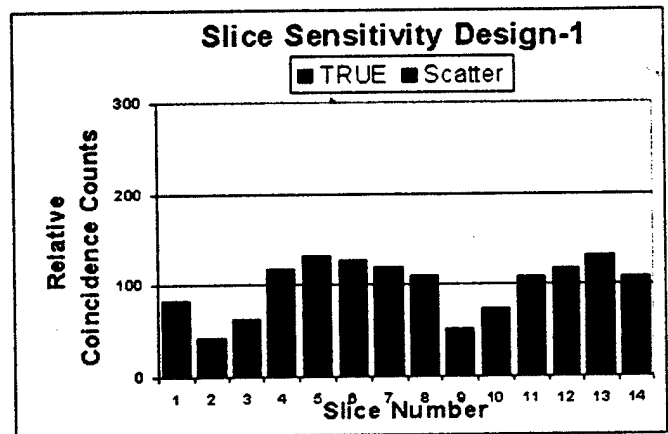


Fig. 4. Comparison of measured (solid lines) and simulated (dots: ■: No-septa, ◆: Design-1, ▲: Design-2) NEC rates for three septa configurations.

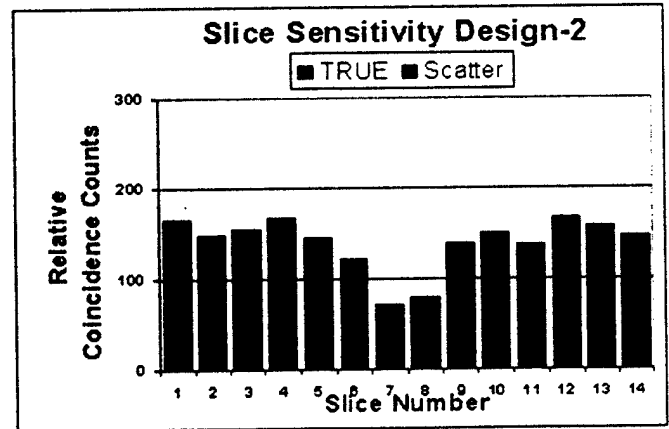
coincidence time window. Scaling factor, τ_c , was calculated analytically for 24-cm FOV.



(a)



(b)



(c)

Fig. 5. Comparison of Monte Carlo simulation results of slice sensitivities for true and scatter coincidence components. (a) No-Septa. (b) Design-1 (7-Septa). (c) Design-2 (5-Septa).

All parameters were estimated based on singles, trues and accidental coincidence measurements for no-septa case [see Fig. 3(a) and (b)]. Estimated parameters are shown in Table II.

The 1.5 mCi, 3.5 mCi, and 2.9 mCi amounts of ^{18}F -FDG were placed in a NEMA water phantom for no-septa, Design-1 and Design-2 cases, respectively. True and accidental count rates were measured in full 3-D acquisition mode as the activity decayed for each configuration in the brain mode. Having measured SF values, trues (T , unscattered and scattered coinci-

TABLE III
COMPARISON OF MONTE CARLO SIMULATION SF RESULTS (IN PERCENT) OF
THREE SEPTA DESIGNS FOR EACH SLICE

Slice Number	No Septa	Design-1	Design-2
1	34.4	43.5	22.6
2	34.1	20.3	23.3
3	32.8	16.9	22.2
4	34.3	16.0	22.1
5	33.3	17.1	20.4
6	33.4	16.0	22.3
7	32.6	29.5	28.2
8	33.3	26.3	26.5
9	32.9	19.5	22.4
10	33.1	18.8	20.5
11	32.7	20.0	22.3
12	34.1	19.8	20.6
13	33.0	23.9	21.1
14	33.6	37.2	19.8

dences) and accidental rates (R), NEC rate was calculated by using following equation:

$$NEC = \frac{T^2(1 - SF)^2}{(T + kR)} \quad (5)$$

where k is 1 or 2 depending on the randoms correction methods. In this paper, k is equal to 2. Experimental results were compared for three configurations.

Comparison of true and accidental count rates was presented in Fig. 3(a) and (b) for all configurations. NEC rates were calculated using (5) and shown in Fig. 4. SF values for 14 individual slices were estimated separately in fully 3-D by Monte Carlo simulations to obtain the scatter components. Fig. 5 compared the slice sensitivities for three detector configurations. It also showed true and scatter components for all slices. Table III summarized the slice-based SF values estimated by the simulation.

VI. MONTE CARLO SIMULATION OF SEVERAL SEPTA CONFIGURATIONS FOR FULL AXIAL FIELD-OF-VIEW (13.1 cm)

The performances of three simple septa configurations (recall Fig. 2) were tested and compared in the previous sections. Unfortunately, limited axial field-of-view (AFOV) (3.85 cm) of the physical detectors is insufficient to completely exhibit the differences in the performance of septa configurations for full AFOV (13.1 cm). However, the measurements and simulations for limited AFOV scanner were essential to determine the deadtime parameters for the scanner electronics. With the same electronics deadtime, parameters extended to a 48-detector-ring-scanner with 13.1 cm AFOV was simulated for various septa designs shown in Fig. 6. 48-detector-ring-scanner was assumed electronically to have three independent regions in one module. Each region was assumed to have the same electronics architecture as the MDAPET prototype scanner so that deadtime constants would be effectively reduced by $48/14 \approx 3.43$ times. τ_{module} and τ_1 were estimated roughly $0.26 \mu\text{sec}$ and $0.56 \mu\text{sec}$, respectively. To estimate the SF values, Monte Carlo simulations were performed for all septa configurations based on NEMA standard as explained in Section IV and results were compared in Table IV. Similarly, true, accidental count rates and NEC rates were presented in Figs. 7(a) and (b) and 8.

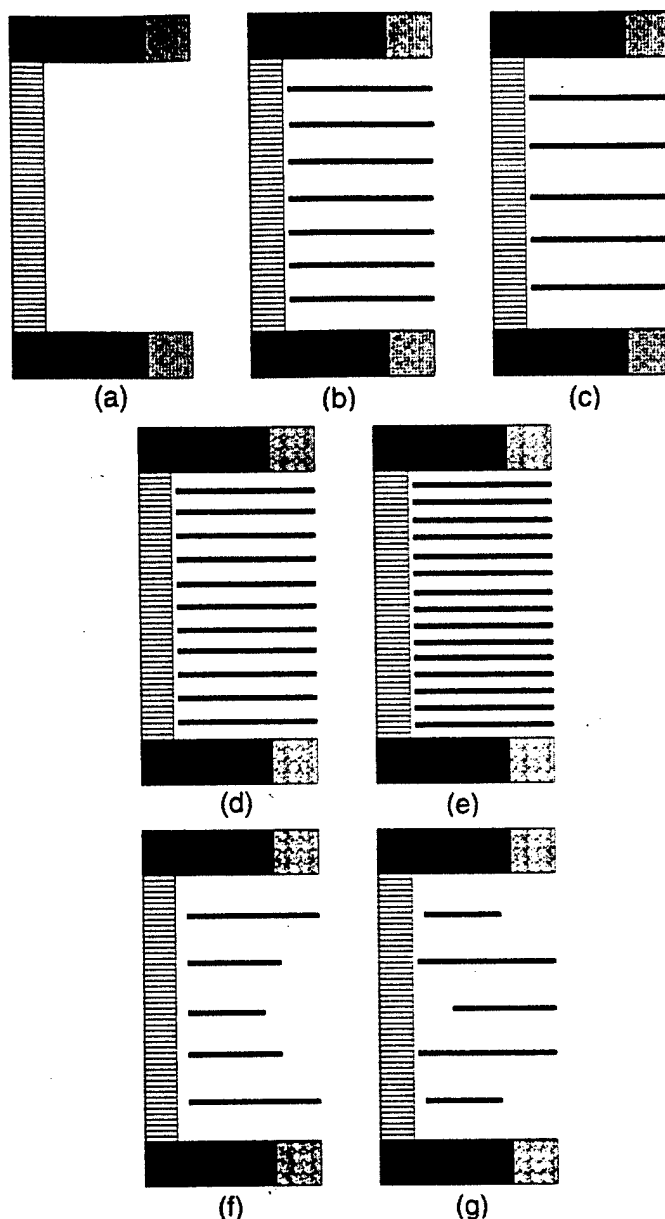


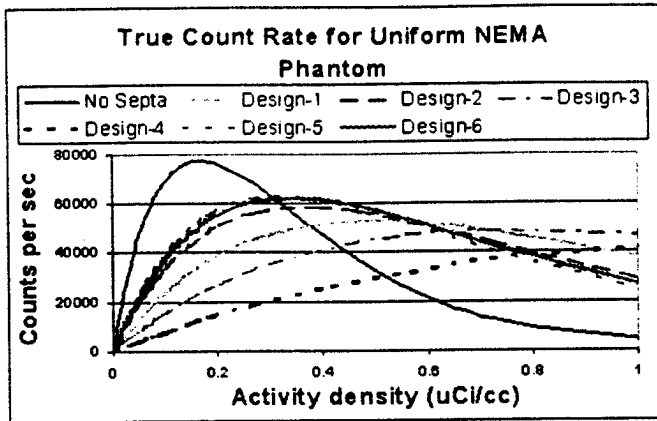
Fig. 6. Axial view of the proposed detector module (48 detector rings, 2.75-mm axial pitch) for seven septa configurations. (a) No-septa. (b) Design-1: 7-septa-in. (c) Design-2: 5-septa-in. (d) Design-3: 10-septa-in. (e) Design-4: 15-septa-in. (f) Design-5: C-shape-design. (g) Design-6: W-shape-design. Septa thickness was chosen to be 2 mm in all designs.

TABLE IV
COMPARISON OF MONTE CARLO SIMULATION SF RESULTS IN PERCENT FOR
13-CM AXIAL FOV PET SCANNER IN BRAIN MODE

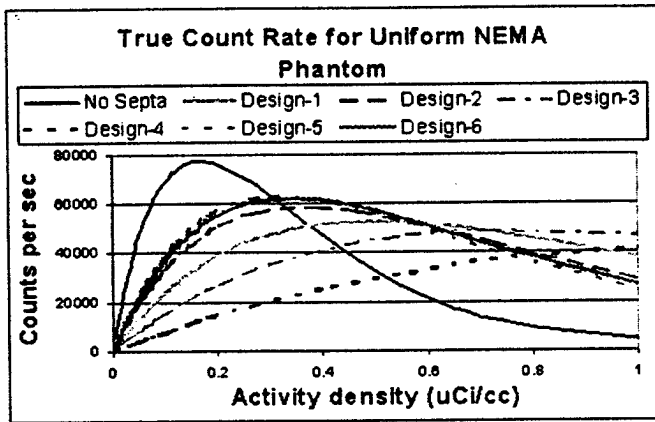
	R=0cm	R=4.5cm	R=9cm	SF(%)
No Septa	33.0	34.1	29.2	31.4
Design-1	18.9	19.9	15.9	17.7
Design-2	22.7	25.0	20.0	22.1
Design-3	13.4	15.5	12.4	13.7
Design-4	9.3	11.1	7.8	9.2
Design-5	25.1	27.1	22.0	24.2
Design-6	23.9	26.9	20.9	23.5

VII. DISCUSSION AND CONCLUSION

As the first part of this paper, the performances of three simple septa configurations were tested and compared for 3.85-cm AFOV having 13.1-cm axial opening. Design-1 and



(a)



(b)

Fig. 7. Comparison of simulated count rates for seven detector configurations, (a) true, and (b) accidental rates.

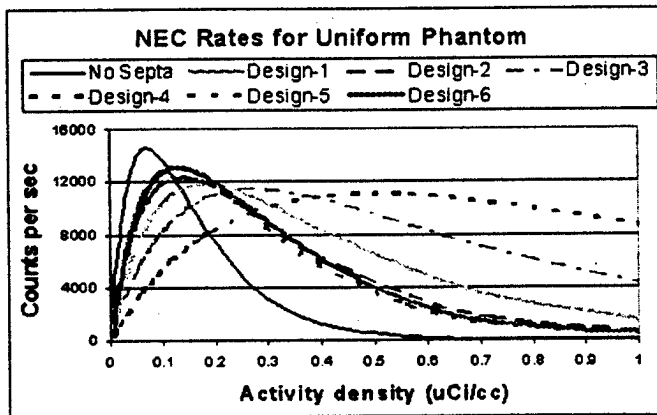


Fig. 8. Comparison of simulated NEC rates for seven septa configurations.

Design-2 have performed better than no-septa case in terms of NEC for limited AFOV. Design-2 peaked at $0.18 \mu\text{Ci/cc}$ with ~ 1.6 Kcps value (see Fig. 4) and the camera sensitivity was estimated 53% compared to no-septa case [see Fig. 5(a) and (c)]. Design-1 peaked at $0.22 \mu\text{Ci/cc}$ with ~ 1.5 Kcps value (see Fig. 5) and the camera sensitivity was estimated 35% compared to no-septa case [see Fig. 5(a) and (b)]. The experimental scatter fractions (recall Table I) were found to be higher than those obtained from simulation results especially in Design-1 and Design-2 configurations. Mechanical tolerances on septum

thickness and positioning might be the only explanation why scatter fractions were measured higher. Similarly, discrepancies between measurements and simulation results were observed on the coincidence sensitivity [recall Fig. 3(a)]. These two factors cause slight mismatch between Monte Carlo predictions and the experimental results in NEC (see Fig. 4). However, there is noticeably better agreement between the experiment and simulation in no-septa case.

NEC rates also change depending on the size of the phantom and ring diameter of the scanner. Having smaller ring diameter increases the sensitivity of the system. However, accidental coincidence rate grows faster resulting in an increase in deadtime and degrading NEC rates as a tradeoff. Having larger phantom affects the SF values significantly, especially in the brain mode. Using smaller cylindrical head phantoms would have been more realistic to compare scanner performance for different configurations. Nevertheless, NEMA phantom with 21-cm diameter and 18-cm height was used in the measurements to be consistent with the standard.

As the second part of this paper, the performances of seven septa configurations were simulated for 13.1-cm AFOV of 48-detector-ring-scanner. NEC for no-septa case peaked nearly at $0.07 \mu\text{Ci/cc}$ with ~ 14 Kcps value and fell off quickly. Monte Carlo simulation program also predicted that NEC for Design-4 using 15 septa peaked around $0.5 \mu\text{Ci/cc}$ with ~ 11 Kcps. Other intermediate septa configurations exhibited peak values of NEC rates between no-septa and Design-3 values.

This paper also suggests a recipe to determine possible intermediate septa configurations. Since scanner electronics plays an essential role in the scanner performance, preliminary measurements for no-septa case help to accurately determine the deadtime parameters. Then, by changing the number, length and thickness of each septum, septa configuration can be optimized to meet the maximum performance for the particular range of activity concentration.

In the brain studies, typical activity concentration value ranges between $0.15 \mu\text{Ci/cc}$ and $0.30 \mu\text{Ci/cc}$ for 10-mCi $^{18}\text{F-FDG}$ injection. In this range, intermediate septa configurations such as Design-1, Design-2, Design-5, and Design-6 might be suggested. For dynamic studies where 50 mCi of $^{15}\text{O-H}_2\text{O}$ is injected, the activity concentration in the FOV is no less than $0.35 \mu\text{Ci/cc}$. Then, Design-3 and Design-4 would perform better compared to others. No-septa configuration reaches its NEC peak rate around $0.07 \mu\text{Ci/cc}$. As a result, in no-septa configuration less amount of activity (e.g., 5 mCi) might be utilized compared to typical clinical 10-mCi dose.

VIII. FUTURE STUDY

In this paper, count rate performances of septa configurations were compared. Lesion imaging in the brain mode will be a follow-up study to investigate the possible use of intermediate septa designs in the clinical studies.

ACKNOWLEDGMENT

The authors would like to thank the Radiation Physics machine shop personnel for their valuable support and assistance in constructing the mechanical parts to modify MDAPET scanner modules.

REFERENCES

- [1] T. J. Spinks, T. Jones, D. L. Bailey, D. W. Townsend, S. Grootenok, P. M. Bloomfield, M. C. Gilardi, M. E. Casey, B. Sipe, and J. Reed, "Physical performance of a positron tomograph for brain imaging with retractable septa," *Phys. Med. Biol.*, vol. 8, pp. 1637-1655, 1992.
- [2] T. K. Lewellen, S. G. Kohlmyer, R. S. Miyaoka, M. S. Kaplan, C. W. Stearns, and S. F. Schubert, "Investigation of the performance of the General Electric ADVANCE positron emission tomograph in 3-D mode," *IEEE Trans. Nucl. Sci.*, vol. 35, no. 1, pp. 2199-2206, 1996.
- [3] D. L. Bailey, T. Jones, T. J. Spinks, M. C. Gilardi, and D. W. Townsend, "Noise equivalent count measurements in a neuro-PET scanner with retractable septa," *IEEE Trans. Med. Imag.*, vol. 10, pp. 256-260, 1991.
- [4] C. W. Stearns, S. R. Cherry, and C. J. Thompson, "NECR analysis of 3-D brain PET scanner designs," *IEEE Trans. Nucl. Sci.*, vol. 42, pp. 1075-1079, 1995.
- [5] E. Tanaka, T. Hasegawa, T. Yamashita, H. Okada, and H. Murayama, "A 2D/3-D hybrid PET scanner with rotating partial slice-septa and its quantitative procedures," *Phys. Med. Biol.*, vol. 45, pp. 2821-2841, 2000.
- [6] T. G. Turkington and W. H. Sampson, "Optimizing septal spacing for gamma camera PET imaging," *IEEE Med. Imag. Conf. Rec.*, vol. 3, p. 17/67, 2000.
- [7] S. J. Glick, C. J. Groiselle, J. A. Kolthammer, and R. Z. Stodilka, "Optimization of septal spacing in hybrid PET using estimation task performance," in *IEEE Med. Imag. Conf. Rec.*, 2001.
- [8] S. C. Strother, M. E. Casey, and E. J. Hoffman, "Measuring PET scanner sensitivity: Relating countrates to image signal-to-noise ratios using noise equivalent curves," *IEEE Trans. Nucl. Sci.*, vol. 37, no. 2, pp. 783-788, 1990.
- [9] C. J. Thompson, "The effect of collimation on scatter fraction in multi-slice PET," *IEEE Trans. Nucl. Sci.*, vol. 35, pp. 598-602, 1988.
- [10] L. E. Adam, J. S. Karp, and G. Brix, "Investigation of scattered radiation in 3D whole-body positron emission using Monte Carlo simulations," *Phys. Med. Biol.*, vol. 44, no. 12, pp. 2879-2895, 1999.
- [11] R. Lecomte, "Analytical study of performance in a 3D PET scanner," *Phys. Med. Biol.*, vol. 37, no. 3, pp. 623-634, 1992.
- [12] C. J. Thomson, C. J. Moreno, and Y. Picard, "PETSIM: Monte Carlo simulation of all sensitivity and resolution parameters of cylindrical positron imaging systems," *Phys. Med. Biol.*, vol. 37, pp. 731-749, 1992.
- [13] J. Uribe, H. Baghaei, H. Li, S. Yokoyama, N. Zhang, J. Wang, F. R. Dobbs, and W. H. Wong, "Basic imaging performance characteristics of a variable field of view PET camera using quadrant sharing design," *IEEE Trans. Nucl. Sci.*, vol. 46, pp. 491-497, 1999.
- [14] NEMA NU 2, "Performance measurements of positron emission tomographs," 2001.
- [15] L. Eriksson, K. Weinhard, and M. Dahlbom, "A simple data loss model for positron camera systems," *IEEE Trans. Nucl. Sci.*, vol. 41, pp. 1566-1570, 1994.
- [16] M. Conti, M. E. Casey, L. Eriksson, and M. Eriksson, "Benchmarking a Monte Carlo simulation code on a prototype LSO scanner," in *IEEE Med. Imag. Conf. Rec.*, 2001.

Effects of Photomultiplier Gain Drift and Radiation Exposure in Position-Sensitive Detectors of Dedicated PET Cameras

Jorge Uribe, *Member, IEEE*, Hongdi Li, *Member, IEEE*, Hossain Baghaei, *Member, IEEE*, Mehmet Aykac, Yu Wang, Yaqiang Liu, Tao Xing, and Wai-Hoi Wong, *Member, IEEE*

Abstract— Arrays of scintillation crystals optically coupled to four single-anode photomultipliers (PMT) are commonly used in PET cameras. The accuracy of the crystal-position decoding relies on the relative gain stability of all 4 PMT over time. The drift in the gain of one PMT relative to the other three distorts the two dimensional (2-D) crystal-decoding map and causes wrong crystal assignment of a gamma hit. We have studied gain stability and its effect on the 2-D decoding map using 4 Philips XP1911 PMT (19mm diameter) coupled in the quadrant-sharing mode (PQS) to a position-sensitive BGO array (7 x 7) over 100-day period. The effect on PMT gain due to radiation exposure of the block was also studied. Using 662 KeV gamma rays from a Cs-137 source and the collimated light of a blue LED coupled to the block we measured the individual PMT gain drift, total composite-energy pulse heights and 2-D decoding maps. Some of the drifts were temperature dependent. The measurements were also corrected for temperature variations of the technique. It was found that throughout the duration of the experiment all four PMT presented similar and continuous gain shifts averaging an 11% drop after 100 days. Gain shift of up to 17% was caused by a 24 hour continuous exposure to radiation with high gain tubes gaining the largest increase. Effects of gain drift on the two-dimensional map were recorded using the position of center and corner crystals in the 2-D map. The change in the decoded crystal positions in this 100-day period was found to be small; a 4-channel position displacement was observed for a gaussian peak with a full-width-half-maximum (FWHM) of 23 channels in 100 days. There were both systematic and random changes in the decoded crystal position. The random changes were mostly due to radiation-exposure variations. The long term (systematic) changes were due to the relative PMT gain-drift variations among the 4 PMT in the 100-day period. For the 7x7 BGO block, the impact was small, but for a much larger array (crystals with high light output), this shift would be important. Radiation induced gain shift is important for clinical situations because it would depend on frequency and type of studies performed.

This work was supported in part by the NIH Grant ROI CA58980, NIH Grant ROI CA61880, NIH Grant ROI CA76246, NIH Grant ROI CA58980S1, Texas Higher Education Advanced Technology Grant, John S. Dunn Foundation Research Grant, Mike Hogg Foundation, and by the Cobb Foundation for Cancer Research.

Jorge Uribe, Hongdi Li, Hossain Baghaei, Mehmet Aykac, Yu Wang, Yaqiang Liu, Tao Xing and Wai-Hoi Wong are with the University of Texas, M.D. Anderson Cancer Center, Houston, TX 77030 USA (J. Uribe's telephone: 713-745-1179, e-mail: juribe @di.mdacc.tmc.edu).

I. INTRODUCTION

POSITION sensitive detector arrays using single-anode photomultipliers are commonly used in commercial PET cameras as well as research / prototype PET cameras due to their low production cost compared to detector arrays coupled to position-sensitive PMT. It is essential that all four single-anode PMT have balanced amplification gain in order to accurately decode the crystal positions in a detector block/array. The PMT gain change due to temperature variation is well known. In this study, we measured the effect of (a) gain drift due to the aging of the Philips (Photonis) XP 1911 PMT, and (b) radiation exposure, on the 2-D crystal decoding map of a position-sensitive BGO detector array.

II. METHODS AND RESULTS

The specific detector array studied was the PMT quadrant-sharing detector (PQS) design introduced by our laboratory [1-2] and used in the prototype whole-body PET camera developed in our laboratory at the University of Texas MD Anderson Cancer Center (MDAPET) (Fig.1) [3-4]. The PQS detector design is also used in the new high resolution LSO PET from Siemens/CTI Corporations [4-6]. The PQS

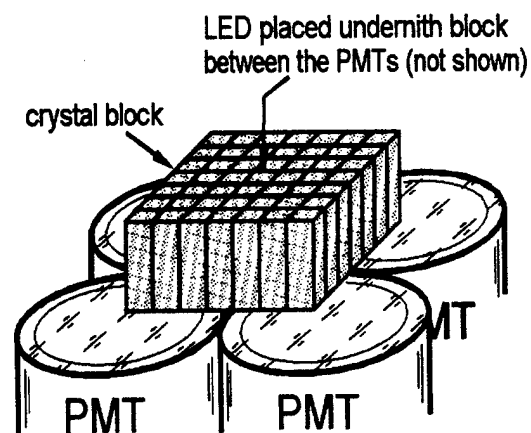


Fig. 1 Detector block coupled to four PMT in Photomultiplier Quadrant Sharing mode

detector design could be particularly sensitive to PMT instability because each PMT participates in the decoding of four detector arrays/blocks.

For a period of 100 days, we have recorded the gain of four PMT (19mm -- Philips XP1911), the 2-D crystal-decoding map of a 7x7 BGO detector array coupled to these PMTs, and the total composite energy spectra (composite pulse-height spectra) from the detector array (Fig. 2) illuminated by a Cs-137 point source.

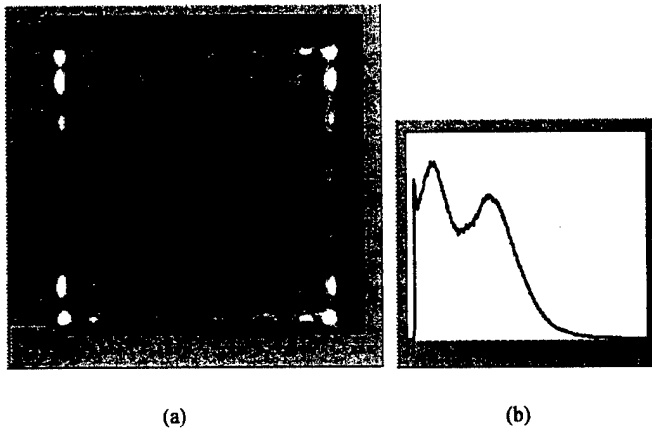


Fig. 2. (a) 7x7 BGO crystal decoding map, (b) total composite energy.

Contrary to the composite pulse-height spectrum that demonstrated a photopeak, the individual pulse-height spectrum of any one PMT does not present a peak. This was due to the fact that the light collected by a single PMT could come from any one crystal in the array when the array was exposed to a non-collimated radioactive source. Hence, it is difficult to track the gain of each individual PMT using radioactive sources. For this reason, we implemented a light-emitting-diode (LED) setup that allowed the measurement of each PMT gain while the 4 PMT are still coupled to the detector block (Fig. 1 and Fig. 3). The LED injected light only into central crystal of the array, which generated a "photopeak" signal in each individual PMT output signal (fig. 3). This LED generated "photopeak" is used for monitoring the gain drift of each individual PMT. In this experiment, it was essential to maintain a fixed geometric placement and light-collection efficiency for each PMT, by keeping the optical coupling between the crystal and PMT unperturbed, in order to avoid introducing additional variables beside the shifts of the PMT gain itself.

Variations in the 2-D crystal-decoding map were monitored using (a) the positions of the center and corner crystals in the crystal-decoding map (Cs-137) like the one shown in Fig. 2, and (b) the center position of the single peak obtained while the LED shone at the center of the block (Fig. 4).

Although, we have taken great care in designing a temperature stable current source to pulse the blue LED, the

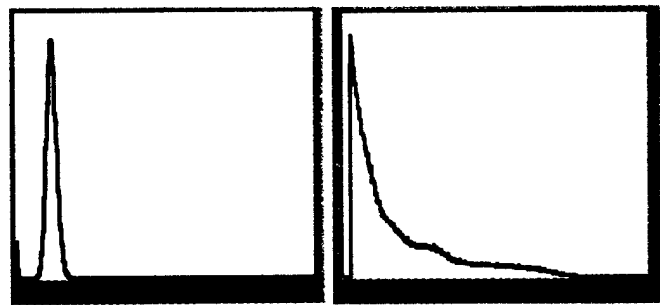


Fig. 3. (Left) PMT energy spectrum when coupled to a detector array with an LED shining at the center crystal. (Right) Using a Cs-137 source shining the whole array

temperature dependency of the LED's light output itself is unavoidable. In fact, the LED light output is much more sensitive to temperature than that of the PMT gain. The LED was located between the four PMT making it susceptible to the heat dissipated by the PMT's voltage dividers, in addition to temperature changes from the environment. The heat dissipation from the LED itself and the LED-pulsing duty cycle (pulsing heating) also change the LED light output. The following compensation method is used to derive the PMT gain that is independent of the temperature effect of LED signals:

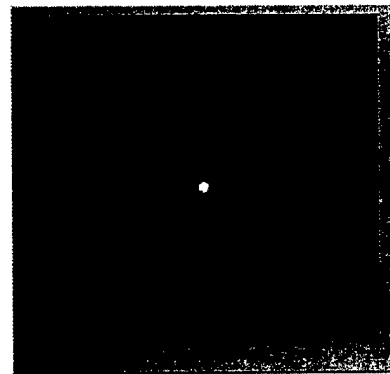


Fig. 4. LED position-decoding map.

Let the gain of the four PMT be $A(t, T)$, $B(t, T)$, $C(t, T)$ and $D(t, T)$, where t is time and T is temperature. Let E be the gamma energy of Cs-137. The gain $A(t, T)$ can be algebraically written as,

$$A(t, T) * E = [A(t, T) * L(T) * E * [A(t, T) + B(t, T) + C(t, T) + D(t, T)]] / [[A(t, T) + B(t, T) + C(t, T) + D(t, T)] * L(T)]$$

$A(t, T) * L(T)$ is the signal output of PMT A under LED illumination at temperature T , which will be denoted as $a(t, T)$. $B(t, T) * L(T)$ is the signal output of PMT B under LED illumination at temperature T , which will be denoted as $b(t, T)$, and so on. Hence, the above equation can be rewritten as

$$A(t,T) * E = [a(t,T) / [a(t,T) + b(t,T) + c(t,T) + d(t,T)]] * E * [A(t,T) + B(t,T) + C(t,T) + D(t,T)]$$

$E * [A(t,T) + B(t,T) + C(t,T) + D(t,T)]$ is actually the C-137 composite photopeak pulse height of the detector array from 4 PMT and will be denoted as Q. Hence, the gain of PMT-A can be written as

$$A(t,T) = (a / (a + b + c + d)) * (Q(t,T) / E) \quad (1)$$

Hence, the absolute gain of PMT-A can be derived from the LED generated "photopeak" pulse heights (a, b, c, d) even though a, b, c, d, are very sensitive to temperature drift of the LED. In essence, in equation-1, the ratio $a/(a+b+c+d)$ cancels the temperature dependence of the LED.

A. PMT Gain-Drift Results

Long-Term Drift

The raw-PMT-gain "a", the corrected PMT-gain "A" for one of the four PMT (PMT-A) and the ambient temperature of the 100-day period are shown in Fig. 5. The gain of PMT-A dropped 11% systematically in 100-day period. All four PMT showed similar changes qualitatively. The gain-drop averaged over 4 PMT was also 11%. The worst PMT dropped its gain by 14% and the best PMT dropped its gain by 9%. It can also be observed from fig.5 that the ambient temperature was relatively stable in the 100-day period. Hence, we concluded that the long term PMT-gain drop is not due to temperature but due to the usage (light load) of the PMT. The individual PMT-gain drift is shown in Fig.6.

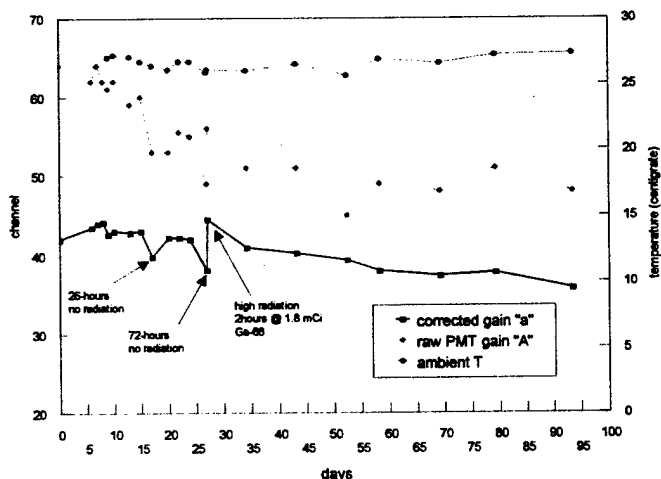


Fig. 5. "Photopeak" pulse height for PMT-A: both uncorrected LED gain "a" and corrected gain A.

Short-Term Drift

The effect of radiation exposure on PMT gain was also investigated. Between data acquisition times the detector block was kept exposed to the ¹³⁷Cs source. Exceptions to this condition took place on days 17 and 27 when the

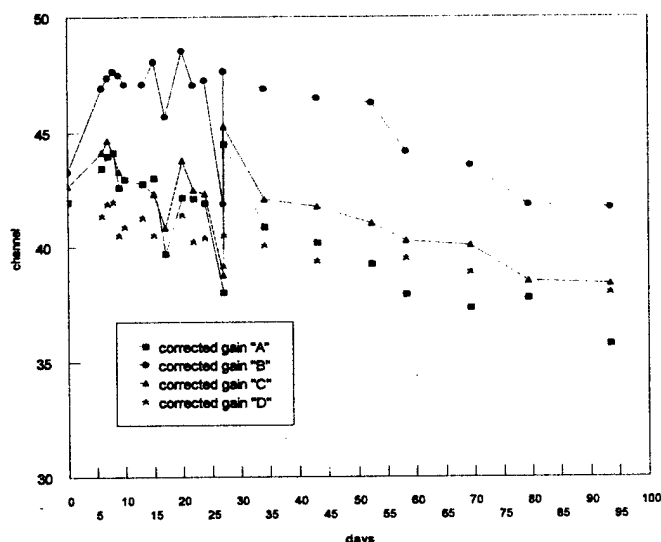


Fig. 6. The corrected PMT gain for all four PMT

radiation source was removed, previous to the measurement, for 26 and 72 hours respectively. Clearly there was a short-term gain drop from temporary idling as indicated by the marks in Fig. 5. For the 26-hr and 72-hr idling, the average gain dropped 4.8% and 9.2%, respectively. The opposite case (exposed to higher level of radiation after the 72-hr idling) was also explored (fig.5). After exposing the system to a 1.8 mCi of ⁶⁸Ga for 2 hrs, some short-term gain increase above long-term ambient values (0%-6%) were shown by the third mark in fig.5, fig.6 and Table I. Hence, idling a camera by 1-3 days may temporarily desensitize its PMT by 3-12%, but a higher radiation load for the camera, especially after a few days of idling, can sensitize its PMT by 4-17%. The magnitude of desensitization/sensitization among PMT was not the same as shown in table I. The misalignment in gain change among the four PMT can be as much as 13% (minimum to maximum change among 4 PMT).

TABLE I
PMT-GAIN SHIFT AND RADIATION EXPOSURE

	PMT-A	PMT-B	PMT-C	PMT-D
gain (A/LmF)	80	80	80	54
Δ gain after idling 26 hrs	-7%	-4%	-5%	-3%
Δ gain decrease after idling 72 hrs	-10%	-12%	-11%	-4%
Δ gain from long term value after 2 hrs of ⁶⁸ Ga	6%	0%	6%	0%
Δ gain from 72-hr idling value after 2 hrs of ⁶⁸ Ga	16%	12%	17%	4%

The summary of gain variation as a function of activity in the radiation source placed in front of the block is shown in Fig.

7. The gain increase was larger for PMT "A" (80 A/lmf from manufacturer) compared to PMT "D" (54A/lmf), indicating that higher gain PMTs show bigger shift. Gain shifts by as much as 17% making it much larger than the shift from PMT aging (5%). Hence, the short-term gain-drift for individual PMT can be much larger than the long-term gain-drift (100 days). The short-term gain-drift misalignment among PMT due to idling and exposure after idling may have the most significant impact in position-decoding accuracy and image-resolution degradation in the operation of a camera.

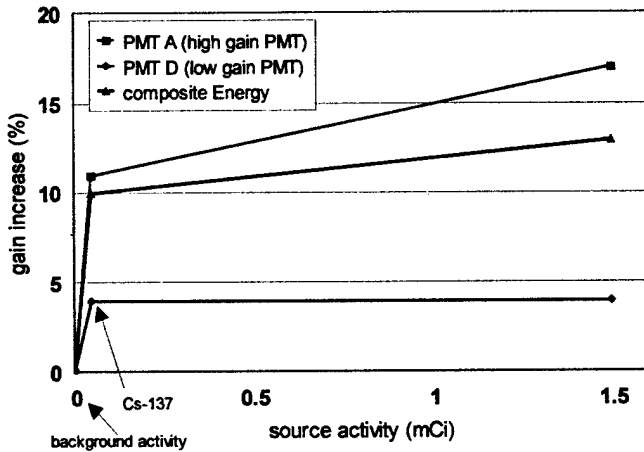


Fig. 7. PMT gain as a function of radiation exposure

B. Decoded-Position-Drift Results

Fig. 8 presents the position of the center peak from the LED 2D map (Fig. 4) for the same time extent. Linear interpolation of the X and Y coordinates show slight decrease by the end of the 100 day period representing a 4 channel shift in a 256x256 2D map. The total 100-day X-Y displacement of 4 channels was 17% of the FWHM (24 channels) of the center crystal peak. For the 7x7 BGO array studied, this long term drift may marginally affect the decoding accuracy, at least for the four PMT samples. However, the same 4-channel drift would be significant in a higher resolution array (say, 12x12) allowed by a high light-output scintillators (e.g. LSO). In a 12x12 array, the center peak FWHM will be reduced to 14 channels and a 4-channel drift would mis-assign many events into the neighboring crystals. Thus, 100-day long-term PMT-gain shift would be significant for LSO and less significant for BGO. The short-term gain drift, after idling for 72 hrs, also generated a displacement of 4 channels that was similar to that of the long-term (100 days) displacement. Hence, the short-term crystal-positioning errors would be as important as the long-term crystal-positioning errors for BGO arrays. The short-term positioning errors would be more significant for LSO arrays as discussed earlier. It should be noted that the positioning errors measured here were dependent on the relative positions of the four PMT. If the four PMT positions

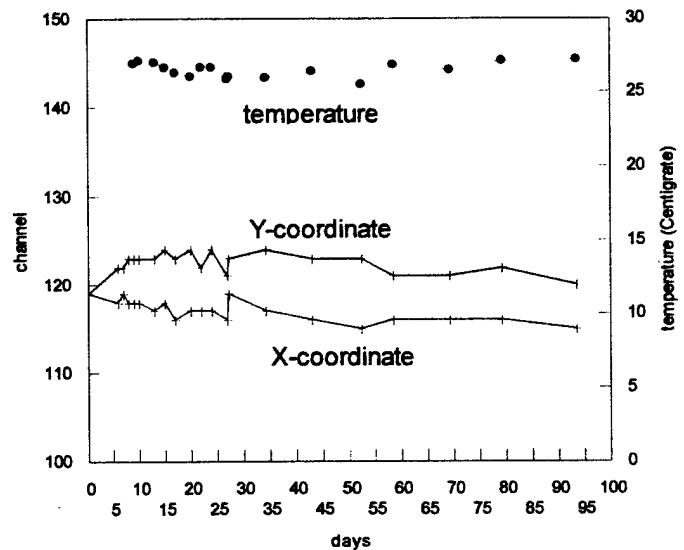


Fig. 8. X and Y Coordinates of the LED position peak in the 2-D detector-position decoding map

were permuted in the experiment, the positioning drift would be different.

III. CONCLUSION AND DISCUSSIONS

Both long-term (100 days) and short-term (2 hrs) gain drift from PMT aging and from radiation exposure has been studied. The average long-term gain-drift for the four PMT studied was found to be -11% with a gain misalignment of 5% among the four PMT. The decrease in gain was mostly due to aging of the PMT. The short-term PMT-gain drift and the decoded-position drift was found to be similar or larger than the long-term drifts. Since the long term-drift would most likely be eliminated by the periodic maintenance (PMT tuning) of cameras. The short-term PMT gain and crystal-position change are more worrisome, especially after idling the camera over a weekend/holiday period, or immediately after exposing the camera to high dose studies. More detailed studies on a much larger number of PMT samples are needed to investigate the short term effect further. Currently, tuning all the PMT in a dedicated PET take 1-4 hours. Hence, it is not practical to tune a PET camera to compensate for the short-term drift, at least currently. The short-drift gain drift and positioning drift will be even more important for the next generation of PET cameras using high light-output crystals such as LSO and GSO.

IV. REFERENCES

- [1] W.H. Wong, "Positron Camera Detector Design with Cross-Coupled Scintillators and Quadrant Sharing Photomultipliers", IEEE Transactions on Nuclear Science Vol.40, number 4 pp. 962-966, 1993.
- [2] Wong W-H, Uribe J, Hicks K, Zambelli M, Hu G: A 2-dimensional detector decoding study on BGO array with quadrant sharing photomultipliers. IEEE Transactions on Nuclear Science. 41(4), 1453-1457, 1994.

- [3] Wong W-H, Uribe J, Lu W, Guoji H., Hicks K: Design of a variable field of view Pet camera. IEEE Transactions on Nuclear Science, 43(3): 1915-1920, 1996.
- [4] J. Uribe, H. Baghaei, H. Li, S. Yokoyama, N. Zhang, J. Wang, F. R. Dobs, W.H. Wong, "Basic Imaging Performance Characteristics of a Variable Field of View PET Camera Using Quadrant Sharing Detector Design", IEEE Transactions on Nuclear Science 46:3 pp. 491-497, 1999.
- [5] Schmand M, Eriksson L, Casey ME, Andreaco MS, Melcher C, Wienhard K, Flugge G, Nutt R. Performance results of a new DOI detector block for high resolution PET-LSO research tomograph HRRT. IEEE Trans Nucl Sci, 45(6): 3000-3006, December 1998.
- [6] Wienhard K, Schmand M, Casey ME, Baker K, Bao J, Eriksson L, Jones WF, Knoess C, Lenox M, Lercher, Luk P, Michel C, Reed JH, Richerzhagen N, Treffert J, Vollmar S, Young JW, Heiss WD, Nutt R. The ECAT HRRT: Performance and first clinical application of the new high resolution research tomograph. IEEE Medical Imaging Conference Record (CD-ROM), 2000,

A Study of Coincidence Line Spread Function (CLSF) Estimation for Small Scintillators Using Quadrant Sharing Technique

Mehmet Aykac, Hongdi Li, *Member, IEEE*, Jorge Uribe, *Member, IEEE*, Yu Wang, Hossain Baghaei, *Member, IEEE*, Yaqiang Liu, Tao Xing and Wai-Hoi Wong, *Member, IEEE*

Abstract— Inter-crystal scatter is one of the primary reasons to misplace the coincidence events in positron emission tomography (PET). The probability of Compton scattering of a 511 KeV photon within the crystal is more than 50 % of all interactions. Unlike one-to-one scintillator-photomultiplier tube (PMT) coupled (discrete) detectors, detector blocks utilizing the light sharing technique must have an additional degradation on their spatial resolution due to shared scintillation photons within the block. This study focuses on an estimation of the coincidence line spread function (CLSF) for 7x7 BGO (bismuth germanate) detector blocks by comparing the simulation results for discrete and light shared detectors. Based on experimental measurements, decoding probabilities, which describe the uncertainty in positioning between neighboring crystals, were estimated from photoelectron statistics. The results were embedded into the Monte Carlo simulation to estimate the CLSF more accurately. In this study, two 7x7 BGO detector blocks (2.68mm x 2.68mm x 18mm) with different surface treatments coupled to 4 PMTs were used to estimate the decoding probability values. For discrete detectors, the FWHM values of CLSF for 7x7 BGO block with crystal dimensions of 2.68mm x 2.68mm x 18mm were approximately found 1.47mm for discrete detectors and 1.51mm for light shared detectors. The intrinsic spatial resolutions of 7x7 light shared BGO block with crystal dimensions of 2.68mm x 2.68mm x 18mm for 20cm, 40cm and 80cm detector ring diameters were projected to 1.57mm, 1.75mm and 2.30mm, respectively. Making the assumption that LSO (lutetium orthosilicate) crystals have 5 times more light output than BGO, 14x14 LSO block with crystal dimensions of 1.32mm x 1.32mm x 20mm can be decoded and intrinsic spatial resolutions for 20cm, 40cm and 80cm detector ring diameters were expected to be 0.87mm, 1.15mm and 1.91mm, respectively.

I. INTRODUCTION

PET detectors generally exhibit spatial resolution limits due to the choice of crystal length, crystal surface area, the gap between scintillators and the scattering between the crystals. Typically, 511 KeV photons within the detector undergo Compton scattering (54 %), Coherent scattering (6 %) and

photoelectric absorption (40 %). Several investigators [1, 2, 3, 4] discussed inter-crystal effect on the spatial resolution for discrete detectors. Shao [1] mentioned that the inter-crystal scattering has insignificant effect on FWHM of CLSF. Murty [2] reported experimental measurements of the coincidence response for the presence of the neighbor crystals. Cho [3] has also discussed the resolution limits of a PET system for narrow width crystal detector arrays. Comanor [4] investigated the Compton scatter in PET detector modules.

In this study, an effect of uncertainty in decoding probabilities on intrinsic detector resolution will be discussed. In light sharing techniques, crystal decoding in a detector block mainly depends on the total generated photoelectron number. The accuracy of controlling of the light distribution is crucial to decode the crystal elements in the detector block. This effect will introduce degradation on the detector spatial

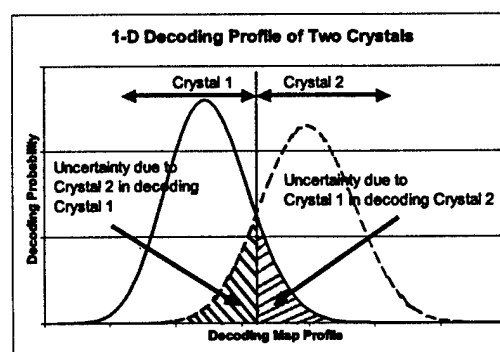


Fig. 1. Representative decoding profile for two neighbor crystals based on deterministic approach.

resolution. Variation in the number of generated photoelectrons causes changes on the uncertainty in crystal decoding. Increased number of collected photoelectrons causes decrease in uncertainty regions between neighboring crystals (see Figure 1), hence provides better decoding map (also known as pseudo map).

II. METHOD

A. Basic Theory of Photoelectron Statistics

Pseudopositions, x and y , shown in Figure 2 can be computed by the following set of equations,

Manuscript received November 20, 2001. This work is supported by NIH grants RO1 CA76246, RO1 CA61880 and RO1 CA58980, the J.S. Dunn Research Foundation, the Cobb Endowment for Cancer Research.

M. Aykac, H. Li, J. Uribe, Y. Wang, H. Baghaei, Y. Liu, T. Xing and W. H. Wong are with the University of Texas, M.D. Anderson Cancer Center, Houston, TX 77030 USA. (Mehmet Aykac's telephone: (713)745-1670, e-mail: aykac2000@yahoo.com).

$$x = \frac{(E_A + E_C)}{(E_A + E_B + E_C + E_D)}, \quad (1)$$

$$y = \frac{(E_A + E_B)}{(E_A + E_B + E_C + E_D)}$$

As suggested by Wong [5], each photoelectron exhibits binomial distribution by going to the PMTs (A+C) with a probability (p) and PMTs (B+D) with a probability (1-p). Therefore the following deterministic equations can describe the photoelectron distribution in x and y dimensions:

$$P(n) = \frac{N!}{(N-n)!n!} \left(\frac{E_{AC}}{N} \right)^n \left(1 - \frac{E_{AC}}{N} \right)^{(N-n)} \quad (2)$$

$$P(r) = \frac{N!}{(N-r)!r!} \left(\frac{E_{AB}}{N} \right)^r \left(1 - \frac{E_{AB}}{N} \right)^{(N-r)} \quad (3)$$

where $N = E_A + E_B + E_C + E_D$: total number of photoelectrons generated in each scintillation event; $E_{AC} = E_A + E_C$: average number of photoelectrons going to PMT A and C; $E_{AB} = E_A + E_B$: average number of photoelectrons going to PMT A and B; n, r ranges from 0 to E_{AC} and 0 to E_{AB} , respectively. Therefore, 2D pseudo map is given by

$$PseudoMap = P(E_{AC})P(E_{AB}) \quad (4)$$

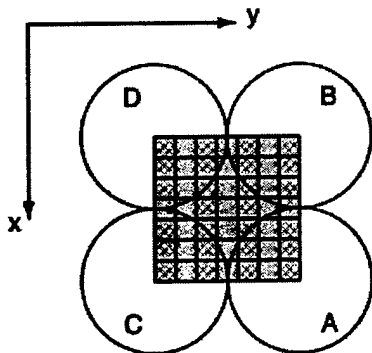


Figure 2. 7x7 scintillator block coupled to 4 PMTs A, B, C, D.

B. Monte Carlo Simulation

Monte Carlo simulation program models the photoelectric absorption, Coherent and Compton scatterings. The interaction probabilities were calculated based on the tabulated values of interaction cross sections for BGO and LSO scintillators. Klein-Nishina formulation was used to estimate the scattering angles for Compton interactions. Elastic scattering was modeled based on Kaplan's [6] implementation. Coherent scattering angles were estimated based on the tabulated scattering amplitudes in Evaluated Photon Data Library. Due to the difficulties of modeling the surface properties of the crystals, scintillation photons were not tracked individually in the scintillators. The photoelectron number was assumed to be proportional to the total energy deposition in the crystal at every interaction.

Positron motion and noncollinearity between annihilation photons were included by using a modified formula of Moses and Derenzo [7]. Same formulation shown in Equation 5 was used to estimate the intrinsic spatial resolution.

$$FWHM_{spa.res.} = \left[FWHM_{CLSF}^2 + 0.0022^2 D^2 + s^2 \right]^{1/2} \quad (5)$$

where D is detector ring diameter, $FWHM_{CLSF}$ is detector coincidence resolution including the decoding and inter-crystal scattering factors, s (0.25 mm) is the ^{18}F positron range in tissue.

C. Experimental Measurements of Decoding Map and Estimation of Decoding Probabilities

To estimate the decoding probability values, pseudo maps were obtained experimentally for two 7x7 BGO detector blocks (2.68mm x 2.68mm x 18mm) with different surface treatments: Cut Type and Lapped Type (removed all blade marks and slightly roughened). 5 surfaces were cut or lapped and the 6th surfaces of the crystals were polished to couple to the PMT. Measurements were performed by using ^{137}Cs and ^{68}Ga sources. Energy thresholds were set to 500 KeV for ^{137}Cs and 380 KeV for ^{68}Ga . Energy spectra were obtained for three individual crystals in each block using predefined regions in 2D pseudo maps: center, bottom middle and bottom right corner (see Figure 2). The centers of crystal elements were chosen manually from the pseudo maps to obtain E_{AC}/N and E_{AB}/N ratios (recall Equations 2 and 3). The number of collected photoelectrons from each crystal was assumed proportional to the corresponding photopeak locations. Based on this assumption, deterministic pseudo maps were calculated by using binomial probability equations given in Equations 2-4. Total photoelectron numbers (N) for every crystal were changed iteratively, until deterministic map matched closely with the experimental pseudo map. Once N values were determined, decoding probability values were calculated using Equation 4 for every crystal in the detector block. These values were used to determine how much spreading occurred to neighboring crystal elements in the block. Average decoding probability values were determined from the individual decoding probability values for 49 crystal elements in the detector block. 7x7 BGO block was considered to have two regions for decoding probabilities: (a) central region (3x3 crystal array) and (b) outer region which surrounds the central region (40 crystals in total). Decoding probabilities were reported separately for two different regions and the entire block.

D. Coincidence Line Spread Function Simulation

Having inter-crystal scatter modeled and decoding uncertainties calculated, two 7x7 BGO scintillator (2.68mm x 2.68mm x 18mm dimensions) blocks were simulated in coincidence. A point source was moved at every 0.2 mm across the detectors and total 500,000 positrons were simulated at every position. CLSF values were estimated based on the energy deposition on the central crystal element

in each detector block. Similar simulations were performed for 14x14 LSO (1.32mm x 1.32mm x 20mm) detector block, intrinsic spatial resolution values were estimated by using the FWHM values of CLSF for different detector ring diameters.

III. RESULTS

Figures 3 and 4 compare the results of experimental and deterministic decoding maps for Cut type 7x7 BGO block. Pseudo maps obtained by using ^{137}Cs (662 KeV) flood source are better decoded than the ones using ^{68}Ga (511 KeV). Figure 5 compares the energy spectra for 3 individual crystals in the block. As expected, 'Center' and 'bottom middle'

crystals lose more scintillation photons than the 'bottom right corner' crystal. Estimated photoelectron numbers are listed for individual crystals in Table I for ^{137}Cs and Table II for ^{68}Ga .

TABLE II
ESTIMATED NUMBER OF PHOTOELECTRONS USING DETERMINISTIC METHOD
FOR 7X7 BGO BLOCK CUT TYPE (^{68}GA)

142	132	120	120	130	134	144
131	124	115	122	126	126	131
128	123	106	120	122	122	133
122	122	113	110	123	122	132
124	123	126	116	120	120	132
126	122	126	122	126	137	143
127	124	121	115	128	138	145

TABLE III
ESTIMATED DECODING PROBABILITIES (%) FOR 7X7 BGO BLOCK CUT TYPE
(^{137}CS)

99.2	97.0	94.3	93.4	95.7	98.3	99.1
94.4	91.3	84.1	79.7	88.1	93.8	96.0
85.2	77.5	78.3	68.5	81.5	80.5	87.4
87.5	79.4	77.4	67.6	72.9	78.4	85.7
84.1	82.0	74.4	74.9	74.3	83.9	90.3
85.0	83.3	78.3	76.6	77.1	89.6	92.9
98.0	92.9	91.0	89.8	91.3	93.3	96.5

TABLE IV
ESTIMATED DECODING PROBABILITIES (%) FOR 7X7 BGO BLOCK CUT TYPE
(^{68}GA)

97.8	94.5	89.5	87.6	93.6	96.8	98.3
91.6	85.8	74.0	65.1	80.0	87.6	92.4
77.2	66.1	65.4	53.4	67.8	71.6	80.8
81.5	68.7	66.7	57.1	61.6	68.2	79.5
77.8	73.3	63.7	60.7	61.3	75.3	84.6
77.3	75.0	68.0	62.1	62.6	80.0	87.8
94.8	88.8	84.1	83.7	83.8	86.5	93.9

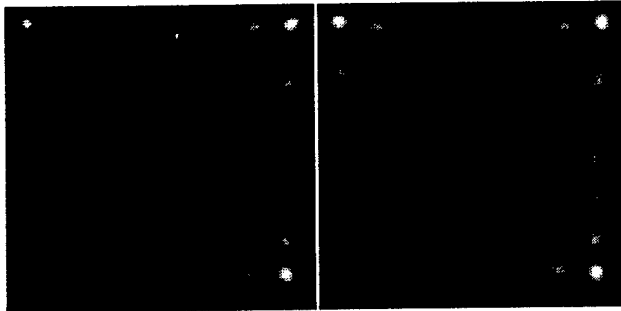


Figure 3. Cut Type. Comparison of 7x7 BGO block decoding maps using ^{137}Cs source. (Left) experiment, (right) deterministic method.

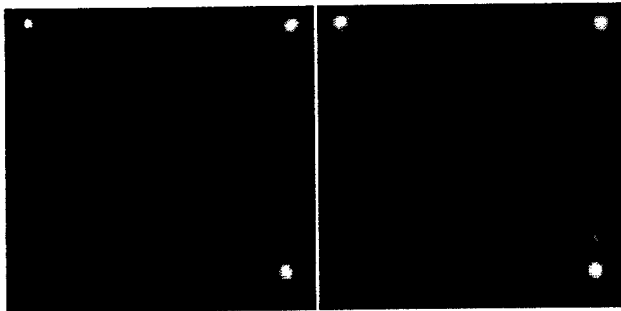


Figure 4. Cut Type. Comparison of 7x7 BGO block decoding maps using ^{68}Ga source. (Left) experiment, (right) deterministic method.

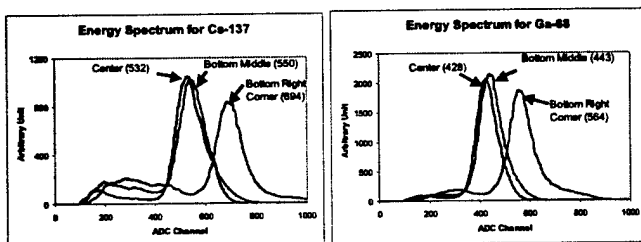


Figure 5. Cut Type. Energy spectra for 3 individual crystals (center, bottom middle, bottom right corner see the detector block in Figure 1). (Left) ^{137}Cs source, (right) ^{68}Ga source.

TABLE I
ESTIMATED NUMBER OF PHOTOELECTRONS USING DETERMINISTIC METHOD
FOR 7X7 BGO BLOCK CUT TYPE (^{137}CS)

176	164	146	150	162	169	178
162	156	143	152	157	157	163
159	152	132	148	152	156	165
154	152	143	138	153	145	164
153	150	143	144	150	146	164
157	147	145	152	157	170	177
158	154	150	143	159	171	181

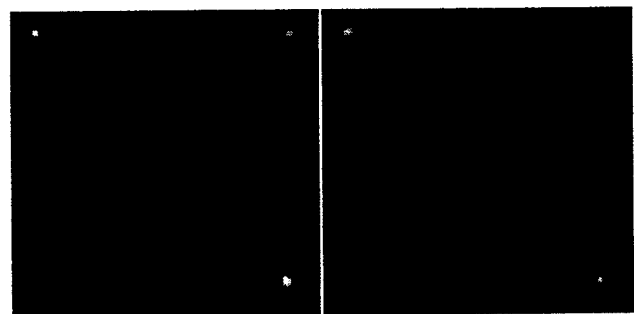


Figure 6. Lapped Type. Comparison of 7x7 BGO block decoding maps using ^{137}Cs source. (Left) experiment, (right) deterministic method.

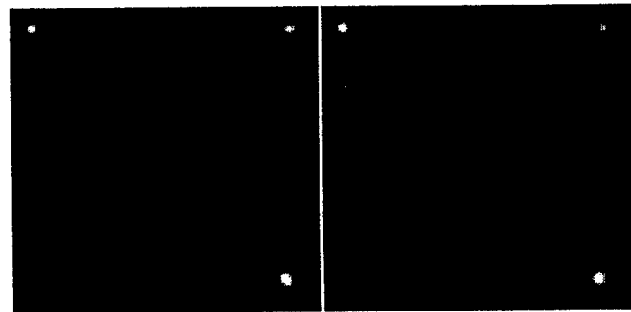


Figure 7. Lapped Type. Comparison of 7x7 BGO block decoding maps using ^{68}Ga source. (Left) experiment, (right) deterministic method.

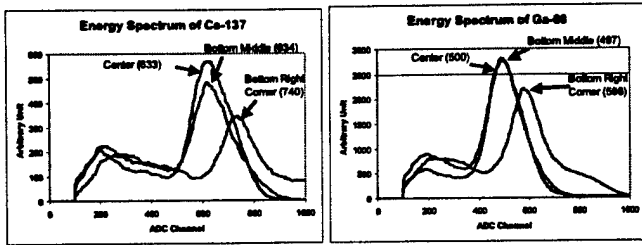


Figure 8. *Lapped Type*. Energy spectra for 3 individual crystals (center, bottom middle, bottom right corner) using (Left) ^{137}Cs source, (right) ^{68}Ga source.

TABLE V

ESTIMATED NUMBER OF PHOTOELECTRONS USING DETERMINISTIC METHOD FOR 7x7 BGO BLOCK *LAPPED TYPE* (^{137}CS)

184	169	161	159	174	177	184
172	162	159	161	171	163	168
163	159	158	167	162	161	171
159	158	162	157	157	161	169
153	158	157	159	156	157	169
159	156	157	163	166	177	183
164	163	157	158	175	179	184

TABLE VI

ESTIMATED NUMBER OF PHOTOELECTRONS USING DETERMINISTIC METHOD FOR 7x7 BGO BLOCK *LAPPED TYPE* (^{68}GA)

150	138	130	130	142	144	150
140	132	130	131	139	133	137
133	130	129	136	132	131	139
130	129	129	128	128	131	138
124	129	126	130	127	128	138
129	127	128	133	135	144	149
133	133	128	129	143	146	150

TABLE VII

ESTIMATED DECODING PROBABILITIES (%) FOR 7x7 BGO BLOCK *LAPPED TYPE* (^{137}CS)

99.2	97.1	94.3	93.4	95.7	98.3	99.1
94.4	91.3	84.1	79.7	88.1	93.8	96.0
85.2	77.5	78.3	68.5	81.5	80.5	87.4
87.5	79.4	77.4	67.6	72.9	78.4	85.7
84.1	82.0	74.4	74.9	74.3	83.9	90.3
85.0	83.3	78.3	76.6	77.1	89.6	92.9
98.0	92.9	91.0	89.8	91.3	93.3	96.5

TABLE VIII

ESTIMATED DECODING PROBABILITIES (%) FOR 7x7 BGO BLOCK *LAPPED TYPE* (^{68}GA)

96.8	93.9	93.5	91.8	91.1	95.0	99.6
83.3	90.2	83.1	72.3	71.0	88.0	93.7
77.8	74.8	71.3	57.9	59.0	74.5	84.0
84.4	68.5	73.2	58.3	58.6	68.9	84.6
83.7	78.5	79.1	66.9	68.9	75.1	89.4
86.3	88.1	78.2	68.4	74.2	85.7	91.5
97.7	94.7	88.6	83.3	83.2	90.5	96.5

Decoding probabilities, which were calculated from the results of deterministic method shown in Figure 3 and Table I, are listed in Table III for 49 individual crystals for ^{137}Cs flood source. Similar estimations were performed for ^{68}Ga source using Figure 4 and Table II. For this case, the decoding results are presented in Table IV. Same analyses were repeated for Lapped type BGO block and the results are shown in Figures 6-8 and Tables V-VIII.

TABLE IX
AVERAGE DECODING PROBABILITIES FOR *CUT TYPE* (^{68}GA)*

Block Region (i)	Block Region (ii)		Block Region (iii)					
0.79	5.28	1.04	1.16	6.74	1.44	2.03	7.96	2.18
3.92	78.07	3.73	1.17	89.45	4.81	6.44	61.96	5.88
1.10	5.32	0.75	1.61	6.91	1.14	2.79	8.66	2.10

* (i) including all 49 crystals, (ii) Outer region (40 crystals total), (iii) central 3x3 BGO region (9 crystals) in 7x7 BGO block.

TABLE X

AVERAGE DECODING PROBABILITIES FOR *LAPPED TYPE* (^{68}GA)*

Block Region (i)	Block Region (ii)		Block Region (iii)					
0.61	4.45	0.71	0.30	3.79	0.42	1.98	7.38	2.01
3.56	81.37	3.49	3.10	84.85	2.79	5.61	65.90	6.61
0.74	4.47	0.60	0.50	3.94	0.31	1.79	6.82	1.90

* (i) including all 49 crystals, (ii) Outer region (40 crystals total), (iii) central 3x3 BGO region (9 crystals) in 7x7 BGO block.

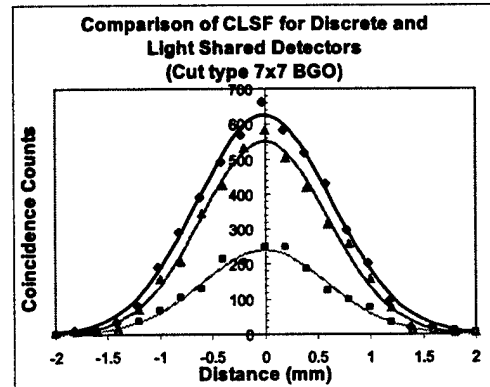


Figure 9. Comparison of CLSF simulation results of 49 discrete detectors versus light shared detectors *Cut Type* for different average probability values. Simulation results are marked as \blacklozenge (black) for discrete detectors, \blacksquare (light gray) *Cut Type* (case (iii) in Table IX above) and \blacktriangle (dark gray) *Cut Type* (case (i) in Table IX above). The solid lines with the corresponding gray colors are Gaussian fits to simulation results.

Average decoding probabilities for Cut and Lapped types of detector blocks were calculated. These values revealed how much spread occurred to neighboring scintillators. Results are listed in Tables IX and X. The center element of 3x3 decoding probability matrix shows how certain the crystal was decoded. Other elements in 3x3 matrix show the spreading probability to neighboring scintillators. Case (i) and (iii) in Tables IX and X were used to simulate the CLSF values for Cut and Lapped types of 7x7 BGO block. Gaussian function was fit to each simulation result to estimate the FWHM values. The CLSF simulation results were compared to the one for discrete detector as shown in Figures 9 and 10. FWHM values for discrete, Lapped overall (case (i) in Table X), Lapped 'central' (case (iii) in Table X), Cut overall (case (i) in Table IX) and Cut 'central' (case (iii) in Table IX) block were found to be 1.47mm, 1.49mm, 1.50mm, 1.51mm and 1.51mm, respectively.

Finally, Table XI compares the intrinsic spatial resolution (recall Equation 5) if we are to build a PET tomograph with ring diameters of 20cm, 40cm and 80cm using 3 types of detectors mentioned above.

Based on the estimated results shown in Table VI and making the assumption that LSO has 5 times more light

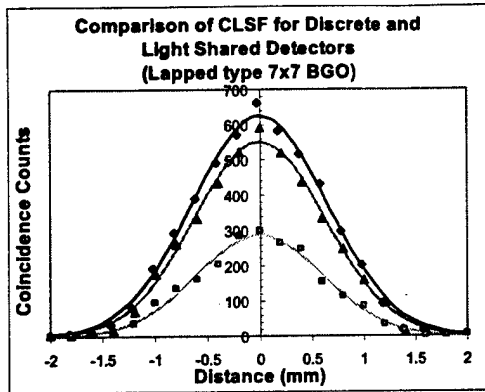


Figure 10. Comparison of CLSF simulation results of 49 discrete detectors versus light shared detectors Lapped type for different average probability values. Simulation results are marked as \blacklozenge (black) for discrete detectors, \blacksquare (light gray) Lapped type (case (iii) in Table X above) and \blacktriangle (dark gray) Lapped Type (case (i) in Table X above). The solid lines with the corresponding gray colors are Gaussian fits to simulation results.

TABLE XI
COMPARISON OF ESTIMATED INTRINSIC SPATIAL RESOLUTION (IN MM) FOR VARIOUS DETECTOR RING DIAMETERS BETWEEN DISCRETE AND LIGHT SHARED DETECTORS

Block Type	Ring Diameter (20cm)	Ring Diameter (40cm)	Ring Diameter (80cm)
Cut	1.59	1.76	2.33
Lapped	1.57	1.75	2.32
Discrete	1.55	1.73	2.30

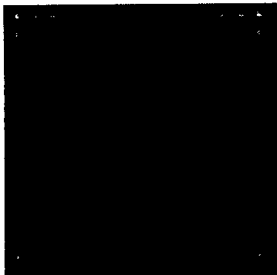


Figure 11. 14x14 LSO block decoding map result using deterministic approach. In this map, light distribution of the crystal elements was assumed to be uniform.

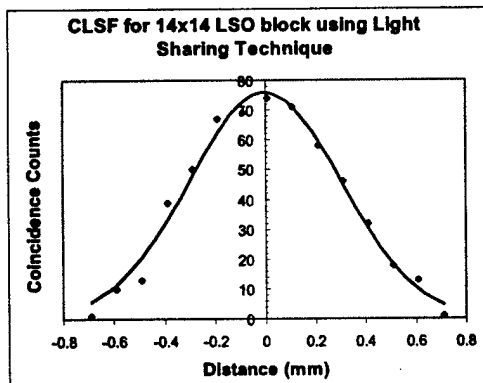


Figure 12. Comparison of CLSF simulation results of 196 light shared detectors. Average probability values for all crystals (case (i) in Figure 11 above) were used in the simulation. Simulation results are marked as \blacklozenge for light shared detectors. The solid line is the Gaussian fit to the simulation result.

output than BGO, a pseudo map with the uniform light distribution shown in Figure 11 was obtained for 14x14 LSO detector block. Each crystal had dimensions of 1.32mm x

1.32mm x 20mm. Table XII presents the decoding probabilities for different regions in the block. The FWHM of CLSF shown in Figure 12 for LSO block was estimated 0.71mm. Hence the intrinsic spatial resolutions for 20cm, 40cm and 80cm ring diameters were expected to be 0.87mm, 1.15mm and 1.91mm, respectively.

TABLE XII
ESTIMATED AVERAGE DECODING PROBABILITIES FOR 14X14 LSO BLOCK (^{68}Ga)*

Block Region (i)			Block Region (ii)			Block Region (iii)		
0.05	1.06	0.05	0.02	0.80	0.02	0.20	2.22	0.20
1.08	95.76	0.96	0.83	96.86	0.74	2.23	90.83	1.92
0.05	0.93	0.05	0.02	0.69	0.02	0.20	2.00	0.20

* (i) including all 196 crystals, (ii) Outer region (160 crystals total), (iii) central 6x6 BGO region (36 crystals) in 14x14 LSO block.

IV. DISCUSSION AND CONCLUSION

In this work, the effect of decoding uncertainty on CLSF was studied for light shared detectors. It has been concluded that the CLSF was insensitive to decoding uncertainty. Hence, intrinsic spatial resolutions for different detector ring diameters were found to be very close for discrete and light shared detectors. Even though the FWHM values of CLSFs were not changed significantly for different regions of the block, not surprisingly the coincidence sensitivity for the crystals in the central region decreased to 44% in Lapped type and 37% in Cut type compared to discrete detectors (see Figures 9 and 10) because of the misplaced coincidence events. Average decoding probability values, shown in Tables IX and X, behaved like a simple low pass filter that degraded the CLSF. If the decoding probability values were averaged for the entire 7x7 BGO block, the coincidence sensitivity values were calculated 86% in Lapped type and 84% in Cut type compared to discrete detector block (recall Figures 9 and 10).

Estimation of total generated photoelectron numbers using deterministic approach was found to be consistent with the locations of the photopeaks in the energy spectra. The energy resolution values of selected crystals were calculated to be in the range of 22% and 32% in both Cut and Lapped types for ^{68}Ga source. This degradation was mainly due to the summation of 4 PMT signals. Photopeak locations of each PMTs appeared at different ADC channels that would degrade the energy resolution of the summed energy spectrum. Therefore, using the energy resolution values of the summed energy spectra would have underestimated the generated photoelectron numbers. In the case of using position sensitive PMTs, cost-effectiveness makes the light shared detectors more desirable to be used in a PET tomograph.

By comparing the decoding maps of ^{137}Cs and ^{68}Ga for both types of BGO blocks, it was concluded that more light output provided better decoding map as expected. Because of its high light output and its speed, LSO would have been a very good choice to be used in the light shared detector design. Even in the central region of 14x14 LSO block,

decoding certainty was estimated nearly to be 91%. Intrinsic spatial resolution was estimated to be 1.91mm for whole-body PET tomograph with 80cm ring diameter by using 14x14 LSO detector blocks.

V. REFERENCES

- [1] Y. Shao, S.R. Cherry, S. Siegel and R.W. Silverman, "A study of inter-crystal scatter in small scintillator arrays designed for high resolution PET imaging", IEEE Transactions On Nuclear Science 43:3 pp. 1938-1944, 1996.
- [2] K. Murty, C.J. Thompson, I.N. Weinberg, F.M. Mako, "Measurement of the coincidence response of very thin BGO crystals", IEEE Transactions On Nuclear Science 41:4 pp. 1430-1435, 1994.
- [3] Z.H. Cho, J.P. Jones, M. Singh, "Foundations of medical imaging", John Wiley & Sons, New York, pp. 221-230, 1993.
- [4] K.A. Comanor, P.R.G. Virador and W.W. Moses, "Algorithms to identify detector Compton scatter in PET modules", IEEE Transactions On Nuclear Science 43:4 pp. 2213-2218, 1996.
- [5] W.H. Wong, J. Uribe, K. Hicks, M. Zambelli, "A 2-dimensional detector decoding study on BGO arrays with quadrant sharing photomultipliers", IEEE Transactions On Nuclear Science 41:4 pp. 1453-1457, 1994.
- [6] M.S. Kaplan, R.L. Harrison and S.D. Vannoy, "Coherent scatter implementation for SimSET", IEEE Transactions On Nuclear Science 45:6 pp. 3064-3068, 1998.
- [7] W.W. Moses and S.E. Derenzo, "Empirical observation of resolution degradation in positron emission tomographs utilizing block detectors", Journal of Nuclear Medicine, Vol 34:5 pp. 101p, 1993.

Inexpensive Position Sensitive Detector Block for Dedicated PET Cameras Using 40-mm Diameter PMT in Quadrant Sharing Configuration

Jorge Uribe, *Member, IEEE*, Mehmet Aykac, Hosain Baghaei, *Member, IEEE*, Hongdi Li, *Member, IEEE*, Yu Wang, Yaqiang Liu, Vincenzo Wong, Tao Xing, Rocio Ramirez, and Wai-Hoi Wong, *Member, IEEE*

University of Texas M.D. Anderson Cancer Center, Houston, Texas 77030

Abstract—Recent approvals by CMS (HCFA) for reimbursement of positron emission tomography (PET) scans fuels the rapid growth of the PET market, thus creating the need for more affordable dedicated PET scanners. The objective of the work presented here was the development of a BGO position-sensitive block with similar detector area (40mm x 40mm) and same number of crystals (8x8) as the block of a commercial BGO PET, using the less expensive photomultiplier quadrant sharing technique (PQS). This block is coupled to four single-anode 40-mm diameter photomultipliers (PMT) instead of the 19-mm PMT used in a popular commercial BGO PET, and each PMT is shared by four adjacent detector blocks. Potentially, this design needs only 25% of the number of PMT used in the commercial BGO PET. In order not to waste the unused half-row of PMT at the edges of a detector panel/module when the module is made up solely of square blocks, an extended rectangular block has to be developed for the edge-blocks in the module, which maximized the use of the PMT and minimized the gap between modules. Only the extended block needs to be developed to derive the design for all the blocks in the module, because the symmetric square block uses same light-distributing partitions as those along the short side of the extended rectangular block. White-paint masks applied with accurate templates and airbrush were fine-tuned for every pair of adjacent crystals. The experimental block developed in this study provided good crystal-decoding. The composite energy spectrum of all 64 crystals showed a prominent photopeak. The worst crystal sitting in the air space between 4 round PMTs still has 60% of the signal pulse height as the best crystal. The average energy resolution was 21.8% for 511 KeV gamma (range 17-28.7%) that compared well with the 22-44% measured with GE and CTI blocks. The image resolution provided by the PQS blocks is expected to be comparable to that of commercial BGO PETs as similar size crystals were decoded.

Manuscript received November 25, 2001. This work was supported in part by the NIH Grant ROI CA58980, NIH Grant ROI CA61880, NIH Grant ROI CA76246, NIH Grant ROI CA58980S1, Texas Higher Education Advanced Technology Grant, John S. Dunn Foundation Research Grant, The Mike Hogg Foundation, and by the Cobb Foundation for Cancer Research.

Jorge Uribe, Mehmet Aykac, Hosain Baghaei, Hongdi Li, Yu Wang, Yaqiang Liu, Tao Xing and Wai-Hoi Wong are with the University of Texas, M.D. Anderson Cancer Center, Houston, TX 77030 USA (J. Uribe's telephone: 713-745-1179, e-mail: juribe@di.mdacc.tmc.edu).

I. MOTIVATION

The approval by HCFA in December of 1999 for reimbursement of PET scans in diagnostic oncology cases initiated a rapid growth in the PET market. Thus the need for affordable clinical PET scanners is greater and there will be an even greater need if the level of reimbursement is lowered as recently suggested by CMS. Our goal was to design a dedicated PET detector block that performs in a manner similar to the position-sensitive blocks in current commercial PET cameras but at a substantially reduced production cost. The lower production cost can also be exploited to substantially expand the axial field-of-view to improve detection sensitivity, image quality and shorten the whole-body imaging time to increase patient throughput.

II. INTRODUCTION

The concept of position sensitive detector blocks for PET cameras using the photomultiplier-quadrant-sharing (PQS) design was introduced by Wong in 1993 [1]. An important advantage of this technique is the near 1:1 ratio of the number of blocks to photomultiplier tubes (PMT) used in a system. The position of a gamma-hit is calculated using Anger logic with the signals from four photomultipliers, but each PMT is coupled to the position-sensitive detector block with only one quadrant of their photocathodes (fig. 1). That is, PQS uses four PMTs like a commercial PET to decode the

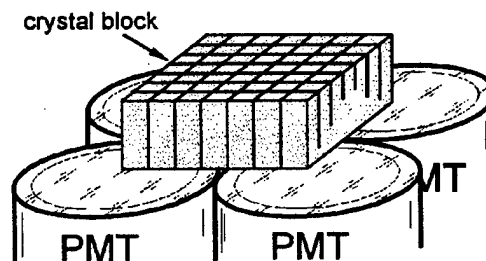


Fig. 1 Detector block coupled to four PMT in Photomultiplier Quadrant Sharing mode

crystals in a detector block [2], but every PMT in the PQS technique serves four blocks instead of one (fig. 2-a). Effectively, this represents a saving of up to 75% in the number of PMTs used compared to a PET camera using four whole PMTs to decode just one block as in commercial BGO PET cameras (Fig 2-b).

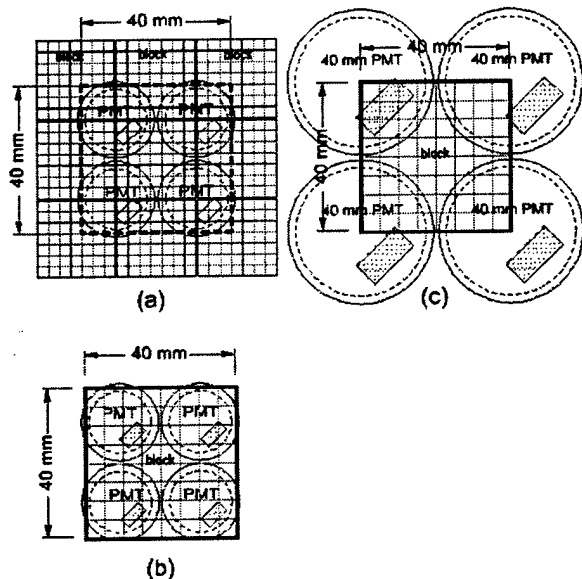


Fig.2. (a) MDAPET quadrant sharing design. (b) commercial camera detector design. (c) Inexpensive 40mm x 40mm block using PQS and 40mm diameter PMT

The first whole-body high-resolution human PET developed using the PQS technique was MDAPET built by our group at The University of Texas MD Anderson Cancer Center [3, 4]. MDAPET utilized circular 19mm-diameter phototubes similar to those used in today's commercial cameras. In this implementation we kept the same PMT size but the detector block was only one quarter of the commercial block (fig. 2-a); hence, the PQS design reduces the crystal size by 75% (in area) from the commercial design (fig.2-b). The ability to resolve the smaller 49 crystals in the new PQS block (7x7 array) translated into higher spatial resolution (2.8 mm transaxial) [3], despite our first-time production method that is quite primitive compared to the much refined mass-production engineering of commercial PET. The resolution compared well to the 4.5 mm transaxial resolution reported for the Siemens ECAT HR+ scanner, the most popular commercial PET camera [5]. Looking at it from another perspective, the dashed-line square in fig. 2-a representing the size of the CTI-HR+ BGO detector block (fig. 2-b) superimposed onto the PQS array with nine blocks encloses 169 crystals, compared to 64 crystals in the commercial camera block. Therefore, with the same number of PMTs and same volume of BGO as a commercial BGO camera, the PQS technique achieved higher resolution. In addition, the PQS design has been adopted by the ECAT HR+'s manufacturer for their latest high-resolution brain PET scanner the ECAT HRRT [6] as well as their next generation PET/SPECT and PET systems [7, 9].

The objective of the work presented here was to develop and test a position-sensitive block with the *same detector area and number of crystals* as a commercial BGO block (64 BGO crystals) but implemented in PQS mode. Rather than keeping the same PMT size and reducing the block size (MDAPET implementation), we kept the block dimensions constant while replaced the 19 mm PMT with 40-mm round PMT (fig. 2(c)). Notice that one 40 mm circular PMT replaces four 19-mm PMTs, i.e. potentially a 75% savings in PMTs, especially when the extended-PQS design is applied to the last row of PMTs along the four edges of a detector module [8].

III. BLOCK DESIGN

Quadrant-sharing detector modules/panels implemented strictly with *square* symmetrical detector-blocks wasted one half of the PMTs at the edge of the detector module/panel (shaded semi-circles labeled as 'waste' in Fig. 3-top). We have previously reported the development of an "Extended/rectangular Position Sensitive Block Detector for PQS Configuration" [8] for 19 mm PMT, which minimized such wasted PMT usage located in the 4 edges of a detector module (Fig. 3-bottom).

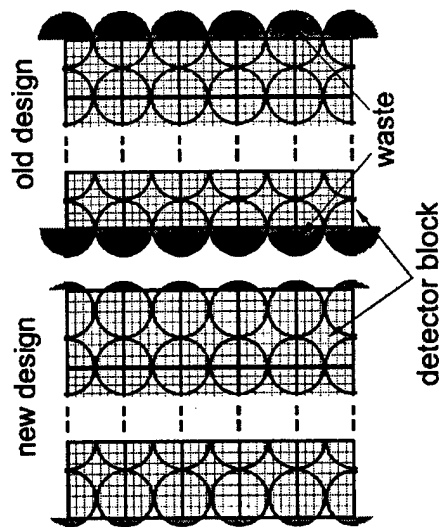


Fig. 3. TOP: PQS design showing unused PMT photocathodes (shaded semi-circles). Circles=PMT, squares = block detectors. Top - only symmetric/square blocks used in module. Bottom - square and extended-rectangular blocks combined to reduce PMT waste or maximize PMT usage in a detector module

The current study was focused on developing the rectangular block again because it is sufficient to develop only the extended-rectangular type to derive the design of both the square blocks and the extended-rectangular block needed in a detector module. The reason is as follows: the scintillation from a crystal in the extended-rectangular block is distributed in two orthogonal directions (Fig. 4). One of the directions is the regular symmetric dimension (Fig. 4-a) that is similar to both sides of a square quadrant-sharing block (extending from the center of one PMT to the center of

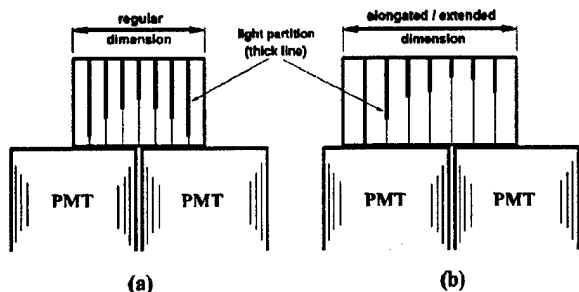


Fig. 4. Light-partition geometry for the two dimensions in an extended-rectangular PQS block: (a) symmetric dimension, (b) asymmetric side

the next PMT); in this dimension, light has to be distributed symmetrically to the associated PMTs with a symmetric set of light partition (saw-cut or white paint) as shown in Fig. 4-a. Hence, in this dimension, the symmetric partition geometry and symmetric crystal/PMT arrangement are exactly like both sides of a square PQS block. Thus, the same partition design developed for this dimension of the extended-rectangular PQS block can be applied directly to the two dimensions of the square PQS block. The extended direction will need an asymmetric set of light partitions as the block is sitting asymmetrically over two PMTs (Fig. 4-b). Along this dimension, the set of asymmetric light partitions (Fig. 4-b) can only be used for the extended block. Hence, the partition design developed in an extended-rectangular block can be used in both the regular square PQS block and the extended rectangular block. This developmental 'shortcut' has been verified experimentally when we compared the light partitions (white paint) developed for our square-19-mm block with that of the extended-19-mm block [8].

The rectangular block developed for the 40 mm diameter PMT consisted of a BGO array of 8 x 8 crystals; each crystal is 5.0 mm long by 6.3 mm wide by 25 mm tall forming a block 40 mm x 50 mm x 25 mm. The pixel size of the crystal was simply determined by the available sizes of the PMT (19mm, 25mm, 40mm, etc.) and the fact we want to achieve the same decoding resolution (6x6 to 8x8 arrays) as the GE and CTI systems. The height of the crystals was selected with enough length to ensure good sensitivity (three half-value layers) but not so long as to compromise image resolution due to parallax error in an 80cm diameter field-of-view camera. The 25 mm chosen is midway between the 20 mm of the CTI-HR+ block and the 30 mm of the GE Advanced block. As discussed before, the design can also be extrapolated regionally to build square blocks with 5x5x25 mm³ BGO detectors which are similar to the detectors used in current commercial BGO PET systems. This detector block was intended for both whole-body scanners and brain/breast scanners (with the detector modules configured into a smaller diameter polygon).

IV. METHOD

We developed light partitions (white paint) with both symmetric and asymmetrical shapes to obtain adequate distribution of scintillation light throughout the block. A sample of the asymmetric partition/masks is shown in Fig.5.

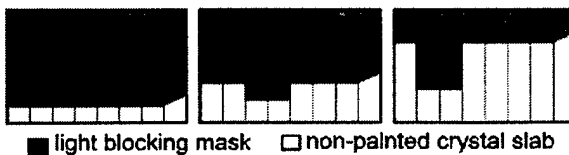


Fig. 5. Asymmetric white-paint mask applied on three rows of crystals to control the light distribution

The light partition is a titanium water-base white paint (Bicron BC-620) applied with airbrush driven with extra-dry nitrogen gas and shaped by high-precision pressure-sensitive paper-stock masks.

Symmetric light partitions were painted on crystal surfaces that affect the distribution of light along the elongated direction of the block (Fig. 4(b) shows the end-view of such masks). Asymmetric light partitions (Fig.5) were painted on surfaces that affect the light distribution along the regular (shorter) direction of the rectangular block (end-view of masks in Fig 4-a), because we need to distribute light from a crystal to the four PMTs but half the block is coupled to a *quarter* of a PMT while the other half of the block is coupled to a *half* of a PMT. The desirable paint partition sizes were determined iteratively with a successive approximation technique (as in some analog-to-digital converter or ADC). At the starting point of the iterative process, all interfaces were painted with a 50% area coverage. Generally, painted masks were only applied to one surface instead of the two facing surfaces of two adjacent crystals. However, for the crystal interfaces near the extended end of the block, additional light-reflecting thickness was needed to obtain good crystal separation (decoding); for this purpose we developed a double-coat painting technique where the same mask is applied on facing surfaces of selected crystal pairs.

As mentioned earlier, partition levels were iterated several times and independently tuned for every crystal-pair interface by inspecting the crystal-decoding results on the two-dimensional decoding map of the block; the objective was a well separated, uniformly distributed decoding map. By using individual crystals it facilitated the iterative experimental process but made it labor intensive because every crystal was painted and handled independently. Fig. 6 shows a close-up look of the crystals after the white-paint masks were applied



Fig. 6. Close-up of individual BGO crystals with white paint masks applied on them. Every crystal is placed at a specific location and orientation in the 8x8 array.

and before assembled into a block. The block was assembled using a home-built jig that keeps the crystal array in a right-angle pattern while being glued together with optical grease (Rexon Components RX-688). The exterior of the block was wrapped with Teflon tape.

In order to test the crystal-position decoding of the experimental block, it was optically coupled to four 40 mm diameter Hamamatsu R580-15 photomultipliers using optical grease. The gain of the four PMT was balanced using a single small BGO crystal placed at the center of each photocathode. The gain provided by the front-end amplifiers was equalized to provide the same photopeak positions for all four PMTs.

By using white-paint light partitions, instead of partial-depth saw-cut partitions as used by some BGO PETs [2], we achieved a much thinner gap between crystals compared to the saw-cut BGO-PET detectors [10, 11]. The average kerf of a diamond saw blade is 0.4 mm compared to the paint-glue thickness of 0.04 mm, representing a gain in packing fraction of 7% (assuming the crystal dimension is 5 mm x 5 mm). Since improvement in packing fraction takes place in both directions, it led to an area packing fraction increase of $(1.07)^2$ or 1.14 times. Furthermore, since PET requires detection in coincidence, the overall coincidence sensitivity would be increased by up to 30% because of the high packing-fraction design.

A. Surface Texture.

We studied various types of crystal-surface finish to optimize (a) scintillation light output, and (b) light

distribution within the block. With no external light guide to transmit light to the four photocathodes, the crystal-to-crystal light transmission is essential for passing light to the photocathodes. Instead of the common practice of providing polished surfaces to every crystal we lapped (roughed) the surfaces on all crystals except for the optical surface facing the PMTs. A lapped surface is basically a ground-glass surface finish. Lapping is generally performed anyway to achieve a precise crystal dimension after a crystal is cut since the crystal-cutting process is not a high precision process. One can specify the size of the abrasive particles used for the lapping process to achieve the desirable surface smoothness or roughness. We found that lapping with 10-micron particles provide the best signal pulse height and crystal decoding. Our PQS-block design technique requires a high level of light-diffusion between crystals and the traditional polished surfaces or acid-etching surfaces (commonly used for long and narrow crystals such as ours) are not favorable in our design. All-polished surfaces degraded our crystal decoding as shown in Fig. 7. The corresponding composite pulse-height spectrum including all 64 crystals is shown in Fig. 8; it shows a broad photopeak because gamma rays hitting crystals placed directly on top of a PMT with most favorable optical coupling produce pulses with higher pulse-height than crystals with no direct PMT coupling (between PMT bottles). Crystals with all surfaces lapped allowed scintillation light to distribute to create a much better crystal decoding map with all 64 crystals well-separated (Fig. 9) and a prominent composite photo-peak (Fig. 10).

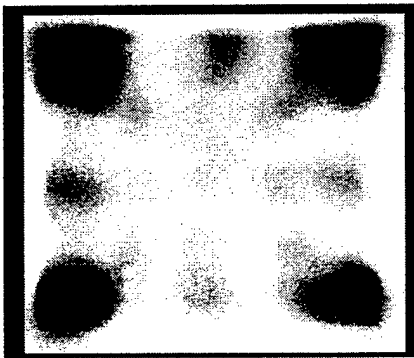


Fig. 7. Position-decoding map of a rectangular BGO block (40mm x 50mm x 25mm) with all crystal surfaces polished

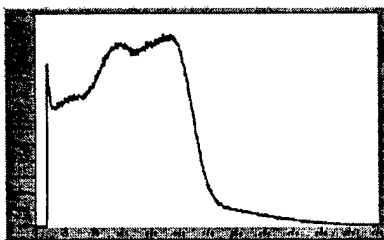


Fig. 8. Composite energy spectrum of all 64 crystals from the block in Fig. 7, with all surfaces polished. The x-axis is ADC channel numbers

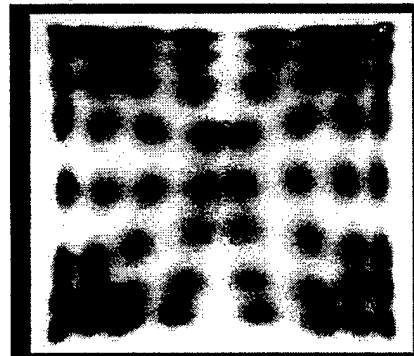


Fig. 9. Position-decoding map of rectangular (40mm x 50mm x 25mm) BGO block. All crystal surfaces lapped except for the optically coupled surface that was polished



Fig. 10. Composite energy spectrum of 64 crystals in the block with all surfaces lapped with 10 micron abrasives, except for the optical surface facing the four PMT. The x-axis is ADC channel numbers.

The individual pulse-height spectra of all 64 crystals were also collected by gating the spectrum data with the position of each crystal in the decoding map (from Fig. 9) as allowed by our home-grown electronics and software. The individual photopeak pulse heights were normalized to the same standard pulse height, and then the individual crystal spectrum was normalized by the counts in the region of interest (ROI) of each crystal. The normalized pulse-height spectra for all 64 crystals were summed to derive an average pulse-height spectrum for the block (Fig. 11). This normalized-average spectrum showed a better energy resolution than the composite spectrum in Fig. 10, and allowed us to measure the average energy resolution and average photo-fraction of the PQS-block constructed. The individual pulse-height spectra for each crystal were also analyzed and presented below.

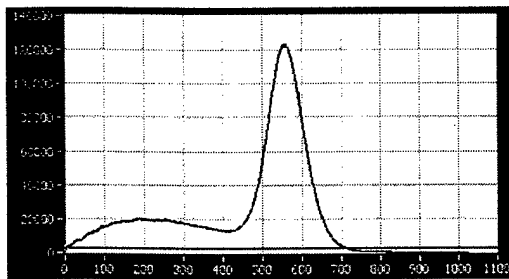


Fig. 11. The normalized-array-average spectrum for the 64 BGO crystals in the PQS array. The x-axis is ADC channel numbers.

V. RESULTS

Fig. 9 shows the two-dimensional crystal-decoding map of the block we developed. Each element is clearly separated and evenly distributed over the map. Fig. 10 is the corresponding composite energy spectrum of all 64 crystals in the block, showing a prominent photo peak and relatively small Compton fraction. It indicates that the block has a very uniform light collection for all crystals despite the asymmetric positioning of the block relative to the center of the four decoding PMT; or to the fact that there were many crystals with no direct coupling to a PMT (the dead zone between four circular PMT). For this block, the ratio between the lowest pulse height to the highest was found to be,

$$\text{Raw Min} / \text{Raw Max} = 0.59.$$

Hence, the worst crystal has 41% lower pulse height than the best crystal in the block. The individual crystal photopeak pulse heights are shown in Fig. 12; the column position (x-axis in Fig. 12) is along the extended direction. Since crystal row-1 and row 8, row-2 and row-7, row-3 and row 6, row 4 and row-5 were mirror rows (relative to the PMT). The 2 mirror crystals on these rows were averaged and the 32 pulse heights are shown in Fig. 12. The photopeak pulse heights of all 64 crystals are also displayed along the orthogonal direction (symmetric direction) in Fig. 13.

The crystals in the block were classified into four types:
Type-1: crystals on the central photocathode region

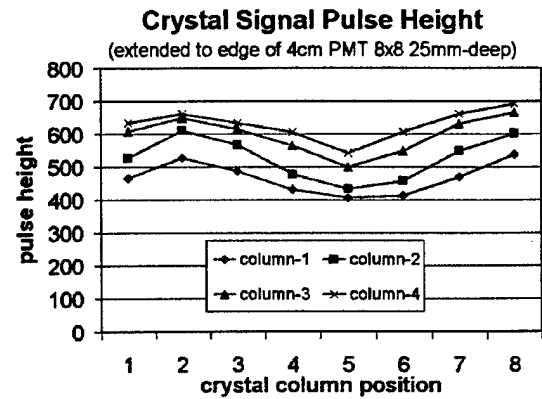


Fig. 12. Pulse-height values for 4 rows of the block with 40mm PMT. The crystal-column position is along the extended block direction.

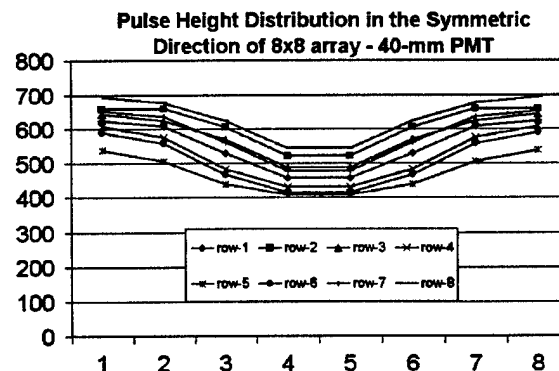


Fig. 13. Photopeak pulse-heights of the block with 40-mm PMT with the crystal-row position along the symmetric direction (short dimension of the block Fig. 4-a).

Type-2: the crystals on the photocathode edge and sidewall
Type-3: the crystals coupled mostly to the glass sidewall
Type-4: the crystals with no direct PMT connection

The types and their average optical efficiencies are shown in Fig. 14. The average optical-efficiency ratio between the least efficient type and best type is 0.68. Hence, as a group the 4 central crystals that were just hanging in space without any optical coupling to a PMT was found to lose 32% of the light

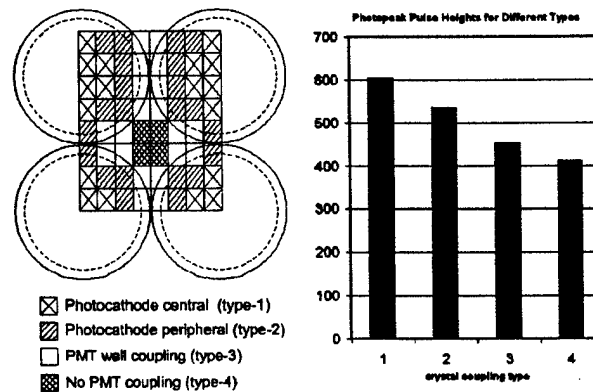


Fig. 14. The crystal-position types and their optical efficiencies

compared to the ideal group (type-1).

The normalized-sum spectrum of the whole array (Fig. 11) was also used to calculate the average photo-fraction and the average energy resolution of the BGO crystals in the block:

Average detection photofraction = 70%.

Average energy resolution (511 KeV) = 21.8 %.

For 511 KeV gamma, the best crystal has 17% energy resolution and the worst crystal has 28.7%. These measured energy resolution range is better than the 22% for the best crystal and 44% for the worst crystal measured in a GE Advanced PET detector block, and the 22.7% for the best crystal and 42.5% for the worst crystal in a Siemens HR+ block reported by Tornai, et al. [10] and Cherry, et al. [11]. The normalized block-average energy resolution of 21.8% measured in the PQS block is better than even the best crystals in both conventional blocks. This indicates that the PQS detector block under study has both very good overall optical efficiency and very uniform optical efficiency, in addition to much lower production cost.

VI. CONCLUSIONS AND DISCUSSIONS

- An extended block using four 40mm-single-anode PMT configured in photomultiplier-quadrant-sharing mode (PQS) was developed.
- This block achieved good crystal decoding and uniform light-output efficiency. The worst crystal location has an optical efficiency of 60% of the best crystal location which is substantially better than the 33% achieved in current commercial BGO blocks [10-11].
- Using PMT four times larger than those used in commercial BGO PET, the new detector system requires as few as 1/4 the number of PMT of a clinical system, while keeping similar imaging capabilities. To achieve this savings, both the PQS technique and the extended-PQS technique were needed. The price of each 40-mm PMT is only 5-7 % more expensive than the 19-mm diameter PMT used in the CTI-HR+ systems (both in large quantities). Hence, this study showed that the major component cost in a PET system can be reduced by up to 70% without sacrificing image resolution. With the large reduction in PMT numbers, the number of front-end electronics (fast amplifiers, amplifiers, discriminators, ADC, etc.) can also be substantially reduced accordingly, leading to a substantial saving in electronics. The front-end electronics is the most expensive part of the electronics cost and its cost is proportional to the number of PMT channels used. Further cost reduction could also come from assembling the BGO crystals with no polished (or etched) surfaces, then after assembly and in one operation the entire PMT face of the block can be polished.
- Crystals with lapped surfaces are essential to achieve appropriate crystal decoding in our position-sensitive block design coupled to single-anode PMT when the block itself is the guide light.
- This block design has no need for special external light guide between the block and the PMT, thereby cutting cost in

both materials and assembly, in addition to minimizing the loss of light due to an external light guide.

- For a hypothetical PET camera constructed with the block developed here, the hypothetical image resolution is expected to be comparable to the resolution of commercial BGO PETs because the size of crystals decoded in this study is about the same as those used in commercial BGO PETs. The image quality may be better because of better energy resolution and more uniform pulse-heights, allowing the PET energy window to be set higher to better reject scatter and single events. We have performed preliminary Monte Carlo simulations of the line spread function using this block in a whole-body PET with an 80-cm diameter detector ring; the preliminary result showed a transaxial resolution of 3.9-mm at the center. Certainly, with engineering and production errors, the achievable spatial resolution would be 4-5 mm that is about the same as current BGO PET. With the substantial reduction in production cost, the cost savings can also be exploited to increase the axial field-of-view of PET to increase detection sensitivity, thereby improving image quality, reducing whole-body imaging time or increasing patient throughput rates.

- If conventional front-end electronics is used, the count-rate capability of the detector design would be decreased by a factor of 2.2 [1]. However, using the high-yield-pileup-event-recovery (HYPER) electronics that we developed and has been shown to increase count-rate by 8-10 times [12-14], a PQS PET system would have a count-rate capability equivalent or better than the current BGO systems.

- In a typical BGO PET with 15-cm axial-field-of-view, there are approximately 1000 PMT. Each PMT with its high-voltage divider and connectors cost about \$160 in large quantities. Hence, reducing 700 PMT would lead to a cost saving of $\$160 \times 700 = \$110,000$ from the production cost. Additionally, there are substantial savings in the front-end electronics and ADC electronics.

VII. ACKNOWLEDGMENT

We want to thank the Radiation Physics machine shop at MD Anderson Cancer Center, his director Jens Bowin and machinist Mark Bushman for their support in the manufacturing of tools necessary for the painting and assembly of the experimental block.

VIII. REFERENCES

- [1] W.H. Wong, "Positron Camera Detector Design with Cross-Coupled Scintillators and Quadrant Sharing Photomultipliers", IEEE Transactions on Nuclear Science Vol.40, number 4 pp. 962-966, 1993.
- [2] M.E. Casey, R. Nutt, "A Multicrystal Two Dimensional BGO Detector System for Positron Emission Tomography", IEEE Trans. Nucl. Sci., vol NS-33, pp. 460-465, 1986.
- [3] J. Uribe, H. Baghaei, H. Li, S. Yokoyama, N. Zhang, J. Wang, F. R. Dobs, W.H. Wong, "Basic Imaging Performance Characteristics of a Variable Field of View PET Camera Using Quadrant Sharing Detector Design", IEEE Transactions on Nuclear Science 46:3 pp. 491-497, 1999.
- [4] W-H. Wong, J. Uribe, L. Weizhao, H. Guoji, K. Hicks, "Design of a variable field prototype PET camera", Trans. Nucl. Sci., IEEE, Volume: 43 Issue: 3 Part: 2, pp. 1915-1920, June 1996.
- [5] L-E. Adam, J. Zacs, H. Ostertag, H. Trjan, E. Bellemann, G. Brix, "Performance Evaluation of the Whole-Body PET Scanner ECAT

- EXACT HR+ Following the IEC Standard", *IEEE Trans. of Nucl. Sci.*, vol 44:3, pp. 1172-1179, 1997.
- [6] K. Wienhard, M. Schmand, M.E. Casey, K. Baker, J. Bao, L. Eriksson, W.F. Jones, C. Knoess, M. Lenox, M. Lercher, P. Luk, C. Michel, J.H. Reed, N. Richerzhagen, J. Treffert, S. Vollmar, J.W. Young, W.D. Heiss, R. Nutt, "The ECAT HRRT: Performance and First Clinical Application of the New High Resolution Research Tomograph. Nuclear Science Symposium Conference Record, 2000 IEEE , Volume: 3 , pp. 17/2 -17/6 vol.3, 2000.
- [7] W.F. Jones, M.E. Casey, A. van Lingen, B. Bendriem, B., "LSO PET/SPECT Spatial Resolution: Critical On-Line DOI Rebinning Methods and Results". Nuclear Science Symposium Conference Record, 2000 IEEE , Volume: 3 , pp. 16/54 -16/58 vol.3, 2000.
- [8] W.H. Wong, S. Yokoyama, J. Uribe, H. Baghaei, H. Li, J. Wang and N. Zhang. "An Elongated Position Sensitive Block Detector Design Using the PMT Quadrant- Sharing Configuration and Asymmetric Light Partition", *IEEE Transactions on Nuclear Science* 46:3 pp. 542-545, 1999.
- [9] Nahmias, C., Nutt, R., Hichwa, R. D., Czernin, J., Melcher, C., Schmand, M., Andreaco, M., Eriksson, L., Casey, M., Moyers, C., Michel, C., Bruckbauer, T., Conti, M., Bendriem, B., Hamill, J. PET tomograph designed for five minute routine whole body studies. *The Journal of Nuclear Medicine JNM Abstract Book Supplement*, Vol. 43(5): 11p, May 2002.
- [10] Tornai, M., Germano, M., Hoffman, E.J.. Position and energy response of PET block detectors with different light sharing schemes. *IEEE Trans. Nucl. Sci.*, vol 41 (4), pp. 1458-1463, 1994
- [11] S.R. Cherry, M.P. Tornai, C.S. Levin, S. Siegel, E.J. Hoffman, "A comparison of PET detector modules employing rectangular and round photomultiplier tubes," *IEEE Trans. Nucl. Sci.*, Vol. 42, no 4 pp. 1064 -1068, Aug. 1995.
- [12] W.H. Wong, H. Li: "A scintillation detector signal processing technique with active pileup prevention for extending scintillation count rates," *IEEE Trans. Nucl. Sci.*, vol. 45, no.3, pp. 838-842, June 1998.
- [13] W.H. Wong, H. Li, J. Uribe, H. Baghaei, Y. Wang, S. Yokoyama: "Feasibility study of a high speed gamma camera design using the high-yield-pileup-event-recovery (HYPER) method," *The Journal of Nuclear Medicine*, vol.42, no. 4, April 2001.
- [14] H. Li, W.H. Wong, N. Zhang, J. Wang, J. Uribe, H. Baghaei, S. Yokoyama, "Electronics for a prototype variable field of view PET camera using the PMT-quadrant-sharing detector array," *IEEE Trans. Nucl. Sci.*, vol. 46, no. 2, pp. 546-550, June, 1999.

Signal Characteristics of Individual Crystals in High Resolution BGO Detector Designs Using PMT-Quadrant Sharing

Jorge Uribe, *Member, IEEE*, Hongdi Li, *Member, IEEE*, Tao Xing, Yaqiang Liu, Hossain Baghaei, *Member, IEEE*, Yu Wang, Mehmet Aykac, Rocio Ramirez, Wai-Hoi Wong, *Member, IEEE*

University of Texas M.D. Anderson Cancer Center, Houston, Texas 77030.

Abstract—The PMT-quadrant sharing (PQS) detector design allows very high resolution detectors to be built with 70% fewer PMT and lower cost. A common concern for the design is that there is a big gap (photo-insensitive area) between 4 circular PMT, and the photoelectron signal (pulse height) may be much lower for the central crystals. The concern increases with the use of smaller PMT for high-resolution designs because small PMT have relatively thicker wall and relatively larger tolerance spaces between them. We measured the pulse heights and energy resolution for each crystal in 3 different types of PQS blocks for 19 mm PMT. For a square 7 x 7 block detector (2.66mm x 2.66mm x 18mm BGO needles), the maximum photopeak signals occurred at the corner crystal of the block. The signals for the worst central-5 crystals (sitting on space with no PMT connection) had pulse heights 0.87 as high as that of the corner crystals. The 12 crystals (outside the central-5) with coupling only to the glass wall but not to the photocathode had a relative pulse height of 0.92. The 8 crystals with partial exposure to photocathodes had a 0.94 relative pulse height. The energy resolution for individual crystals was 22-30% with an average of 26%. Asymmetric photopeaks, especially for the corner crystals, were observed, and these were found to be the result of the depth-of-interaction effect. In the latest PQS design, extended blocks with asymmetric light distributions were used on the 4 edges and 4 corners of a large detector module so that the previously unused (wasted) half-row of peripheral PMT could be covered by crystals. An asymmetric block, single-extended (7 x 8 crystals) was also tested. The pulse-height ratio between the worst and best group of crystals in the single-extended block was 0.72 and that of the double-extended block was also 0.72. In a more demanding, higher spatial resolution 8 x 8 array (2.3mm x 2.3mm x 10mm BGO) for mouse PET with shallower crystals, the pulse-height ratio

was 0.73 with an average energy resolution of 20%. This study demonstrated that pulse height uniformity for the PQS design using circular PMT was excellent, being better than the typical 3/1 pulse-height ratio in conventional block detectors.

I. INTRODUCTION

The PMT-quadrant sharing (PQS) detector design [1]-[3] allows very high resolution detectors to be built with 70% fewer PMT, fewer front-end electronic channels and lower cost. We used this design to build very high resolution PET cameras [4], and it has been adopted by Siemens/CTI for its next generation LSO PET cameras [5]. A common concern for the design is that when 4 circular PMTs are used to further reduce the cost, the circular PMTs leave a big gap (photo-insensitive area) between the 4 PMTs. The dead-space issue is especially challenging with smaller diameter PMT ($D < 20$ mm), as the glass wall cannot be made proportionally thinner, which aggravates the dead-space problem. Furthermore, since the glass bottles of PMTs do not have high mechanical precision, a small amount of tolerance space between PMTs has to be built into the design (e.g. 0.5-1 mm), which further expands the dead-space. The dead space would imply that the photoelectron signal pulse heights may be much lower for the central crystals (of the crystal array) that sit on the dead space, thereby degrading imaging resolution and energy resolution. To determine whether these concerns are relevant, we evaluated the detail signal characteristics of PQS block detectors with respect to the large dead-space issues. The pulse heights and energy resolution for each crystal in 3 different types of PQS blocks based on 19 mm round PMT were measured and studied.

II. METHODS

The experiments were performed with randomly chosen blocks among our stock of second-generation PQS BGO detector blocks. These blocks had painted interfaces between discrete crystals for distributing scintillation light, and the discrete crystals were optically glued together. The sizes and shapes of the painted areas were determined by the desired levels and directions of light distribution from each crystal. Three types of PQS block designs based on 19 mm round PMT were studied:

Manuscript received Nov 27, 2002. This work was supported in part by NIH Grant RO1 CA58980, NIH Grant RO1 CA61880, NIH Grant RO1 CA76246, NIH Grant RO1 EB00217, NIH Grant RO1 EB001038, US Army Breast Cancer Grant, Texas Higher Education Grant, John S. Dunn Foundation Research Grant, Mike Hogg Fund Research Grant, Cobb Fund for Cancer Research.

Jorge Uribe, Wai-Hoi Wong, Hongdi Li, Hossain Baghaei, Yu Wang, Yaqiang Liu, Tao Xing and Rossio Farrell are with the University of Texas M.D. Anderson Cancer Center, Box 217, 1100 Holcombe Blvd., Houston, Texas 77030, USA.
(Contact person: Jorge Uribe (e-mail: juribe@di.mdacc.tmc.edu))

III. RESULTS

- 7 x 7 square block (each crystal was 2.66mm x 2.66mm x 18mm),
- 8 x 8 square block (each crystal was 2.3mm x 2.3mm x 10 mm),
- 7 x 8 elongated asymmetric block (each crystal was 2.6mm x 3.1mm x 18 mm).

The in house developed front-end electronics of our prototype PET camera were used to acquire the data. The electronics employed the pileup-restoration technique recently developed by us [6], [7]. Four Photonis XP1911 PMT were used for the 19 mm circular PMT, with each PMT having one quadrant of its photocathode coupled to the BGO block by optical grease. The PMT high voltage was fixed at 1450 V, providing about 10^6 anode amplification gains. Cs-137 was used as the radiation source for all the voltage. The gains of all four PMT were equalized with their voltage-control variable-gain fast amplifiers by two different methods: (a) using just the crystal sitting at the center of each PMT and (b) using a region of 3x3 crystals corresponding to the relevant quadrant of the PMT. For the four PMT used, both methods of equalization were within 5% of each other (data not shown), so the center-crystal equalization was used for all the studies. No particular criterion was followed while selecting the photomultipliers themselves from the pool of PMT used for the construction of our second-generation PET camera. PMTs for this camera were ordered from the manufacturer with relative gain values that differ by no more than 2.5 times.

The electronics were interfaced to a personal computer. We also developed the data-acquisition software, controlling the data-acquisition electronics, and the analysis software for this study for a PC platform. The hardware and software have been compared and validated against a commercial NIM multi-parameter data-acquisition system (FAST from ComTec) by comparing both the pulse-height spectra and crystal-decoding map. Our system provides a higher data acquisition speed plus some custom-designed analysis capability such as recording the signal pulse-height spectrum for each pixel in the crystal-decoding map.

For each crystal block/array, the composite (total sum) pulse-height of all the crystals in the block was first measured with a distal point source. This composite pulse height measurement provided a first-pass energy-acceptance threshold for the whole array. The crystal position-decoding map as shown in Fig.1 was acquired with this first-pass energy threshold. This first-pass crystal-decoding map was then used to draw a region-of-interest map for each crystal in the array. The signal-pulse-height spectrum for each crystal region was analyzed and presented in the Results section. From these results, the best energy-acceptance threshold for each crystal region-of-interest (ROI) was also determined; an energy-threshold lookup table for each crystal ROI in the crystal decoding map was created for each detector array tested. A second-pass data acquisition was then performed for each detector array to obtain a crystal-decoding map with individualized crystal-energy-thresholds. The results are presented in the next section.

The second generation PQS BGO position-sensitive array has a much better production method [8] that mated all the crystals together with a minuscule gap of only 0.05-0.06mm producing a very high packing fraction (Fig.1). There was a white-paint window between crystals for controlling the distribution of light, and the crystal were optically glued together as a solid block. The painted windows allowed any shape and size to be painted thereby enabling optimal crystal decoding and the minimization of barrel or pincushion distortion in the decoding map. One such crystal block (7 x 7 array, 2.66mm x 2.66mm x 18mm BGO) is shown in Fig.1 with its raw position-decoding map.

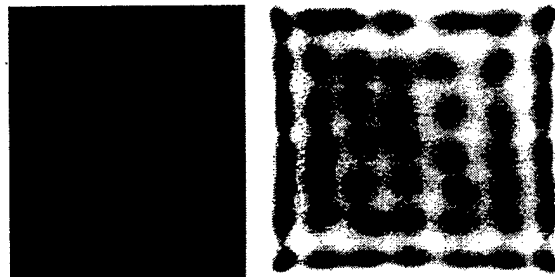


Fig. 1. A second-generation PQS position-sensitive BGO block and its raw crystal-decoding map without distortion correction and with only one energy acceptance threshold for the whole block.

A. 7x7 array, 2.66mm x 2.66mm x 18mm with 19mm round PMT

For this 7 x 7 block, the maximum photopeak signals occurred near the corner of the block as expected, while the signals for the worst central-9 crystals (sitting on space with no photocathode coupling) were found to have the lowest pulse heights. The low pulse heights are due to the extra distance traveled by the scintillation light from the center crystals to the PMT windows through the block. This path for the light is possible thanks to finely tuned paint barriers placed between crystals. The ratio between the lowest pulse height to the highest was found to be,

$$(\text{raw Min}) / (\text{raw Max}) = 0.78.$$

Hence, the worst crystal had 22% lower pulse height than the best crystal in the block. The raw pulse-height spectra of

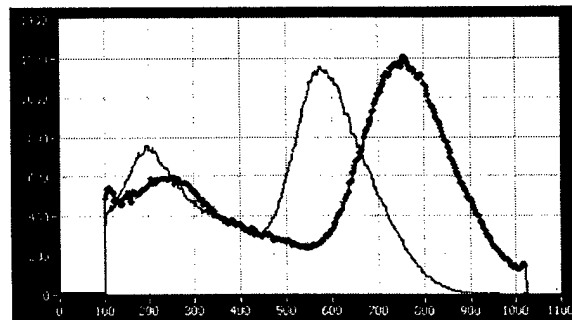


Fig. 2. Pulse-height spectra of the best and worst optical efficiency crystals

the worst (center crystal) and best crystal (near the corner) are shown in Fig.2.

However, this raw ratio included the influence of all the regional nonuniformities of each PMT photocathode and the anisotropic orientation effect of each PMT [9]. To minimize such spatial PMT influences, we averaged values for crystals with the same rotational symmetry, i.e., the same up-down and left-right crystal-locations relative to the center of the block. After the symmetric averaging, the ratio between the lowest pulse height and the highest pulse height was found to be,

$$(\text{symmetry-restored Min}) / (\text{symmetry-restored Max}) = 0.81.$$

This ratio may be a better measure of the geometrical optical efficiency difference between the worst crystal and the best crystal in a PQS block design, since the individual PMT variations and photocathode differences are thereby minimized. Hence, for the 7x7 BGO PQS array, the center crystal (the most disadvantageous, since it has no direct coupling to any PMT) had an optical efficiency 19% lower than that of a crystal that was directly coupled to the middle of a PMT, the most sensitive part of a PMT.

The pulse-height distribution of the upper four rows of crystals is shown in Fig.3 for the raw signal and Fig. 4 after the above symmetry averaging.

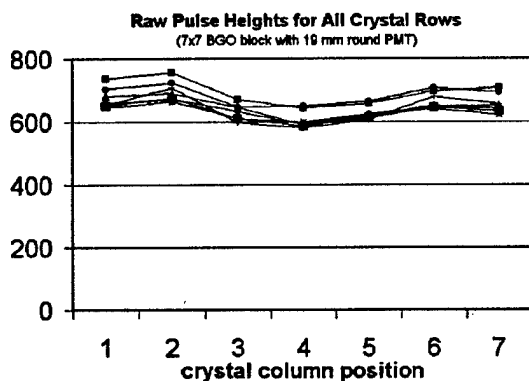


Fig. 3. The raw crystal pulse-heights for all 7 rows of crystals

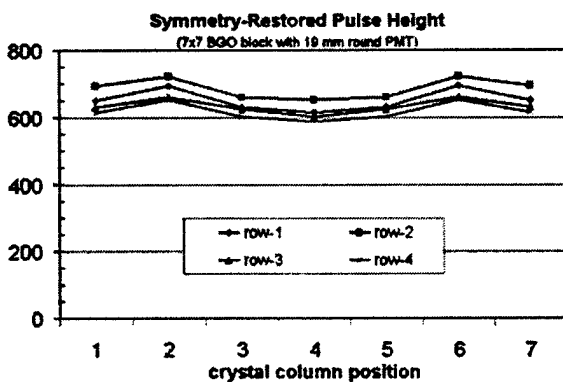


Fig. 4. The symmetry-restored pulse-heights for the first 4 crystal rows

The average pulse height was highest for the second row of crystals, although the first row of crystals was at the center of

the PMT. This disparity was due to almost total (95%) optical isolation of the first and last row of crystals from the rest of the block; hence all the scintillation light had to travel down the long and narrow crystal (2.66 mm x 2.66 mm x 18 mm) to be detected, during which some light was lost. This phenomenon was due to the very high spatial resolution of the block.

To categorize the crystal pulse height, the crystals were grouped into four types:

- Type-1: the crystals on the photocathode central region.
- Type-2: the crystals on the photocathode edge and sidewall.
- Type-3: the crystals only coupled to the glass side wall.
- Type-4: the crystals with no PMT connection (5 crystals).

The types and their optical efficiencies are shown in Fig.5.

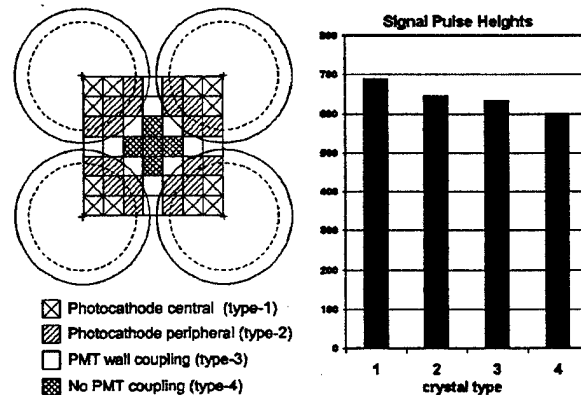


Fig. 5. The crystal-position types and their optical efficiencies

The optical efficiency ratio between the least efficient type and best type was found to be,

$$(\text{Type-4 pulse height}) / (\text{Type-1 pulse height}) = 0.87.$$

Hence, as a group the central 5 crystals, which were just hanging in space without any optical coupling to a PMT, lost only 13% of the light compared to the ideal crystal group (type-1).

The measured energy-resolution distribution, after the symmetry restoration discussed earlier, is shown in Fig.6.

The average energy resolution including all the crystal was found to be 25.6 %.

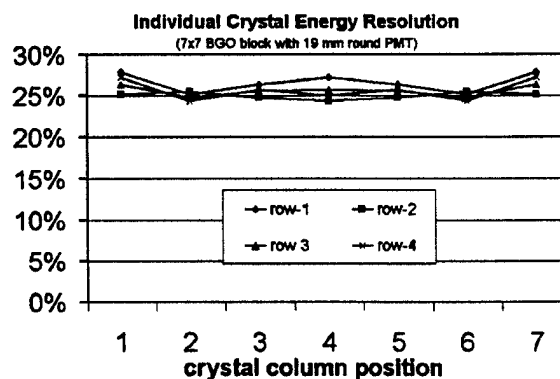


Fig. 6. The symmetry-restored energy resolution distribution

The average energy resolution was also measured in a different way. The photopeaks of all the crystals were normalized to the same standard pulse height and then normalized by the counts in the region of interest (ROI) of each crystal. The normalized pulse-height spectra for all the crystals were summed, and the energy resolution for the normalized-sum spectrum was calculated. This "normalized-sum" energy resolution was found to agree with that of the first method.

In the normalized-sum spectrum for the whole array (Fig. 7), an asymmetry in the photopeak can be observed. We determined that it was due to the variation of light output with the depth of interaction. By collimating the beam toward the first 1/3 and the last 1/3 of the crystal depth on the last row of crystals in the array, 2 different photopeak pulse heights appeared. Because of the high stopping power of BGO, most of the interaction occurred at the front-end of the crystal (farther away from the PMT); this gave rise to the lower overall pulse-height. But some interactions occurred near the back-end (the PMT end), thereby yielding a higher pulse height than the average peak energy.

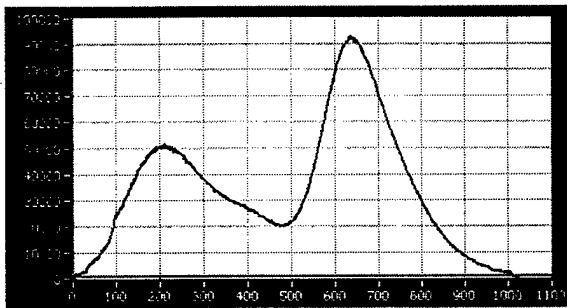


Fig. 7. The normalized-array-average spectrum for the 49 BGO in array

The normalized-sum spectrum of the whole array (Fig. 7) was also used to calculate the average photo-fraction of the small BGO crystals (2.66mm x 2.66mm x 18mm) in the array:

$$\text{Average detection photofraction} = 70\%.$$

B. 8x8 array, 2.3mm x 2.3mm x 10mm with 19mm round PMT

This BGO crystal-block geometry can be used for building less expensive mouse-PET system, since its crystal dimension is close to that of the MicroPET (2.4mm x 2.4mm pitch and 10 mm deep) and it uses the large low-cost 19 mm PMT and BGO instead of the more expensive design of the MicroPET that uses LSO crystals with position-sensitive PMT together with an optical fiber bundle. For this 8 x 8 block, the ratio of the lowest pulse height to the highest was found to be,

$$(\text{raw Min}) / (\text{raw Max}) = 0.67.$$

Hence, the worst crystal had 33% lower pulse height than the best crystal in the block. As discussed earlier, to minimize the PMT regional gain variation and anisotropy, crystals with the same rotational, up-down and left-right symmetries

(relative to the center of the block) were averaged, and the symmetry-restored ratio min/max was:

$$(\text{symmetry-restored Min}) / (\text{symmetry-restored Max}) = 0.72$$

Hence, for the 8x8 BGO PQS array, the central crystal (worst case with no connection to PMT) had an optical efficiency 28% lower than that of a crystal that is directly coupled to the middle of a PMT.

The pulse-height distribution of the upper four rows of crystals is shown in Fig.8 for the raw signal and Fig.9 after the above symmetry averaging.

Crystal Signal Pulse Height
(8x8 BGO block with 19mm round PMT)

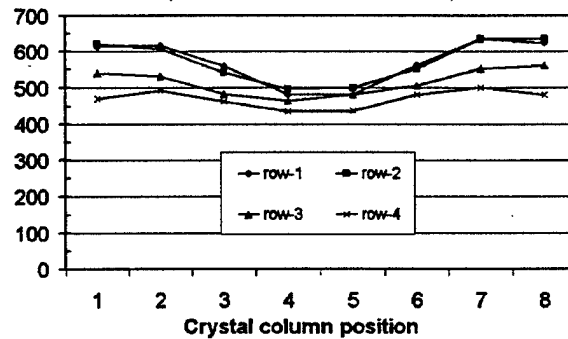


Fig. 8. Raw pulse-height distribution for 8x8 array with 19mm PMT

Symmetry-restored Pulse Height
(8x8 BGO block with 19mm round PMT)

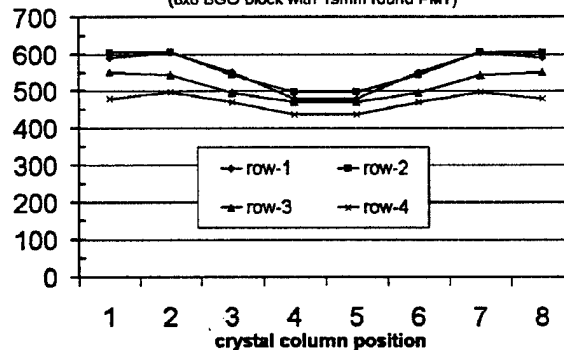


Fig. 9. Symmetry-restored pulse height distribution

As discussed earlier, the crystals were grouped into four types:

- Type-1: the crystals on the photocathode central region.
- Type-2: the crystals on the photocathode edge and sidewall.
- Type-3: the crystals only coupled to the glass side wall.
- Type-4: the crystals with no PMT connection (4 crystals).

The types and their optical efficiencies are shown in Fig.10.

The optical efficiency ratio between the least efficient type and best type was found to be,

$$(\text{Type-4 pulse height}) / (\text{Type-1 pulse height}) = 0.73.$$

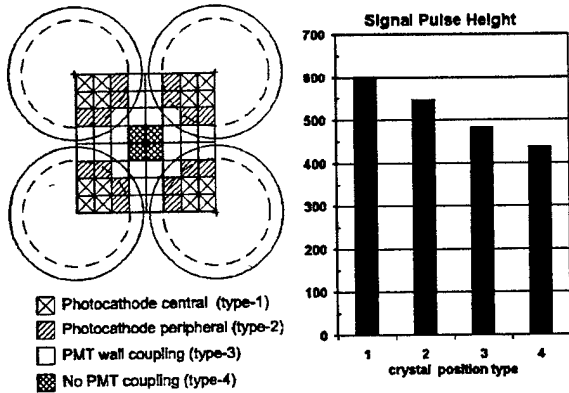


Fig. 10. The crystal-position types and their optical efficiencies

Hence, as a group the central four crystals that were just hanging in space without any optical coupling to a PMT lost 27% of the light compared to the ideal group (type-1). This is not as good as the 13% difference in the 7x7 array with the same PMT. It is, however, significantly better than the traditional block detectors used in current commercial PET cameras, where the most optically efficient crystal has 3 times higher pulse height than the least efficient crystal [10]. Similar to the 7x7 case, there was some asymmetric photopeak shape. But because of the shorter crystals used in this array (10 mm), the asymmetry in the photopeak was smaller. The shorter array decreased the light-output variation as a function of the depth of interaction, even though the crystals here were also narrower (2.3 mm x 2.3 mm).

The measured energy-resolution distribution (symmetry restored) is shown in Fig.11. The four abnormally large energy resolutions in Fig.11 had asymmetric photopeaks. Overall, asymmetry of the energy spectrum due to depth of interaction in taller crystals, as discussed earlier, did not occur with shorter crystals (presented later in this section). However, in shorter crystals larger number of gamma interactions might take place deep inside the crystal and just outside the PMT's sensitive area in places with impaired light distribution; for instance, on the edge-crystals of the block and between the glass bottles. The four crystals with large energy resolution in Fig. 11 are this type of crystal.

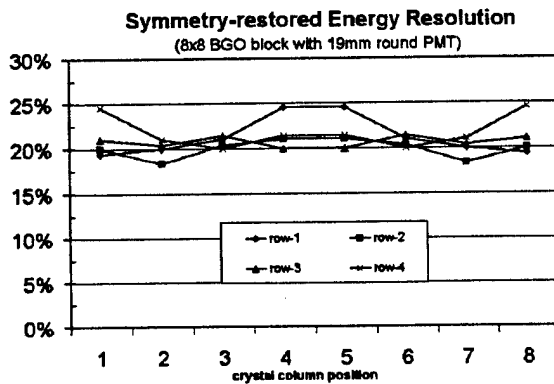


Fig. 11. Symmetry-restored energy resolution distribution

The normalized or equalized pulse-height spectra for all the crystals were summed, and the energy resolution for the normalized-sum spectrum was calculated. The normalized-sum spectrum of the whole array is shown in Fig.12. The average energy resolution including all the crystal was found to be,

$$\text{Average energy resolution} = 20.9 \%$$

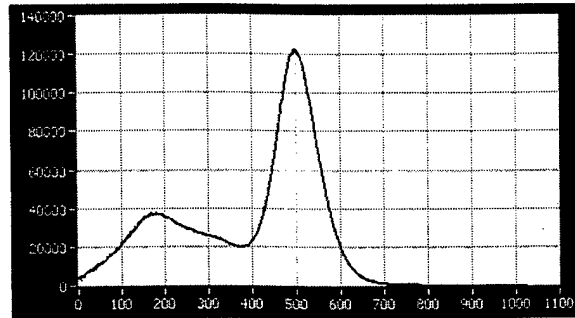


Fig. 12. The array-average spectrum for the 2.3 mm x 2.3 mm x 10 mm BGO

And if only the regularly shaped photopeaks were used, the "screened" averaged energy resolution was 20.4%. This energy resolution for this shallower block (10 mm) was better than the 25.6% for the deep crystals (18 mm) used in the 7x7 array, a difference that may be due to higher light-output efficiency of the shallower block. This 20.4% average energy resolution is comparable to the 19% average energy resolution measured for the LSO detectors (2.2mm x 2.2mm x 10mm) in the MicroPET that uses LSO's much higher light output (5X) and position-sensitive PMT (PSPMT) for position decoding [11].

Because the light output of an event is less dependent on the depth of interaction in shorter crystals, the photopeak in the normalized-sum spectrum for all 64 crystals (Fig.12) was found to be symmetrical for this 10 mm deep array, compared to the asymmetrical photopeak observed in fig.7 for the 18-mm-deep array.

The normalized-sum spectrum of the whole array (Fig. 12) was also used to calculate the average photo-fraction of the small BGO crystals (2.3mm x 2.3mm x 10mm) in the array:

$$\text{Average detection photofraction} = 62.3 \%$$

Because the crystals in this array were smaller, this photo-fraction was smaller than the 70 % of the 2.66mm x 2.66mm x 18mm BGO reported above.

C. 7x8 elongated array, 2.66mm x 3.1mm x 18mm with 19mm round PMT

This BGO elongated block was designed for use at the edge of a panel-detector module for extending the useful field of view to the edge of the last row of PMT [3]. Without the extended block design, half of the edge row of PMT in a panel detector module would be wasted, thereby reducing the advantage of the quadrant-sharing design. The pulse-height distribution (symmetry averaged) is shown in Fig.13.

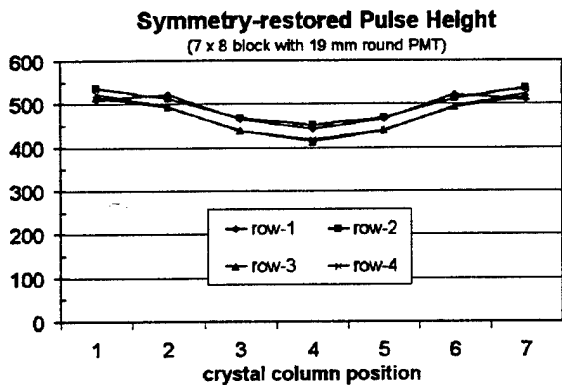


Fig. 13. Pulse-height distribution for the 7x8 array with 19 mm PMT

For this 7 x 8 block, the raw ratio between the lowest pulse height to the highest was found to be,

$$(\text{raw Min}) / (\text{raw Max}) = 0.71$$

Hence, the worst crystal had 29 % lower pulse height than the best crystal in the block. The symmetry-restored ratio min/max was:

$$(\text{symmetry-restored Min}) / (\text{symmetry-restored Max}) = 0.72$$

As earlier, the crystals were grouped into four types. Each geometrical coupling types and their optical efficiencies

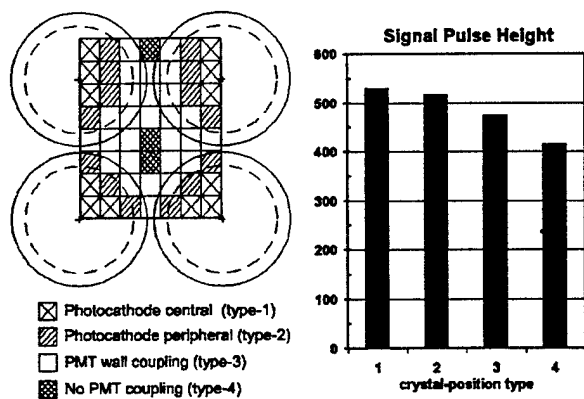


Fig. 14. The crystal-position types and their optical efficiencies are shown in Fig.14.

For this 7 x 8 block, the ratio of the pulse heights of the type-4 (worst) to type-1 (best) crystals was found to be,

$$(\text{Type-4 pulse height}) / (\text{Type-1 pulse height}) = 0.79$$

Hence, the worst crystal group had a 21% lower pulse height than the crystals with the best geometry in the block.

The measured energy-resolution distribution (symmetry restored) is shown in Fig.15. The average energy resolution

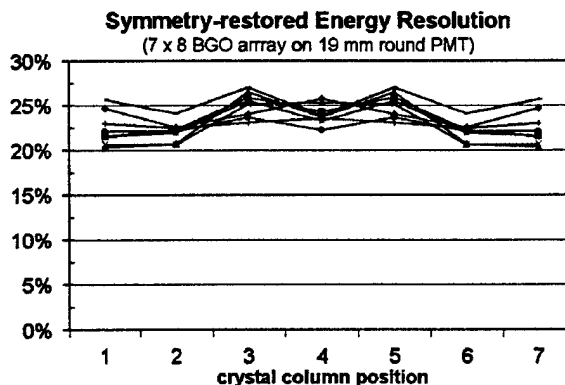


Fig. 15. Symmetry-restored energy resolution distribution for 7x8 array

for this 7x8 block was 23%, which is better than the 25% in the 7x7 array because of more favorable optical geometry.

IV. CONCLUSION AND DISCUSSIONS

Detailed signal characteristics for a very high resolution BGO detector design using the low cost quadrant-sharing (PQS) block decoding scheme with less expensive 19 mm round PMT were analyzed. There are some disadvantages in this type and size of PMT: (a) the relatively large gap (photo-insensitive area) between 4 round PMTs, (b) the dead-space of the 1-mm glass wall, and (c) the 0.8-1.0 mm mechanical tolerance space between PMTs due to the lack of precision in glass bottles. These disadvantages compounded the dead photo-detection area in the detector. The dead space would imply that the photoelectron-signal pulse heights may be much lower for the crystals sitting on the dead space, thereby degrading imaging resolution and energy resolution.

This study showed that, for the very high resolution BGO detectors using the second-generation PQS block design and production, the worst crystal positions had signal pulse heights that were only 13-27% lower than that of the best crystal group sitting on the middle of a PMT. The 7x7 block showed the most uniform light output (13%), while the 8x8 block was the worst (27%).

These individual crystal pulse-height measurements compare favorably to typical 3:1 difference in pulse heights in the conventional PET block-detector designs [10],[12]. Another similar pulse-height measurement for the Siemens HR-plus PET detectors using the same 19 mm circular PMT showed a 3:1 difference in pulse-height between the best and worst crystals [12]. Hence, the crystal optical-efficiency uniformity of the PQS block-detector design is better than the conventional PET block-detector design.

The high optical uniformity of the design is advantageous in that it simplifies the fast front-end electronics by using only one energy-discrimination level (one analog discriminator) for the entire detector module and still producing good crystal decoding (Fig.1). In fact, energy discrimination is a two step process as we have implemented it in both generations of PET cameras built by our group using the PQS decoding technology. The first level rejection is based on one module-wide discrimination value significantly reducing the number of hits that need processing

by the front-end analog electronics, whereas the second crystal-by-crystal cutoff is performed to fine tune rejection of scattered events. Quality of the two-dimensional decoding map alone is not enough testing for the quality of the final image. Therefore both levels of discrimination are needed for the whole system.

The 8x8 BGO array results also demonstrated that 64 crystals with a detector pitch of 2.3 mm x 2.3 mm can be decoded with 23% energy resolution (normalized from our test source Cs-137 to Ga-68) using low-cost BGO and effectively one \$140 circular PMT. These results approach those of the MicroPET that also decoded 64 crystals (2.4 mm x 2.4 mm pitch) with 19% energy resolution. It should be remembered, however, that the MicroPET detectors use more expensive LSO crystals (which generate 5 times more light), an optical fiber bundle and a \$4500 position-sensitive-photomultipliers (PSPMT) for every 64 crystals to achieve the decoding [11]. This study showed that a very low-cost mouse PET camera may be developed with the PMT quadrant-sharing technology.

V. REFERENCES

- [1] W-H. Wong, "A positron camera detector design with cross-coupled scintillators and quadrant-sharing photomultipliers," *IEEE Trans. Nucl. Sci.*, vol. 40, no 4, Aug. 1993.
- [2] W-H. Wong, J. Uribe, K. Hicks, M. Zambelli, G. Hu. "A 2-dimensional detector decoding study on BGO array with quadrant-sharing photomultipliers," *IEEE Trans. Nucl. Sci.*, vol. 41 no. 4, pp. 1453-1457, Aug. 1994.
- [3] W-H. Wong, S. Yokoyama, J. Uribe, H. Baghaei, H. Li, J. Wang, N. Zhang, "An elongated position sensitive block detector design using the PMT quadrant sharing detector array," *IEEE Trans. Nucl. Sci.*, vol 46 no. 3, pp. 542-545, 1999.
- [4] J. Uribe, H. Baghaei, H. Li, S. Yokoyama, N. Zhang, J. Wang, F. Dobbs, W-H. Wong, "Basic imaging performance characteristics of a variable field of view PET camera using quadrant sharing detector design," *IEEE Trans. Nucl. Sci.*, vol. 46 no. 3, pp. 491-497, Jun, 1999.
- [5] C. Nahmias, R. Nutt, R. Hichwa, J. Czernin, C. Melcher, M. Schmand, L. Andreaco, L. Eriksson, C. Moyers, C. Michel, M. Bruckbauer, M. Conti, B. Bendriem, J. Hamill, "PET tomography designed for five minute routine whole body studies," *J. Nucl. Med.*, vol 43 (5) supplement, pp. 11p, May, 2002.
- [6] W-H. Wong, H. Li, "A scintillation detector signal processing technique with active pileup prevention for extending scintillation count rates," *IEEE Trans. Nucl. Sci.*, vol. 45, no.3, pp. 838-842, Jun. 1998.
- [7] H. Li, W-H. Wong, J. Uribe, H. Baghaei, Y. Liu, Y. Wang, T. Xing, M. Aykac, "A new pileup prevention front-end electronic design for high resolution PET and gamma cameras," *IEEE Trans. Nucl. Sci.*, vol 49, no. 5, pp. 2051-2056, Oct. 2002.
- [8] J. Uribe, W-H. Wong, H. Baghaei, R. Farrell, H. Li, M. Aykac, D. Bilgen, Y. Liu, Y. Wang, T. Xing, "An Efficient Detector Production Method for Position-Sensitive Scintillation Detector Arrays with 98% Detector Packing Fraction", conference proceedings IEEE, Nuclear Science and Medical Imaging conference, Norfolk, VA, November, 2002.
- [9] J. Uribe, W-H. Wong, G. Hu, K. Hicks, J. Wang, H. Baghaei, N. Zhang, H. Li, S. Yokoyama, "Effect of the rotational orientation of circular photomultipliers in a PET camera block detector design," *IEEE Tran.Nucl. Sci.*, vol. 44, no. 3, pp. 1266-1270, Jun. 1997.
- [10] M. Tornai, M. Germano, E. J. Hoffman, "Position and energy response of PET block detectors with different light sharing schemes," *IEEE Trans. Nucl. Sci.*, vol 41, no. 4, pp. 1458-1463, Aug. 1994.
- [11] S. R. Cherry, Y. Shao, R. W. Silverman, K. Meadors, S. Siegel, A. Chatziioannou, J. W. Young, W. Jones, J. C. Moyers, D. Newport, A. Boutefnouchet, T. H. Farquhar, M. Andreaco, M. J. Paulus, D. M. Binkley, R. Nutt, M. E. Phelps, "MicroPET: A high resolution PET scanner for imaging small animals," *IEEE Trans. Nucl. Sci.*, vol. 44, no. 3, pp. 1161-1166, Jun. 1997.
- [12] S. R. Cherry, M. P. Tornai, C. S. Levin, S. Siegel, E. J. Hoffman, "A comparison of PET detector modules employing rectangular and round photomultiplier tubes," *IEEE Trans. Nucl. Sci.*, Vol. 42, no 4 pp. 1064-1068, Aug. 1995.

An Efficient Detector Production Method for Position-Sensitive Scintillation Detector Arrays with 98% Detector Packing Fraction

Jorge Uribe, *Member, IEEE*, Wai-Hoi Wong, *Member, IEEE*, Hossain Baghaei, *Member, IEEE*, Rocio Farrell, Hongdi Li, *Member, IEEE*, Mehmet Aykac, D. Bilgen, Yaqiang Liu, Yu Wang, Tao Xing

University of Texas M.D. Anderson Cancer Center, Houston, Texas 77030

Abstract—Position-sensitive scintillation-detector arrays (PSSDA) are used in nuclear-imaging methods such as PET. The kind of technique selected in producing the PSSDA determines the imaging resolution, sensitivity, labor/part cost, and reliability of the system. Production of PSSDA is especially challenging and costly for ultra-high-resolution systems that have large numbers of very small crystal needles, so we developed a new slab-sandwich-slice (SSS) production method. Instead of using individual crystal needles, the construction started with crystal slabs that are 15-crystal-needles wide and 1-needle thick. White-paint was deposited onto slab surfaces to form shaped optical windows. The painted slabs were grouped into two crystal-sandwich types. Each sandwich type consisted of a stack of 7 slabs painted with a distinctive set of optical windows, held together with optical glue. For a 40,000-crystal system, only 192 type A and 144 type B sandwiches are needed. Sandwiches were crosscut into another slab formation ("slices"). Each slice was again 1-needle thick; each slice was basically a stack of needles glued together, optically coupled by the glue and the painted windows. After a second set of white-paint optical-windows was applied on the slices' surface, 3 slices of type B were grouped between 4 slices of type A to form a 7x7 PSSDA. We used SSS production method to build 7x7, 7x8 and 8x8 crystal blocks needed for a high-resolution 12-module prototype PET camera. The method reduced the more than 400,000 precision painting and gluing steps into 55,500 steps for a 40,000-BGO-crystal system, thus lowering the labor cost. The detectors fabricated with the method were of high quality: 2.66 mm x 2.66 mm crystals were separated by only a 0.06-mm gap for a 98% linear detector packing fraction or 96% area packing fraction. Compared to 90% linear-packing (81% area) from conventional methods, the 20% increase in packing density translates into a 1.2-1.44 times higher coincidence-detection sensitivity in PET. Crystal cost was halved, and production yield increased to 94%. It generated very small crystal-positioning errors ($\sigma=0.09$ mm), required for ultrahigh resolution detectors.

Manuscript received November 30, 2002. This work was supported in part by the NIH Grant RO1 CA58980, NIH Grant RO1 CA61880, NIH Grant RO1 CA76246, NIH Grant RO1 CA58980S1, Texas Higher Education Advanced Technology Grant, John S. Dunn Foundation Research Grant, The Mike Hogg Foundation, and by the Cobb Foundation for Cancer Research.

Jorge Uribe, Hongdi Li, Hossain Baghaei, Yu Wang, Yaqiang Liu, Tao Xing, Rocio Farrell and Wai-Hoi Wong are with the University of Texas, M.D. Anderson Cancer Center, Houston, TX 77030 USA (J. Uribe's telephone: 713-745-1179, e-mail: juribe@mdanderson.org).

I. INTRODUCTION

Position-sensitive scintillation detector arrays (PSSDA) are commonly used in nuclear imaging, especially in PET cameras. Other than the design of the detector, the most important decision in building a PET is the detector production method, because it directly determines the ultimate imaging resolution, sensitivity, labor cost, and reliability. In position-sensitive scintillation array systems, each scintillation crystal distributes a unique amount of scintillation light to a number of photodetectors/photomultipliers (PMT). The PMT signals identify each firing crystal from each crystal's unique light-distribution pattern. Imaging resolution is determined by (a) how finely the light distribution from each crystal can be controlled and (b) the precision with which the light-distribution design is executed in a mass-production process.

We have developed a new production method for PSSDA that fulfills the following 7 important conditions:

- (1) Finely control the distribution of light from each crystal to achieve high imaging resolution,
- (2) Efficiently distribute the scintillation light to photodetectors for maximum imaging resolution,
- (3) Achieve a high crystal-packing density for maximum sensitivity,
- (4) Precisely and reproducibly manufacture the light-distribution devices according to design specifications,
- (5) Lower costs for both labor and raw material,
- (6) Maintain long term reliability, and
- (7) High yield detector production (less detector breakage or substandard detectors).

The process of producing a position-sensitive crystal array involves (a) cutting, lapping, etching, polishing, and cleaning each crystal, (b) making the light-distributor for each crystal, (c) optically mating each crystal to the light distributor, and (d) assembling all the crystals and light distributor into an array. An ultra-high-resolution PET system may have more than 40,000 crystals (and light distributors), each as small as 2.66 mm x 2.66 mm as in our experimental **High-resolution-Oncologic-Transformable-PET (HOTPET)** [1]. The sheer number and small crystal size can make such a system

unrealistic to produce both in terms of the raw material and the labor cost. Since the crystal pitch is very small in an ultrahigh resolution system, the traditional sawing technique (**partial-depth sawing** of a crystal block or a plastic light-guide) would significantly decrease the detection sensitivity. A diamond-blade's kerf of as little as 0.35 mm lowers the packing-area efficiency to $[2.66/(2.66+0.35)]^2 = 78\%$; translated into a coincidence efficiency of only 61% $(0.78)^2$. We remedied the sensitivity loss by first developing a partial-crystal-surface painting technique to control the light through the crystal surfaces; the shape of the mask depends on the location of the crystal in the array and on the surface orientation. Second, by removing any gap between crystals except for the space occupied by the glue and paint layers (0.06 mm), which is less than one fifth of the diamond-blade's kerf and increases the coincidence detection efficiency by 50% over the partial sawing technique. However, precise manufacturing, painting, and gluing of 40,000 tiny crystals would still require over 400,000 steps, which is extremely labor intensive and expensive.

A. Motivation

The PET instrumentation group at MD Anderson Cancer Center is involved in the design and development of a second generation, very-high resolution and versatile, PET camera for clinical and research applications. The camera can be transformed from an extra-large patient port for radiotherapy planning to a small-diameter high-sensitivity breast/animal system [1], [2]. It consists of 12 independent modules that move radially and turn around their own axis transforming the camera into the various configurations. The design of its highly pixilated detector modules is based on the **photomultiplier quadrant sharing technology "PQS"** [3], developed by the same group. PSSDAs arranged in PQS mode make optimum use of the PMT's photocathode (no gaps between arrays) except for the PMTs at the edge of the module, where just one half of the photocathode is utilized. We have developed asymmetrical crystal arrays [4], which extend the size of the detector module and include the unused part of the edge PMTs; double-extended crystal arrays for the module's four corners were also developed. Fig. 1 shows

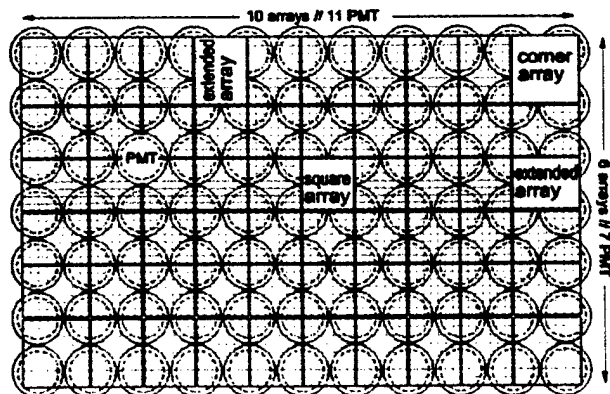


Fig. 1. HOTPET's detector module design requires three different types of PSSDA arranged in PQS mode for optimum use of the PMTs at the edge of the module. Edge blocks are known as "extended" blocks.

HOTPET's detector module design combining the three types of PSSDA, including 3168 crystal-needles (38,016 total system) coupled to 77 PMTs. This module design implements PQS's cost savings by using fewer PMTs, and improves sensitivity by minimizing the gaps between detector blocks, as compared to today's commercial PET cameras [1].

The first-generation PET camera developed by our group (MDAPET [5]) served as the testing ground for two PSSDA production techniques: "partial-depth sawing" and "paint and glue masking" [1]. Fig. 2 shows a BGO block from MDAPET build using these two techniques. The camera's axial resolution was the result of controlling the scintillation light throughout the block by "partial-depth sawing" light-barriers, whereas the trans-axial (in-plane) resolution was the result of the "paint and glue" light-blocking technique. The 2.8 mm trans-axial resolution we achieved was superior to the 3.4 mm axial resolution of the "partial-depth sawing" proving the benefits of the paint-and-glue technique.

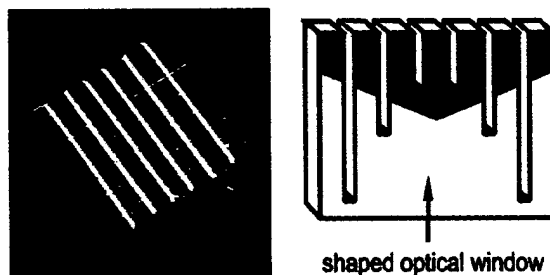


Fig. 2. (Left) MDAPET's 7x7-BGO-array combining the "partial-depth sawing" and the "paint and glue mask" techniques to control the scintillation light inside the block. (Right). Painted-mask used in the "paint and glue" block direction for optimum gamma-hit crystal decoding.

Combined with better linear packing fraction, compared to the kerf left by the saw, the paint-and-glue technique was the obvious choice to design the detector of the second generation PET camera. The major drawback of this approach was that it turned each crystal into an individual element, rather than a section of a slab defined by the saw cuts (Fig. 2-right), which logically leads to the handling of nearly 40,000 separate pieces. An added complication came from the fact that the shape of the painted masks were more than simple bands across the crystal array. They had convoluted shapes optimized for better identification of gamma hits from different crystal needles within the block, as shown in Fig. 2(right). Furthermore, the development of "extended" PSSDA for the edge and corners of HOTPET's modules was possible because asymmetrical masks of different shapes were applied along the extended direction.

The overall detector requirements, reproducibility, and the need for a low-cost production method to build HOTPET's detectors motivated us to develop the process described here. We have designed and implemented the "slab-sandwich-slice" (SSS) production technique necessary for efficiently producing large numbers of very small PSSDA with almost 100% packing fraction. Using it we can produce both symmetric and asymmetrical blocks and still allow use of fine-tuned convoluted light-barriers between needles. The SSS method lowered the production cost, increased yield, and increased detection efficiency.

II. THE SLAB-SANDWICH-SLICE METHOD

The SSS production algorithm topology is illustrated in Fig.3. Instead of using individual crystal needles, we started the construction with BGO slabs that were 15 crystal-needles wide and 1 crystal-needle thick (2.66 mm, Fig. 4). There was no actual constraint on the length of the slabs, which can be of arbitrary length. We chose the 15-needle length to

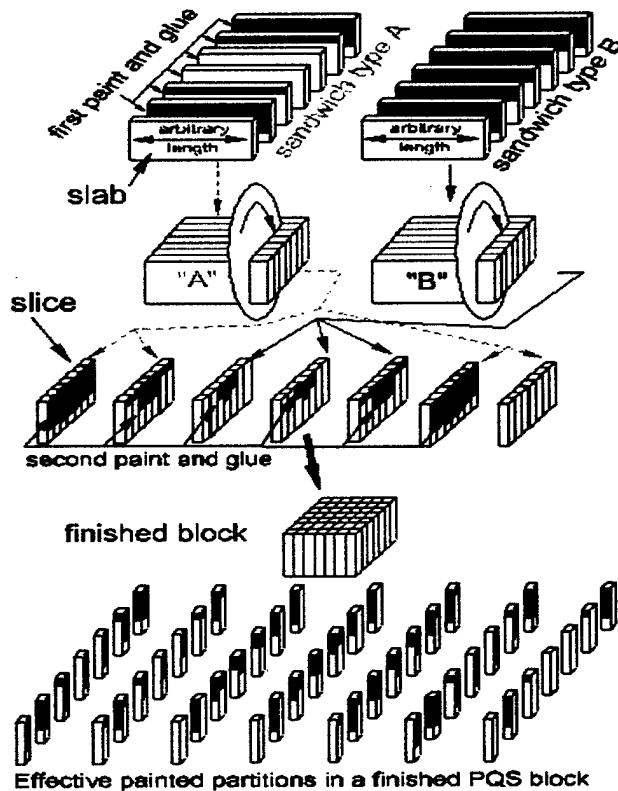


Fig. 3. The "slab-sandwich-slice" (SSS) production method for position-sensitive scintillator detector arrays (PSSDA).

accommodate the BGO supplier's tooling and production capabilities [6]; overall costs were reduced as a result. A stack of 7 slabs were painted with optical masks (window) and optically glued together to form a crystal sandwich (top arrays Fig. 3, Fig. 4). The mask on each slab was a fixed height straight band of white paint applied along the entire length of the slab (Fig. 3, Fig. 5(a)). Then, the slabs were grouped into 2 different "sandwich types" (A and B in Fig.3) following a specific order according to the size of their masks. For sandwich type A, only four of the seven slabs were painted with two different mask patterns (top-left -- Fig.3). For sandwich type B, six slabs were painted with a different set of masks (top right -- Fig. 3).

All the sandwiches are crosscut into another slab formation, which we call "slices" (picture in Fig. 4). The thickness of each slice was again one crystal width (2.66 mm), and each slice was in essence a stack of individual crystal needles optically coupled together by the glue and paint masks between them. All the slices cut from a given sandwich had the same mask pattern between the crystal needles, defined by the parent sandwich. Three slices of type

B were grouped between 4 slices of type A (follow the dash and solid arrows in Fig.3) to form an array of slices. Before the 7 slices of this new array were glued together to form the final PSSDA ("finished block" in the same figure), a new set of masks was painted (masks shown on the face of each slice).

Details of the 49 crystal needles that form the final PSSDA, with the correct masking, are shown in the block's exploded view at the bottom of Fig.3. In this view, each crystal needle has a set of masks and windows that are relevant only to the specific crystal location and face orientation within the block. The PSSDA described in Fig. 3 is a square symmetric block, confirmed by observing that every set of masks facing a *column* of crystals also appears as a set of masks facing a *row* of crystals and they are repeated symmetrically from the center of the block (Fig. 3 - bottom).

Pictures of a slab, a sandwich, a slice and the final 7x7 PSSDA are shown in Fig. 4. Comparison of this array with the one in Fig. 2 shows very small inter-crystal separation, increasing packing fraction and detection sensitivity.

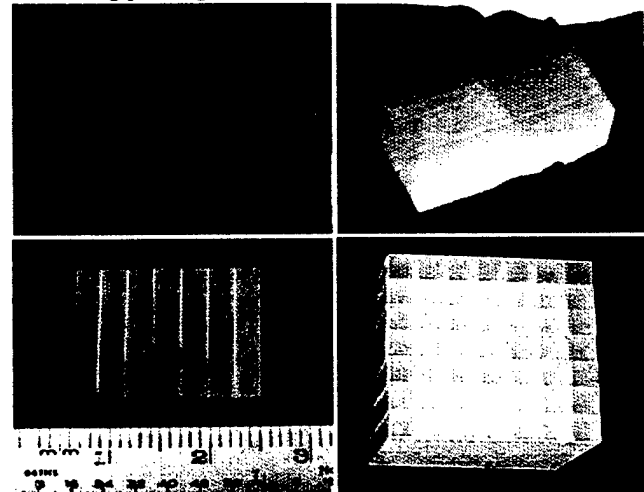


Fig. 4. Pictures of four stages of the SSS production process. Clockwise direction: slab (top-left), sandwich, slice and 7x7- PSSDA.

The SSS method is not limited to the production of symmetric or square detector arrays. In fact, it allows fine-tuning of the shaped optical windows between needles by introducing the "stepped" light barrier, which makes possible asymmetric light partitions. The paint-and-glue barrier used in the first-generation PET, shown in Fig. 2(right), allowed non-uniform blocking of the light between a slice and the adjacent one. The crystals in the middle had a larger blocked surface than the end crystals, but the shape of the mask was limited to two straight lines due to the masking process. In the second generation the stepped light-barrier has a straight horizontal boundary at each crystal and can be adjusted individually for every element, as shown in Fig. 5(b), 5(c) and 5(d). Fig. 5 shows the mask types used in the production of the new detector for HOTPET. It shows symmetric patterns used for the symmetric 7x7 block (Fig. 5(b)), as well as non-symmetric mask patterns used for the extended-rectangular 7x8 PSSDAs placed at the edges of the detector module (Fig. 5(c)) and masks for the larger-square asymmetric 8x8 arrays for the module's corners (Fig. 5 -- column (d)).

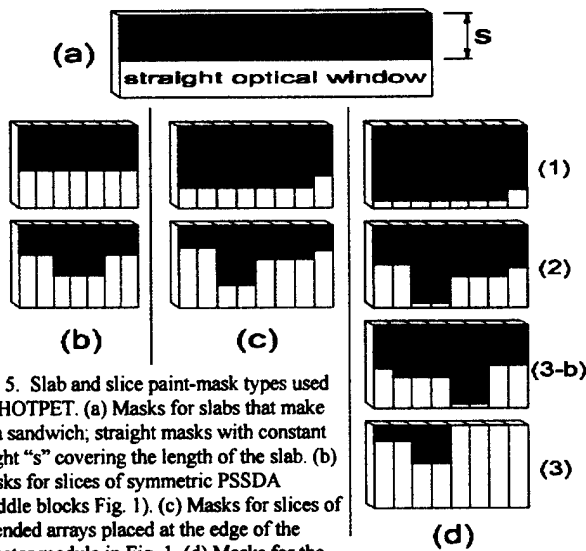


Fig. 5. Slab and slice paint-mask types used for HOTPET. (a) Masks for slabs that make up a sandwich; straight masks with constant height "s" covering the length of the slab. (b) Masks for slices of symmetric PSSDA (middle blocks Fig. 1). (c) Masks for slices of extended arrays placed at the edge of the detector module in Fig. 1. (d) Masks for the corner arrays of the same module

The SSS method can also use greater number of sandwiches than the two shown in Fig. 3. More complicated crystal arrays, like the edge and corner blocks for HOTPET, required 4 types of sandwich because the design required asymmetry in the blocks along the extended direction. For instance, the rectangular 7x8-crystal PSSDA was built by placing one slice from a type A sandwich (not shown) between two slices from sandwich type B, these three slices were placed between two slices of type C, and slices from type D one on each end completed the block.

In some instances, light blocking provided by the white paint was not enough to decode the gamma hits from all needles in a PSSDA. We applied paint on facing surfaces of adjacent crystals, resulting in a double coat of paint for stronger light blocking. This technique is easily incorporated into the SSS production method by applying paint masks on both sides of the same slab or slice. For instance, 3 adjacent slices for HOTPET's corner block were painted using masks (d)(1), (d)(2), and (d)(3) from Fig. 5, but additional paint was needed between the last two slices. Thus, a fourth mask (Fig. 5(d)(3-b)), the mirror image of Fig. 5(d)(2), was applied on the backside of the third slice. A similar technique was used to mask the slabs of a sandwich, introducing double paint-coat along the axial and trans-axial directions.

Table I summarizes the slab-sandwich-slice production process of the detector for HOTPET. A total of 720 PSSDAs of three different types were built starting with 2,541 slabs. It is important to note that in spite of the variety of types and block-designs used for this detector, only two size slabs were purchased. One was 15 needles long (50 mm) and 2.68 mm thick and the other was 15 needles long and 3.06mm thick. This limitation in raw materials greatly simplified crystal manufacturing and lowered cost, reducing the method to two considerations, *mask design* and *layout of combinations of slices* from different sandwiches, to form a single PSSDA.

From Table I, the total number of steps (operations) needed to build the entire detector is as follows:

TABLE I

Summary of HOTPET detector production (parts and steps involved).
12 module system with 38,016 crystals¹

Block type	7x7 symmetric	7x8 extended	8x8 corner-extended	TOTAL CAMERA
Number of blocks	384	288	48	720
Types of Sandwich (quantity)	2 (179)	4 (134)	4 (27)	10 (340)
Number of slabs	1253	1072	216	2541
Types of slab-masks (paint steps)	5 $\left(\frac{1077}{4} = 270\right)$	11 $\left(\frac{828}{4} = 207\right)$	11 $\left(\frac{258}{4} = 64\right)$	27 $\left(\frac{2163}{4} = 541\right)$
Number of slices (one cut/slice)	2688	2016	384	5088
Types of slice masks (paint steps)	3 $\left(\frac{2304}{4} = 576\right)$	3 $\left(\frac{1728}{4} = 432\right)$	10 $\left(\frac{480}{4} = 120\right)$	16 $\left(\frac{4512}{4} = 1128\right)$

- Cut and lap of each element:

$$(2541 \text{ slabs}) \times (3 \text{ cuts} + 6 \text{ lap}) = 22,869 \text{ operations.}$$

$$(5088 \text{ slices}) \times (1 \text{ cut} + 2 \text{ lap}) = 15,264 \text{ operations.}$$

-Paint & glue:

$$\text{sandwich: } 2705 \text{ mask \& paint} + 3941 \text{ clean \& glue} = 6646 \text{ operations.}$$

$$\text{slices: } 5640 \text{ mask \& paint} + 5040 \text{ clean \& glue} = 10680 \text{ operations.}$$

Thus, the total number of operations was 55,500, which is only one eighth of the number of steps needed to build the same detector starting with individual needles (see Results section).

A. Tooling

A special set of tools was developed to assure the accuracy and reproducibility of crystal arrays built with the SSS technique.

To create the painted pattern, the slabs and slices need to be masked. Each slab/slice was mounted onto a painting jig and covered by a disposable painting mask. White paint was applied using an airbrush.

Developing a fast way to mask the crystals with high geometrical accuracy was essential. Masking and painting were performed on multiple slabs/slices simultaneously. Multiple slabs were placed in a precise masking painting jig. The jig has recesses that the slabs can slide into snugly, and the slab surfaces are flush with the jig surface (Fig. 6). The jig has 5 precisely placed steel studs for mask alignment. A paper mask with corresponding alignment holes to fit these studs was placed on the jig to cover both the jig and the slabs (Fig. 6). The masks were laser cut [7] from pressure sensitive

¹ The ratios in parenthesis in Table I show the number of slabs or slices masked divided by 4, because there were four pockets in each painting jig holder and all 4 are painted in one operation (see Tooling section).

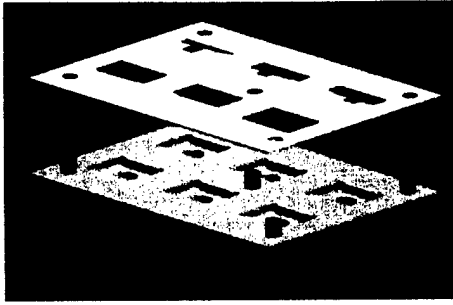


Fig. 6. Bottom: precision painting jig. Top: Laser-cut mask. The jig shown here was built for painting slices (6 pockets). Jigs for painting slabs could hold only 4 slabs due to their larger size.

stock [8]. Removable adhesive on one face of the mask kept it adhered to the jig and crystals while the paint was applied; yet it allowed easy removal of the paper mask leaving no residue on the BGO surface. A laser was used to precisely cut a stack of several sheets of paper at one time. Laser cut patterns are reproducible within 25- μm and accurate within 60- μm , and they cost only \$0.50 per sheet (including raw materials), which could be used to make up to 6 masks (Fig. 6). Ten jigs can be painted at a time.

The paint had to be applied evenly and with a precisely controlled thickness so that many layers of crystals, slabs, and paint could be stacked together with high precision. We used the airbrush technique driven by pressure-regulated N_2 gas from a gas cylinder. Pressure-regulated gas drove a constant rate of paint delivery to control the paint thickness, in addition to being clean and dry. Six coats per surface, applied at 30-minute intervals, were needed for a final thickness of 45- μm .

A precision gluing technique for the slabs and slices was needed. All the slabs and slices were glued together using optically transparent glue [9]. Because of high mechanical precision and optimum optical coupling requirements, the thickness of the glue layer and its application technique were carefully studied. From test run experiments we optimized pre-curing time of the glue to achieve ideal viscosity before application. We designed and built high-precision gluing jigs so that all three dimensions of a sandwich or PSSDA could be tightly compressed and dimensionally regulated (Fig. 7). The setting time of the glue while the array sits in the jig was also studied. It needed to be long enough to harden and avoid compromising the mechanical tolerances at the time of disassembly, yet fresh enough to allow removal from the jig

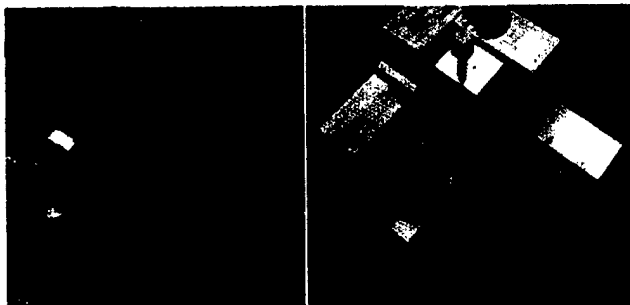


Fig. 7. Left: Gluing jig with sandwich compressed in 3 dimensions. Right: final PSSDA (slices) inside the jig with the top compression removed.

and easy cleaning of excess glue. From these studies we concluded the following timeline for the gluing process: glue mix | pre-curing and air bubble removal (venting) | glue application and array assembly into gluing jig | curing | disassembly and glue excess removal | re-mount into gluing jig | curing | disassembly and final cleaning.

III. RESULTS

The SSS method utilizes painted reflecting barriers on the crystal surfaces to precisely control the light distribution because *any shape can be painted*; this feature optimizes crystal decoding.

Throughout the entire process *no* single crystal needle is *handled individually*, making it a very efficient process.

Crystal needle separation is reduced to a few hundreds of a millimeter, improving detector sensitivity.

All these features of the SSS production method were evaluated with the construction of the detector for our high-resolution clinical-PET prototype HOTPET.

A. Cost and Production

Instead of working with each individual crystal needle, we bought a slab that has the same length as 15 needles stacked side by side. The price per BGO needle was \$4 (\$60 for 15), but the price for a BGO slab (15 wide) was \$31 (due to less processing). Hence, building the detectors from slabs instead of individual needles saved 50% in raw material costs.

The HOTPET detector has nearly 40,000 crystals in it (Table 1). The number of steps (operations) involved in the construction of this detector starting with individual needles is shown below.

- Cut and lap of each element:
(38,016 needles) \times (3 cuts + 6 lap) = 342,144 operations.
- Paint & glue:
 - Painting and masking 15 needles in one operation; from Table I:
541 mask & paint + [541 sets \times 4 (groups of 15) \times 15 needles] clean = 33001 operations.
 - Gluing 7(8) needles together into a slice and painting the slice:
7 \times 7-crystal-block = 18,816 operations
7 \times 8 and 8 \times 8 blocks = 19,200 operations.
 - Slice painting = 5,640 operations.
 - Final glue, put slices together into a PSSDA = 5,040 operations.

Thus, the total number of operations would be 423,800, compared to 55,500 operations with the SSS production method. That is an 87% reduction in labor costs and lowers the probability of mistakes during assembly because fewer parts are handled. Notice the large disparity in the number of operations between the two methods, in spite of attempts to reduce the number of steps involving individual needles; e.g., 15 needles would be placed next to each other and painted together, and groups the size of a slice would be first glued and then painted together. If the process is not optimized, and every crystal is cut, lapped, painted and glued *separately*, the production process for our new detector would require in excess of 0.5 million operations.

The SSS method has a high production yield because if a slice is broken during cutting, the broken slice can be replaced by the next cut from the same sandwich. Hence only 1/7 or 1/8 of the final block is wasted, whereas in the traditional partial-depth sawing method the whole block (49-64 crystals) would be wasted with one bad cut. Production of detector blocks for our first-generation camera MDAPET using the traditional partial-depth method had only a 70% production yield. In contrast, the SSS production method had a slice-cutting yield of 94%. Once we perfected the method, slicing of the sandwiches was performed by the manufacturer of the BGO slabs [6].

The entire painting process of applying masks on slabs and slices had a 98.9% yield.

B. Mechanical Tolerances

Nominally, we had set out to build three types of PSSDA with the following dimensions: 7x7-symmetric – 19 mm x 19 mm x 18 mm, 7x8-non-symmetric-extended – 19 mm x 24.76 mm x 18 mm, 8x8-corner-non-symmetric – 24.76 mm x 24.76 mm x 18 mm. Most of the 720 blocks for HOTPET have been built and we studied their mechanical characteristics to evaluate the mechanical consistency of the SSS method.

The SSS method imposes no mechanical constrain on the length of the slabs that form a sandwich because they are cut into slices. Thus, we purchased 50 mm long slabs with a wide tolerance of ± 0.1 mm to lower material costs, but with tight enough tolerances to facilitate the assembly of the sandwich inside the painting and gluing jigs. The thickness of the slabs and slices, on the other hand, were crucial to the overall size of the finished PSSDA. We specified a tolerance of only $(-0.05$ mm below the nominal thickness of 2.68 mm and 3.06 mm to the BGO manufacturer. These are the only two types of slabs purchased to produce all the detector arrays for HOTPET.

We evaluated size variations of nearly 200 slices and slabs and more than 120 assembled blocks, and have identified

four factors that affect their dimensions. These variations are important because they directly affect the actual placement of a needle within the PSSDA. These factors are depicted in Fig. 8.

(a) Length variations among slices from the *same* sandwich type (nominal value 19 mm, and 24.76 mm; $\sigma = 0.04$ mm, Fig. 8(a)). This variation, caused by differences in thickness of the slabs, paint layer, and/or glue layer, is a measure of the reproducibility of the SSS method.

(b) Length differences in slices from *different* sandwich types (average difference 0.1 mm, Fig. 8(b)). These differences are due to the variation in number of masks painted in each sandwich type. The parent sandwich of a slice with less number of masks in it will yield shorter slices than another sandwich with greater number of masks supplying the adjacent slice for the same PSSDA. This is a source of systematic error in the SSS method.

(c) Slices show vertical slant (average top-bottom difference 0.15 mm, Fig. 8(c)). All masks are applied closer to the patient end of the PSSDA, with nothing on the PMT end to make up for this extra thickness. Therefore, slices can tilt. Inadequate sliding constrains of the compression pieces in the gluing jig allowed this displacement of the slices.

(d) Axial and trans-axial dimensions of square blocks are not equal (average difference 0.07 mm Fig. 8(d)). This is due to the fact that equal force was applied by the compression pieces of the gluing jig to the side of a sandwich (50 mm x 18 mm surface – axial direction) and to the side of slice (19 mm x 18 mm surface – trans-axial direction). Therefore, the pressure difference results in glue layers of different thicknesses.

The typical thickness of the paint plus glue layer between crystals was 0.06 mm.

Overall, the four factors described above combined with the inter-crystal gap produced PSSDAs with the following dimensions: 7x7 array – 18.97 mm x 19.12 mm x 18.1 mm; 7x8array – 19.13 mm x 24.85 mm x 18.1 mm; 8x8array – 25.48 mm x 25.39 mm x 18.1 mm. The variance of these dimensions were all under $\sigma^2 = (0.09 \text{ mm})^2$; and they were 98.5% to 99.8% within the target values. It is important to note that the variance and mechanical tolerances described above come from dimensions of complete slices and arrays; that is, they describe the positioning error of the last crystal in a stack of 7-8 needles. Thus, the *average* crystal-positioning error is smaller than the values shown above.

The very small gap between crystals results in a 98% linear detector packing fraction (96% in area). Compared with the typical 90% linear packing fraction (81% in area) in commercial systems [10], the 96/81 (1.2x) higher detector-packing density would result in a 1.2-1.44 times higher coincidence detection sensitivity.

The solidly glued blocks are very robust mechanically. Note the superior mechanical tolerance of the block produced by the SSS production method in Fig. 4 bottom-right.

C. 2D map decoding and energy spectra

We evaluated the crystal decoding capability of PSSDAs built with the SSS method. Fig. 9 presents the two-dimensional decoding map and the block's composite energy

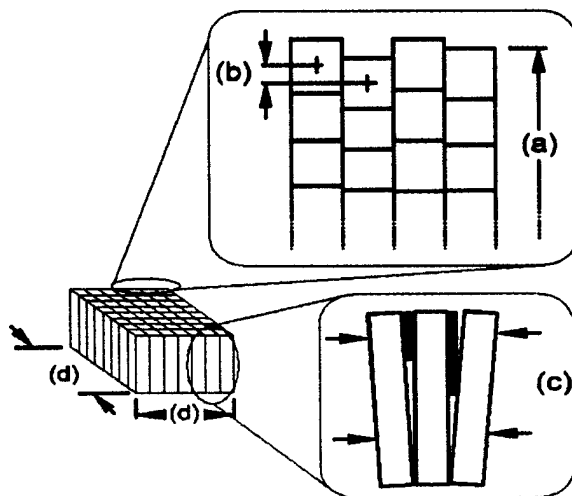


Fig. 8. Four sources of mechanical tolerances from the SSS manufacturing process: (a) glue, paint and slab thickness (needle positioning error, measures repeatability); (b) systematic differences between sandwich types; (c) needle slant (paint placement, gluing jig limitations); (d) axial vs. trans-axial dimension differences (size of surface glued).

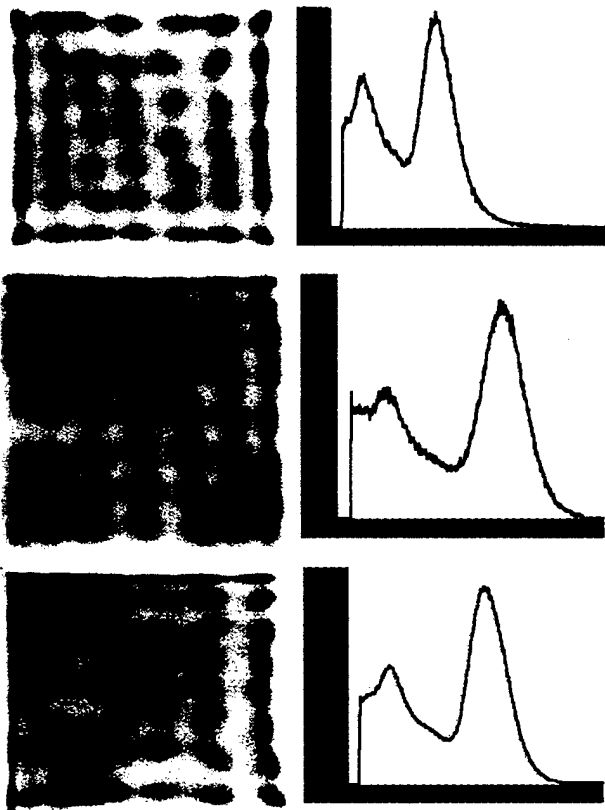


Fig. 9. Two-dimensional decoding map (left) and composite energy spectra (right) of all needles from the three types of PSSDA used in HOTPET (Fig. 1). (top) 7x7 symmetrical array, (middle) 7x8 extended non-symmetrical array, (bottom) 8x8 optically-non-symmetrical array used for the module's corners. (Electronic gain and PMT high-voltage settings not equal for all configurations)

spectrum for the three types of arrays built for the prototype camera HOTPET. Energy resolution for these blocks is as follows: 7x7-array = 25.6%; 7x8-extended-array = 29%; and 8x8-corner-array = 31%.

A detailed study of crystal signal characterization of the square-7x7 and extended-7x8 arrays can be found in [11].

IV. CONCLUSIONS

- The slab-sandwich-slice "SSS" production method for position sensitive scintillator detector arrays (PSSDA) was developed and evaluated by building 720 PSSDA (40,000 crystals) for the high-resolution PET camera HOTPET.

- SSS utilizes painted reflecting barriers on the crystal surfaces to precisely control the scintillation-light distribution, allowing optical windows of *any shape*. Barriers were optimized for crystal identification of gamma hits on the PSSDA (Fig.5 and Fig. 9), improving intrinsic detector resolution. Construction of asymmetric PSSDA was possible thanks to these versatile light barriers, minimizing the unused PMT photocathode area left by PMT-quadrant sharing detector technology.

- Instead of working with each individual crystal needle, the SSS method handles only arrays (sandwich, slices) of needles, making the production of PSSDAs 8 times more efficient; and because the raw material is purchased in large slabs, many needles long, it cuts material cost by 50%.

- The average crystal-positioning error was very small ($\sigma < 0.09$ mm), which is essential for an ultrahigh resolution detector. Sources of positioning error were linked to four mechanical variations in the PSSDA construction method.

- The gap between crystals was only 0.06 mm, producing PSSDAs with good linear packing fraction (98%, 96% area), or equivalently a coincidence efficiency of 92%, which is 1.4 times higher than in commercial cameras.

- The SSS method was flexible and easy to implement. It could be applied to detector arrays manufactured with other materials (LSO, GSO, etc).

- Two *patents* titled "A Production Method for Making Position Sensitive Radiation Detector Arrays" and "Asymmetrically Placed Cross-coupled Scintillation Crystals" (U.S. patent office, filed Feb/2002), describe the SSS method.

V. ACKNOWLEDGMENT

We want to thank the machinists at the Radiation Physics shop at M.D. Anderson, M. Bushman, J. Bowin, P. Barnet, J. Griffin, K. Danniell, and T. Ziegler, for their support manufacturing the tools necessary for this project. We want to thank P. Mayes (physical plant manager) for providing materials and making modifications to our laboratories to accommodate the detector construction.

VI. REFERENCES

- [1] W-H. Wong, J. Uribe, H. Baghaei, H. Li, Y. Wang, M. Aykac, Y. Liu, "Design of a whole-body high resolution PET with changeable transaxial and axial fields of view", *Abstract Book, Society of Nuclear Medicine 48th Annual Meeting*, Toronto, Canada, June 2001.
- [2] W-H. Wong, J. Uribe, H. Li, H. Baghaei, Y. Wang, M. Aykac, Y. Liu, T. Xing, D. Bilgen, R. Farrell, "The design of a high resolution transformable wholebody PET camera," *IEEE Trans. Nucl. Sci.* vol. 49, no. 5, pp. 2097-2102, Oct. 2002.
- [3] W-H. Wong, "A positron camera detector design with cross coupled scintillators and quadrant sharing photomultipliers," *IEEE Trans. Nucl. Sci.*, vol 40, pp. 962-966, 1993.
- [4] W-H. Wong, S. Yokoyama, J. Uribe, et al, "An elongated position sensitive block detector design using the PMT Quadrant Sharing detector array," *IEEE Trans. Nucl. Sci.*, vol 46(3), pp. 542-545, 1999.
- [5] J Uribe, H. Baghaei, H. Li, et al, "Basic imaging performance characteristics of a variable field of view PET using quadrant sharing detectors," *IEEE Trans. Nucl. Sci.*, vol 46, no.6, pp. 491-497, 1999.
- [6] Institute of Inorganic Chemistry, Siberian Branch, Russian Academy of Science 3, Acad.Lavrentyev Prospect, 630090 Novosibirsk, Russia.
- [7] Lasercraft Inc. 3300 Coffey Ln. Santa Rosa, CA 95403-1917.
- [8] FASSON® Crack 'N peel Satin Litho, #316, pressure sensitive stock. Avery Dennison Corp. 150 North Orange Grove Blvd. Pasadena, CA 91103-3596.
- [9] Reflector paint and glue from SaintGobain, Newbury, OH 44065.
- [10] S.R. Cherry, M.P. Tornai, C.S. Levin, S. Siegel, E.J. Hoffman, "A comparison of PET detector modules employing rectangular and round photomultiplier tubes," *IEEE Trans. Nucl. Sci.*, Vol. 42, no 4 pp. 1064 -1068, Aug. 1995.
- [11] J. Uribe, H. Li, Y. Liu, T. Xing, H. Baghaei, Y. Wang, Rocio Farrell, W-H. Wong, "Signal characteristics of individual crystals in a high resolution BGO detector design using PMT-Quadrant Sharing," *Conference Record IEEE, Nuclear Science and Medical Imaging conference*, Norfolk, VA, November, 2002.

An Iterative Energy-Centroid Method for Recalibration of PMT Gain in PET or Gamma Camera

Yu Wang, Wai-Hoi Wong, *Member, IEEE*, Mehmet Aykac, Jorge Uribe, *Member, IEEE*, Hongdi Li, *Member, IEEE*, Hossain Baghaei, *Member, IEEE*, Yaqiang Liu, and Tao Xing

Abstract—In gamma and positron emission tomography cameras, photomultiplier tubes (PMT) are still the most popular photosensors. Gain uniformity of the PMTs in these instruments is very important for preventing degradation in image resolution and distortion. When an Anger decoding detector head is exposed to a uniform flood source without lead collimation, the energy spectrum acquired by any single PMT has no photopeak for conducting recalibration. A method using the centroid of a wide energy spectrum even without photopeak as a gain-tuning index is presented in this paper. With a uniform flood illumination, without collimation, the gain equalization of PMTs within an array can be tuned to its initial level by an iterative centroid match. If an electrically adjustable gain control circuitry such as tunable PMT high-voltage or variable-gain amplifier is applied, the recalibration can be done automatically with this method. Our experiments demonstrated a 2.5%–3% gain accuracy that is enough to eliminate distortion in total energy and two-dimensional decoding. Counting efficiency increases significantly, and the calibration or system-tuning time will be shortened because of efficiency improvement.

Index Terms—Energy spectrum, gamma camera, PET camera, photomultiplier tube, recalibration.

I. INTRODUCTION

TO OBTAIN AN image with the least distortion from a gamma or positron emission tomography (PET) camera, the photosensors' gain uniformity must be kept as high as possible. If the detection system is simply one detector with a single PMT (photomultiplier) [1], a radioactive source or light-emitting diode (LED) allows one to use the photopeak for calibration. However, it is not easy to determine the gain of a PMT that is grouped in a PMT array such as in the gamma or PET camera if the photopeak is absent.

When using LEDs, there are two major problems. The first problem is that assembling the LEDs in the detectors requires extra cost. The second problem is that the LEDs themselves need to be calibrated, because the light output from an LED changes with temperature and age.

When using radioactive sources, the conventional photopeak detection requires fine collimation. Collimation decreases de-

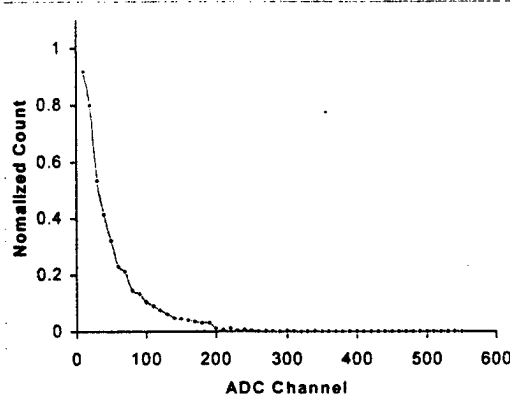


Fig. 1. Normalized energy spectrum of a single PMT used in an Anger decoding PMT array.

tection efficiency significantly. Low efficiency is not an issue if the number of PMTs in the array is small, for example, in gamma cameras. However, if the number is several hundred or more, the low efficiency lengthens the recalibration or gain adjustment. In addition, aligning a collimator with a detector is somewhat complicated. To simplify the recalibrating operation and shorten the recalibration time, one can remove the collimator. Without a collimator, using a uniform flood illumination, each individual PMT's energy spectrum does not have a photopeak for tune-up, as illustrated in Fig. 1.

After analyzing the relationship between the PMT's gain and its energy spectrum in Fig. 1, we have developed a method that can determine the PMT gain-tuning direction through calculating the centroid in a wide energy window. Therefore, even the Compton scattered part of the spectrum would be used for calibration. As a result, the efficiency and accuracy (because of a smaller statistical error) of the gain recalibration can be improved greatly, and tuning time can be reduced.

II. METHOD

A. Principle

Once a detector is fabricated, the amount of scintillation light impinging on a PMT from a uniform field of activity is almost fixed during the detector's on-duty life, because it depends on the characteristics of the scintillator, the geometry, and the light coupling between the crystal and the PMT. For this reason, when recalibrating a PMT, if the shape of the energy spectrum without photopeak is identical to its initial setting, the gain of the PMT

Manuscript received November 21, 2001; revised July 22, 2002. This work was supported in part by the National Institutes of Health Grant ROI CA58980, Grant ROI CA61880, Grant ROI CA76246, Grant ROI CA58980S1, by a Texas Higher Education Advanced Technology Grant, by the J.S. Dunn Research Foundation, and by the Cobb Endowment for Cancer Research.

The authors are with the M.D. Anderson Cancer Center, University of Texas, Houston, TX 77030 USA (e-mail: wangy_km@yahoo.com).

Digital Object Identifier 10.1109/TNS.2002.803773

is finely tuned. The centroid of the energy spectrum can be regarded as an index for conducting gain adjustment, because it represents the weighted average energy of the gamma events acquired by the PMT. If the PMT and the amplifier all work in their linear ranges, the centroid is proportional to the product of the PMT gain and the input scintillation to the PMT. By providing a uniform flood gamma illumination from the same radioisotope, we can keep the input scintillation light relatively constant. Consequently, if the centroid of the energy spectrum moves, it means that the PMT gain has changed.

To reduce the interference from noise, a wide window is applied. Thus, the centroid within the wide window can be calculated as

$$\text{Centroid} = \frac{\sum_{i=cl}^{ch} i \times \text{Count}(i)}{\sum_{i=cl}^{ch} \text{Count}(i)} \quad (1)$$

where i is channel number; $\text{Count}(i)$ is the event count in channel i ; cl is low energy threshold; and ch is high energy threshold. The values of cl and ch must be determined through experiments. Because we know where the photopeak of the total energy is after the first calibration, cl can be roughly set to around 15% of the photopeak channel, and ch can be set to 2–2.5 times the photopeak channel.

B. Realization

In order to recalibrate the PMTs with this method, a centroid reference must be established for each PMT. Based on the total energy spectrum from the first calibration, we can choose the low and high margins (cl, ch) of the energy-acceptance window for centroid calculation as mentioned above. For both reference creation and PMT recalibration, a uniform gammaradioactive flood source is placed in front of the detectors. The gains of all other PMTs except the one undergoing testing need to be set as close to zero as possible in order to minimize signal interference. In each data acquisition, about 200 000 events are required to calculate the energy centroid accurately.

For reference creation, shown in Fig. 2(a), the following three main steps are taken.

- Step 1) Acquire data and create energy spectra 10–20 times to reduce the statistical error.
- Step 2) Calculate the centroid of each acquired energy spectrum and then calculate the mean and the variance of all centroid values.
- Step 3) Record the margins (cl, ch) of energy-acceptance window, the mean, and variance of centroid values as the reference for future recalibration.

During the recalibration [Fig. 2(b)], data acquisition, centroid calculation within the reference energy-acceptance, and centroid comparison are iteratively performed until the centroid falls within the referred variance margins.

Fig. 3 illustrates the values of the mean and the variance of the centroids calculated from the energy spectra by setting high voltage to different levels to simulate different PMT gain. The variance of the centroid determines the gain-tuning resolution that this method can achieve.

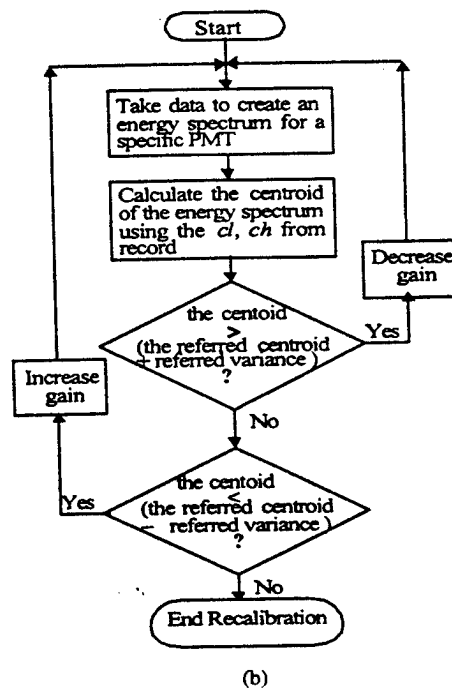
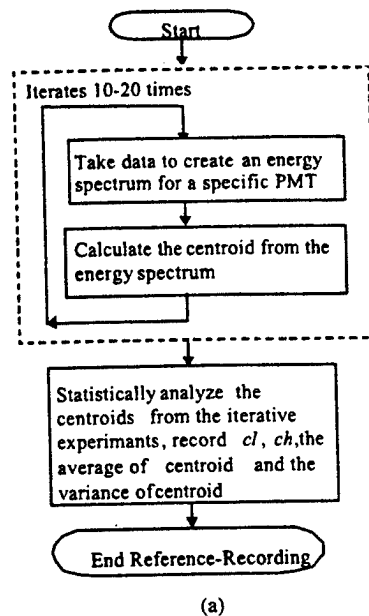


Fig. 2. Realization diagrams for (a) reference creation and (b) recalibration.

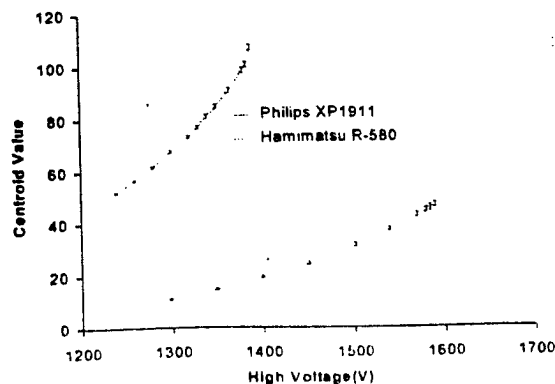


Fig. 3. Energy spectrum centroid versus high voltage.

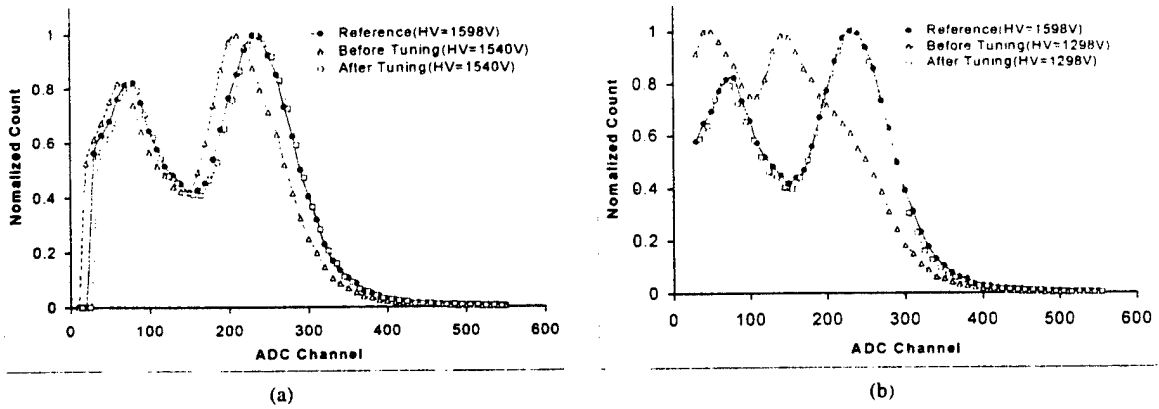


Fig. 4. Total Energy (sum of four PMTs' energy) spectrum comparison before and after calibration. (a) With the under-test PMT's high voltage set to 1540 V. (b) With the under-test PMT's high voltage set to 1298 V.

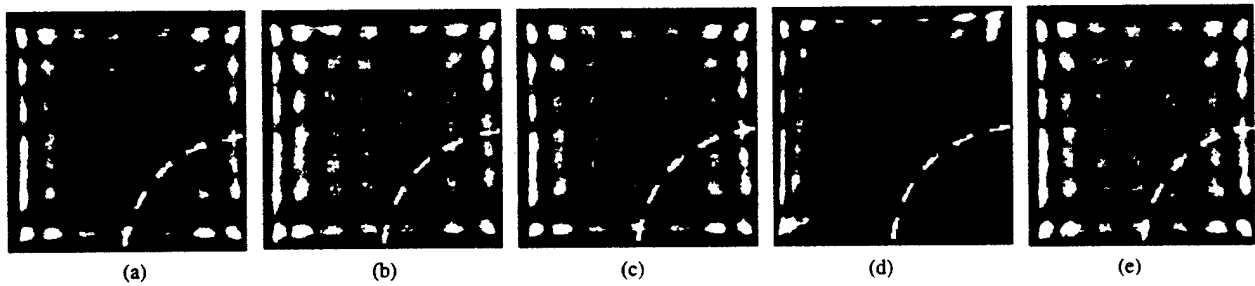


Fig. 5. Two-dimensional decoding map comparison before and after recalibration. (a) Reference for the comparison with all PMTs' high voltage set to 1598 V. (b) Before recalibration with the lower-right (marked by the white dashed line) PMT's high voltage reduce to 1540 V. (c) After recalibration with same setting as (b). (d) Before recalibration with the lower-right (marked by the white dashed line) PMT's high voltage set to 1298 V. (e) After recalibration with same setting as (d).

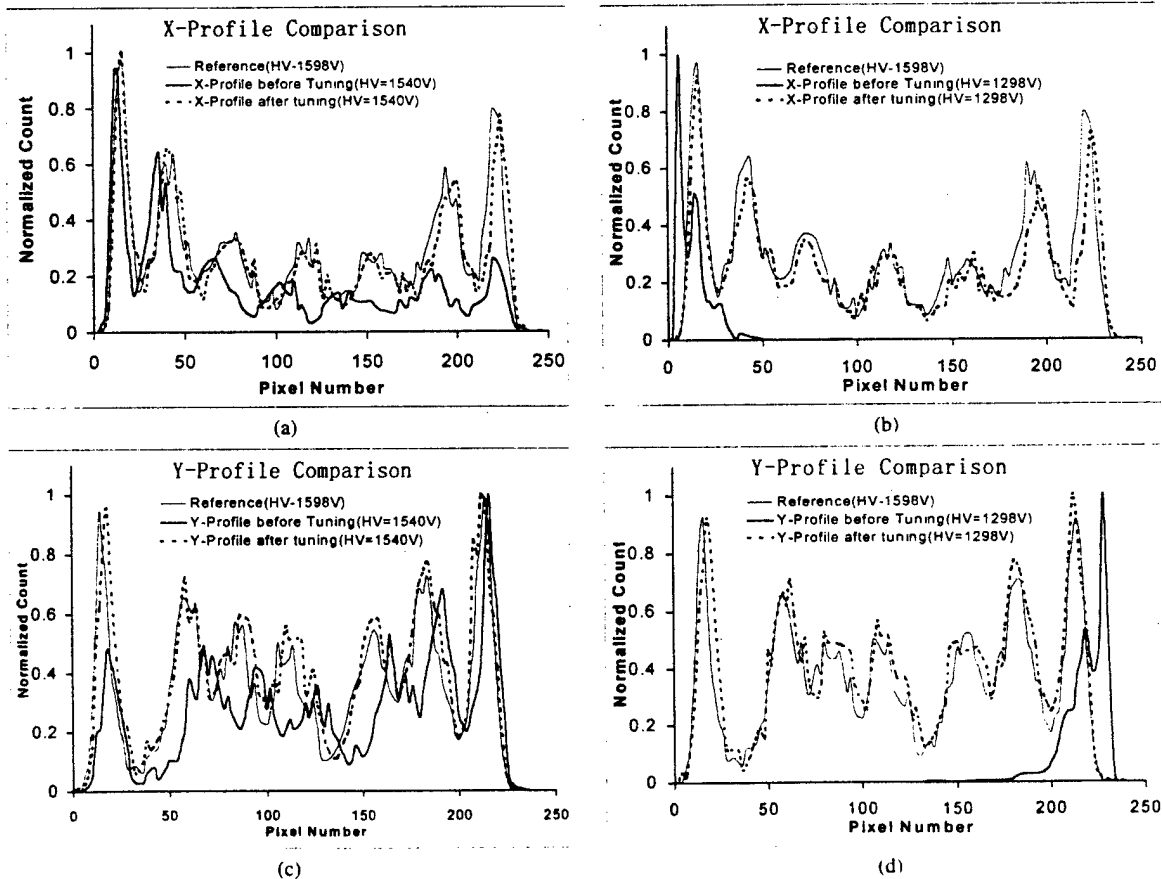


Fig. 6. 2-D decoding map X-profile (bottom row in Fig. 5) and Y-profile (rightmost column in Fig. 5) comparison before and after calibration. (a) X-profile comparison with the under-test PMT's high voltage set to 1540 V. (b) X-profile comparison with the under-test PMT's high voltage set to 1298 V. (c) Y-profile comparison with the under-test PMT's high voltage set to 1540 V. (d) Y-profile comparison with the under-test PMT's high voltage set to 1298 V.

III. RESULTS

We have tested the method on two PET detector configurations with PMT quadrant-sharing design [3], [4], one used four Hamamatsu R580 and an 8×8 Bismuth-Germanate-Oxide (BGO) block that was $40 \text{ mm} \times 50 \text{ mm}$, and the other used four Philips XP1911 and a 7×7 BGO block that was $19 \text{ mm} \times 19 \text{ mm}$. As small as 3-V high-voltage variation can be perceived with the proposed method. It is equivalent to 2.5%–3% accuracy when recalibrating PMT gain. Moreover, the total energy (sum of four PMTs' energy) spectrum after tuning matches the original energy spectrum well (see Fig. 4). Meanwhile, the two-dimensional (2-D) crystal decoding map and its X - and Y -profile comparisons show that the original 2-D decoding map can be reproduced after tuning (see Figs. 5 and 6). All the data shown in Figs. 4–6 are from the configuration of the XP1911 PMTs and the $19 \text{ mm} \times 19 \text{ mm}$ BGO block.

IV. CONCLUSION AND DISCUSSION

In this study, we have developed an efficient PMT equalization method that does not rely on the presence of photopeaks in each PMT signal. Hence, it can be applied to PET or

Gamma cameras without collimators. In our experiments, about 2.5%–3% recalibration accuracy has been achieved. Furthermore, compared to the method using collimator, the recalibration time is reduced about ten times.

The iterative energy centroid method is not only applicable to energy spectra without photopeaks, but also applicable to spectra with photopeaks. Because more events can be used, this method improves the recalibration accuracy as well as recalibration time, even for spectra with photopeaks. Such a method also facilitates autotuning with an electrically adjustable gain control circuitry such as tunable PMT high-voltage or a variable-gain amplifier.

REFERENCES

- [1] W. Taylor, "External calibration system for a photo multiplier tube," U.S. Patent 6 016 192, Dec. 18, 1997.
- [2] D. Vickers, "Gamma camera with on the fly calibration for PMT drift," U.S. Patent 5 677 536, June 19, 1996.
- [3] W.-H. Wong, "A positron camera detector design with cross-coupled scintillators and quadrant sharing photomultipliers," *IEEE Trans. Nucl. Sci.*, vol. 40, pp. 962–966, Aug. 1993.
- [4] W.-H. Wong, J. Uribe, K. Hicks, and M. Zambelli, "A 2-dimensional detector decoding study on BGO arrays with quadrant sharing photomultiplier," *IEEE Trans. Nucl. Sci.*, vol. 41, pp. 1453–1457, June 1994.

A New Pileup-Prevention Front-End Electronic Design for High-Resolution PET and Gamma Cameras

Hongdi Li, *Member, IEEE*, Wai-Hoi Wong, *Member, IEEE*, Jorge Uribe, *Member, IEEE*, Hossain Baghaei, *Member, IEEE*, Yaqiang Liu, Yu Wang, Tao Xing, and Mehmet Aykac

Abstract—A new method for processing signals from Anger position-sensitive detectors used in gamma cameras and positron emission tomography (PET) is proposed for very high count-rate imaging. It has a same concept as high yield pileup-event recover (HYPER) method we introduced before by using 1) dynamically integrating a present event, the integrating will stop immediately before the next event is detected; 2) estimating a weighted-value to indicate the total energy inside the scintillation detector; and 3) remnant correction to remove the residual energy of all the previous events from the weighted-value. This paper introduces two improved practical techniques to get a better weighted-value with low noise sensitivity in order to improve the final pileup-free energy resolution. One is applying a low-pass filter combined with multiple sampling to a weight-sum of the instantaneous signal and integrated signal. The other one is weighting the integration value of the income signal; the weighting also includes exponential distortion compensation. This paper also describes the application of the HYPER electronics in a high resolution low cost PET camera with 12 photomultipliers (PMTs)-quadrant-sharing (PQS) detector modules that can decode 38 016 bismuth-germanate (BGO) crystal elements using 924 PMTs. Each detector module has four Anger-HYPER circuits to further increase the count-rate. To use the HYPER circuit in coincidence imaging applications, there is a serious synchronization problem between the arrival time of an event and the end time of integration that is variable from event to event. This synchronization problem is solved by a field programmable gate array (FPGA) circuit with real time remnant correction and a high-resolution trigger delay unit with a small dead-time for recovering the synchronization of data and the event-trigger.

Index Terms—High count rate, high-speed electronics, nuclear imaging, positron emission tomography.

I. INTRODUCTION

IN THE application of bismuth-germanate (BGO) scintillation detectors, the time integration is generally fixed for 800 ns to collect 93% of the scintillation signal. However, in high count-rate situations, many of these derived signals are erroneous due to pileups. We have proposed a high yield pileup-event recover (HYPER) method [1], [2] that can process scin-

tillation signals in very high count-rate situations where multiple-event pileups are normal. We have proven theoretically that if all the time integrations of the electron charges for each gamma are dynamically variable and only are carried out from the onset of this gamma i th to the onset of the next gamma $(i + 1)$ th, the pileup-free signals for each gamma ray can be extracted as follows:

$$\begin{aligned} X_i &= \left[\tau X'_i(t_{i+1}) + \int_{t_i}^{t_{i+1}} X'_i(u) du \right] - \left[\tau X'_{i-1}(t_i) \right. \\ &\quad \left. + \int_{t_{i-1}}^{t_i} X'_{i-1}(u) du \right] * e^{-(t_i - t_{i-1})/\tau} \\ Y_i &= \left[\tau Y'_i(t_{i+1}) + \int_{t_i}^{t_{i+1}} Y'_i(u) du \right] - \left[\tau Y'_{i-1}(t_i) \right. \\ &\quad \left. + \int_{t_{i-1}}^{t_i} Y'_{i-1}(u) du \right] * e^{-(t_i - t_{i-1})/\tau} \\ E_i &= \left[\tau E'_i(t_{i+1}) + \int_{t_i}^{t_{i+1}} E'_i(u) du \right] - \left[\tau E'_{i-1}(t_i) \right. \\ &\quad \left. + \int_{t_{i-1}}^{t_i} E'_{i-1}(u) du \right] * e^{-(t_i - t_{i-1})/\tau} \end{aligned} \quad (1)$$

(all the variables with a “prime” sign are the raw exponentially decaying signals from photomultipliers (PMTs) with pileup/remnant from previous events), where τ is the characteristic scintillation-emission-time constant of the scintillation crystal.

This equation set is easy to implement in fast electronic hardware in real time for three reasons.

- 1) The position X , Y , and energy E are processed the same way by three identical circuits.
- 2) It involves only the summing of the amplified instantaneous/fast signals $[X'(t), Y'(t), \text{ and } E'(t)]$ and their dynamically-variable integrations.
- 3) It only needs the last gamma-sum signal weighted by the time lapse between the present gamma and last gamma event; it is a simple two-gamma recurring relationship where the last sum can be temporarily stored into a register and the weighting factor can be read from a lookup table addressed by the time lapse. We have proven that this two-gamma recurring relationship can correct for all the signal remnants from multiple prior signals that the current event is riding on [1], [2].

Manuscript received November 19, 2001; revised May 19, 2002. This work was supported in part by the National Institutes of Health (NIH) under Grants RO1 CA76246, RO1 CA61880, and RO1 CA58980, by the Texas Higher Education Advanced Technology (ARP/ATP) Grant 003657-0058-2001, the J.S. Dunn Research Foundation, the Cobb Endowment for Cancer Research, and by the 1999 RSNA Education and Research Seed Grant.

The authors are with the M.D. Anderson Cancer Center, University of Texas, Houston, TX 77030 USA (e-mail: hli@di.mdacc.tmc.edu).

Digital Object Identifier 10.1109/TNS.2002.803804

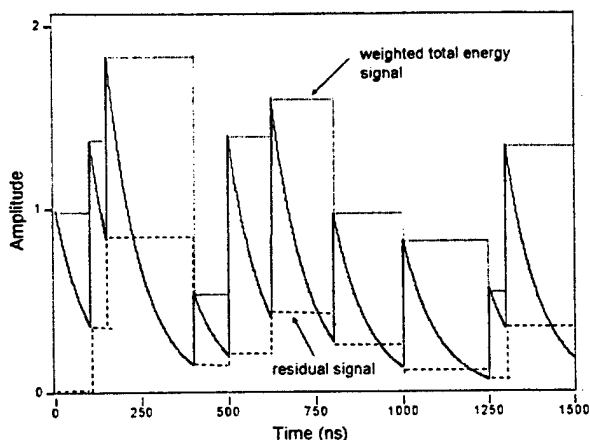


Fig. 1. HYPHER method in a continuous pileup condition at high count-rates. (Solid line: amplified fast signal, dashed line: residual signal, dotted line: sum or total energy signal). The total energy signal is equal to the energy of this pulse plus a residual energy signal, which is decayed from the preceding total energy signal. The residual signal = (the total signal of the preceding pulse) $\times \exp(-(\text{time lapse between this event and the preceding event})/\tau)$.

However, for the application of BGO scintillation detector, the low scintillation light emitted by BGO increases the statistical noise in the fast signals (X' , Y' , and E') which in turn increases the statistical uncertainty in the measured pileup-free X , Y , and E . This BGO-specific problem is solved by finding a better total energy estimation with low noise sensitivity in two different ways. First, smoothing the sum signals and multisampling the smoothed outputs, then using the average value of the multisamples as the new estimated sum signals. The low-pass smoothing and multisampling circuits greatly minimize the error in deriving X , Y , and E . Second, using the integrated charge and the measured time lapse of two continuous events coupled to an exponential distortion compensation circuit to estimate the total charge (since we also know the characteristic time-constant of the exponential emission function).

II. METHODS

A. Basic HYPHER Method

The basic idea of the HYPHER method we suggested for prevent signal pileups in scintillation detector is: a) dynamically integrating the signal from the detector; the gated integration of the present event will stop immediately at the coming edge of the next event in order to reject the pileup from the next event; b) estimating a total energy inside the scintillation which includes the energy from the present event and the remnant energy from all the previous events; c) remnant correction. The energy of this event can be derived by subtracting the residual energy (a decay-weighted of the previous total energy) from this total energy; and d) the HYPHER method is correct for both energy and prenormalized position signals in Anger type gamma camera or PET.

Fig. 1 shows the relations of the pulse signal, the total energy and the residual signal in continuous pileup situation. In our first HYPHER design, we used a weighted-sum value for estimating the total energy inside the scintillation by summing the amplified pulse signal and its own time-integration signal.

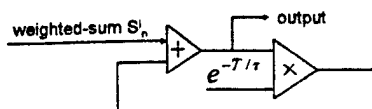


Fig. 2. Example of decay filter.

B. Improved HYPHER Methods

Since the low scintillation light emitted by BGO increases the statistical noise in the fast signals (X' , Y' , and E') which in turn increases the statistical uncertainty in the measured pileup-free X , Y , and E . In this paper we studied several alternate methods that may be especially beneficial to implementing the low light-output scintillation detector. The idea is to have a better estimation of the total energy with low noise sensitivity by processing the signal in different ways (no change in the fast-trigger channel).

1) *A Low-Pass Filter Combined With Multisampling for the Sum Signal of Basic HYPHER Method:* The weighted-sum signal of the integrated signal and the instantaneous signal amplified by τ is a constant in time, and is always a measure of the total radiation energy before the next event is detected, regardless of when the sum-signal is sampled. Since the instantaneous signal is noisier than the integrated signal, a low-pass smoothing circuit is applied to the weighted-sum signal in order to reduce the noise. To further increase the signal to noise ratio, the weighted-sum signal is multiple-continuously sampled, and a digital low-pass filter (e.g., a median value filter or a weighting processing) is applied to the samples to get a better estimated total energy signal. For example

$$S_n = W_1 S_n^1 + W_2 S_n^2 + \dots + W_m S_n^m \quad (2)$$

$$W_1 + W_2 + \dots + W_m = 1 \quad (3)$$

$$W_i = W_{i+1} e^{-T/\tau} \quad (4)$$

where S_n^i indicates the i th sample of the weighted-sum signal for event- n and S_n is the estimated total energy output. Since a later sample of the weighted-sum has a better statistics than an earlier sample, the weighting factor for an earlier sample should be smaller than that for a later sample. Refer to (4), where T is sampling period, the weighting factor follows the same exponentially decay as the pulse signal. Fig. 2 shows the diagram of this decay filter. Since the number of samples (N) is not fixed, the accumulated output signal has to be normalized by a factor $(1 - e^{-N \cdot T/\tau}) / (1 - e^{-T/\tau})$ to generate the estimated total energy.

To have a simple electronic design, we just buffered the several latest samples of the weighted-sum signals and created an average of the buffered signals for the estimated total energy. Fig. 3 shows an experimental result using this method. At the count-rate of 700 Kcps, about 3% of the events recorded were about the photo-peak that was mainly come from the pileup of undetected low-energy scatter events. This could happen to all the different methods mentioned later since they had a same event-trigger circuit. To improve the performance of the fast trigger circuit will not be discussed in this paper.

Although the noise in sum signal contributed by the fast signal E' decreases the energy resolution, it may have a small affect on

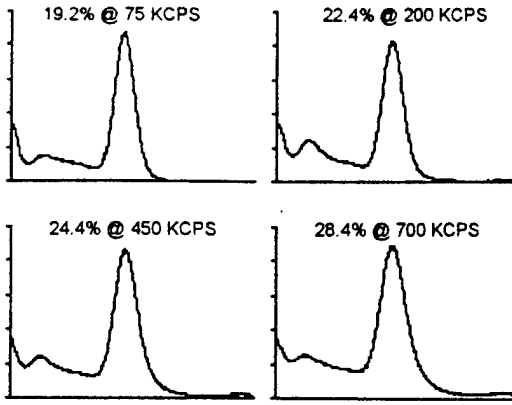


Fig. 3. FWHM energy resolution versus count-rate of Cs-137 measured by a 1'' x 1'' x 3'' BGO detector using a low-pass filter/two-samples weighted-sum HYPER method.

position decoding resolution. Because if a noise is caused by the low scintillation light and collected by PMTs, it will also have a weighted contribution to the sums of X' , Y' in Anger method, hence, it can still generate a correct position after normalizing prenormalized position signal (X' , Y') with the energy E' .

The advantages of using a weight-sum signal/multisampling to estimate the total energy in implementation are: a) it can produce the total energy directly; no further calculation will be involved; b) since the sampling time for the time-constant sum signal is not critical, instead of using the expensive flash ADC, a very cheap pipe-line sampling ADC (analog to digital converter) with a fixed sampling period can be used to digitize the sum signal. Sampling ADCs are widely used in telecommunications and digital cameras; the price of an ADC with 80 MSPS sample-rate with 10 b resolution is only about US \$10.

2) *Using a Weighted Integration to Estimate the Total Energy:* If the total instantaneous signal (the signal of present event and the remnant signal of all the previous events) is purely exponentially decaying, the total expected energy can be expressed by (5) or (6). Equation (5) is the weight-sum signal we used in the basic HYPER method

$$S_i = \int_{t_i}^{\infty} \frac{S_i}{\tau} e^{-(t-t_i)/\tau} dt$$

$$= \tau \frac{S_i}{\tau} e^{-(t-t_i)/\tau} + \int_{t_i}^t \frac{S_i}{\tau} e^{-(t-t_i)/\tau} dt \quad (5)$$

$$S_i = \int_{t_i}^{\infty} \frac{S_i}{\tau} e^{-(t-t_i)/\tau} dt$$

$$= \frac{1}{1 - e^{-(t_{i+1}-t_i)/\tau}} \int_{t_i}^{t_{i+1}} \frac{S_i}{\tau} e^{-(t-t_i)/\tau} dt. \quad (6)$$

Equation (6) indicates that the total energy signal can be calculated from the charge integration output (charge integration starts at the arrival of i th event and stops at the arrival of the $(i + 1)$ th event). It is basically the compensation term to make up for the charge deficit of the prematurely stopped integration, when the next $(i + 1)$ th event comes in too early (pileup). The integrated charge and the measured time lapse between two events can be used to estimate this charge deficit, hence, the total charge. Replacing the weight-sum part in (1) with the estimation value mentioned in equation (6), the position and energy are now

derived from just two integration terms without the noisier instantaneous-signal terms, and the integration terms have lower statistical noise. Hence, this modified HYPER may provide a better estimation of positions and energies.

However, this method is very sensitive to both systemic and random timing errors. Systemic timing distortion can be caused by crystals with longer rise time such as GSO and CsI(Tl), or by a slow PMTs and electronics, which distort the ideal exponential decay. Random timing errors in measuring the arrival of events (timing-trigger errors) and the time lapse between two events are also carried to the final energy measurement, because the charge-deficit correction is totally dependent on these time values, refer to (6); While the basic HYPER method is very insensitive to the triggering time or data sampling time as the sum is a time-constant.

We have tried both weighted-integration and weighted-sum methods in our first prototype HYPER circuit in 1997, the weighted-integration method generated a worse energy resolution than the weighted-sum method at high count rate because of the systemic timing distortion problem, although we had a 2 ns random timing resolution. Beside that, the weighted-integration method also needs one more calculation to derive the total energy from the integrated value.

3) *Using a Distortion Compensated Weighted-Integration to Estimate the Total Energy:* From electronic implementation standing point, the signal is not a purely exponentially decaying because of the systemic timing caused by the PMTs rising time and signal smoothing in the processing electronics. Electronic smoothing may be intentional to quench noise and it may also be inevitable from amplifiers, delay lines (especially analog ones), capacitors, etc., in the processing circuits. When the exponentially decaying scintillation signals are smoothed, the rise of the integrated charge will deviate from that of the expected exponential function. This unavoidable real-life deviation from the expected "perfect" function will generate errors in the estimation of position and energy. A larger smoothing will produce a larger error. We propose a new HYPER algorithm with distortion compensation term e^{T_0} to take care of all the distortion in the circuit

$$S_i = \frac{1}{1 - e^{T_0} e^{-(t_{i+1}-t_i)/\tau}} \int_{t_i}^{t_{i+1}} E'_i(t) dt \quad (7)$$

where $E'_i(t)$ is the smoothed distorted detector signal and T_0 is a time adjustment based on the total time distortion that includes signal-smoothing time.

Fig. 4 shows a simulated detector signal (230 ns decay time-constant) and its integrated signal in nondistorted signal (thin lines) and a 70 ns smoothing (thick lines) case. The integration of the smoothed signal always underestimates the nondistorted signal, while the amplified smoothed signal overestimates the nondistorted signal after a certain time delay. In the weighted-sum method, those underestimated and overestimated values are compensative; however, in the weighted-integration method the underestimated error will be carried to the total estimated energy and further enlarged by the multiplying the factor, refer to (6). In order to minimize deviation in the estimated total energy caused by underestimated integrated-signal, we enlarge this correction factor by e^{T_0} in (7).

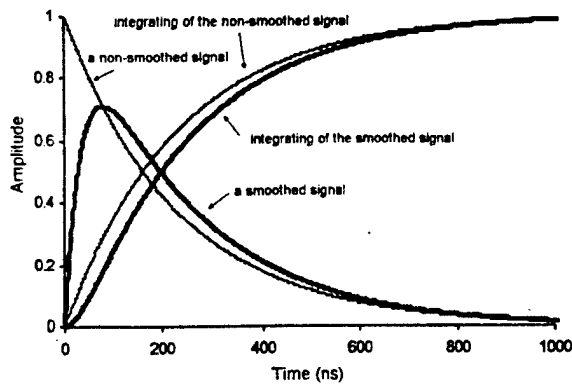


Fig. 4. Comparison of simulated both smoothed and nonsmoothed exponentially decaying instantaneous signals and their integrating outputs.

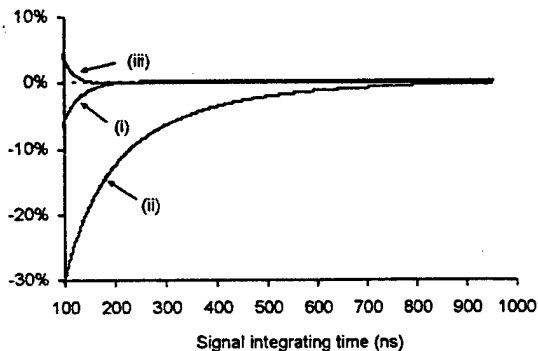


Fig. 5. Total energy estimation errors for smoothed signal at different integrating time using methods: i) basic weight-sum (single sample); ii) weighted-integration; and iii) distortion compensated weighted-integration.

Fig. 5 shows the weighted-integration method gives a large error of estimated total energy (70 ns smooth time of the detector signal); while both the weight-sum and the distortion compensated weighted-integration methods give a good result even for very small integrating time.

We configured our first generation HYPER hardware and software for the three different methods under a same condition. Fig. 6 shows the FWHM energy resolution versus count-rate with NaI(Tl) scintillation detector (a) and BGO scintillation detector (b). The experimental results showed that the basic weighted-sum HYPER method (single-sampling) gave a better energy resolution than the weighted-integration HYPER method; and the distortion compensated weighted-integration HYPER method generated the best energy resolution especially in high count-rate. We could not directly compare the weight-sum with multisampling HYPER method here, since it uses a different electronic board. But we expect that the result should be close to the distortion compensated weighted-integration method.

4) *All-Digital Method*: The all digital method includes digital integrating, digital weighting and digital smooth-correction to calculate the estimated total energy. An ultrafast ADC (100 million samples per second or higher) is used to continuously digitize the instantaneous signal and outputs are accumulated in real time as the integrated value for each event. The weighting- and smooth-time correction processing is the same as we mentioned in Section II-B-3. Unlike analog integration, digital integration has no dead-time for discharging the integrated value.

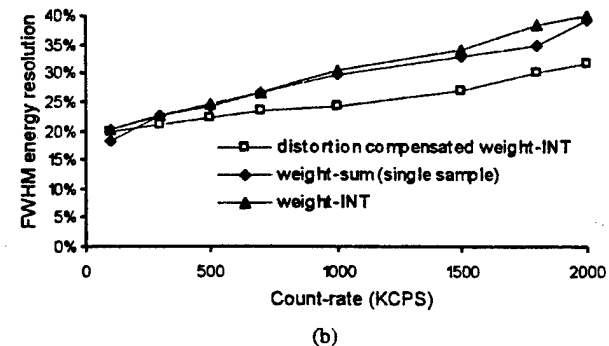
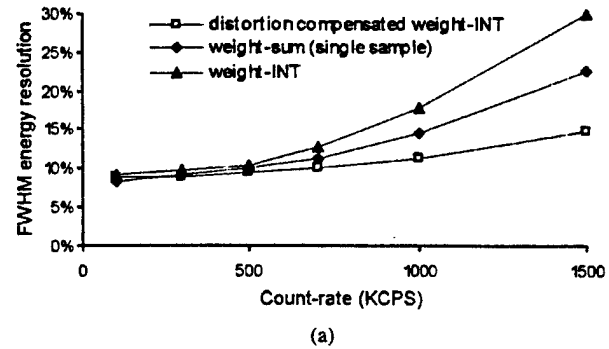


Fig. 6. Measured energy FWHM resolution versus count-rate with different methods using Cs-137 source for NaI(Tl) detector (a) and BGO detector (b).

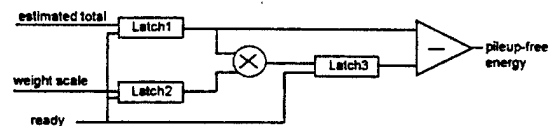


Fig. 7. Schematic of real time residual correction.

This method also can eliminate an analog delay line which is used to delay the detector signal in order to balance the time delay of the pileup trigger circuit. Since the signal is already digitized, we can use shift registers to buffer the digital outputs, hence to get time delay before they are accumulated. By eliminating the analog delay line, it will reduce the signal distortion which in turn will increase the measurement resolution of the weighted integration. The disadvantage of this method is requiring an ultrafast ADC and a fast digital accumulator.

C. Real Time Residual-Remnant Correction

The "residual correction" is very important part in the HYPER method for high count-rate application; it has been proved mathematically correct in our peer-reviewed scientific publications [1], [2]. The "residual subtraction" is a weighted subtraction with one estimated total-energy scaled by an exponential term determined by time-lapse between any two consecutive pileup events.

Fig. 7 shows a real time pipeline residual correction method. A ready signal indicating the end of digitization latches the estimated total energy signal, which is generated by the weight-sum mentioned earlier, as well as the output of an exponential decay lookup table of time-lapse, and the same ready signal also latches the preceding residual result outputted from the multiplier (latch3 in Fig. 7). The pileup-free energy signal is generated by subtracting the current estimated total signal with the preceding residual signal that is already registered in latch3. We

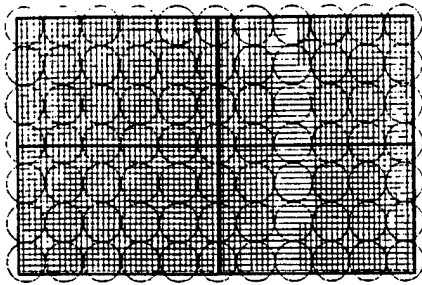


Fig. 8. New large-field-of-view PQS detector module with 10×6 BGO blocks (3168 crystal elements) coupled to 77 PMTs (18.7 mm diameter). Each module is divided into four Anger camera zones in electronics and served by four HYPHER Anger circuits.

have developed the electronics that three residual corrections for energy and position X , Y of an Anger camera can be implemented in one Altera's field programmable gate array (FPGA) chip EFP10K30ATC144-1.

III. APPLICATIONS

We have successfully developed a high-resolution low cost prototype PET camera—MDAPET to demonstrate the concept of PQS (PMTs quadrant sharing) detector. However, the electronics has some limitation in count-rate for large-field-of-view PQS detector design [3].

We will use HYPHER electronics in the new PET camera with 12 detector modules. To further increase the count-rate in this large detector (Fig. 8), 60 block arrays in each module are divided into four zones, and each zone has one HYPHER Anger circuit working as an ultra-highspeed Anger camera. Therefore, there are 48 HYPHER Anger-type high performance cameras in this PET camera. In order to have a better performance, each HYPHER circuit will work under a maximum count-rate of 800 Kcps.

A. Using HYPHER in Coincidence Imaging

In conventional methods, the signal integration time for each event is fixed. Therefore, the end of integration and signal digitization (for energy and position) is synchronized with the trigger signal (delayed by the fixed integration time). Coincidence detection may be performed between the end of digitization signals or the trigger signals.

HYPHER, however, uses a dynamic integrating method, which means that the measured energy and position signals are no longer synchronized with the leading-edge of the present trigger signal. If there is no pileup, the energy and positions will be generated in a maximum time of $1 \mu\text{s}$, on the other hand, if a pileup is detected, they are generated or digitized immediately at the arrival of the next event (arriving at a random time from present event). It is all right for gamma camera, since it only needs the energy and positions. But for coincidence application such as PET which needs both time and energy/position, an additional circuit has to be implemented for recovering the synchronization between event-trigger and the energy/position signals before they go to a coincidence procedure.

Fig. 9 shows the concept of restoring the synchronization of the energy/position signal and event-trigger. The pileup-free

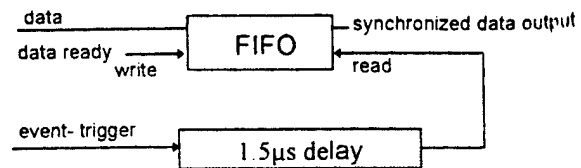


Fig. 9. Restoring the synchronization between data and the event-trigger for HYPHER in coincidence application.

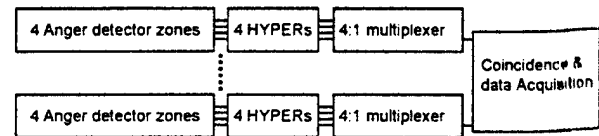


Fig. 10. Overall architecture of PET electronics based on HYPHER method. Each PQS detector module is organized as four Anger cameras in electronics and served by four HYPHER Anger circuit boards.

signals created by the residual correction circuit are continuously buffered into a temporary first-in-first-out (FIFO) memory in the order that they arrive, and then they will be continuously clocked out (readout) by a delayed event-trigger signal; the delay time of the event-trigger should be longer than the maximum processing time, for example a $1.5 \mu\text{s}$. This delay time equals to the sum of event integration time and the waiting time in FIFO. It is the waiting (holding) time of an individual event in the FIFO that synchronizes the FIFO readout time to the original event-arriving time (except for the fixed delay-time shift).

A pipeline digital delay circuit with a 1.7 ns resolution and 50 ns dead-time has been developed for this special purpose. In each HYPHER-Anger zone, only one delay unit is used to clock out the three FIFO channels (E , X , Y) at the same time.

B. Overall Architecture of PET Electronics

Electronic design based on HYPHER method for a high-resolution PET with 12 PQS BGO detector modules has been finished (see Fig. 10). Four individual real-time HYPHER circuits of each module create the pileup-free signals and restore the synchronization with the event-trigger. A digital multiplexer, also working as a motherboard for the HYPHER's, merges the four HYPHER outputs for further coincidence processing. The whole camera is consisted of 12 electronic sets; each set includes "Anger positioning," "HYPHER," and "digital multiplexer." All the electronics are mounted in a gantry and can be rotated with the gantry. A computer parallel port controls the gains of preamplifiers, trigger analog threshold, energy digital threshold, the width of coincidence time-window, and the gain equalization of 924 PMTs. The 12 outputs of the digital multiplexer boards go to a coincidence processing board to detect the true or random coincidence events. Each module will do the coincidence with other seven opposing modules.

IV. CONCLUSION

This paper studied several improved methods to prevent signal pileup based on basic HYPHER method, which is consisted of: a) dynamically integrating; b) total energy estimation; and c) remnant correction. The improvement is focused on getting a

better estimated total energy and in turn to improve the final measurement resolution of the pileup-free signal. Both simulation and experiment studies showed that the distortion compensated weighted integration gave the best energy resolution, however it needs more real-time calculation hardware; and a low-pass filter combined with multisampling for the weight-sum signal of basic HYPER method generated a good energy and position decoding resolution and it is easy to be implemented for real-time application. With more samples of weight-sum signal, the basic HYPER would theoretically generate a same result as the distortion compensated weighted integration method.

Electronic design based on the HYPER method for a high resolution low cost PET camera with 12 PQS BGO detector modules has been developed. This design resolved the serious

synchronization problem between the triggered time of an event and the end of integration that is variable from event to event, hence, allowing HYPER to be used for coincidence detection.

REFERENCES

- [1] W. H. Wong and H. Li, "A scintillation detector signal processing technique with active pileup prevention for extending scintillation count rates," *IEEE Trans. Nucl. Sci.*, vol. 45, pp. 838-842, June 1998.
- [2] W. H. Wong, H. Li, J. Uribe, H. Baghaei, Y. Wang, and S. Yokoyama, "Feasibility study of a high speed gamma camera design using the high-yield-pileup-event-recovery (HYPER) method," *J. Nucl. Med.*, vol. 42, no. 4, Apr. 2001.
- [3] H. Li, W. H. Wong, N. Zhang, J. Wang, J. Uribe, H. Baghaei, and S. Yokoyama, "Electronics for a prototype variable field of view PET camera using the PMT-quadrant-sharing detector array," *IEEE Trans. Nucl. Sci.*, vol. 46, pp. 546-550, June 1999.

A Programmable High-Resolution Ultra-Fast Delay Generator

Yaqiang Liu, Hongdi Li, Yu Wang, Tao Xing, Hossain Baghaei, Jorge Uribe, Rocio Farrell, Wai-Hoi Wong

Abstract--This paper presents a high-resolution, low-dead-time digital delay method in which the performance is independent of the total delay time. We have implemented a low-dead-time (50 ns) and high-resolution (± 0.9 ns) delay generator with delay times up to hundreds of milliseconds. We propose high-resolution whole-body positron emission tomography (PET) with a 12-module photomultiplier tube-quadrant-sharing (PQS) detector design. This high-resolution delay unit is an important part of the new PET electronics in which a high-yield pileup event recovery (HYPER) method is used. Using the HYPER method, the energy/position signals are generated or digitized upon the arrival of the next event (arriving at a random time after the present event). If the present event is piled up by the next event, the energy/position signals are no longer synchronized with the leading edge of the triggering signal. To detect a coincidence event by using the HYPER method, the original trigger signal must be delayed by a fixed time (1.5 μ s for a PET using a bismuth germinate crystal) and a new synchronization process must also be set up between the delayed trigger and the energy/position signals before being passed to the coincidence detection electronics. Each HYPER processor requires one delay generator; there are 48 delay units inside the whole PET system. This high-resolution delay generator also can be used in other PET systems in which a delay is needed to synchronize the fast timing trigger to the slower integration or detection address outputs; this low timing jitter delay can also be applied to automatic test equipment and communications.

Index Terms— Delay Generator, High-yield pileup event recovery (HYPER), Positron emission tomography (PET), Tube-quadrant-sharing (PQS), .

I. INTRODUCTION

WE propose a dynamic signal-integration approach called high-yield pileup event recovery (HYPER) [1] to prevent signal pileup for position emission tomography (PET) and gamma cameras. We have deployed the HYPER electronic processing in our modular high-resolution PET system that is under construction. This PET system has 12 detector modules. Each module has 4 HYPER-Anger-positioning zones generating

48 modular electronic channels [2-3]. The HYPER method combined with multiple Anger-positioning zones can significantly increase the count-rate capability and dose efficiency of PET and gamma cameras. But for coincidence detection applications and other timing-detection applications, such as positron-coincidence imaging, an additional trigger-delay technique must be used. In traditional scintillation detector electronics, the signal integration time for each event is fixed. Hence, the end of the integration and the signal digitization time (for energy and position) are synchronized with the timing trigger signal but delayed by a fixed integration time. The trigger signal is generated at the leading edge of the timing trigger pulse or the arrival time of the event. Coincidence detection can be performed between the ends of the digitization signals or the trigger signals. However, since HYPER uses a dynamic integrating method in which the energy and position signals are digitized upon the arrival of the next event (arriving at a random time after present event), the measured energy and position signals are no longer synchronized with the leading edge of the present triggering signal. To detect a coincidence event using the HYPER method, (a) the original trigger signal must be delayed by a fixed time that is longer than the maximum possible integration and digitization time, and (b) the current energy/position digitized signal must also be resynchronized to the delayed timing trigger. After the delay and resynchronization, all the signals relating to the current event can then be passed to the coincidence-checking processor. Except for the fixed delay time, both the timing trigger and the energy/position signals would maintain the fast timing integrity of the event if the delay circuit can maintain a negligible timing jitter. Hence, the coincidence timing resolution of the PET camera hinges on the timing resolution (fidelity) of this delay circuit. This type of accurate delay is not necessary in one conventional coincidence-processing method [4] that finds the coincidence event pairs by sorting (table lookup) the time marks generated by latching a master clock's time at the onset of an event. However, this type of "latching-sorting" design would be quite cumbersome for our system with 48 timing channels that will need 48 fast latches and ribbon cables with timing skews corrected. Hence, we developed this high-timing-fidelity delay circuit because of engineering requirements and practical necessity. This high-resolution delay circuit can also be used in other coincidence electronics designs that use the "timing-AND-logic" concept employed by some commercial PET systems, because such systems also require a long delay to synchronize the timing trigger and the energy/position signals.

This work was supported in part by NIH Grant RO1 CA58980, NIH Grant RO1 CA61880, NIH Grant RO1 CA76246, NIH Grant RO1 EB00217, NIH Grant RO1 EB001038, US Army Breast Cancer Grant, Texas Higher Education Grant, John S. Dunn Foundation Research Grant, and Cobb Fund for Cancer Research.

Yaqiang Liu, Hongdi Li, Yu Wang, Tao Xing, Hossain Baghaei, Jorge Uribe, Rocio Farrell, and Wai-Hoi Wong are with The University of Texas M. D. Anderson Cancer Center, Houston, TX USA (Yaqiang Liu's telephone: 713-745-1671; e-mail: yaqiang_l@yahoo.com).

II. METHODS

A. Pre-coincidence synchronization of signals in the dynamic integrating approach.

As discussed earlier, the HYPER dynamic integration and correction method requires a timing delay and a resynchronization between the timing trigger and the energy/position signal of the same events. In the synchronization process, the energy and position signals of all events are first pipeline buffered into a first-in/first-out (FIFO) temporary memory, then a delayed trigger signal is used to read them out individually so that the sequential order of events within the data stream can be maintained. Since the readout of the energy and position signals from the temporary holding FIFO memory is time-latched by the delayed trigger, and since the delayed trigger signal is synchronized with the trigger signal (except for the fixed delay-time shift), the energy and position signals are now synchronized to the trigger signal (Fig. 1).

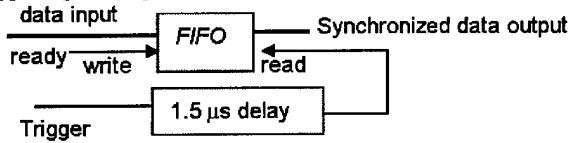


Fig. 1: Circuit to restore synchronization of HYPER signals before coincidence processing.

The fixed delay time should be longer than the maximum integration time. The trigger delay circuit should have a good timing resolution and low dead time. Table 1 illustrates the processing of 5 continuous events using FIFO and delay technique to restore the synchronization between the event trigger signal and the data output signal (except for the fixed delay-time shift).

Event number	1	2	3	4	5
Event arrival time (μs)	0	0.2	1.5	2.0	2.7
Event integration-sampling time = input time of event into FIFO (μs)	0.2	1.2	2.0	2.7	*
Event readout time from FIFO (μs)	1.5	1.7	3.0	3.5	4.2
Waiting (holding) time of event in FIFO (μs)	1.3	0.5	1.0	0.8	*

Table1: Synchronization restoring

- 1) Event integration-sampling time equals next event's arrival time if the current event is piled up by the next event, if there is no pileup on the current event, it will be integrated for a fixed maximum period of 1 microsecond;
- 2) Waiting time is the time difference between the FIFO readout time and the event arrival time;
- 3) * means that the value is dependent on the next event arrival time (not illustrated in Table 1).

Hence, the order of the data in a FIFO is the same as the order of events coming in. We are using the linear structure of a FIFO to line up all the events in the order in which they arrive. Then we apply a large fixed delay (larger than the longest integration time) for the event trigger, and use the delayed event trigger to "clock" the readout of events from the FIFO. Hence, each event in the FIFO is clocked out (read out) synchronously with the event triggering time (except for a fixed delay). It is the waiting (holding) time of an individual event in the FIFO (as controlled by the delayed trigger) that synchronizes the FIFO readout time to the original event-arrival time.

B. B Delay Method

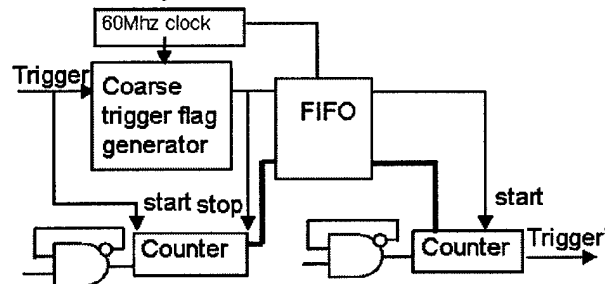


Fig. 2: Diagram of the digital delay unit

Fig. 2 and 3 show the design and timing of the high-resolution pipeline delay unit. The design includes three sections: a high-resolution time recorder, a major/coarse time-delay, and a high-resolution trigger restoration. Each input trigger signal is recorded by a main clock (60 MHz) generating a clock-synchronized coarse trigger flag signal. Meanwhile an ultra fast counter (see Fig. 2), driven by a 700-MHz burst oscillator, counts the time lapse between the original trigger and this coarse trigger flag. The arrival time of the trigger signal can be recorded very accurately by combining the coarse trigger flag and the fast counter. The burst oscillator only works for a very short time to reduce the system noise level and the power dissipation. The main time delay section consists of a synchronized FIFO memory. The coarse trigger flag and the recorded number from the fast counter will be put into the FIFO, which is driven by the same main clock to create the main time delay. The FIFO has a pipeline structure, and the length of the FIFO times the clock period determines the main time delay. To restore the delayed trigger accurately, the delayed number of the counter readout from the FIFO will be reloaded into another ultra fast counter (see Fig. 2), and the delayed trigger flag output from the FIFO will start the second counter clocked by a second burst oscillator. The high-resolution delay trigger signal will be created when the second counter becomes full.

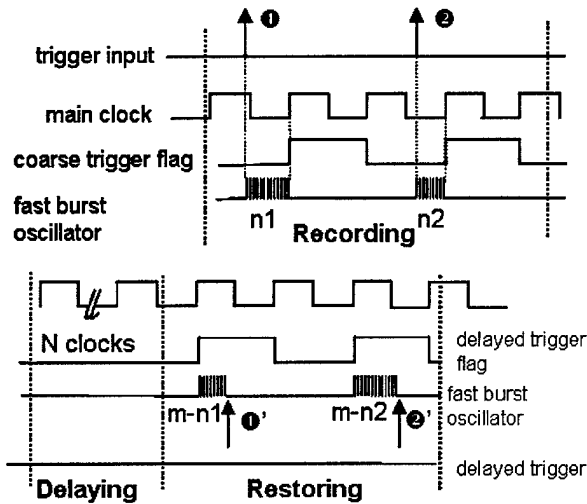


Fig. 3: Timing of the delay generator, which consists of three sections: time jitter recording, main time delaying, and fine-delay restoring.

In Fig. 3, n_1 is the time lapse between the event trigger input and the associated coarse trigger flag. This is the time jitter caused by the main clock. Here, we use a fast clock to record it. In the same figure, m is the full range or maximum count of the second fast counter, and $(m-n_1)$ is the adjusted delay time needed to accurately restore the trigger signal from the delayed coarse trigger flag. To have the $(m-n_1)$ fine delay time in the second counter, it will be reset to n_1 and then run until it reaches m when an accurate delay trigger is generated. Hence, the time difference between the recovered delay trigger and the original event trigger is equal to $n_1 + (\text{main clock delay}) + (m-n_1) = (\text{main clock delay}) + m$, therefore it is a time constant, and the jitter n_1 can be canceled. An additional fine delay time can be achieved by adding or subtracting a time offset to the preset time n_1 for the second counter. Both the length of the FIFO and the time offset can be programmed using a field-programmable gate array. The programmable time-offset is useful if front-end electronic boards need a high-resolution time alignment for coincidence measurement. The counters and burst oscillators used for recording the time lapse and restoring the delay trigger are ultra-fast emitter-coupled logic (ECL) picoseconds devices. Since the jitter time n_1 is measured by the first counter and the compensating delay time $(m-n_1)$ is clocked by the second counter, any difference between the two burst clock periods would cause an extra timing error. To reduce this timing error, we built the two burst oscillators in one ECL chip so that they could have the same frequency, unaffected by changes in the temperature and other environmental conditions such as the voltage of the power supply. To reduce system noise, the two burst oscillators work for only a very short time. This introduces a new technical problem, however, because the first several cycles after the oscillators start working are not very stable. Tests showed that the cycle time was not consistently stable until the 5th cycle. To solve this problem, a logic circuit is designed to have some selectable function: the trigger signal is caught by the main clock rising edge only when the count number n is greater than 5; otherwise it will be caught by the

next main clock rising edge. For the same reason, the counter's full number m is big enough to make the restoring number " $m-n$ " greater than 5. As shown in Fig. 4, if the 2 burst oscillators have the same characteristics, their first 5 cycles' total time is T_s , assuming the oscillators have stable cycles with time t after the first 5 cycles. If the number recorded by the first counter is n , the time lapse between the event trigger signal and the next main clock is $T_s + (n-5)t$. When restoring the signal, the time lapse between the main clock and the restoring signal is $T_s + [(m-n)-5]t$. If the main clock cycle time is T and there are k main clock cycles between the recording and restoring, the total delay time is $kT + 2T_s + (m-10)t$. The n is canceled, and we get a time constant. In designing the delay, temperature-effect monitoring is a very important to achieving the timing goal.

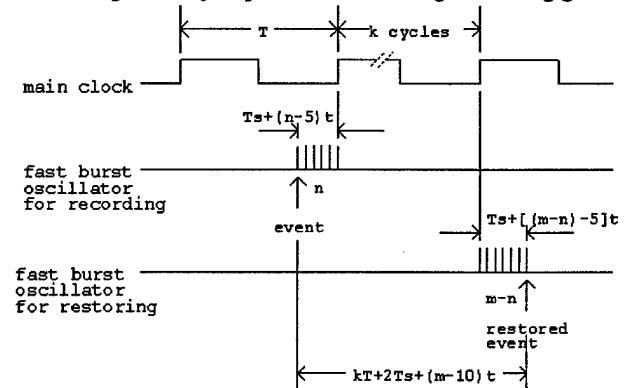


Figure 4: The delay time is independent of the event arrival time by ensuring fast oscillators working more than 5 cycles in both recording and restoring signals. T is the main clock period; t is the period of burst oscillator; T_s is the time of the first 5 cycles of the burst oscillator.

C. Time alignment

In our design, each detector module is divided into 4 electronic sections; each zone has its own HYPER and trigger delay circuit. Before performing coincidence checking, there is a "4-to-1" board to combine the energy/position data and trigger signals of the 4 zones back into a single module. Thus, for the following circuits, all the signals would look like those from an integral module. All the modules' trigger signals will go to the coincidence board for time coincidence, as shown as Fig. 5.

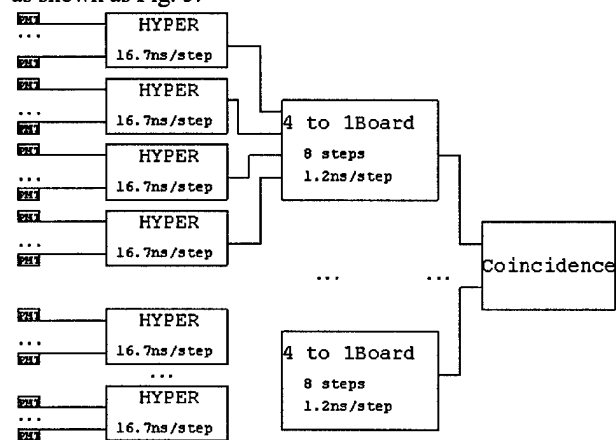


Figure 5: Two programmable time alignment mechanism: coarse steps (16.7ns/step) on the HYPER boards and fine steps (1.2ns/step) on the 4-to-1 boards.

Our PET system has 12 modules; and each module has 4 zones. Each zone has its own delay unit, but the delay times normally differ from each other. Hence all the delayed signals should be aligned in time before time coincidence is performed. Each HYPER board has a software-controllable switch that can introduce a 16.7 ns delay. The 4-to-1 board has 4 simple delay units that could provide further delay times for each zone. This simple delay unit has 8 steps, and each step has a 1.2 ns delay time. These two ways of adjusting time delay make it possible to align the time difference of the delayed signals among the different zones and modules. The delay time steps can be controlled by software through a parallel port, which makes time alignment easier than the traditional cable delay method.

III. PERFORMANCE

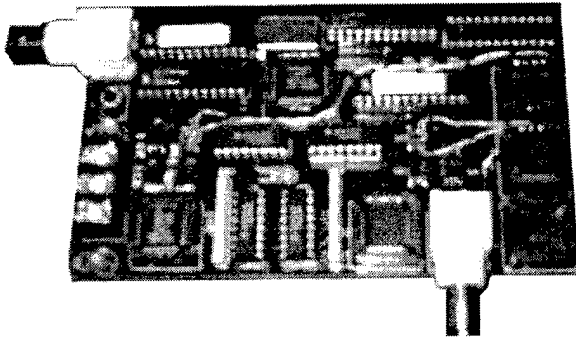


Figure 6: A prototype delay generator.

We have designed and implemented a high-resolution delay generator with a very low dead time. This delay generator has also been integrated successfully into our HYPER circuit for the PET application. All the performance tests have been done on an independent prototype circuit (see Fig. 6).

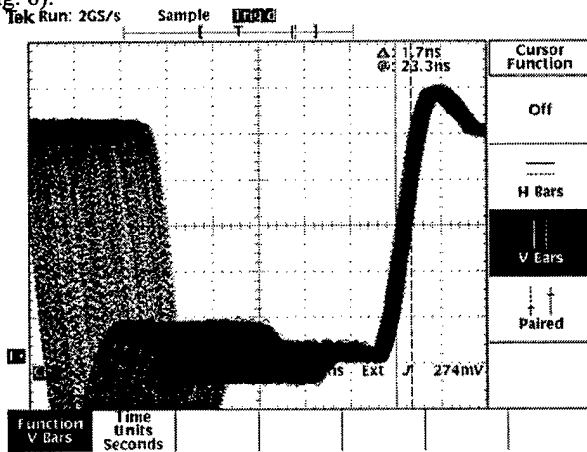


Figure 7: The delay signal result observed from the oscilloscope.

Fig. 7 shows delayed pulse signals, produced by the delay generator, on a Tektronix digital oscilloscope (TDS3032) with an infinite display time. The oscilloscope was triggered by the rising edge of the same pulse input to the delay generator. Since the delay timing applied only to the rising edge and not to the falling edge, we found the delayed pulses had a larger jitter (16.7 ns) in the falling edge than in the rising edge. The rising edge time jitter (resolution) was less than ± 0.9 ns. This delay timing resolution is good enough for the coincidence measurement of BGO PET detectors with a typical 12- to 20-ns coincidence-timing window. The circuit has a 50-ns dead time. Thus, if two pulses are too close together (less than the 50 ns dead time), they will not be delayed correctly. We also found the delay timing resolution and the dead-time performance were not degraded as the total delay time increased (by increasing the FIFO length for the main delay).

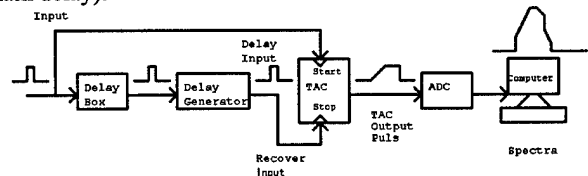


Figure 8: The delay time distribution detection method.

We also set up another test bench with nuclear instrumentation modules (see Fig. 8). A time-to-amplitude converter (TAC) module (model 2145) was used to measure the delay time. The TAC was started by the original pulse signal and stopped by its delayed pulse signal. The TAC result was digitized by an analog-to-digital converter (ADC) module (model 8075), and a spectrum was then created in a computer. To calibrate the time for an ADC channel, we added an extra 4.0-ns delay using an analog delay box in the pulse delay channel. By adding this 4.0-ns delay, the spectrum was shifted to upper channels by an offset of 80 channels (see Fig. 9). Hence, each ADC channel indicated a 50-ps delay. The ideal spectrum of the delay time distribution is a rectangle. A full width at half maximum of 1.55 ns and a full width at tenth maximum of 1.80 ns for the spectrum were measured with this method.

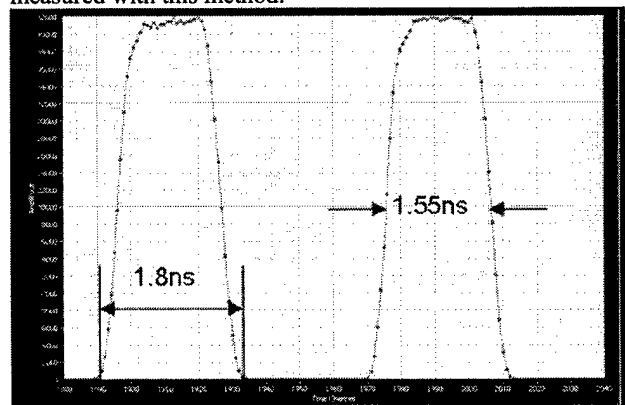


Figure 9: the delay time distribution result.

IV. CONCLUSIONS AND DISCUSSION

A programmable, high-resolution, ultra-fast delay generator has been designed and constructed. Our test results showed: (1) the delay generator had a timing jitter of less than ± 0.9 ns, a figure small enough for timing and coincidence measurement; (2) the delay generator had a dead time of about 50 ns and could handle input pulse rates of up to 20 MHz; (3) the total delay range of the delay generator could be as long as hundreds of milliseconds with no performance degradation; (4) the delay time can be programmed in coarse steps of 16.7 ns and in fine steps of 1.2 ns. This high-resolution delay generator is an important component when using dynamic scintillation integration such as the HYPER circuit we proposed for PET coincidence detection, and it has been successfully integrated into the HYPER electronics. This delay generator can also be used as a general device in other applications, such as automatic test equipment and communications.

V. REFERENCES

- [1] W.H. Wong, H. Li, J. Uribe, H. Baghaei, Y. Wang, S. Yokoyama, "Feasibility study of a high speed gamma camera design using the high-yield-pileup-event-recovery (HYPER) method," *The Journal of Nuclear Medicine*, vol.42, no. 4, April 2001.
- [2] W.H. Wong, "The design of a high resolution transformable whole body PET camera," *IEEE Trans. Nucl. Sci.*, vol. 49(5), October, 2002.
- [3] H. Li, et al, "Front-end electronics based on high-yield-pileup-event-recovery method for a high resolution PET camera with PMT-quadrant-sharing detector modules," *Conference record of the 2002 IEEE MIC Conference*.
- [4] J.P. Martin and K. Ragan, "A programmable nanosecond digital delay and trigger system," *Conference record of the 2000 IEEE MIC Conference*.

A HOTLink/Networked PC Data Acquisition and Image Reconstruction System for a High Resolution Whole-Body PET with Respiratory or ECG-Gated Performance

Hongdi Li, *Member, IEEE*, Tao Xing, Yaqiang Liu, Yu Wang, Hossain Baghaei, *Member, IEEE*, Jorge Uribe, *Member, IEEE*, Rocio Ramirez, Wai-Hoi Wong, *Member, IEEE*

Abstract—An ultra high resolution PET camera in whole-body scanning or gated imaging study needs super computer-processing power for creating a huge sinogram as well as doing image reconstruction. A fast HOTLink serial bus attached to networked cluster personal computers (PC) has been developed for this special purpose. In general, the coincidence data from a PET camera is unidirectional; therefore an additional daisy-chain bus using high speed HOTLink (400Mbit/s, Cypress Semiconductor, inc.) transmitters and receivers is designed to carry the coincidence data to the entire networked (LAN) computers (PCs), the data from HOTLink are interfaced to a PC through a fast PCI I/O board (80Mbyte/s). The overall architecture for the image acquisition and reconstruction computing system for a whole-body PET scanning is a pipeline design. One PC will acquire sinogram data for one bed position, and after completion of data acquisition that PC will begin to reconstruct the image. Meanwhile, another PC in the network will start data acquisition for the next bed position. The image results from the previous PC will be sent to a master computer for final tabulation and storage through the standard network, and then it will be free for processing a new bed position. In gated respiratory or gated ECG imaging study, each cycle is divided into many time-segments; and each PC will be reconfigured for processing one specified time-segment image. We are developing a high resolution PET camera with 38,016 BGO crystal elements that requires 1 to 2 gigabytes sinogram memory. This HOTLink/networked structure design also allows us to distribute the huge sinogram real-time binning into several PCs; and the image reconstruction can be done in parallel.

I. INTRODUCTION

WE have proposed a high resolution transformable whole body clinical PET camera with 12 detector modules in PMT-Quadrant-Sharing (PQS) design that decodes 38,016 BGO crystal elements[1]. This high

resolution PET camera doing a whole-body multiple bed position scanning will require a huge sinogram memory and a long-time for image reconstruction. Respiratory-gating or motion-tracking are also demanded in high resolution PET study. The electrocardiogram-gated (ECG-gated) imaging method allows assessment of regional myocardial perfusion and evaluation of ventricular wall motion. Hence, to have a fast imaging performance, the computing power becomes more critical for a high resolution clinical PET camera. The paper presents a method of implementing a fast but cheap data acquisition and image reconstruction computer system for a high resolution PET camera. This method is also good for existing commercial PET cameras in order to achieve a higher patient throughput.

With the availability of inexpensive high power PC-based computing, many of data acquisition and image reconstruction methods have been moving to a PC-based model. A data acquisition system with networked cluster PC structure will be widely accepted. We want to use the networked PC cluster design for both real-time data acquisition and image reconstruction in our PET camera. However, a standard PC networking has a problem in real-time broadcasting and the network protocol is not easy to be integrated into front-end electronics without a special micro-processor involved. Since the coincidence data generated by a PET camera is unidirectional (from the camera to a data acquisition system), hence, we can design another special fast bus attached to the standard networked computers for broadcasting the coincidence data to the entire networked PCs. This fast serial bus is daisy-chain linked with fiber optical or twisted-pair driving by 400Mbit/s HOTLink transmitter and receiver. Both the HOTLink transmitter and receiver are 32-pin chips and have a CMOS/TTL logic compatible interface, and further more, no special protocol is demanded for this additional bus. Hence, it is very easy to integrate the HOTLink components into front-end electronics. Each PC can real-time grab the data from the serial bus as demanded, and a master PC can order a slave PC to do a special task through the standard LAN. For example, to split a huge sinogram memory, the master PC would send a message to each slave PC through a TCP/IP specifying sub-sinograms to be processed.

Manuscript received December 2, 2002. This work was supported in part by NIH under Grant RO1 CA58980, NIH Grant RO1 CA61880, NIH Grant RO1 CA76246, NIH Grant RO1 EB00217, NIH Grant RO1 EB001038, US Army Breast Cancer Grant, Texas Higher Education Grant, John S. Dunn Foundation Research Grant and Cobb Fund for Cancer Research.

H. Li, T. Xing, Y. Liu, Y. Wang, H. Baghaei, J. Uribe, R. Farrell and W.-H. Wong are with the Department of Experimental Diagnostic Imaging, University of Texas M.D. Anderson Cancer Center, Houston, TX 77030 USA (H. Li's telephone: 713-745-3732, e-mail: hli@di.mdacc.tmc.edu).

II. METHODS

A. Why HOTLink?

A high resolution and high sensitivity PET camera may generate 32-to-64 bits width parallel coincidence data with a rate up to 10 million coincidence events per second. Operating this high speed parallel bus over significant distances can be problematic due to signal distortion, skew, and crosstalk. These effects can lead to loss of data and failure of the bus.

As system speeds increase, serial interfaces are often used to extend the high performance of a parallel interface well beyond the distances possible in parallel link. By only sending a single signal (though sending each bit much faster) both the signal-to-signal and signal-to-clock skew limits are removed. HOTLink (Cypress Semiconductor inc.) makes it easy and economical to move the same data over a high-speed serial connection using fiber-optic or twisted cables [2, 3].

Figure 1 shows a serial link design using HOTLink (transmitter CY7B923 and receiver CY7B933, [4]) for moving streams of 8-bit parallel bytes from one location to another. HOTLink offers a built-in standard 8B/10B encoder/decoder and PLL (Phase Locked Loop) based clock and data recovery circuits. These 8-bit data characters are encoded into 10-bit transmission characters and the 10-bit characters are sent serially across a link. At the receiving end of this link these serial bits are grouped together to 10 bits at a time (framed), and decoded back into their equivalent 8-bit data characters. Only 256 valid 10-bit characters selected from the entire 1024 characters map to the 256 valid 8-bit input data characters. HOTLink also provides 12 valid special codes, selected from the 1024 characters, as different communication synchronization character and violation symbol (RVS) are two of these special codes.

In a sum, HOTLink is almost protocol-free for fast serial communication and has a COMS/TTL compatible interface, which can be easily integrated in an application system. And, it also reserves about 10 special codes that you can use as commands in serial communications. In addition, serializing a parallel bus allows for operation of the bus over extended distance. The reduced bus width also makes it practical to pass the data through a simple slip-ring in a PET camera with CT function.

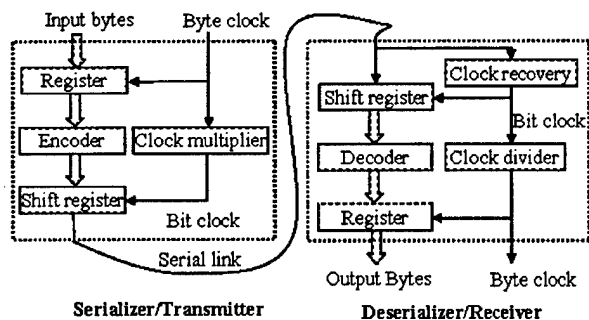


Figure 1: HOTLink architecture

B. Whole-body scanning

A clinical PET camera usually needs to acquire 5 to 8 bed positions in whole-body scanning. For our proposed high resolution PET camera with 38,016 crystals and 5,184 sinograms, we estimated the reconstruction time with 15 minutes for 2D and 250 minutes for 3D filtered back-projection (FBP) for each bed position using a single 2.8 GHz Pentium-IV personal computer. Hence, about one to two reconstruction hours is demanded using 2D FBP for whole-body scanning with 5-8 bed positions, this is very time consuming. Definitely we need a super-power computing system for data acquisition and imaging reconstruction as well.

However, the coincidence data from a PET camera are always unidirectional; a fast serial bus is very suitable to carry the data to the acquisition computer. We have designed a data acquisition and image reconstruction system based on a fast HOTLink (400 Mbit/s) daisy-chain bus combined with a standard local area network (LAN) that consists of 6-8 personal computers (PCs), see figure 2. One PC will act as a master (server) computer, and the others will function as the slave (client) computers. The communication between the master and the other 5-7 slave PCs is established through a standard LAN using TCP/IP. The server has a large hard disk that will be used to store the raw data as well as the reconstructed images. Each slave PC has 1-2 gigabytes memory of its own for binning the sinogram data of one bed position in real time.

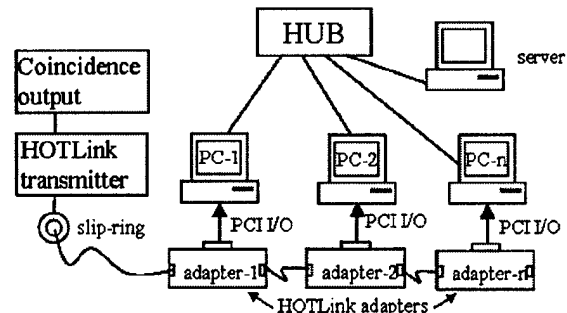


Figure 2: Architecture of HOTLink/Networked computers

After the completion of the sinogram acquisition for one bed position, the sinogram for the just completed bed position will be used by the same slave PC in the network for image reconstruction. The image result from each slave PC will be sent to the master PC for final tabulation and storage. The overall architecture for the image acquisition and reconstruction computing system is a pipeline design. In this pipeline design, one PC will be used to reconstruct the image of one bed position. In scanning the first bed position, the first client PC (PC-1) will be instructed by the server to grab the data from the HOTLink daisy-chain bus. After scanning the first bed position, PC-1 will reconstruct the image of this bed position. In scanning the second bed position, PC-2 will grab the data from the HOTLink bus and after scanning the second bed position, PC-2 will reconstruct the image of this second bed position while PC-1 may still be working on the

reconstruction for the first bed position. If a whole-body scan takes 8 bed positions, up to a maximum of 8 reconstruction PCs will be needed. However, if the reconstruction time of each bed position is less than the scanning time of 5 bed positions (for example), then only 5 PCs will be needed, because PC-1 will be free after scanning 5 bed positions and can be used for processing the bed position-6. For the same reason PC-2 can be used for position-7. We choose this multi-PC design instead of a typical SUN/HP workstation-based design using 1-2 high power workstations or expensive VME system with multiple processors linked by RACEWAY crossbar, because this PC system is more flexible, cheaper and easy to be maintained. Furthermore, performance of a PC-based system can be improved more frequently, cheaply, and compatibly.

C. Respiratory/ECG-gated imaging

In pulmonary nodules PET imaging, respiratory motion produces lesion blurring and an apparent increase in lesion size. This results in a decrease in the activity concentration per pixel within the lesion and an underestimation of SUV. Improved measurement of lesion volume and quantification of FDG uptake can be achieved with respiratory gated PET imaging [5]. In cardiac nuclear imaging, ECG-gating not only provides added information about global and regional left ventricular and right ventricular function, enhancing its prognostic value, but also helps to differentiate real defects from attenuation artifacts [6].

Recently most of the gated high resolution PET imaging is performed under list-mode only. Time-marks, generated by a respiratory or ECG sensor, are inserted into the coincidence data streams and recorded in list-mode. Each respiratory or ECG cycle is divided into many time-frames as demanded. And the time-frame sinogram-binning as well as image reconstruction will be performed after the data acquisition is finished.

The HOTLink/networked PC structure designed for whole-body scan discussed in Section II. B can also be used for real-time gated PET imaging. For example, each ECG period is divided into, say, 6 time-frames. The front-end electronics generates 25 milliseconds free-running timing-ticks attached to the coincidence data streams broadcasting to the networked PCs through the HOTLink serial link. Each ECG cycle is divided into 6 time-frames according to those timing-ticks. Each slave computer is configured to process one specified time-framed sinogram binning and image reconstruction. Each slave PC has two memory buffers organized in ping-pong mode for recording the list-data from two most recent ECG cycles. The list-data will be sorted by frame-numbers; and only one specified frame will be processed by each PC, the data from rest frames will be discarded by this PC. If the total number of time-ticks in one ECG cycle is too long or too short that means an irregular ECG cycle has happened, and the entire list-data buffer for that ECG cycle will be discarded. This time-framed real-time data acquisition and image processing method can also be used for respiratory-gated imaging. However, since the respiratory cycle is more regular and slower than ECG cycle and patients can be further trained to have a regular cycle [7],

therefore we can predict the next respiratory period accurately by linear-fitting several measured previous periods. It is not necessary to attach the 25 milliseconds timing-ticks into data streams for respiratory gating. With a predictable cycle time, the time-frame numbers can be generated ahead or real-time and we can attach frame-numbers to the coincidence data streams directly. Hence, a slave PC can process time-framed sinogram binning immediately without ping-pong buffering the list-data of the entire cycle as used in ECG-gating method mentioned above. If both the cardiac and respiratory gating is needed simultaneously, the maximum time-frame number for ECG and respiratory gating are limited to four. A maximum of 16 slave PCs are needed (since ECG and respiratory signals are not synchronized, there are 16 total combinations of the ECG and respiratory time-frames); however, if one slave PC can store 2 time-framed sinograms, then only 8 slave computers are needed.

D. Network parallel sub-sinogram reconstruction

It is very time consuming to reconstruct a high resolution PET imaging. To speedup the processing, one solution is using multiple parallel processors to work on the huge sinogram data. However, accessing the same sinogram memory by the multi-processors becomes a new bottle-neck; and the communication among the processors also needs some extra CPU time. Hence, the maximum processor number in this design is limited; the computing power is not increased linearly as the number of processors increased. Besides, the reconstruction algorithm has to be redesigned and optimized specially for this multi-CPU parallel processing system.

A new network parallel sub-sinogram reconstruction method has been designed that is benefited from the HOTLink/network PC structure. The huge sinograms (5,184 sinograms for our proposed PET camera) are sorted into many groups. Each slave PC will do the sinogram rebinning of one group with its local memory. Only the coincidence data that belong to the group will be grabbed by the PC from the HOTLink serial bus. The reconstruction algorithm is simply modified, so that each PC can start the reconstruction locally (with no necessary to access other sinogram groups) after the data acquisition is finished. This is a fully parallel processing design. In this design, there is no communication between PCs and no bottle-neck problem of accessing a common/shared memory. The reconstructed image results from each slave PC will be added together by a server.

III. RESULTS AND DISCUSSION

A. Sending coincidence data using HOTLink transmitter

In the proposed high resolution PET camera, the coincidence system will give two separate coincidence data outputs, one is for true coincidence and the other is for random coincidence [8]. The coincidence processing board passes through 64-bits pre-normalized Anger-position and energy signals of the pair-events; and another digital processing board will convert them into crystal and slice information by using lookup tables. Both the true and random

coincidence data after the lookup-table-processing will become 32-bits (for gamma-1 position: 7-bits slice1, 6-bits crystal1; for gamma-2 position: 7-bits slice2, 6-bits crystal2; and 6-bits coincidence bank-pair number). The 32-bits true and random coincidence data are first shifted into a 2k x 8-bits FIFO (first-in-first-out memory) individually. Whenever the half-full flag of one FIFO is detected, that FIFO output will be switched to a HOTLink transmitter by a multiplexer, see figure 3. A selected HOTLink command identifying a true or random buffer will be sent first and then immediately followed by the coincidence data with a half buffer size of that FIFO. In other words, the HOTLink command is a buffer-head indicating all the following data (with half of FIFO length) will be either true or random events. In this way, the two coincidence outputs are simply merged and sent to a fast serial bus using a HOTLink (400Mbits/s, CY7B923) transmitter.

In the coincidence data format of our prototype MDAPET camera, one bit is used to identify true or random events and the data acquisition software needs to check that bit for every single event. In our new design, the software only needs to check the buffer-head once and then process the buffer continuously. Another big advantage is that the coincidence data are still limited within 32-bits width (33-bits were necessary if following the MDAPET data format) which simplified the PC I/O interface design.

The gate signals from ECG and respiratory sensors are also connected to the digital look-up-table processing board. The time-frame numbers or timing-ticks can be real-time inserted into the HOTLink data streams for further processing.

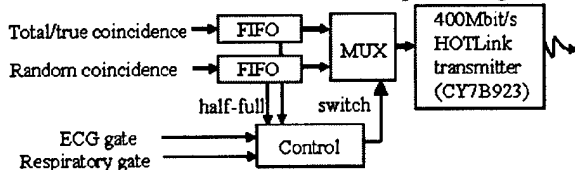


Figure 3: Sending coincidence data with HOTLink transmitter

B. PC HOTLink adapter

A custom-constructed PC HOTLink adapter has been developed to receive coincidence serial data from the front-end using a HOTLink receiver CY7B933, the received data are interfaced to a fast 32-bit PCI I/O board (National Instrument PCI-6534 [9]) inside each slave PC. Meanwhile the same data from the receiver are feed back into another HOTLink transmitter on the adapter board passing the data to the next adapter board and slave PC as well. Hence, a fast daisy-chain serial bus is formed among these adapters for real-time broadcasting the coincidence data to the entire slave PC cluster at a rate up to 400Mbit/sec. This serial bus can carry up to 10 million coincidence events per second, which is good enough for a high efficient PET camera. Figure 4 shows the design of HOTLink daisy-chain bus, data from the serial link are deserialized first and then will be interfaced to a PCI bus, meanwhile the deserialized data will be serialized again and sent to next adapter through the onboard HOTLink transmitter. In fact, the deserializer and serializer act as an active serial bus driver, thus the entire link quality is not limited by the number of adapters inside the daisy-chain link.

The twisted copper cable between two boards can be as long as 100 feet. By disabling/blocking the input deserialized data, a slave PC is able to send data from its memory to the serial link output, so that data from one slave PC can be moved to next slave PC very fast.

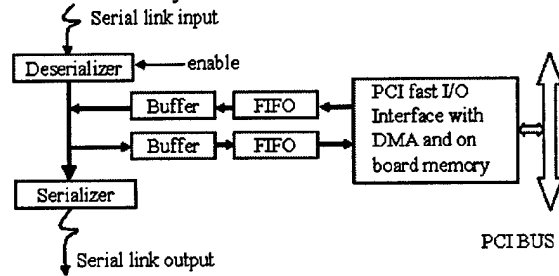


Figure 4: PCI HOTLink daisy-chain serial bus

Figure 5 shows HOTLink adapter-board design for PCI-6534 fast PCI I/O board. Figure 6 is the photograph of the adapter board. The adapter-board can be initialized by the PCI-6534 through standard I/O and the data communication between them is achieved by pattern I/O [9]. The PCI-6534 board has a 64Mbyte onboard memory working as first-in-first-out mode, data can be written into the memory as fast as 80Mbytes/sec. The adapter-board can be initialized for different modes: HOTLink self-testing mode for checking the link quality, PC data acquisition mode, PC transferring mode for fast communication between PCs, and sinogram real-time selection mode for splitting a huge sinogram into several PCs. Two gate-signal inputs are reserved for some special purposes such as the position signals of a rotating rod for the data acquisition of transmission imaging. The entire logic was implemented by one Altera programmable logic device EPM7256SQC208.

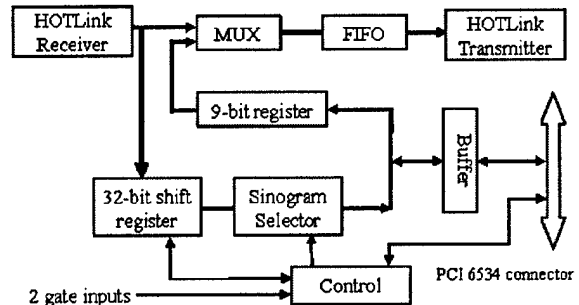


Figure 5: PCI-6534 HOTLink adapter design

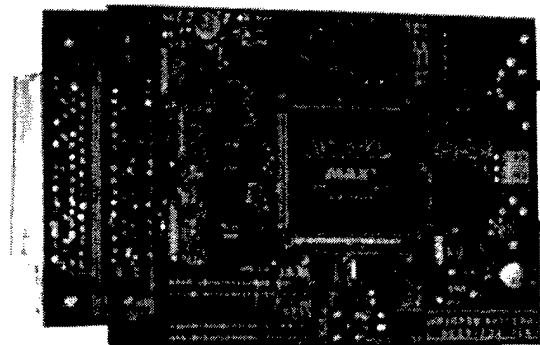


Figure 6: Photograph of HOTLink adapter

The output of a HOTLink receiver is consisted of 8bits data plus 1 bit data/command flag, however the coincidence data in our PET system are 32-bits, therefore an 8-to-32-bits shifter register is demanded. Synchronization in data shift-processing should be carefully designed. Without the synchronization an error happened in the shifter, such as one extra shift operation triggered by a noise, might kill the entire rest of the data. We use the HOTLink commands, such as the selected true/random buffer-head command or the ECG/respiratory start command, to reset/synchronize the 32-bits coincidence data so that one error may only kill a maximum of one buffer size (half length of the FIFO in the front-end processing board).

A normally HOTLink system rarely experiences one error per hour (a bit error rate of $1 \times 10^{-12} \approx 1$ error/hour @ 266 Mbaud) [10]. When the receiver detects an error in the sequence of received transmission code (an error that corrupts a single bit), it asserts a RVS signal during the character-decoding-time following the error. Single-bit errors can cause changes in the data streams running disparity. In extreme cases, where the errors cause PLL cycle-slipping or loss of framing, the received streams will never match. A special circuit has been developed by monitoring the status of RVS signal to automatically disconnect and reconnect the input signal continuously until the endless running errors disappeared. Our data showed that the system could be recovered less than 100ms, if endless disparity errors were detected.

Another important application of the HOTLink adapter is to split a huge sinogram memory into the slave PC cluster; and the image reconstruction algorithm can apply to those sub-sinograms individually. The reconstructed sub-image results from the slave PCs are integrated together by a master computer for further processing. Hence, by using the HOTLink network design, we not only can handle the huge sinograms, but also can speed up the image reconstruction in a way of parallel processing.

The "sinogram selector" in figure 5 is designed specially for the purpose of real-time sinogram splitting mentioned above. The 5,184 sinograms are sorted by the "slice-difference" of the two coincidence gamma events. And those sinograms will be grouped together if their "slice-differences" are within a specified range. Two registers in the "sinogram selector" can be initialized by a slave PC and define a range of a "slice-difference" window, so that if the difference of two slice numbers, identified by the coincidence-gamma events, is belonged to that window, the coincidence event will be accepted by this slave PC. In order to reconstruct the image locally, the parallel reconstruction algorithm requires every slave PC to have directory sinograms (slice difference = 0). This can be achieved easily by the broadcasting capability of the HOTLink bus. The coincidence data belong to the direct sinograms or to the specified sub-sinograms defined by the "slice-difference" window can be real-time grabbed by a slave PC from the HOTLink daisy-chain bus. This parallel processing method has been proved by using two slave computers in our prototype MDAPET camera that we developed [11, 12].

IV. CONCLUSIONS

We have developed a high speed HOTLink (400Mbit/s) serial bus that can broadcast 32-bits coincidence data of a PET camera to local networked computers. Using the HOTLink for serializing bus is very simple, no additional protocol is demanded and it can be easily integrated into a front-end electronics. The HOTLink/networked PC cluster design is very suitable for online pipeline data acquisition and image reconstruction for an ultra-high resolution PET camera doing whole-body multiple bed position scanning and respiratory/ECG gated imaging study. By using this design, a huge sinogram real-time binning can also be achieved by the slave PC cluster. The pipeline data acquisition and image reconstruction method will increase the throughput of patient scan.

This HOTLink/networked PC data acquisition system can be easily applied to an existing PET camera. It has been successfully used in our prototype MDAPET camera to replace the VME data acquisition system. Our VME data acquisition system is aged, unstable and further more, the IRONICS data interface board is no longer supported by the manufacturer.

The prototype HOTLink adapter combined with the National Instrument fast I/O board (PCI-6534) has strongly demonstrated the real-time processing power for PET study. A PCI HOTLink network board merging the functions of HOTLink and the fast PCI I/O will be designed in the future.

V. REFERENCES

- [1] W.H. Wong, "The design of a high resolution transformable whole body PET camera," *IEEE Trans. Nucl. Sci.*, vol. 49(5), October, 2002.
- [2] "HOTLink Design Considerations", application notes in the HOTLink User's Guide, Cypress Semiconductor Co.
- [3] "Use HOTLink for 9- and 10-Bit Data", application notes for the HOTLink, Cypress Semiconductor Co.
- [4] Datasheets for CY7B923, CY7B933, Cypress Semiconductor Co.
- [5] Nehmeh SA, et al. "Effect of respiratory gating on quantifying PET images of lung cancer". *J Nucl Med* 2002; 43: 876-881
- [6] Germano G, Erel J, Lewin H, et al. "Automatic quantification of regional myocardial wall motion and thickening from gated technetium-99m sestamibi myocardial perfusion single photon emission computed tomography," *J Am Coll Cardiol* 30: 1360-1367, 1997
- [7] Sadek Nehmeh, Yusuf Eridi, Clifton Ling, et al. "Effect of respiratory gating on quantifying PET images of lung cancer", *The Journal of Nuclear Medicine*, vol. 43, No.7, pp. 876-881, July 2002.
- [8] Y. Wang, et al, "A modular low dead-time coincidence system for high resolution PET cameras," *Conference record of the 2002 IEEE MIC Conference*.
- [9] User guide for PCI-6534, National Instrument.
- [10] "HOTLink built-in self-test (BIST)", application notes for the HOTLink, Cypress Semiconductor Co.
- [11] W.H. Wong, J. Uribe, W. Lu, K. Hicks, "Design of a variable field prototype PET camera," *IEEE Trans. Nucl. Sci.*, vol. 36, pp. 1915-1920, June 1996.
- [12] J. Uribe, H. Baghaei, H. Li, S. Yokoyama, N. Zhang, J. Wang, F. Dobbs, W.H. Wong, "Basic imaging characteristics of a variable field of view PET camera using quadrant sharing detector design," *IEEE Trans. Nucl. Sci.*, vol. 46, pp. 491-497, June 1999.

Front-end Electronics Based on High-yield-pileup-event-recovery Method for a High Resolution PET Camera with PMT-quadrant-sharing Detector Modules

Hongdi Li, *Member, IEEE*, Wai-Hoi Wong, *Member, IEEE*, Yu Wang, Yaqiang Liu, Tao Xing, Jorge Uribe, *Member, IEEE*, Hossain Baghaei, *Member, IEEE*, Rocio Farrell

Abstract— Front-end electronics based on a high-yield-pileup-event-recovery (HYPER) method has been developed for a high resolution PET camera with 12 PMT-quadrant-sharing (PQS) detector modules that decoding 38,016 BGO crystal elements. Each module has 60 BGO blocks coupled to 77 PMTs that are organized as four Anger cameras in electronics. Each Anger camera is served by one HYPER decoding board to solve the pileup problem in order to have better count-rate and dead-time performance. There are 48 HYPER boards and only 144 A/D converters are used in the entire PET scanner. EPLD/FPGA based real time pileup remnant-correction algorithm and high-resolution digital trigger delay unit are developed for HYPER in PET coincidence application. Random coincidence events can also be acquired with the same digital delay method. A fast automatic PMT gain equalization method has been proposed to equalize the gains of 924 PMTs within two minutes. This instantaneous LED tuning can be performed between patient scans; hence it gives a better PET quality control. A standard daisy parallel port is used to control all the parameters such as gains of preamplifiers, trigger thresholds, signal DC offset control, trigger delay alignment, and as well as the coincidence time windows. A fast HOTLink (400Mbit/s, Cypress Semiconductor inc.) serial bus is used to transfer the coincidence data to networked data acquisition and image processing computers, and the sinogram binning and image reconstruction can be processed in parallel. This camera also has an ECG/respiratory gated imaging capability.

I. INTRODUCTION

WE have proposed a high resolution transformable whole-body clinical PET camera with 12 PQS modular detector design where 924 PMTs decode 38,016 BGO crystal elements [1]. This camera has 6 times more decoded crystal elements than our prototype MDAPET camera [2, 3] and

requires more complicated electronics with much higher count-rate performance. This paper presents a new flexible modular electronic architecture and design for this particular PET camera. The modular electronics can be easily integrated for different PET configurations such as six modules animal or mammography PET camera.

The PQS design increases the number of decoded crystal elements per PMT, therefore increased the resolution. In the proposed PET camera, each PMT can decode about 41 crystal elements in average. However, the increased number of crystals to be served by each PMT will inevitably increased the chance of signal pileup in the detection system. Pileups degrade image quality and creased image distortions. Due to the significant increase in the number of small detector elements the system requires the properties of a high resolution decoding, low imaging artifacts and as well as a better quality control. Hence, to fully realize the benefits of the PQS detector design, we apply the HYPER processing electronics [4] developed by us to process the pileup events in high count-rate situation in order to lower the image artifacts. To further increase the count-rate capability and have a better dead-time performance, we divide each detector module into 4 “Anger-gamma-camera” zones by Anger-positioning the PMT signals electronically according to their physical locations. Each Anger-camera has one HYPER electronic board to do real-time pileup signal processing. Hence, there are 48 high speed Anger-HYPER cameras inside each PET scanner. Figure 1 shows one detector module design, in this design 60 BGO blocks (32 standard blocks with 7x7 elements, 24 extended blocks with 8x7 elements and 4 extended blocks with 8x8 elements) are coupled to 77 PMTs.

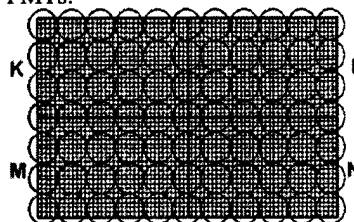


Fig.1 Large-field-of-view PQS detector module with 10x6 BGO blocks (3168 crystal elements) coupled to 77 PMTs (18.7mm diameter) is divided into four HYPER zones (K, L, M and N).

Manuscript received December 2, 2002. This work was supported in part by NIH under Grant RO1 CA58980, NIH Grant RO1 CA61880, NIH Grant RO1 CA76246, NIH Grant RO1 EB00217, NIH Grant RO1 EB001038, US Army Breast Cancer Grant, Texas Higher Education Grant, John S. Dunn Foundation Research Grant and Cobb Fund for Cancer Research.

H. Li, W.-H. Wong, Y. Wang, Y. Liu, T. Xing, J. Uribe, H. Baghaei and R. Farrell are with the Department of Experimental Diagnostic Imaging, University of Texas M.D. Anderson Cancer Center, Houston, TX 77030 USA (H. Li's telephone: 713-745-3732, e-mail: hli@di.mdacc.tmc.edu).

II. METHODS

A. Overall architecture

The electronics has been developed for the proposed whole-body clinical PET camera with 12 BGO detector modules in PQS design. Each module has one set of electronics including 'pre-amplifier', 'Anger positioning', 'HYPER' and 'digital multiplexer', see figure 2. Inside each module, the 77 PMT signals are amplified and Anger-weighted as four Anger-cameras by a position matrix board generating four set outputs of pre-normalized position and energy signals. Each Anger-camera is served by one individual real-time pileup prevention HYPERS circuit. A digital multiplexer, also working as a motherboard for the HYPERS circuits, merges the four HYPERS outputs and passes data to a coincidence processing system. The coincidence system is also based on a modular architecture with daughter-boards sitting on a mother-board. It can be reprogrammed for a different PET configuration with vary number of modules. In the 12-module camera, each module will have both the true and random coincidence with other 7 opposing modules. All the electronics are mounted on the gantry and can be rotated with the gantry. The gains of pre-amplifiers, analog trigger thresholds, digital energy thresholds, the width of coincidence timing window, the front-end LEDs for PMT auto-tuning, and as well as the PMT high voltage can be controlled through a computer parallel port.

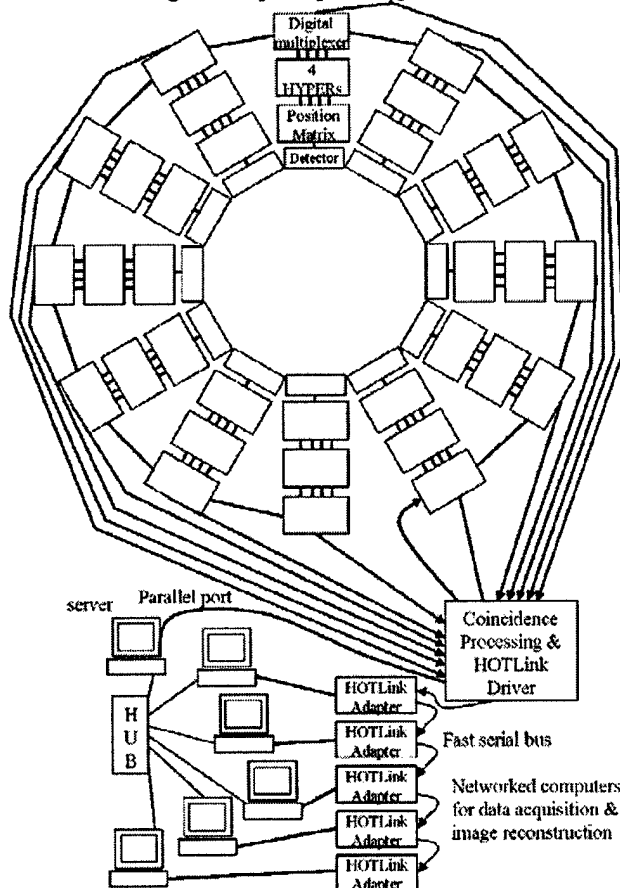


Fig. 2 Overall electronics structure

This is an inexpensive, flexible and easy to be maintained electronics design comparing to the traditional PET electronics. By using Anger-HYPER design, we do not need one HYPERS circuit for each PMT; otherwise 924 HYPERS channels would be used (costly). Only 144 ADCs are used in the whole camera with 924 PMTs, and still can work in high count-rate situation that benefited from the pileup prevention techniques. An important advantage of the HYPERS design is that HYPERS electronics works on both the total-energy signal (E) and the total-position signals (X', Y') in the same way. Hence, only 3 HYPERS channels (X', Y', E) are used for each Anger-camera zone. Furthermore, dividing a detector module into 4 zones in electronics, each of which is served by 3 HYPERS channels (X', Y', E), that increases the count rate by a total of 30X over the conventional processing method [4].

Another important improvement that reduces the components and simplifies the electronic design is that we assigned the functions of position normalization, the crystal identification lookup table and the fine crystal energy-threshold lookup table after the coincidence board. Generally the decoding electronics needs one real-time processing board doing these functions mentioned above, hence the entire camera needs 48 processing boards; and by applying these functions after coincidence, the 48 processing boards can be reduced to one board. Because the event-rate after the coincidence board is much lower and further more the real-time performance is not necessary after coincidence, hence, to design the lookup processing board after coincidence is much easier, and on the same board we use HOTLink transmitter to serialize the processed coincidence data into 1 bit output. There are two reasons that can allow those processing functions to be done after coincidence: (1) the coincidence circuit only uses the time information of events, and the energies and positions of the events are simply passed through. Hence, the above functions can be done either before or after coincidence. (2) A major concern is that many scatter-events may be sent to the coincidence board if there is no fine crystal energy cut-off in the front-end, which will increase the dead-time of the coincidence processing. However, an advantage of the PQS design is that the difference of the photo-peak signal amplitude of all crystals is less than 30% [5], and thus one universal energy low threshold can reject most of the scatter-events for all crystals. Therefore, we don't need to perform those functions mentioned above until the events passed coincidence detection. This PQS advantage allows us to greatly simplify the front-end electronics.

B. HYPERS method for PET

We have suggested a HYPERS method to solve the pileup problem and recover the events at very high count-rate [4]. The main idea is: **a.** estimating a weighted value to indicate the total energy inside the detector; **b.** the energy of this event can be derived by subtracting a residual signal from the previous weighted value; **c.** this method is also correct for Anger-energy and pre-normalized position signals.

energy of this pulse = weighted value of a pulse - (weighted value of the preceding pulse) $\times e^{-(\text{time difference between this and the preceding event})}$

In HYPHER method the event processing time is not fixed. If there is no pileup on the event, the signal will be integrated for a maximum time of $1\mu\text{s}$, however, if the circuit detects a pileup, the integrating stops immediately and A/D converter samples the weight-sum signal. Because of this dynamic processing time in HYPHER method, the ready signal given by A/D converter is not synchronized with the event-trigger. It is all right for gamma camera, but for coincidence application, an additional high-resolution delay component has to be implemented in the HYPHER circuit to restore the synchronization between data and the event-trigger. Other special techniques associated with HYPHER and PQS detector design will be addressed in the following section.

III. RESULTS AND DISCUSSION

A. An improved HYPHER method

We have addressed different improved HYPHER methods in a recent publication [6]. An improved HYPHER method of applying multi-sampling on the weight-sum signal was adopted by this PET electronics. The weighted-sum signal of the integrated signal and the instantaneous signal amplified by τ is a constant in time, and is always a measure of the total radiation energy before the next event is detected, regardless of when the sum-signal is sampled. Since the instantaneous signal is noisier than the integrated signal, a low-pass smoothing circuit is applied to the weighted-sum signal in order to reduce the noise. The advantages of using a weight-sum signal/multi-sampling to estimate the total energy in implementation are: (a) it can produce the total energy directly; no further calculation will be involved; (b) since the sampling time for the time-constant sum signal is not critical, instead of using the expensive flash ADC, a very cheap pipeline sampling ADC with a fixed sampling period can be used to digitize the sum signal. Sampling ADCs are widely used in telecommunications, digital cameras and high-definition TV; the price of an ADC with 80MSPS sample-rate with 10 bit resolution is only about US \$10.



Figure 3: Crystal decoding map acquired by Anger-Hyper unit

We have tested the electronics of one Anger-camera zone with three BGO detector blocks, each block has 7×7 elements with a size of $2.7\text{mm} \times 2.7\text{mm} \times 1.8\text{mm}$, coupled to Photonis 19mm PMTs (XP1911) in PQS design setup in a dark box. Figure 3 showed all the crystals are well decoded by this Anger-HYPHER design. The entire system has 48 Anger-

HYPHER cameras (with multiple zones design); our target single rate for the whole camera is about 30 MCPS.

Following listed some additional techniques developed for the HYPHER in PET application.

(1) Trigger synchronization recovering

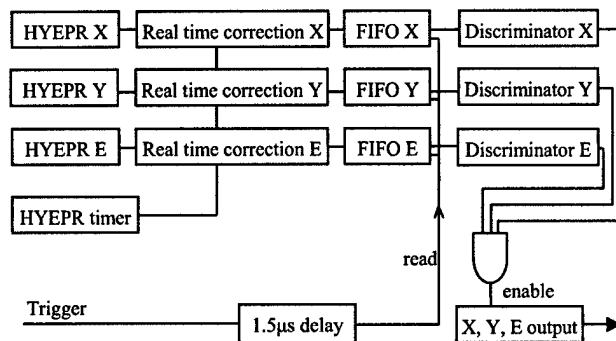


Figure 4: The HYPHER design for PET application.

In the HYPHER method, a random next-event can terminate the integrating of the current-event; hence the data-ready signal of the A/D converter is not synchronized with the event-trigger anymore. Figure 4 shows the concept of recovering the synchronization. The data from the A/D converter are first stored into a FIFO (first in first out memory) and then will be read out by a delayed trigger signal. The trigger delay time should be longer than the maximum event processing time, for example here it is $1.5\mu\text{s}$ and the maximum event processing time is $1.0\mu\text{s}$. We have developed a very high resolution ($\pm 0.9\text{ns}$) and small dead-time (50ns) delay unit for this special purpose. The data readout from the FIFO is synchronized to the delayed trigger and the original trigger as well (only a fixed $1.5\mu\text{s}$ time offset). The coincidence processing will apply on the delayed trigger signals.

(2) Signal baseline restoring

The dynamic integrating time in HYPHER method needs a DC couple signal input. This requires a big challenge to eliminate the signal's DC offset that can be caused by the pre-amplifier's input bias current or voltage output offset. The DC offset may also drift as the system temperature changes. Due to the DC offset, a longer integrating time will create a larger error than a short integrating time in the integrator output. Since this error is sensitive to the random integrating time, we can not easily correct it after digitization. In the traditional method with a fixed integrating time, this error is fixed and can be derived after energy calibration.

We have developed a new method to measure the signal DC offset and then generate a compensative DC signal to cancel it directly. This method can work with or without radioactivity. To measure the DC offset, the circuit continuously generates automatic self-trigger pulses at 750KCPS rate (dash arrows in Fig. 5); each self-trigger starts integrating the input signal for a fixed period of $1\mu\text{s}$ and then digitizes the integration result. However, if a real gamma-event trigger is detected within a self-trigger integration period, the current self-trigger will be rejected, and

meanwhile the self-trigger generating circuit will be reset. New self-trigger pulses will start in about $1.5\mu\text{s}$ waiting time, see Fig. 5. This $1.5\mu\text{s}$ waiting time is to guarantee that no energy from the real event could contribute to the next self-trigger integration. Hence, a clean "baseline spectrum" is separated from the gamma spectrum; and according to the "baseline-peak" location, a DAC is initialized (according to a DC offset lookup table) and its output is feed-back to the pre-amplifier to cancel the DC offset therefore to restore the baseline back to the ground level. Since the "baseline spectrum" is always sharp and narrow, a few thousand events are good enough to locate the "baseline-peak" accurately. It only takes a few milliseconds with 750 KCPS self-trigger rate to restore the baseline. Since the DC offset drifts slowly, the baseline restoring can be done before a patient scan or even in the period of camera rotating or bed positioning within a scan.

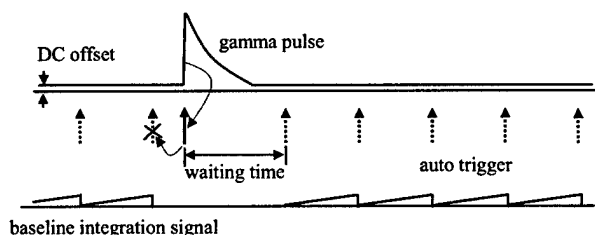


Figure 5: A method of DC offset measurement

(3) Multiple HYPER zones design

To further increase the count-rate capability, a large detector is divided into several local Anger-camera zones by weight positioning PMTs in electronics. Figure 1 shows a detector module is divided into four zones (zone K, L, M and N). Since every two neighbor zones share one row or one column PMTs, one gamma hit may trigger two zones simultaneously if its energy is collected by the shared PMTs. A new simple method has been invented to identify a zone that is hit by a real gamma and to reject the false hit in other zones. To find out the zone with a real hit, a threshold is set for the pre-normalized position signals of each zone (discriminator-X, -Y in figure 3). To demonstrate the idea, fig. 6 shows a simple example of two zones design, each zone has one independent block detector coupled to 4 PMTs in PQS design. The pre-normalized position of zone-1 is $X1=A+D$, and pre-normalized position of zone-2 is $X2=C+F$. If a gamma hits zone-2, there is no contribution of light to $X1$. However, if a gamma hits zone-1 (even in the corner crystal located in the center of PMT-B or PMT-E), it still has more than 3-5% of total light/energy going to PMT-A and PMT-D benefited from the PQS block design. That means the pre-normalized position signal ($A+D$) will have more than 3-5% of total energy of a real hit. Therefore, in data acquisition, a real hit in a zone should pass both the energy-acceptance threshold and pre-normalized position-acceptance threshold which are about 3-5% of $E0$ (the zone-1 energy-acceptance threshold); however, a false hit in zone-1 caused by its neighbor's zone may be accepted by the energy threshold but it will not be accepted by the pre-normalized position threshold that is set to 3-5% of $E0$. The simultaneous acceptance of the energy threshold and the pre-normalized position threshold is a simple way to reject

the false trigger (event) within a zone. This is a very robust discrimination because it is immune to differences in electronic-gain balance between different zones. This design also reduces electronic complexity and cost.

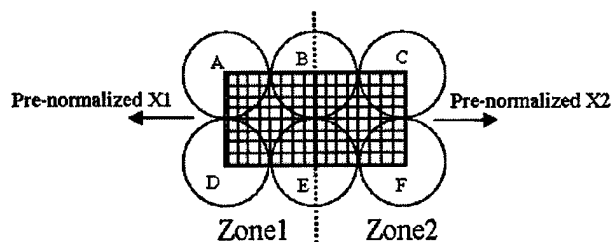


Figure 6: A simple example for zone identifying

B. Digital multiplexer--HYPER motherboard

Digital signal outputs from the four HYPER zones are merged into one output by a real-time digital multiplexer and passed to coincidence processing system. The multiplexer board is also a mother-board, all the four HYPER boards are sitting on it (see Fig. 7); it reads the energy and pre-normalized position results from the four HYPER boards and it also distributes the parallel port control signals as well as the DC power supplies to all the four HYPER boards. The 12 modular electronics are controlled by a computer parallel port linked in daisy-chain. The parallel port cable is driven by each HYPER motherboard and goes to the next motherboard.

The digital multiplexer board has a dead time about 30ns, and the dead time for each HYPER board is about 50ns. If two HYPER outputs are detected within the 30ns dead time, the multiplexer-board will pickup the one with a large energy; and if more than two HYPER outputs are found within the dead time, it will pickup one in random or by a token ring.

To align the timing difference of the four HYPER boards, four individual programmable delay units are built on each multiplexer board with a resolution of 1.2ns per step. The HYPER board also has a limited delay adjustment capability in about 0.8ns resolution. Since the multiplexer outputs will directly go to the coincidence processing board, those timing adjustments are necessary in order to balance the time delay difference caused by digital multiplexer, components, cables and connectors.

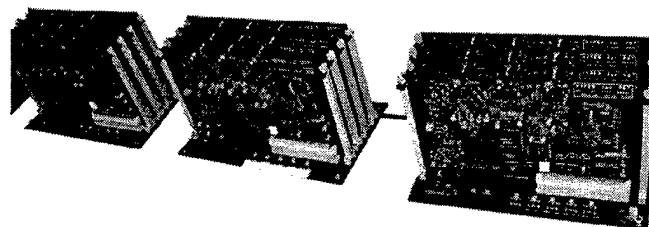


Figure 7: Photograph of modular decoding electronics. In each module there are four HYPER boards sitting on one multiplexer motherboard.

C. Coincidence electronics

A coincidence electronic system with backplane/plug-in architecture has been developed specially for the PET camera with modular detector design [7]. Benefited from the DSP and programmable EPLD/FPGA technology, the coincidence

hardware can be reprogrammed for different PET configuration consisted of from 2 modules up to 12 modules. For 12 detector modules, see Fig. 8, each module will have the coincidence with other 7 opposite modules. Each event will generate a gate signal with a specify time width, and a traditional AND logic is used to detect the true coincidence events among those single gate signals. Simultaneously, pipeline delayed gate signals are generated (a varied delay time for each module, from 200ns to 2200ns), and another AND logic is used to detect the random coincidence events among those delayed gate signals. Our test result shows the system has 21ns dead-time and is able to operate up to 10million events per second, and the gate width can be on-line programmed from 6.5ns to 16ns at 0.5ns resolution.

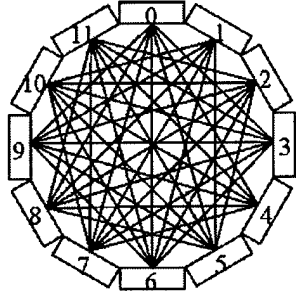


Figure 8: Coincidence design for 12 detector modules

D. Instantaneous PMT auto-tuning

The high decoding power of the PQS technique has more stringent requirement that the amplification of PMT needs to be more accurately equalized. Since all PMT-gain drifts with time, temperature and extended radiation exposure [8, 9], we have developed an ultra fast LED auto-tuning method to equalize the PMT gains for a better quality control. With this new method the gains of 924 PMT can be tuned within 2 minutes. Hence, the camera tuning can be done between patient scans.

One true blue LED is placed in the center of the empty space of every 4-PMT group in a detector module (fig. 9). The light of LED is directly injected into the center of a crystal array from the coupling side and distributed by the array back into the four decoding PMT. Each PMT has a variable-gain-amplifier (VGA) connected to the output and the VGA can be turned on/off individually. The four PMT gains are balanced by changing the four VGA gains to have a same amount of light output. The light outputs of every two neighboring LEDs can be aligned by adjusting the LED pulse width to have a same light output on a common PMT that is shared by the two LEDs. The LED tuning control logic is implemented in the front-end Anger-positioning matrix board inside the detector module.

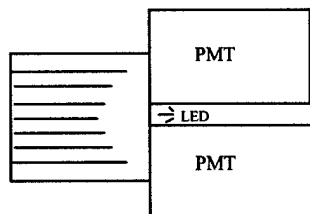


Figure 9: LED is used for PMT gain equalization in PQS detector

E. HOTLink/networked computer system

We have developed a HOTLink/networked computer system for the high resolution PET camera in whole-body scanning or gated imaging study [10]. A 400Mbit/s daisy-chain HOTLink is used to serialize the coincidence output and broadcast the data to networked PC cluster. The data will be interfaced to PC through a fast PCI I/O board. The overall architecture is good for pipeline processing. In a whole-body scanning, each PC will acquire sinogram data for one bed position, and after completion of data acquisition the PC begins to reconstruct the image meanwhile another PC will start data acquiring for the next bed position. And after sending its result to a server through a standard TCP/IP network, this PC will be free for processing a new bed position. In gated imaging study, each respiratory or ECG cycle is divided into many time-segments and each PC will be reconfigured for processing one specified time-segment image. The HOTLink/networked structure design also allows us to split the huge sinogram into several PCs in real-time and the image reconstruction can be done in parallel.

IV. CONCLUSIONS

A very low cost and high performance with large-field-of-view PET camera can be achieved by combining both PMT-quadrant-sharing and HYPER state-of-the-art designs. This paper presented an inexpensive, flexible (programmable) front-end modular electronics for PQS detector based on an Anger-HYPER method. The designs of coincidence, LED auto-tuning method as well as HOTLink/networked computer system are also addressed in this paper. All the electronics have been designed and constructed. More performance tests will be done in the near future.

V. REFERENCES

- [1] W.H. Wong, "The design of a high resolution transformable whole body PET camera," *IEEE Trans. Nucl. Sci.*, vol. 49(5), October, 2002.
- [2] W.H. Wong, J. Uribe, W. Liu, K. Hicks, "Design of a variable field prototype PET camera," *IEEE Trans. Nucl. Sci.*, vol. 43 pp, 1915-1920, June 1996.
- [3] H. Li, W.H. Wong, N. Zhang, J. Wang, J. Uribe, H. Baghaei, S. Yokoyama, "Prototype electronics for a variable field of view PET camera using the PMT-Quadrant-Sharing detector array," *IEEE Trans. Nucl. Sci.*, vol. 46, pp. 546-550, June 1999.
- [4] W.H. Wong, H. Li, J. Uribe, H. Baghaei, Y. Wang, S. Yokoyama, "Feasibility study of a high speed gamma camera design using the high-yield-pileup-event-recovery (HYPER) method," *The Journal of Nuclear Medicine*, vol.42, no. 4, April 2001.
- [5] J.Uribe, W.H. Wong, et al, "Signal characteristics of individual crystals in a high resolution BGO detector design using PMT-Quadrant-Sharing", *Conference record of the 2002 IEEE MIC Conference*.
- [6] H. Li, W.H. Wong, et al, "A new pileup-prevention front-end electronics design for high resolution PET and gamma cameras," *IEEE Trans. Nucl. Sci.*, vol. 49(5), October 2002.
- [7] Y. Wang, et al, "A modular low dead-time coincidence system for high resolution PET cameras," *Conference record of the 2002 IEEE MIC Conference*.
- [8] Matheoud R, Zito F, Canz C, Voltini F, Gerundini P. "Changes in the energy response of a dedicated gamma camera after exposure to a high-flux irradiation," *Phys. Med. Biol.*, 44, N129-N135, 1999.
- [9] J. Uribe, et al, "Effect of photomultiplier gain-drift and radiation exposure on 2D-map decoding of detector arrays used in positron emission tomography," *Conference record of the 2001 IEEE MIC Conference*.
- [10] H. Li, T. Xing, et al, "A HOTLink/networked PC data acquisition and image reconstruction system for a high resolution whole-body PET with respiratory or ECG gated performance," *Conference record of the 2002 IEEE MIC Conference*.

A Modular Low Dead-Time Coincidence System For High-Resolution PET Cameras

Yu Wang, Hongdi Li, *Member, IEEE*, Yaqiang Liu, Tao Xing, Jorge Uribe, *Member, IEEE*, Hossain Baghaei, *Member, IEEE*, Rocio Farrell, Wai-Hoi Wong, *Member, IEEE*

Abstract—A high resolution oncologic transformable positron emission tomography (HOTPET) is currently under development. The detector ring of the camera consists of 12 detector modules. Because the High-Yield-Pile-Up-Event-Recovery (HYPER) front-end electronics are applied in this new-generation PET camera, a low-dead-time coincidence circuitry is needed to take advantage of the improved efficiency from this technology. The coincidence matching of events coming from different detector modules is performed by an AND-logic on the arriving edges of the module output timing pulses. A flexible modular architecture has been adopted to facilitate the use of the coincidence circuitry for different detector module configurations in addition to different electronic and mechanical implementations. The application of backplane/plug-in architecture and programmable devices (EPLD/FPGA) along with a DSP (Digital Signal Processor) provide reprogrammable flexibility and expandability, allowing scans ranging from animal and breast PET to whole-body PET. There are 42 possible combinations of module pairs derived from the maximum 12 detector modules in coincidence with 7 opposite modules. Both the accidental and total (true + accidental) coincidences are simultaneously collected in real time; the accidental timing shift is ≥ 200 ns relative to true events. The timing-gate window for the coincidence AND-logic can be dynamically, digitally adjusted during data acquisition between 6.5 ns and 16 ns to optimize the signal-to-noise ratio in the data. The prototype circuit showed that the timing accuracy is far better than 0.5 ns and the coincidence dead-time is less than 21 ns.

I. INTRODUCTION

The detection of coincident events is at the core of a positron emission tomography (PET) camera. In recent PET developments, the popular implementation of coincidence detection [1, 2, 3] is to use the digitized timing mark of the arrival of each gamma event. By comparing the timing-marks of the events from the pairs of the detector groups whose lines of response span the tomograph field-of-view, the coincidence can be picked up from the sea of the single events. This method has some advantages, such as reliability and less sensitivity to noise. On the other hand, it also has some drawbacks, such as relatively lower timing

Manuscript received December, 2002. This work was supported in part by the NIH Grant ROI CA58980, NIH Grant ROI CA61880, NIH Grant ROI CA76246, NIH Grant ROI EB00217, NIH Grant ROI EB001038, US Army Breast Cancer Grant, Texas Higher Education Advanced Technology Grant, the J.S. Dunn Research Foundation, and by the Cobb Endowment for Cancer Research.

Yu Wang, Hongdi Li, Yaqiang Liu, Tao Xing, Jorge Uribe, Hossain Baghaei, Rocio Farrell, Wai-Hoi Wong are with University of Texas M. D. Anderson Cancer Center, Houston, TX, USA (Yu Wang's telephone: 713-745-1671, e-mail: wangy_km@yahoo.com)

resolution, because the timing mark usually comes from a system main clock; and more bits of data to transfer requiring more complex front-end electronics and more connectors.

In our high resolution oncologic transformable PET (HOTPET) [4, 5], we chose Pulse-AND logic as a coincidence-realization method because of its simplicity. By adopting a modular backplane/plug-in architecture and using modern programmable devices and a digital signal processor (DSP), the coincidence circuitry is flexible and reprogrammable, so it can be used for different detector configurations to construct PET cameras for different purposes without redesigning the hardware.

II. SYSTEM DESIGN

A. Overall Description

As shown in Figs.1 and 2, the coincidence system is designed to be expandable/reprogrammable to cover from 2 to 12 detector modules. The backplane/plug-in architecture facilitates the tailoring of this system for different size cameras, ranging from animal and breast PET to whole-body PET. For handling up to 12 detectors, there are 7 slots on the coincidence backplane to accommodate 6 data buffer plug-in modules and 1 DSP embedded controller. Each data buffer deals with data from 2 detector modules.

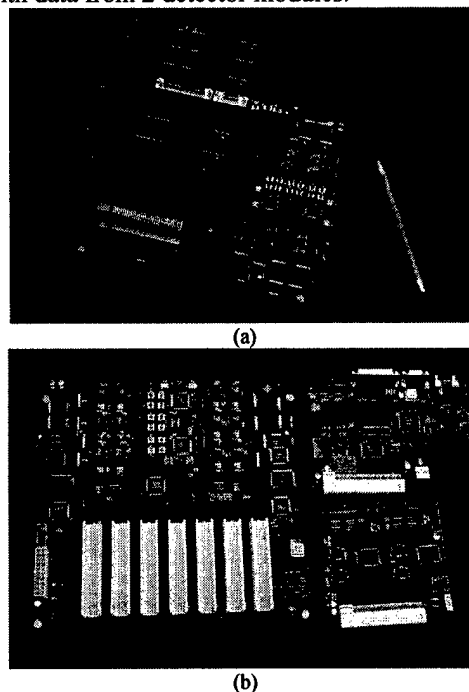


Fig. 1. Photos of the whole coincidence system (a) and its comprising boards (b). The photo (b) shows the coincidence backplane (left), DSP controller (right top), and gamma-event FIFO buffer board (right bottom).

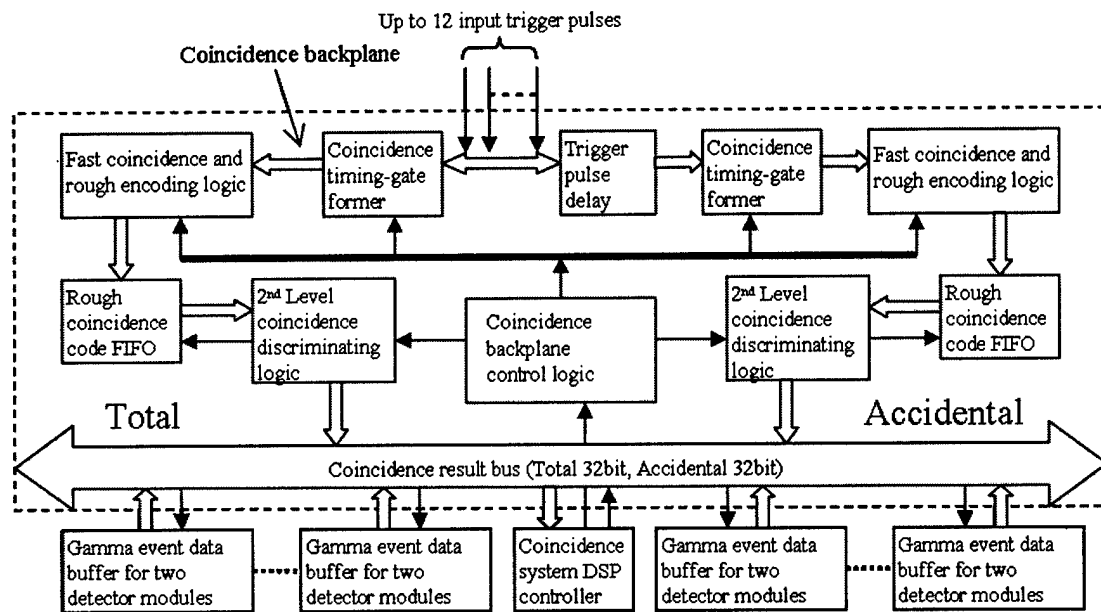


Fig. 2. Block diagram of the modular low dead-time coincidence system.

B. Coincidence-Logic Circuitry Backplane

The coincidence-logic circuitry is on the backplane board. Up to 12 trigger pulses from the front-end electronics [6] of the detector modules enter the backplane through coaxial cables. The rising edges of the trigger pulses represent the arrival of the gamma events. There are 42 module pair combinations derived from the 12 detector modules looking for coincidence with 7 opposite modules. The events picked from the coincidence of the prompt trigger pulses are regarded as total (true + accidental) coincident events. Meanwhile, as shown in Fig 3, each trigger pulse is delayed with a ≥ 200 ns timing shift to any of the other pulses. The events picked from coincidences of the delayed pulses are regarded as accidental coincident events. All of the delaying shifters are realized in 2 field-programmable gate array (FPGA) chips from Altera Inc. As a result, the logic circuits for both total and accidental coincidences are identical, simplifying the design and implementation. Moreover, performing the data delay and timing pulse delay within the coincidence system reduces the number of cables (both coaxial and flat ribbon cables) connecting the detector modules to the coincidence system and makes the design of the front-end electronics output simpler. The reduction in the number of cables has an appreciable advantage for simplifying the gantry assembly, especially for a rotating gantry.

By using the digitally configurable delay lines, the coincidence windows can be easily changed on the fly to optimize for a better signal-to-noise ratio in different countrate environments; for example, when scanning different parts of a body during a whole-body scan.

Because the high-yield pile up event recovery (HYPER) [5] front-end electronics are applied in this new PET camera, low dead-time is necessary for the coincidence circuitry to take advantage of its improved efficiency. To reduce the coincidence dead-time as much as possible, a 2-level

coincidence detection and selection logic structure has been adopted. As Fig 4 depicts, the first level is performed in a fast erasable programmable logic device (EPLD) for fast coincidence detection. This level basically is an AND-logic array that detects 42 probabilities of coincidences and encodes the detected coincidences roughly and rapidly, then writes the rough coincidence code into a first-in/first-out (FIFO) buffer for further selection and encoding. As long as the AND-logic detects a coincidence, it will generate a FIFO write signal to push the rough coincidence code and the data from all of the detector modules into the corresponding FIFOs at the same moment, regardless of whether some detector modules have invalid data output. The second-level discriminating logic then distinguishes and accepts the valid data while rejecting the invalid data.

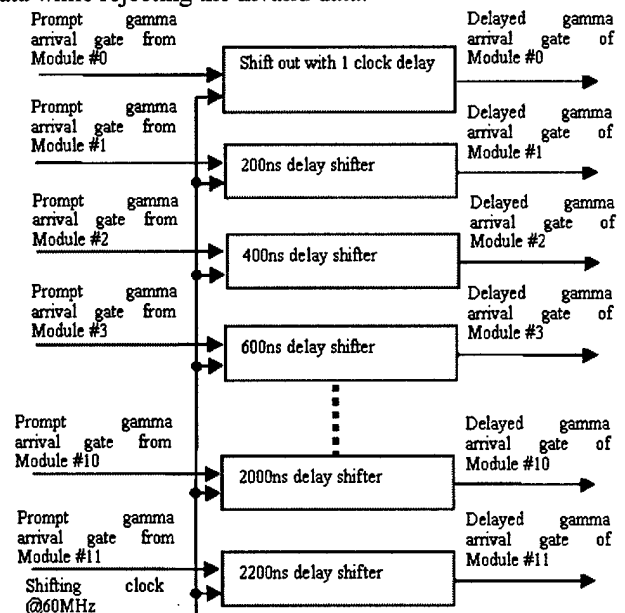


Fig. 3. Diagram of trigger shifting delay for accidental coincidences.

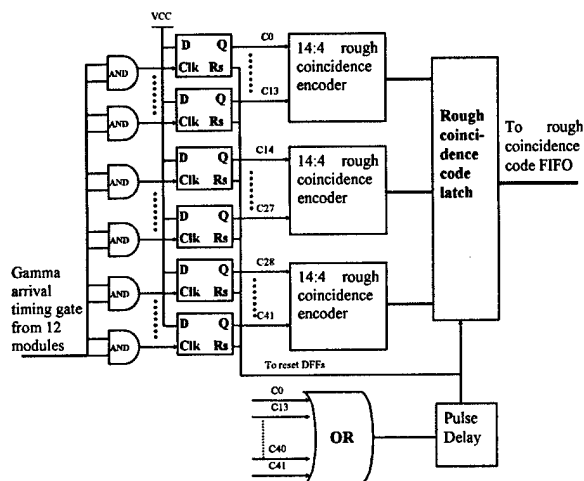


Fig. 4. The first-level rapid coincidence logic.

Being driven by a 40-MHz clock, the second-level discriminating logic reads the rough coincidence code from the rough-coincidence-code FIFO, selects valid coincidences, then combines the data of 2 coincident gamma events into a 64-bit coincidence data unit. The logic monitors the almost-full and almost-empty flags of the rough-coincidence-code FIFO and performs selection operations when an almost-full flag is detected. Fig. 5 shows 4 phases needed for a second-level selection. In phase I, at the rising edge of the clock, a read pulse is sent to the rough-coincidence-code FIFO. A logic circuitry decodes the data fetched from the FIFO to check for a valid coincidence. If there is a valid coincidence, the logic will prepare the output-enable signals for the corresponding data-buffer FIFOs. If there is no valid coincidence, the output-enable signals will be kept invalid. In phase II, at the rising edge of the clock, a read pulse is sent to all data buffer FIFOs to pop out the data written by the write signal of the rough-coincidence-code FIFO; In phases III and IV, if a valid coincidence has been found in Phase I, the output-enable signals will allow the corresponding data FIFOs to place their data on the coincidence-result bus sequentially, and the write signal of coincidence-result FIFO will be generated once in each phase to store the 64-bit coincidence-result data. If no valid coincidence has been found in Phase I, neither the output-enable signals nor the coincidence result FIFO write signal will be asserted. The performance continues until an almost-empty flag is detected. Accordingly, the system can sustain a throughput of 10 million events per second.

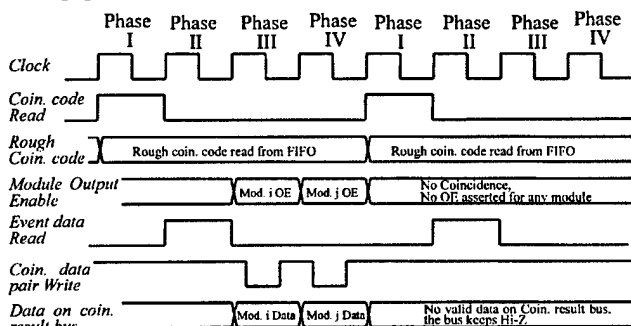


Fig. 5. Timing diagram of the second-level coincidence processing logic (module number $i < j$, $i, j \in 1, \dots, 12$).

Because many FIFOs are used to buffer the rough coincidence code and gamma-event data, a FIFO-output order mismatch will lead to unrecoverable coincidence misregistration. To avoid this kind of mishap, an order-checking mechanism is designed and implemented by pushing a toggling bit into all of the FIFOs. The toggling bit changes its status when there is a rough coincidence output from the first-level AND-logic. Dedicated logic circuitry on the DSP controller board monitors the output of the toggling bit from the gamma-event FIFOs and the rough-coincidence-code FIFO. If a status mismatch is detected, the monitoring logic will send an interrupt request to the DSP and then the DSP will reset and reinitialize the whole coincidence system to stop generating misregistration data.

The multiple coincident events are rejected from both the total and the accidental coincidences because the coincident events chosen from multiple coincidences will degrade the signal-to-noise ratio rather than improve it, although the countrate may increase.

C. Gamma-event data FIFO buffer

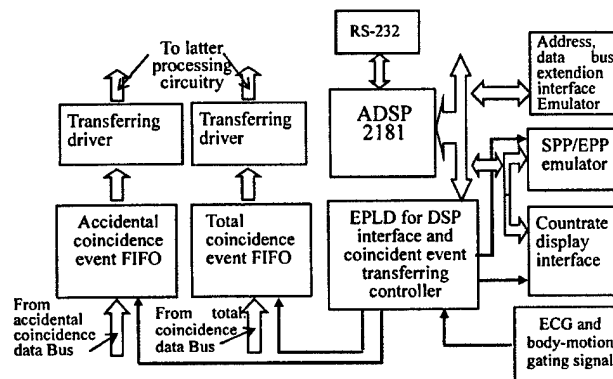


Fig. 6. Diagram of Gamma-event data FIFO buffer

Because of the 2-level coincidence-discrimination structure, fast coincidence data FIFO buffers are needed to match the speed of the low-dead-time first-level coincidence detection logic. Data showing position and energy of a detected gamma-event are digitized and converted into a 32-bit data unit from the front-end electronics. The data from all detector modules are fed into the data buffer plug-in modules through flat ribbon cables. Each buffer module receives data from 2 detector modules. As mentioned above, once the first level coincidence circuit detects a rough coincidence, all prompt gamma-event data will be written into FIFOs synchronously. After the second-level coincidence-selection logic makes a final selection, the buffered data from the selected pair of detector modules will be sent to the coincidence-result bus on the backplane. Only FIFOs with valid coincidence data will have valid output-enable signals. Then, these data will be pushed into the coincidence-result FIFO buffer on the DSP controller board.

Since accidental coincidence detection is based on a digital timing-shift-delay method, the gamma-event data must be delayed to match their delayed trigger pulses. The data delay is implemented by adding an extra FIFO before the rough-coincident-gamma-event-data FIFO, writing the

data into the FIFO with a prompt trigger pulse and reading it out with a delayed trigger pulse. Then, the accidental data FIFOs perform operations similar to those of the total coincidence data FIFOs.

D. DSP based System Controller

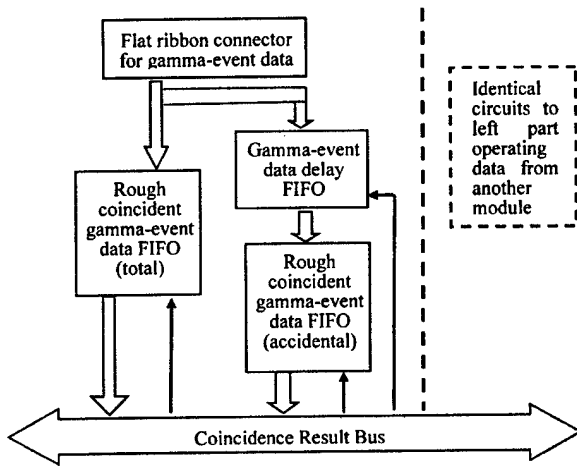


Fig. 7. Diagram of DSP-based coincidence system controller

The DSP controller resides in the middle slot of the 7-slot bus interface and has its own interface to the coincidence backplane to extend the control to the backplane. The 2 major tasks of this controller are: (1) buffering the coincident result (as mentioned before) and interfacing to the latter processing circuitry, which could be a crystal look-up board or an interface to a data acquisition computer; (2) and controlling the coincidence system and potentially controlling the front-end electronics. It also has features such as: (1) communication with a host computer through an RS-232 port, (2) counting and displaying the coincidence countrate and the single countrate of each detector module in real time, and (3) monitoring and tracking electrocardiograph (ECG) signals or lung motion signals for cardiac and respiratory gating.

A custom made real-time monitor program running inside the ADSP2181 (40-Mhz clock DSP) carries out all the control tasks. Some basic operating-system-like functions are also available within the real-time monitor; such as loading a piece of program to the DSP, starting execution of a program, and loading the contents of a segment of memory from the DSP. These functions can facilitate some future functional development without the need to modify the monitor program and to burn it into an erasable programmable read only memory (EPROM) before finalization of the code.

A Labview based function library has also been developed to support the integration of the coincidence system with a host PC.

III. RESULTS OF TEST

A. Coincidence timing uncertainty test

The timing uncertainty is very important to a coincidence system. To test it, we used the method illustrated in Fig. 8.

Three representative coincidence (timing overlap) cases were studied by using a variable delay to achieve the desirable timing overlap. In case 1, as illustrated in Fig.8, the overlap between the pulse and its delayed counterpart was bigger than the timing uncertainty, so the AND-logic always enabled an output pulse. In case 2, the overlap between the pulse and its delayed counterpart was smaller than the timing uncertainty, so the AND-logic enabled an output pulse only when the timing jitter caused an overlap between the pulse and its delayed counterpart. In case 3, the overlap between the pulse and its delayed counterpart had no overlap anyway, so the AND-logic did not enable an output pulse. By counting the coincidences between a pulse and its delayed counterpart within a specific timing window, we can measure the coincidence countrate as a function of the delay. In the graph of coincidence countrate vs delay, (Fig. 9), 0.5-ns timing uncertainty is represented by the edge where the coincidence countrate drops from the maximum to zero. However, since the timing uncertainty measured in Fig. 9 was limited by the minimum delay step (0.5 ns) of our delay box (EGG DB463), we could not get a more accurate result. Therefore, the coincidence timing uncertainty induced by the coincidence system was expected to be far less than 0.5 ns.

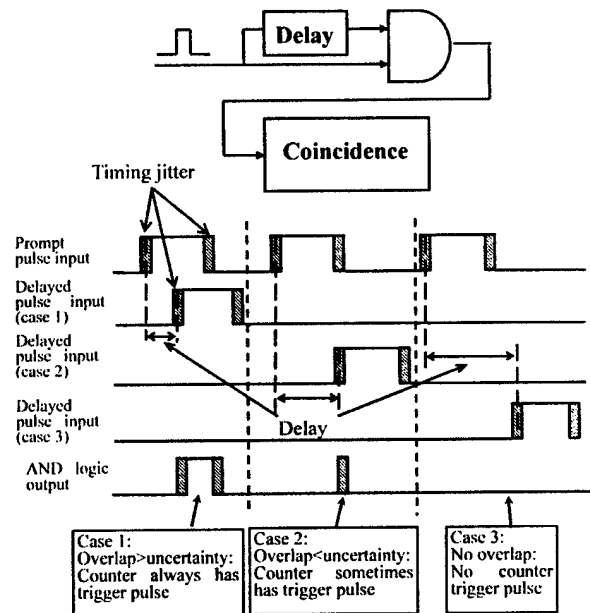


Fig. 8. Diagram of the coincidence timing uncertainty testing method.

Coincidence countrate vs. pulse delay

(Module 1 vs. Module 5 with timing gate width=6.5 ns)

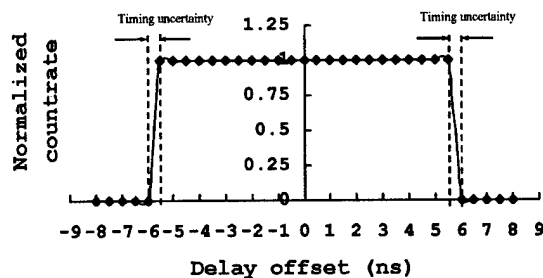


Fig. 9. Typical coincidence countrate and pulse delay relationship between two modules.

B. Coincidence circuitry dead-time test

Encoding a coincident event takes some time. Before an encoding process is finished, the first-level coincidence detection and encoding logic must be paralyzed to guarantee that the correct module pair information is determined and recorded. The paralysis causes a short period of dead-time.

We tested the dead-time of the coincidence system and found that the dead-time was about 21 ns. The testing method is shown in Fig. 10. Two pulse generators fed pulses to the coincidence system, simulating trigger signals from front-end electronics. Each generator provided pulses to 2 module inputs, which were considered within the domain of coincidence combinations. Correspondingly, there were 2 coincidences occurring independently at the respective rates of the 2 generators. We can record the input pulse rate of each generator and the output rate of the coincidence logic on the system's countrate monitor. The dead-time of the circuit was calculated using equation (1) [7]. Table 1 shows the test result.

$$\tau_{dead} = \frac{f_1 + f_2 - f_{coin}}{2 f_1 f_2} \quad (1)$$

where, τ_{dead} is the dead-time of the coincidence circuit, f_1 and f_2 are the input rates of the generators, and f_{coin} is the output rate of the coincidence system.

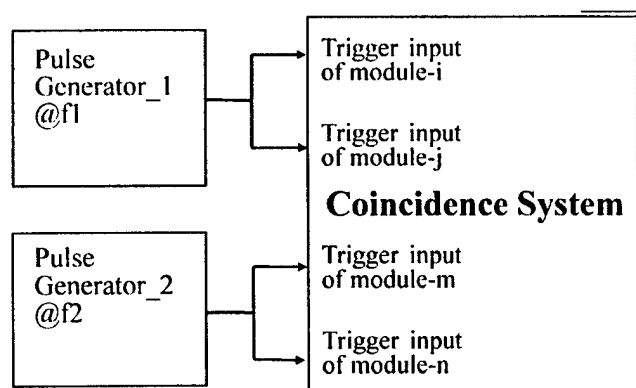


Fig. 10 Diagram of the coincidence dead-time testing method

The dead-time measured with the above method is a feature of the coincidence electronics other than the dead-time of the entire system. Because of the arbitrary frequencies of two pulsers, the phase warble guaranteed the full coverage of all the timing relationships between two coincidences, although the dead-time was measured with periodic pulses, statistically it's completely equivalent to that being measured with random signal feeding.

TABLE 1 COINCIDENCE DEAD-TIME TEST RESULT

Test-module combination	Generator_1 input rate (f_1) kHz	Generator_2 input rate (f_2) kHz	Coincidence output rate (f_{coin}) kHz	Dead-time (τ_{dead}) ns
Modules (1,4,7,10)	190.3	1303	1483	20.8
	4698	4658	8440	20.9
Modules (2,5,8,11)	721.7	788.8	1487	20.6
	4593	4442	8181	20.9
Modules (3,6,9,12)	1656	1310	2877	20.5
	4787	4066	8038	20.9
Average dead-time of all modules				20.8

IV. CONCLUSION AND DISCUSSION

In this paper, we present a modular, low-dead-time coincidence system for modular PET cameras. The system is based on a fast coincidence discrimination structure consisting of a first-level rapid AND-logic and a clock-driven second-level fine selection logic. A modular backplane/plug-in architecture that we've adopted supports different detector module configurations in addition to different electronic and mechanical implementations.

The coincidence system functionally works well for as many as 10 million coincident events per second (with periodic testing pulses). The gate width for the AND-logic is on-line changeable online from 6.5 ns to 16 ns and has better than 0.5ns adjustment accuracy. The coincidence timing uncertainty is far less than 0.5 ns. The dead-time of coincidence logic is around 21 ns which is smaller than that found in normal designs.

The test results satisfy our design specifications. However, improvement will be pursued. The first improvement would be to reduce timing gate window from current 6.5 ns because a large timing gate limits the coincidence timing resolution. For a PET camera with bismuth germinate crystals (BGO), like our HOTPET, the relatively wide timing gate is good enough. However, for systems with faster scintillators, such as lutetium oxyorthosilicate (LSO) or gadolinium oxyorthosilicated (GSO), the 6.5 ns gate may not be suitable. Though the improvement might make the circuit a little more complex, we believe a narrower timing gate can be accomplished.

V. REFERENCES

- [1] H.M. Dent, et al, "A Real Time Digital Coincidence Processor for Positron Emission Tomography", *IEEE Transaction on Nuclear Science*, vol. 33, pp 556-559, February 1986.

- [2] D.F. Newport, et al, "Coincidence Detection and Selection in Positron Emission Tomography Using VLSI", *IEEE Transaction on Nuclear Science*, vol. 36, pp.1052-1055, February 1989.
- [3] J.W. Young, et al, "Optimum Bandwidth Usage in Digital Coincidence Detection for PET", *Conference Record of the 1993 IEEE MIC Conference*, Vol. 2, pp 1205-1208.
- [4] W.H. Wong, et al, "Feasibility of a High Speed Gamma Camera Using the High-Yield-Pile-Up-Event-Recovery (HYPER) Method", *J. Nucl. Med.*, 42(4), pp 624-632.
- [5] W-H. Wong, et al., "The Design of a High Resolution Transformable Whole body PET camera". *IEEE Transactions on Nuclear Science*, 49(5): October, 2002 and *IEEE MIC Conference Record 2001*.
- [6] H. Li, et al, "Front-end electronics Based on High-yield-pileup-event-recovery Method for a High Resolution PET Camera with PMT-quadrant-sharing Detector Modules", *IEEE MIC Conference Record 2001*.
- [7] William R. Leo, "Techniques for Nuclear and Particle Physics Experiment", *Springer-Verlag Berlin*, 1987, pp 114-118.

An Evaluation of the Effect of Filtering in 3-D OSEM Reconstruction by Using Data From a High-Resolution PET Scanner

Hossain Baghaei, *Member, IEEE*, Jorge Uribe, *Member, IEEE*, Hongdi Li, *Member, IEEE*, Yu Wang, Mehmet Aykac, Yaqiang Liu, Tao Xing, and Wai-Hoi Wong, *Member, IEEE*

Abstract—We evaluated the effect of filtering in the three-dimensional (3-D) ordered subset expectation maximization (OSEM) algorithm for reconstruction of projection data obtained with a high-resolution 3-D positron emission tomography (PET) scanner. For this study, we used the inter-update Metz filtered OSEM (IMF-OSEM) algorithm, which was developed by the PARAPET project. IMF-OSEM is an implementation of the OSEM algorithm with some additional capabilities such as inter-update filtering. The projection data were acquired using the high-resolution PET camera developed at the University of Texas M. D. Anderson Cancer Center (MDAPET). This prototype camera, which is a multiring scanner without any septa, has a transaxial resolution of 2.8 mm, which allows better evaluation of the algorithm. We scanned three phantoms: a cylindrical uniform phantom, a cylindrical phantom containing four small lesion phantoms, and the Hoffman brain phantom. The effect of inter-filtering in OSEM reconstruction was evaluated by computing the noise level of the reconstructed images of the uniform phantom, studying the contrast recovery for the hot lesions in a warm background, and visually inspecting images especially those of the Hoffman brain phantom. In addition, the effect of post-filtering on the reconstructed images was evaluated. For the high statistics data, a good compromise between contrast recovery and noise level was achieved using 20–50 iterations for the plain OSEM algorithm. By visually inspecting the images of the Hoffman brain phantom and hot lesions, we observed that the plain OSEM algorithm, especially when followed by post-filtering, and the inter-update filtering with Metz power of 1 could reasonably reproduce the phantom's structure. We also found that inter-update filtering has the potential to produce a noise level and contrast recovery comparable with that using the plain OSEM algorithm at a lower iteration number; however, it also has a greater tendency to develop noise artifacts.

Index Terms—Filtering, iterative algorithms, OSEM, PET, three-dimensional (3-D) image reconstruction.

I. INTRODUCTION

THE maximum likelihood expectation maximization (ML-EM) algorithm and its accelerated variant, ordered subset expectation maximization (OSEM), are iterative reconstruction methods for estimating tracer distribution from the measured projection data [1], [2]. It has been found that the

three-dimensional (3-D) OSEM algorithm can produce images of higher quality in terms of resolution and contrast than the conventional filtered back-projection algorithms [3]. However, ML-EM and OSEM have some drawbacks, including a tendency to develop noise artifacts with increasing the number of iterations. In addition, for the OSEM algorithm to converge some stringent conditions must exist. To control noise artifacts and drive the image estimate sequence toward a smoother convergence, several methods have been used to regularize the image updating mechanism for EM and OSEM algorithms. One of the methods of controlling noise in reconstructed images is to add a smoothing step between iterations. The inter-update Metz filtered OSEM (IMF-OSEM) algorithm, developed by the PARAPET project, incorporates a filtering action into the image updating process to improve the quality of the reconstruction [4]. With this technique, the multiplicative update image is applied to a Metz-filtered version of the current estimate rather than the current estimate itself at certain intervals. Recently, the noise-reducing iteration filtering scheme has also been used in the coincidence list ordered sets expectation maximization (COSEM) algorithm using the Metz filter [5]. In this work, we used the IMF-OSEM algorithm, as implemented in the PARAPET software package, to test the performance of 3-D OSEM and the effects of inter-update and post-filtering.

II. METHODS

The effect of filtering in the 3-D OSEM algorithm was evaluated quantitatively by computing the coefficient of variation and contrast recovery. The algorithm was also evaluated qualitatively via visual inspection of the reconstructed images. For this investigation, three phantoms were scanned: 1) a uniform cylindrical phantom; 2) a cylindrical phantom containing four small lesion phantoms having a diameter of 3, 4, 5, and 6 mm; and 3) the Hoffman brain phantom [6].

All the OSEM images presented here were reconstructed with nine subsets. So, a cycle of nine iterations (subiterations) constituted one full iteration. We used the Metz filter for both the inter-update filtering and the post-filtering. The Metz filter is able to both attenuate high-frequency noise and amplify mid-range frequencies. In frequency space, the Metz filter, as a function of frequency f , is given by

$$M(f, s, N) = \frac{1 - (1 - G(f, s))^2(N+1)}{G(f, s)}$$

Manuscript received November 26, 2001; revised May 1, 2002. This work was supported in part by the NIH Grant ROI CA58980, NIH Grant ROI CA61880, NIH Grant ROI CA76246, NIH Grant ROI CA58980S1, Texas Higher Education Advanced Technology Grant, John S. Dunn Foundation Research Grant, and the Cobb Foundation for Cancer Research.

The authors are with the M. D. Anderson Cancer Center, University of Texas, Houston, TX 77030 USA (e-mail: hbaghaei@di.mdacc.tmc.edu).

Digital Object Identifier 10.1109/TNS.2002.803681

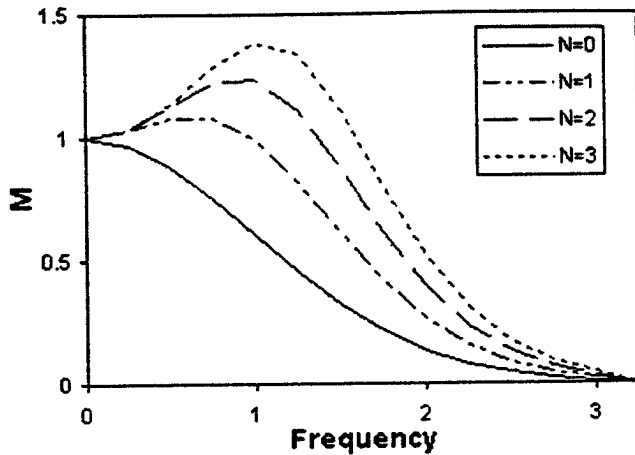


Fig. 1. Metz filters for various values of the Metz power ($s = 1$).

where N is the Metz power and $G(f, s)$ is the Fourier transform of a Gaussian filter with the full width at half maximum (FWHM) of s . For power $N = 0$, the Metz filter is just a Gaussian filter and for higher power the mid-range frequencies are more amplified compared to the Gaussian case. Fig. 1 illustrates the dependency of M on N for $s = 1$.

Prior to image reconstruction, the 3-D projection data were corrected. These corrections included random coincidence subtraction, attenuation correction, and geometric and detector-pair efficiency corrections [7]. Random subtraction can produce negative pixels in the true projection data that were set to zero to prevent divergence of the algorithm. All data were acquired with the ^{18}F -fluorodeoxyglucose (FDG) tracer.

We used the high-resolution MDAPET camera, a prototype PET scanner developed at the University of Texas M. D. Anderson Cancer Center (MDAPET) to scan the three phantoms. This camera, which is based on the photomultiplier-quadrant-sharing (PQS) technique, has 14 detector rings covering an axial field-of-view of 3.85 cm. The camera's detection system is divided into eight independent, movable modules. Each module can be translated radially to alter the size of the patient opening, optimizing the detection sensitivity for different body cross-sections. Each ring consists of 448 individual bismuth germanate (BGO) crystals having an in-plane and axial crystal pitch of 2.66 and 2.80 mm, respectively. Also the gantry can be rotated during data acquisition in 0.10° steps up to 45° . The gantry rotation is necessary to fill the gaps in the sinograms. The standard procedure for this camera is to acquire data in 1° steps. The gantry design, detector parameters, PQS design, and electronics of the MDAPET camera were described previously [8]–[12].

The MDAPET scanner has several modes of operation. Data presented here were acquired while the camera was in brain mode. In this mode, the camera has a ring diameter (the distance between two facing detector modules) of 44 cm and transaxial image resolution of 2.8 mm. Fig. 2 shows the MDAPET scanner in brain mode, with the eight modules forming a closely packed octagon and a patient opening of 32 cm. The imaging performance characteristics of the camera were described previously [13], [14].

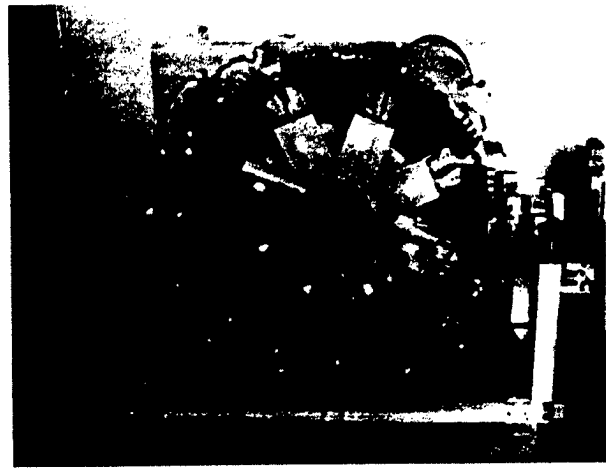


Fig. 2. The MDAPET camera in brain mode.

The MDAPET scanner has no septa and all data were acquired in 3-D mode which produces 196 sinograms. In the present study, each sinogram had 239 radial bins and 180 azimuthal views. The camera allows simultaneous imaging of 27 transaxial slices with 1.38-mm thickness.

III. RESULTS

A. Uniform Phantom Study

The scanned cylindrical uniform phantom had a diameter of 17 cm and axial length of 6 cm. We acquired 100 million true events for this study. The coefficient of variation (CV), a measure of the noise level in the reconstructed image, was calculated for the uniform phantom data. The coefficient of variation was measured by computing σ/μ , in which σ and μ are the standard deviation and mean of the pixel values over some region of interest, respectively.

A plain 3-D OSEM (no filtering) reconstructed image of a central slice (slice number 13) of the uniform phantom, created after 5th, 10th, 20th, and 40th iteration, is shown in Fig. 3. Results for the same central slice after post-filtering of the plain OSEM results at the 20th and 40th iteration are shown in Fig. 4. For post-filtering we used a Metz filter having a FWHM of 4 mm and a Metz power parameter of 2. For all calculations presented here, the FWHM was chosen to be 4 mm. Also, in Figs. 5 and 6 images are shown for the same central slice after the 10th iteration and 20th iteration when all inter-update filters in IMF-OSEM were applied at intervals of nine and four iterations, respectively. In both Figs. 5 and 6 the top images were obtained with Metz power $N = 1$ and lower images were obtained with $N = 2$. Axial and transaxial Metz filters were chosen to have the same parameters.

Figs. 5 and 6 clearly show artifacts in the images reconstructed using inter-update filtering at much lower iterations than plain OSEM. This can also be seen in the calculated noise (CV) of the central image slice, which is shown in Fig. 7 as a function of the number of iterations. Data in Fig. 7 are for the plain OSEM, post-filtering, and inter-update filtering methods. Inter-update filtering was applied at intervals of four or nine iterations with Metz power of one or two. In all cases,

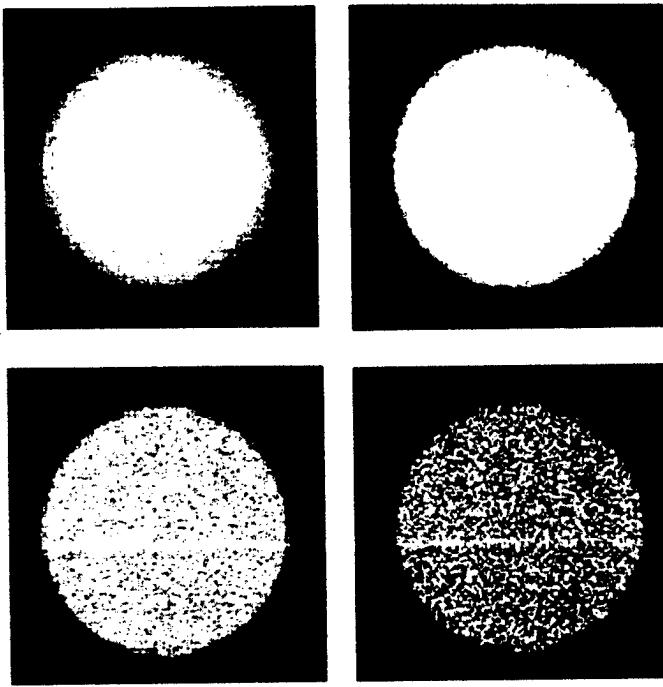


Fig. 3. Reconstructed image of the central slice of the uniform phantom after the fifth iteration (top left), 10th iteration (top right), 20th iteration (bottom left), and 40th iteration (bottom right).

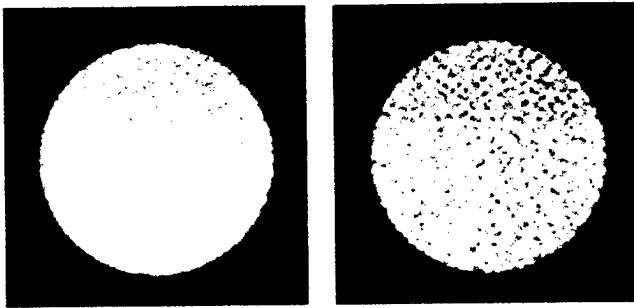


Fig. 4. Reconstructed image of the central slice of the uniform phantom (left) after the 20th iteration followed by post-filtering and (right) after the 40th iteration followed by post-filtering.

the CV grew as the number of iterations increased and in particular, growth was very drastic in the case of inter-update filtering when it was applied too frequently or Metz power was relatively large. For example, for a Metz power of 1 when the inter-update filter was applied at intervals of nine iterations, the CV was comparable to post-filter results; however when the inter-update filter was applied at intervals of four iterations, the CV increased drastically at the 26 iterations. For Metz power of 2, artifacts could be seen after 18 iterations (two full iterations).

B. Hot Lesion Study

The contrast recovery (CR) data were obtained from the scanning of the cylindrical phantom containing four small lesion phantoms. A cylindrical phantom, with internal diameter of 16 cm, was filled with activity to form a warm background. The diameter of the embedded lesion phantoms was 3, 4, 5, and 6 mm and they all had the same standard uptake value (SUV). For the data presented here, the approximate activity concentration ratio of the lesions to the background was 6 : 1.

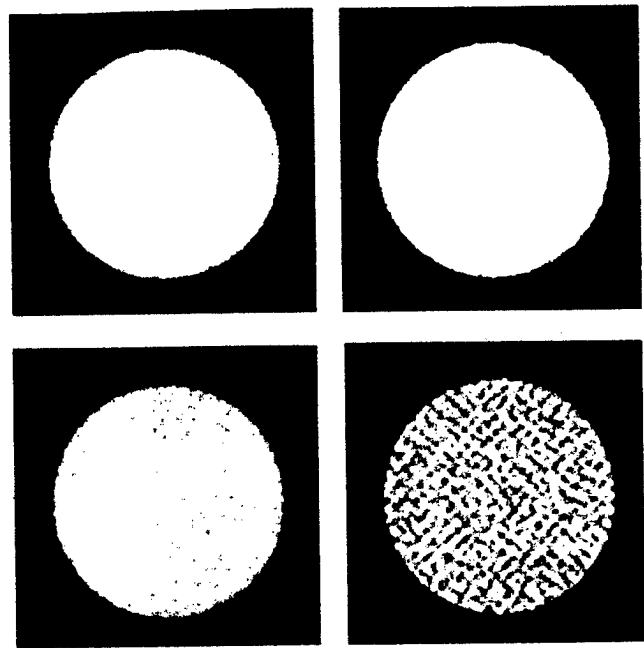


Fig. 5. Reconstructed image of the central slice of the uniform phantom when the inter-update filter was applied at intervals of nine iterations: (left) after the 10th iteration and (right) after the 20th iteration. Top (bottom) images were obtained with Metz power of 1 (2).

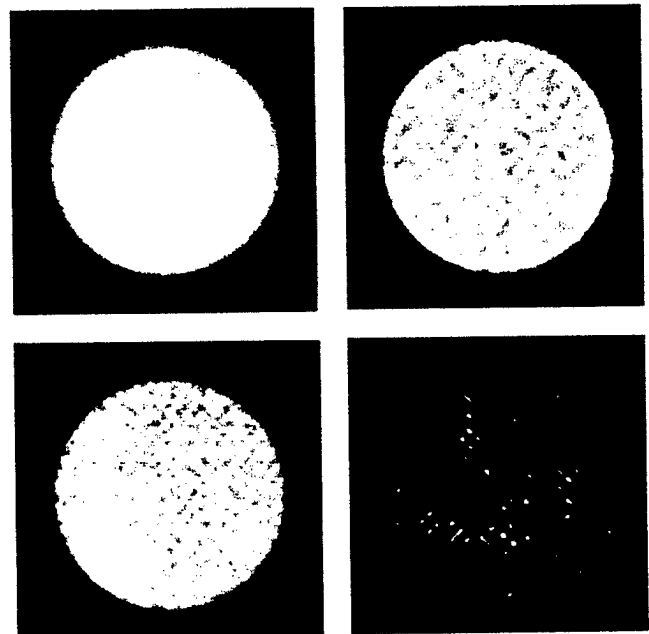


Fig. 6. Reconstructed image of the central slice of the uniform phantom when the inter-update filter was applied at intervals of four iterations: (left) after the 10th iteration and (right) after the 20th iteration. Top (bottom) images were obtained with Metz power of 1 (2).

A reconstructed image slice of the four hot lesions after the 10th and 40th iteration using the plain OSEM algorithm is shown in Fig. 8. Also, images for the same slice after the 10th and 40th iteration images were subjected to a post-filter action, using the Metz filter, are shown in Fig. 9. Although all four lesions are observable in Fig. 8, they can be more clearly seen in Fig. 9. In Fig. 10 images are shown for the same slice after the tenth and twentieth iteration when all the inter-update filters in IMF-OSEM, using the Metz filter, were applied at intervals

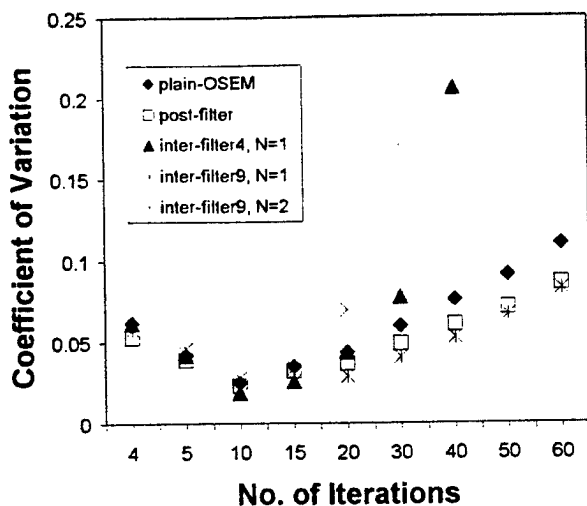


Fig. 7. Coefficient of variation for a central slice of the uniform phantom as a function of number of iterations for five different calculations. Inter-update filtering was applied at intervals of four (inter-filter4) or nine (inter-filter9) iterations with the Metz power of $N = 1$ or $N = 2$.

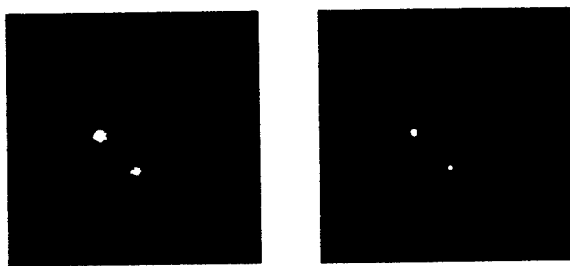


Fig. 8. An image of four hot lesions in the warm background reconstructed using the plain OSEM algorithm after the (left) 10th iteration and (right) 40th iteration.

of nine iterations. The upper images were obtained with Metz power $N = 1$ and the lower images were obtained with $N = 2$. As was the case for the uniform phantom data, artifacts can be seen clearly in Fig. 10 for $N = 2$ at the 20th iteration.

The contrast recovery was defined as $(S - B)/B$, in which S and B are the integrated counts in the region of interest of the hot lesion and background, respectively. The extracted contrast as a function of the number of iterations for the 6-mm lesion is shown in Fig. 11 for plain OSEM, post-filtering, and inter-update filtering methods. The horizontal profiles running along the middle of the images are shown in Figs. 12 and 13. The profile data for each image was normalized according to the average count in the background for each case. Figs. 11–13 show that plain OSEM followed by post-filtering, using the Metz filter with appropriate parameters generated the best results in terms of contrast recovery and spatial resolution. Results of the inter-update filtering method (for $N = 1$ and updating intervals of nine iterations) were close to those from the post-filtering method.

C. Hoffman Brain Phantom Study

We used the Hoffman brain phantom to evaluate how accurately the reconstruction methods could reproduce the structure of the brain phantom from a high statistics study (approximately

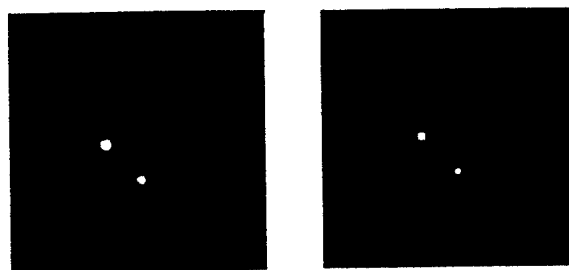


Fig. 9. Reconstructed image of the same slice shown in Fig. 8 when post-filtering was performed on the images obtained with plain OSEM after the (left) 10th iteration and (right) 40th iteration.

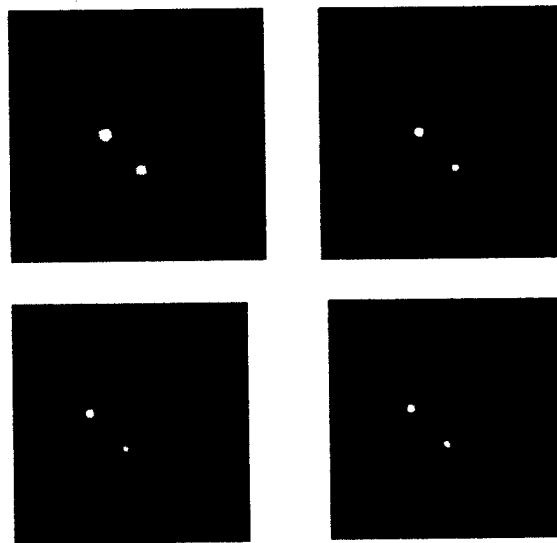


Fig. 10. Reconstructed images of the same slice shown in Figs. 8 and 9 when all inter-update filters in the IMF-OSEM were applied at intervals of nine iterations: after the (left) 10th iteration, and (right) 20th iteration. Top (bottom) images were obtained with Metz power of 1 (2).

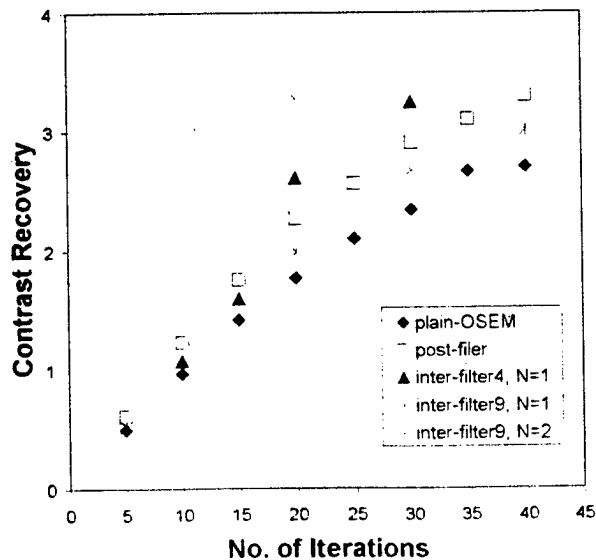


Fig. 11. Contrast recovery as a function of the number of iterations for five different calculation methods. Inter-update filtering was done at intervals of four or nine iterations with the Metz power of 1 or 2. The activity concentration ratio of the lesions to the background is about 6:1.

200 million counts in all sinograms). In Fig. 14, a reconstructed image of a central slice of the Hoffman brain phantom is shown

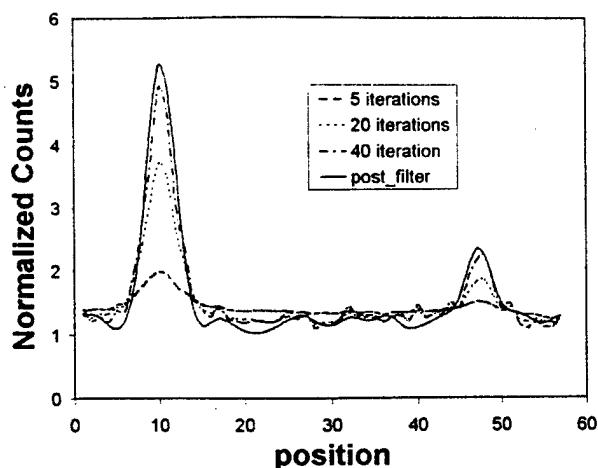


Fig. 12. A horizontal profile running along the middle of the image for a central slice. Results are shown for plain OSEM at the 5th, 20th, and 40th iterations and for post-filtering after the 40th iteration. The 6- and 4-mm hot lesions are clearly observable.

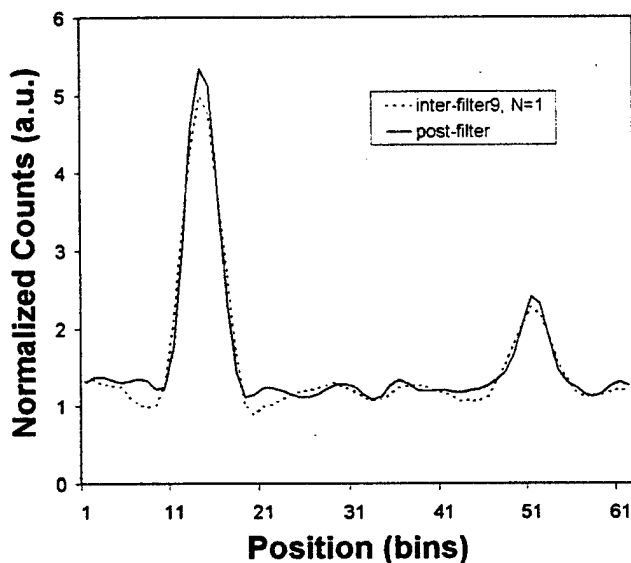


Fig. 13. A horizontal profile along the middle of the image for the inter-update filtering at interval of nine iterations is compared with the post-filtering results shown in Fig. 12. Images were obtained for the 40th iteration.

for the plain OSEM algorithm after the 10th and 30th iterations and for the inter-update filtering method when applied at intervals of four or nine iterations with a Metz power of 1. In Fig. 15, the same image slice reconstructed with the plain OSEM when followed by a post-filtering action at the 40th iteration is compared to the picture of the corresponding phantom's slice. Fig. 16 shows the same slice when the image was reconstructed using the Metz inter-update filter applied at intervals of four iterations.

As can be seen in Figs. 14 and 15, the plain OSEM, the post-filtering, and the inter-update filtering at intervals of 9 iterations with Metz power of 1 all reasonably reproduced the structures of the Hoffman brain phantom. However, results for the post-filtering and inter-update filtering methods visually looked better. For inter-update filtering, similar to uniform phantom and

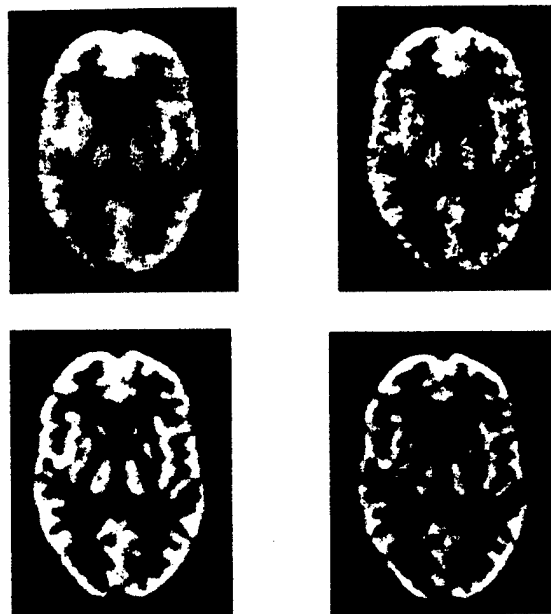


Fig. 14. Reconstructed image slice of the Hoffman brain phantom after the 10th iteration (top left), 30th iteration (top right); after the 30th iteration with inter-updating at intervals of nine iterations (bottom left) and after the 20th iteration with inter-updating in intervals of four iterations (bottom right). Metz power was 1 for two lower images.

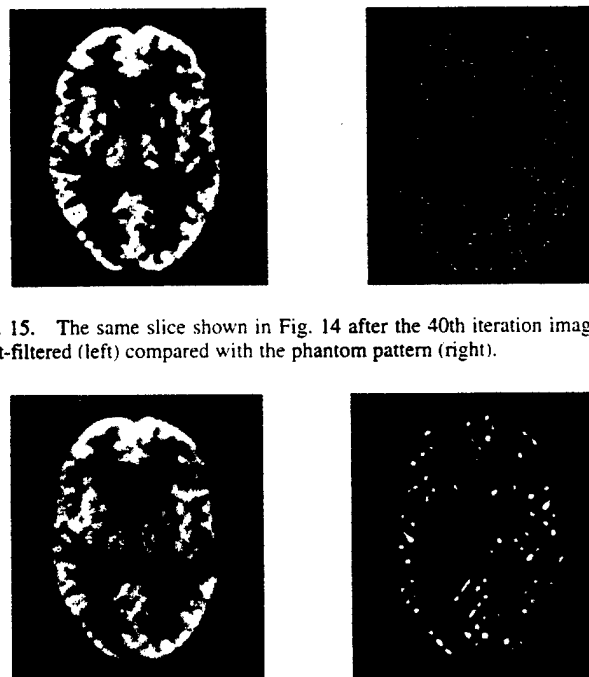


Fig. 15. The same slice shown in Fig. 14 after the 40th iteration image was post-filtered (left) compared with the phantom pattern (right).

Fig. 16. Reconstructed image of the same slice shown in Figs. 14 and 15 when all the inter-update filters were applied at intervals of four iterations. Images are shown after the 10th iteration (left) and 20th iteration (right). Metz power was $N = 2$.

hot lesion studies, the image clearly shows artifacts when filtering applied too frequently (e.g., every four iterations) or the Metz power was large (e.g., 2) after the 20th iteration.

IV. CONCLUSION

We evaluated the effect of filtering in the 3-D ordered subset expectation maximization algorithm by reconstructing the

projection data from a high-resolution 3-D PET scanner. For this purpose, we used the inter-update Metz-filtered OSEM algorithm. We observed that for our high statistics phantoms data with the plain 3-D OSEM algorithm a good compromise between contrast recovery and noise could be achieved using 20 to 50 iterations (three to five full iterations). A further increase in the number of iterations resulted in a greater increase in the noise level in the reconstructed images. We observed that when plain OSEM images were post-filtered using a Metz filter with the appropriate parameters the image quality in terms of noise level, contrast recovery, and appearance could be improved. By visually inspecting the images of the Hoffman brain phantom, we observed that the plain OSEM algorithm, especially when followed by post-filtering, could reasonably reproduce the phantom structure without creating artifacts. Even though we obtained the best results with the post-filtering method, we also observed that with inter-update filtering, when a Metz power of 1 is used and filtering is applied at intervals of nine iterations (one full iteration), we could obtain with fewer iterations results close to those from the post-filtering. So, the inter-update filtering has the potential to achieve the desired noise level and contrast recovery with less iteration. This is especially true when filtering is applied more frequently or $N > 1$; however this method also has a greater tendency to develop noise artifacts which needs further investigation.

REFERENCES

- [1] L. A. Shepp and Y. Vardi, "Maximum likelihood reconstruction for emission tomography," *IEEE Trans. Med. Imaging*, vol. MI-1, pp. 113-122, Oct. 1982.
- [2] H. M. Hudson and R. S. Larkin, "Accelerated image reconstruction using ordered subsets of projection data," *IEEE Trans. Nucl. Sci.*, vol. 13, pp. 601-609, Aug. 1994.
- [3] A. J. Reader, D. Visvikis, K. Erlandsson, R. J. Ott, and M. A. Flower, "Intercomparison of four reconstruction techniques for positron volume imaging with rotating planar detectors," *Phys. Med. Biol.*, vol. 43, pp. 823-834, 1998.
- [4] M. Jacobson, R. Levkovitz, A. Ben-Tal, K. Thielemans, T. Spinks, D. Belluzzo, E. Pagani, V. Bettiardi, M. C. Gilardi, A. Zverovich, and G. Mitrai, "Enhanced 3D PET OSEM reconstruction using inter-update Metz filtering," *Phys. Med. Biol.*, vol. 45, pp. 2417-2439, 2000.
- [5] R. Levkovitz, D. Falikman, M. Zibulevsky, A. Ben-Tal, and A. Nemirovski, "The design and implementation of COSEM, an iterative algorithm for fully 3-D listmode data," *IEEE Trans. Med. Imaging*, vol. 20, pp. 633-642, July 2001.
- [6] E. J. Hoffman, P. D. Cutler, W. M. Digby, and J. C. Mazziotta, "3-D phantom to simulate cerebral blood flow and metabolic images for PET," *IEEE Trans. Nucl. Sci.*, vol. 37, pp. 616-620, Apr. 1990.
- [7] H. Baghaei, W.-H. Wong, J. Uribe, H. Li, N. Zhang, and J. Wang, "The correction factors for a high resolution variable field of view PET camera," *J. Nucl. Med.*, vol. 40, p. 279P, May 1999.
- [8] W.-H. Wong, "A positron camera detector design with cross-coupled scintillators and quadrant sharing photomultipliers," *IEEE Trans. Nucl. Sci.*, vol. 40, pp. 962-966, Aug. 1993.
- [9] W.-H. Wong, J. Uribe, W. Lu, and K. Hicks, "Design of a variable field prototype PET camera," *IEEE Trans. Nucl. Sci.*, vol. 43, pp. 1915-1920, June 1996.
- [10] W.-H. Wong, J. Uribe, K. Hicks, and M. Zambelli, "A 2-dimensional detector decoding study on BGO arrays with quadrant sharing photomultipliers," *IEEE Trans. Nucl. Sci.*, vol. 41, pp. 1453-1457, June 1994.
- [11] W.-H. Wong, G. Hu, N. Zhang, J. Uribe, J. Wang, H. Li, H. Baghaei, and S. Yokoyama, "Front end electronics for a variable field PET camera using the PMT-quadrant-sharing detector array design," *IEEE Trans. Nucl. Sci.*, vol. 44, pp. 1266-1270, June 1997.
- [12] H. Li, W.-H. Wong, N. Zhang, J. Wang, J. Uribe, H. Baghaei, and S. Yokoyama, "Prototype electronics for a variable field of view PET camera using the PMT-quadrant-sharing detector array," *IEEE Trans. Nucl. Sci.*, vol. 46, pp. 546-550, June 1999.
- [13] J. Uribe, H. Baghaei, H. Li, S. Yokoyama, N. Zhang, J. Wang, F. Dobbs, and W.-H. Wong, "Basic imaging characteristics of a variable field of view PET camera using quadrant sharing detector design," *IEEE Trans. Nucl. Sci.*, vol. 46, pp. 491-497, June 1999.
- [14] H. Baghaei, W.-H. Wong, J. Uribe, H. Li, N. Zhang, and Y. Wang, "Breast cancer studies with a variable field of view PET camera," *IEEE Trans. Nucl. Sci.*, vol. 47, pp. 1080-1084, June 2000.

Evaluation of the Effect of Filter Apodization for Volume PET Imaging Using the 3-D RP Algorithm

Hossain Baghaei, *Member, IEEE*, Wai-Hoi Wong, *Member, IEEE*, Hongdi Li, *Member, IEEE*,
Jorge Uribe, *Member, IEEE*, Yu Wang, Mehmet Aykac, Yaqiang Liu, and Tao Xing

Abstract—We investigated the influence of filter apodization and cutoff frequency on the image quality of volume positron emission tomography (PET) imaging using the three-dimensional re-projection (3-D RP) algorithm. An important parameter in 3-D RP and other filtered backprojection algorithms is the choice of the filter window function. In this study, the Hann, Hamming, and Butterworth low-pass window functions were investigated. For each window, a range of cutoff frequencies was considered. Projection data were acquired by scanning a uniform cylindrical phantom, a cylindrical phantom containing four small lesion phantoms having diameters of 3, 4, 5, and 6 mm and the 3-D Hoffman brain phantom. All measurements were performed using the high-resolution PET camera developed at the M.D. Anderson Cancer Center (MDAPET), University of Texas, Houston, TX. This prototype camera, which is a multiring scanner with no septa, has an intrinsic transaxial resolution of 2.8 mm. The evaluation was performed by computing the noise level in the reconstructed images of the uniform phantom and the contrast recovery of the 6-mm hot lesion in a warm background and also by visually inspecting images, especially those of the Hoffman brain phantom. For this work, we mainly studied the central slices which are less affected by the incompleteness of the 3-D data. Overall, the Butterworth window offered a better contrast-noise performance over the Hann and Hamming windows. For our high statistics data, for the Hann and Hamming apodization functions a cutoff frequency of 0.6–0.8 of the Nyquist frequency resulted in a reasonable compromise between the contrast recovery and noise level and for the Butterworth window a cutoff frequency of 0.4–0.6 of the Nyquist frequency was a reasonable choice. For the low statistics data, use of lower cutoff frequencies was more appropriate.

Index Terms—Filtering, positron emission tomography (PET), three-dimensional (3-D) image reconstruction, 3-D re-projection (3-D RP).

I. INTRODUCTION

THE filtered backprojection technique used in positron emission tomography (PET) image reconstruction amplifies the statistical noise present in the acquired projection data. To reduce the noise in the reconstructed image, a low-pass window function usually is applied to the ramp filter [1]–[4]. We investigated the influence of the smoothing window function on image quality. Specifically, three apodization functions:

Manuscript received November 26, 2001; revised May 29, 2002. This work was supported in part by the NIH Grant RO1 CA58980, NIH Grant RO1 CA61880, NIH Grant RO1 CA76246, NIH Grant RO1 CA58980S1, Texas Higher Education Advanced Technology Grant, John S. Dunn Foundation Research Grant and by the Cobb Foundation for Cancer Research.

The authors are with the M.D. Anderson Cancer Center, University of Texas, Houston, TX 77030 USA (e-mail: hbaghaei@di.mdacc.tmc.edu).

Digital Object Identifier 10.1109/TNS.2002.807945

the Hann, Hamming and Butterworth window functions with a range of cutoff frequencies were investigated in volume PET imaging. For image reconstruction we used the three-dimensional (3-D) re-projection algorithm of Kinahan and Rogers (3-D RP), which is widely used in 3-D PET imaging [5].

The 3-D RP algorithm incorporates a preliminary step in which projections that are partially measured in the 3-D data acquisition are, because of the truncated cylindrical geometry of the scanner, completed by forward projection of an initial low statistics image obtained from the completely measured (direct) projections. The forward projected sinograms are less noisy than their measured counterparts and show some loss in spatial resolution [6]. Differences between measured sinograms and forward projected sinograms have a differential effect on the final 3-D reconstructed images because proportionately more forward projected data is used in the outer planes. In order to also investigate the influence of the filter apodization in the first-pass [initial two-dimensional (2-D)] reconstruction on the final images, we reconstructed the first-pass images either using a rectangular window (ramp filter) or using the same apodization window used in the second-pass reconstruction.

II. METHODS

The influence of the low-pass apodization function and the cutoff frequency for volume PET imaging using the 3-D-re-projection algorithm were evaluated quantitatively by computing the coefficient of variation (CV) and the contrast recovery (CR). The smoothing functions were also evaluated qualitatively by visual inspection of the reconstructed images. For this investigation, 3-D PET data from the scan of three phantoms were used. These phantoms were: a) a uniform cylindrical phantom; b) a cylindrical phantom containing four small lesion phantoms having a diameter of 3, 4, 5, and 6 mm; and c) the 3-D Hoffman brain phantom [7].

The 2-D filter was defined as the product of a low-pass smoothing function and the 2-D filter derived by Colsher [8], [9]. The filter was set to zero for frequencies larger than the Nyquist frequency. The three smoothing functions that we tested were the Hann, Hamming, and Butterworth functions [10], [11]. The Hann window function was defined as a function of frequency $f = \sqrt{f_x^2 + f_y^2}$ using

$$R(f) = 0.5 + 0.5 \cos\left(\frac{\pi f}{f_m}\right), \text{ if } |f| \leq f_m$$



Fig. 1. The MDAPET camera in brain mode.

in which f_m is the cutoff frequency. The Hamming window function was defined as

$$R(f) = 0.54 + 0.46 \cos\left(\frac{\pi f}{f_m}\right), \text{ if } |f| \leq f_m.$$

The rectangular window function $R(f) = 1$ gives the Colsher (ramp) filter. The above window functions were set to zero for $|f| > f_m$. Finally, the Butterworth window was defined using

$$R(f) = \frac{1}{\sqrt{1 + \left(\frac{|f|}{f_m}\right)^{2n}}}$$

in which n is the order parameter of the Butterworth filter. Images were reconstructed using a cutoff frequency less than or equal to the Nyquist frequency.

We used the high-resolution prototype PET scanner developed at M. D. Anderson Cancer Center (MDAPET), University of Texas, to scan the three phantoms. This camera, which is based on the photomultiplier-quadrant-sharing (PQS) technique [12], has 14 detector rings covering an axial field-of-view of 3.85 cm. The camera's detection system is divided into eight independent, movable modules. Each module can be translated radially to alter the size of the patient opening, optimizing the detection sensitivity for different body cross sections. Each ring consists of 448 individual bismuth germanate (BGO) crystals having an in-plane and axial crystal pitch of 2.66 and 2.80 mm, respectively. Also, the gantry can be rotated during data acquisition in 0.10° steps up to 45° . The gantry rotation was used to fill the gaps in the sinograms. The standard procedure for this camera is to acquire data in 1° steps. The gantry design, detector parameters, PQS design and electronics of the MDAPET camera have been described previously [12]–[16].

The MDAPET scanner has several modes of operation. The data presented here were acquired while the camera was in brain mode. In this mode, the camera has a ring diameter (the distance between two facing detector modules) of 44 cm and intrinsic transaxial image resolution of 2.8 mm. Fig. 1 shows the MDAPET camera when it is in the brain mode. In this mode, the eight modules form a closely packed octagon and the camera has

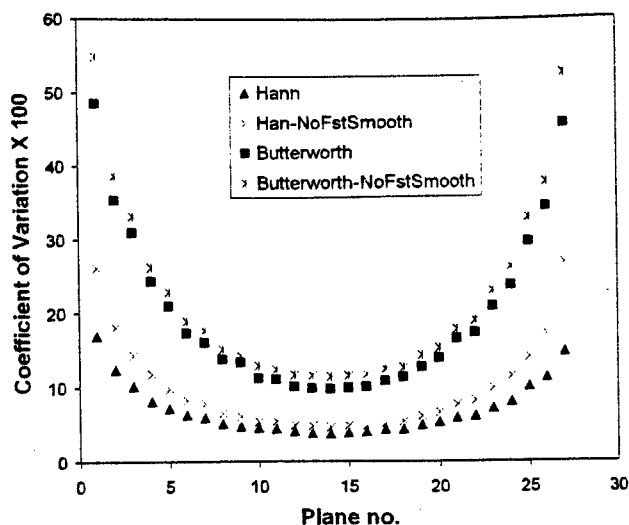


Fig. 2. Coefficient of variation, for the Butterworth and Hann smoothing functions, plotted as a function of the image slice number. For each filter two cases for the reconstruction of the first-pass-images are shown: with and without smoothing function. The cutoff frequency was 0.6 of the Nyquist frequency. The order parameter for the Butterworth filter was 3.

a patient opening of 32 cm. The imaging performance characteristics of the prototype camera have been described previously [17], [18].

The MDAPET camera has no septa and all data were acquired in 3-D mode, which produced 196 sinograms. In the present study, each sinogram had 231 radial bins and 180 azimuthal views and no axial or transaxial compression was performed on projection data. The camera allows simultaneous imaging of 27 transaxial slices with 1.38 mm thickness. Each reconstructed image had 231×231 pixels.

Prior to image reconstruction, the 3-D projection data were corrected. These corrections included random coincidence, attenuation, geometric and detector-pair efficiency corrections [19]. The random coincidence correction was accomplished by subtracting the measured accidental sinograms from the measured total sinograms. Attenuation correction was calculated assuming a uniform attenuation. No scatter correction was performed.

III. RESULTS

A. Uniform Phantom Study

The coefficient of variation (CV), which is a measure of the noise level in the reconstructed image, was calculated for the uniform phantom data. We acquired about 100 million true coincidence events for this study. The scanned cylindrical uniform phantom had an inner diameter of 17.1 cm and axial length of 6 cm. The CV was measured by computing σ/μ , in which σ and μ are, respectively, the standard deviation and mean of the pixel values over some region of interest. The circular region of interest had a radius of 60 pixels (about 8.3 cm).

In Fig. 2, the coefficient of variation is shown as it was calculated for each of the 27 image slices for the Butterworth and Hann apodization functions using a cutoff frequency of 0.6. In this work, the cutoff frequency value is always expressed relative to the Nyquist frequency (about 3.61 cycles/cm). The ord-

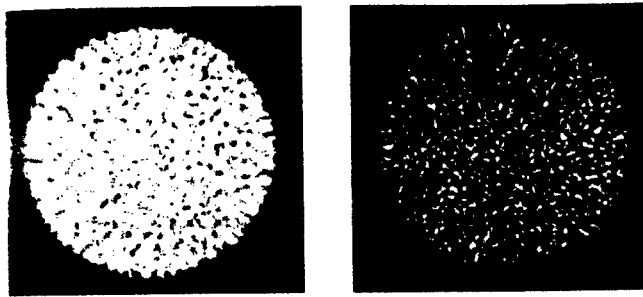


Fig. 3. Image of a central slice of the uniform phantom reconstructed with the 3-D RP algorithm when the Butterworth smoothing function was used with a cutoff frequency of (left) 0.4 and (right) 0.8 of the Nyquist frequency. The order parameter was 3.

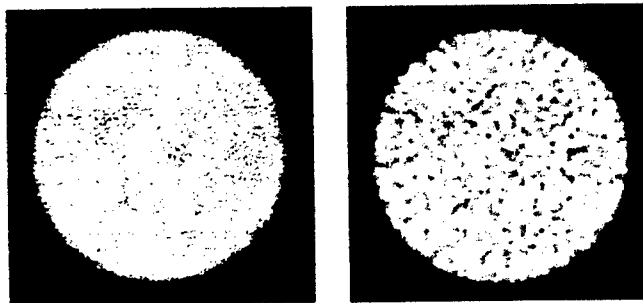


Fig. 4. The image of the same slice shown in Fig. 3 when it was reconstructed with the 3-D RP algorithm using the Hann smoothing function and a cutoff frequency of (left) 0.4 and (right) 0.8 of the Nyquist frequency.

parameter for the Butterworth function was 3. For each window function, results are shown for two cases depending on whether the first-pass images were reconstructed with the same filter that was used for the second pass or without a smoothing function (using ramp filter). The noise shows the expected pattern, decreasing toward the center of the axial field-of-view, where the sensitivity is greatest [6], [20]. The variation in coefficient of variations among the different planes for the Hann were smaller than those obtained for the Butterworth window, especially in the image planes near the edge of the axial field of view. As can be seen, the use of the apodization function in the reconstruction of the initial 2-D first-pass images mainly affected the end slices of the final images and the effect was more pronounced for the Hann filter. Results for the Hamming smoothing function (not shown) were very similar to those for the Hann window function.

Reconstructed images of a central slice of the uniform phantom created using the Butterworth window function with an order parameter of $n = 3$ and cutoff frequencies of 0.4 and 0.8 are shown in Fig. 3. A similar image created using the Hann window function is shown in Fig. 4.

The coefficient of variation for a central slice (slice number 3) versus the filter cutoff frequency for the Butterworth, Hamming and Hann smoothing functions are shown in Fig. 5. For comparison, the CV for the Colsher (ramp) filter is also shown. As expected, the CV results for the Hann and Hamming filter were very similar, while the CV values for the Butterworth filter were between those of the ramp and Hamming filters.

To investigate the sensitivity of the Butterworth smoothing function to the order parameter (n), we calculated the CV for several values of n and the results are shown in Fig. 6 for a

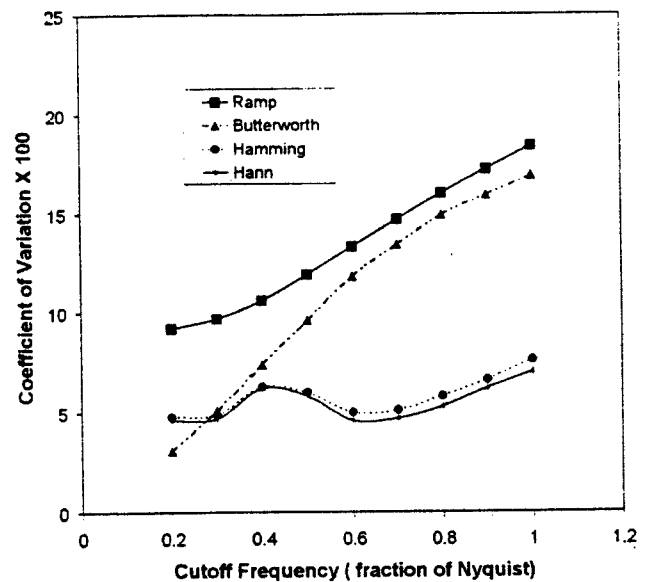


Fig. 5. Coefficient of variation for a central slice as a function of the cutoff frequency (using the 3-D RP algorithm) for several different filters. The lines simply connect the points. The order parameter for the Butterworth filter was 3.

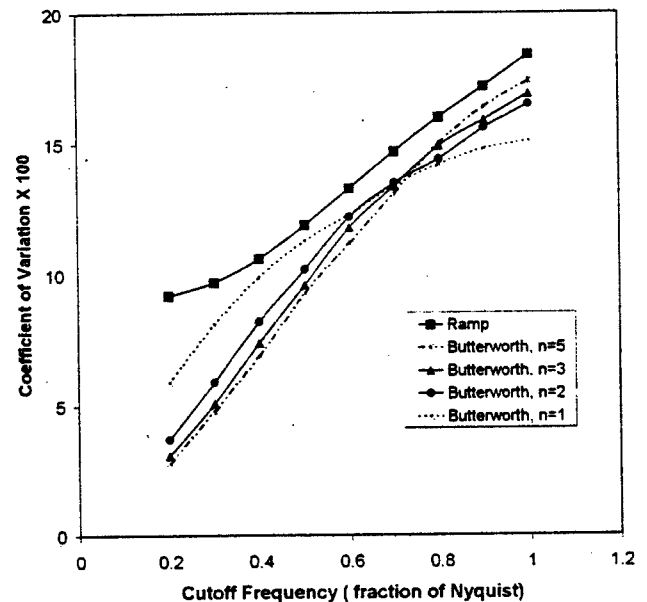


Fig. 6. Coefficient of variation for a central slice as a function of the cutoff frequency for several different order parameters of the Butterworth window. The lines simply connect the points.

central slice. For comparison, results for the ramp filter are also shown. For our high statistics data and for the range of n values that we studied results were very similar especially for the cutoff frequencies in the range of 0.6 to 0.8 of the Nyquist frequency.

B. Hot Lesion Study

The contrast recovery data were obtained from the scanning of the cylindrical phantom containing four small lesion phantoms. The cylindrical phantom, which had a diameter of 17.1 cm, was filled with a mixture of water and activity to form a warm background. The diameters of the four embedded

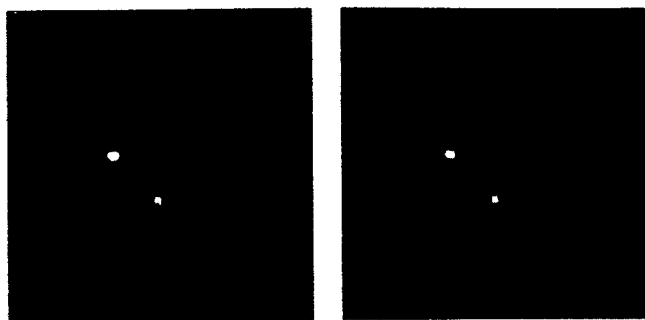


Fig. 7. Reconstructed image slice of the cylindrical phantom containing four small hot lesions using (left) Hann window with a cutoff frequency of 0.6 and (right) Butterworth window with a cutoff frequency of 0.4.

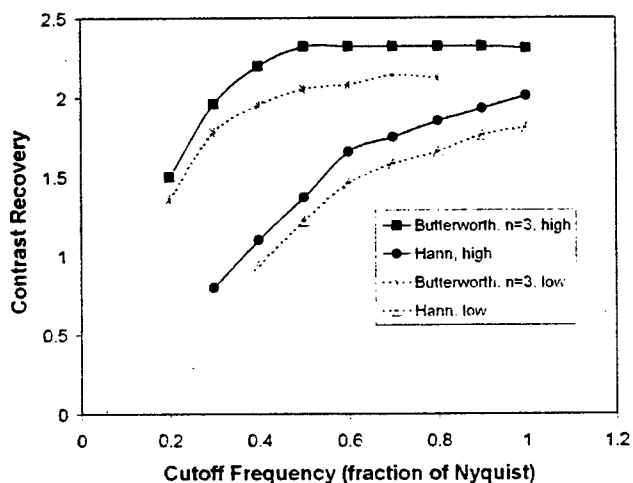


Fig. 8. Contrast recovery for the 6 mm lesion in a central slice using the Butterworth and Hann apodization functions as a function of the cutoff frequency for both high and low statistics acquisitions. The lines simply connect the points.

lesion phantoms were 3, 4, 5, and 6 mm and all have the same standard uptake value (SUV). The lesions were placed at the center of the axial field-of-view. For the data presented here, the ratio of the activity concentration of the lesions to the background was approximately 6:1. We acquired two sets of data: a high counts acquisition with about 125 000 000 true coincidence events and a low counts acquisition with about 6 000 000 true coincidence events.

Reconstructed image slices of the four hot lesions, for high counts acquisition, using the Hann apodization function with a cutoff frequency of 0.6 and the Butterworth apodization function with a cutoff frequency of 0.4 are shown in Fig. 7. All four lesions were clearly observable for both cases; however, the image constructed using the Butterworth filter showed better contrast.

The contrast recovery for the hot lesions surrounded by the warm background was defined as $(S-B)/B$, in which S and B are the average counts in a region of interest of the hot lesion and background, respectively. The extracted contrast as a function of the cutoff frequency for the 6-mm lesion is shown in Fig. 8 for both high and low counts acquisitions. The circular region of interest had a radius of 2 pixels (about 2.8 mm) for the lesion and 10 pixels for the background. The CR results for the Hamming filter, which were similar to those for the Hann filter, are not

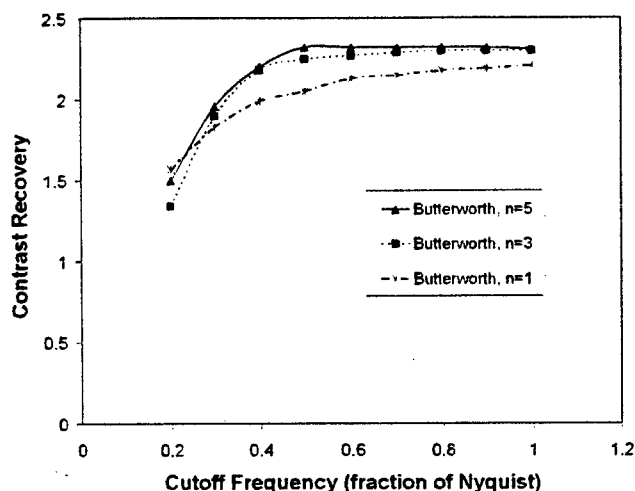


Fig. 9. Contrast recovery for the 6 mm lesion in a central slice using the Butterworth smoothing function for several values of the order parameter (n). For comparison results for Colsher (ramp) filter is also shown. The lines simply connect the points.

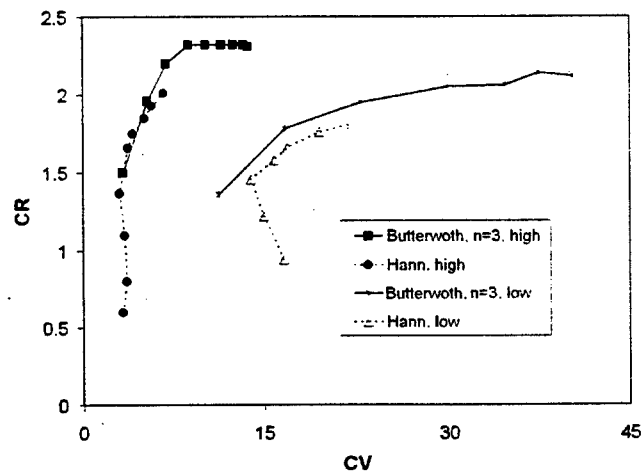


Fig. 10. The contrast-noise tradeoff for the 6 mm lesion using the Butterworth and Hann smoothing functions. Results are shown for both high and low counts acquisitions. The lines simply connect the points.

shown. For the Butterworth filter, for cutoff frequencies greater than 0.6 the CR was almost flat for high counts data. The CR was not extracted for the other lesions since their smaller sizes made defining the region of interest in a consistent way more difficult, especially for the 3 and 4 mm lesions and we found the results to be less reliable.

To investigate the sensitivity of the Butterworth smoothing function to the order parameter, the CR was extracted for several values of n and results are plotted in Fig. 9 for a central slice. For comparison results for the ramp function are also shown. Fig. 10 shows the contrast-noise tradeoff for both high statistics and low statistics acquisitions where the CR values were extracted for the 6 mm lesion and the CV values obtained from the warm background data. In Fig. 11, the contrast-noise tradeoff curve is shown for the Butterworth smoothing function for several values of the order parameter (for high statistics acquisition).

A horizontal profile running along the middle of the image slice in Fig. 7 (going through the middle of the 6 and 4 mm le

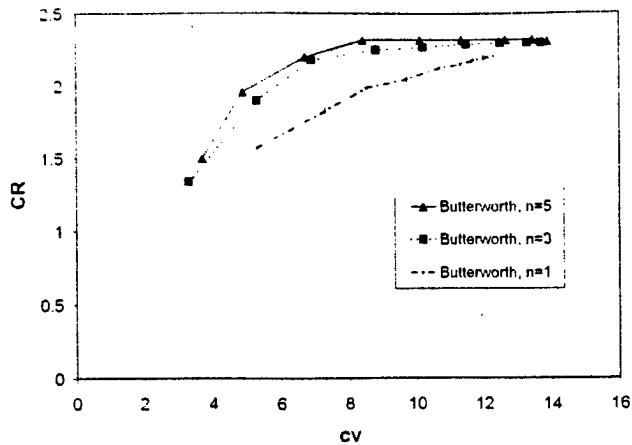


Fig. 11. The contrast-noise tradeoff for the 6 mm lesion using the Butterworth window for several values of the order parameter (high statistics acquisition data). The lines simply connect the points.

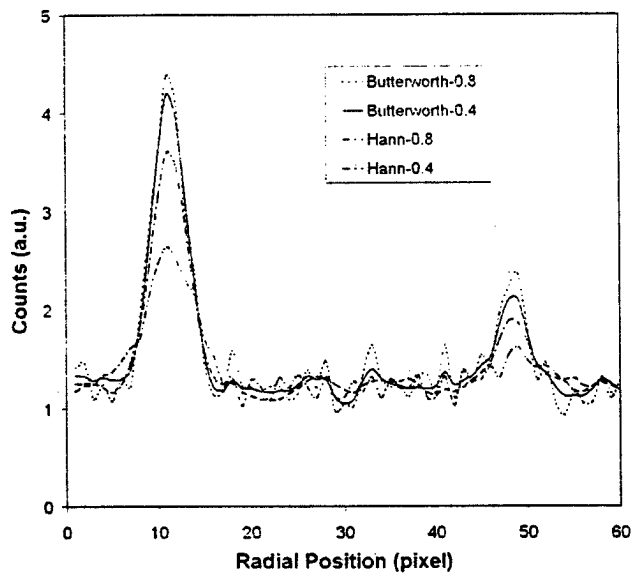


Fig. 12. A horizontal profile running along the middle of the central image slice shown in Fig. 7. The peaks corresponding to the 6 and 4 mm lesions are observable. Images were reconstructed with the Butterworth and Hann smoothing functions and using cutoff frequencies of 0.4 and 0.8 of the Nyquist frequency (high statistics acquisition data).

sions) is plotted in Fig. 12. The profile data for each image were normalized accordingly to the average counts in the background in each case. The results for two different cutoff frequencies (0.4 and 0.8 of Nyquist) for both the Butterworth and Hann apodization functions are shown. These data show that the peak to background ratio for the Butterworth filter is higher than for the Hann filter (consistent with the contrast recovery results shown in Fig. 8) and also that the full width at half maximum (FWHM) is smaller for the Butterworth filter. For example, at the cutoff frequency of 0.8, the FWHM was 4.5 and 5.2 pixels, respectively, when the Butterworth and the Hann smoothing function were used.

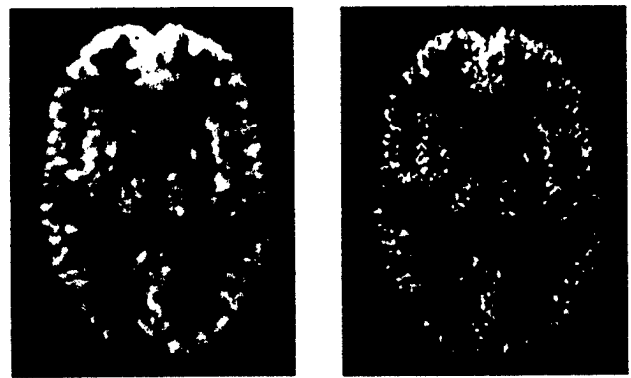


Fig. 13. An image slice of the Hoffman brain phantom reconstructed with the 3-D RP algorithm using the Butterworth window and a cutoff frequency of (left) 0.4 and (right) 0.8 of the Nyquist frequency.

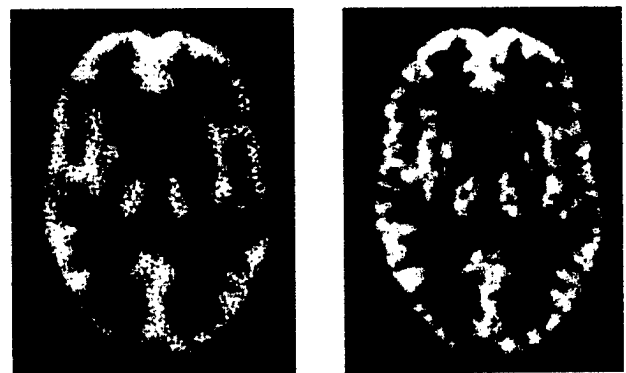


Fig. 14. The same slice of the Hoffman brain phantom shown in Fig. 13 when reconstructed with the 3-D RP algorithm using the Hann window and a cutoff frequency of (left) 0.4 and (right) 0.8 of Nyquist frequency.

C. Hoffman Brain Phantom Study

We used the 3-D Hoffman brain phantom to evaluate, via visual inspection, how accurately the reconstruction method could reproduce the structure of the brain phantom and how the filter apodization affects the image quality. We acquired two sets of data: a high statistics set with approximately 200 000 000 true coincidence counts and a low statistics set with about 24 000 000 true coincidence events.

In Fig. 13, a central image slice for the high statistics acquisition reconstructed with the 3-D RP algorithm using the Butterworth smoothing function is shown for two different values of the cutoff frequency. In Fig. 14, the same slice is shown after projection data were reconstructed with the Hann smoothing function for the same cutoff frequency values. Visually, images reconstructed with the Hann filter with a cutoff frequency of 0.8 were relatively similar to the one reconstructed with the Butterworth filter with a cutoff frequency of 0.4; however, the Butterworth results showed slightly better contrast. Results for the Hamming filter (not shown) were very close to those for the Hann filter.

In Fig. 15, the best result for the Butterworth filter is compared with the picture of the corresponding phantom's slice, which shows how accurately the phantom's structures were reproduced. In Figs. 16 and 17, the same slice image is shown for the low counts data when projected data were reconstructed with the Butterworth and Hann smoothing functions, respectively.



Fig. 15. The same slice of the Hoffman brain phantom shown in Fig. 13 when reconstructed with the Butterworth function and a cutoff frequency of 0.5 (left) compared with the phantom's pattern (right).

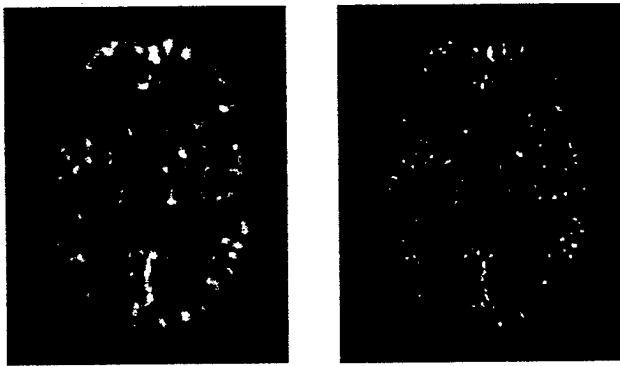


Fig. 16. An image of the Hoffman brain phantom reconstructed from the low statistics acquisition using the Butterworth smoothing function with a cutoff frequency of (left) 0.3 and (right) 0.6.

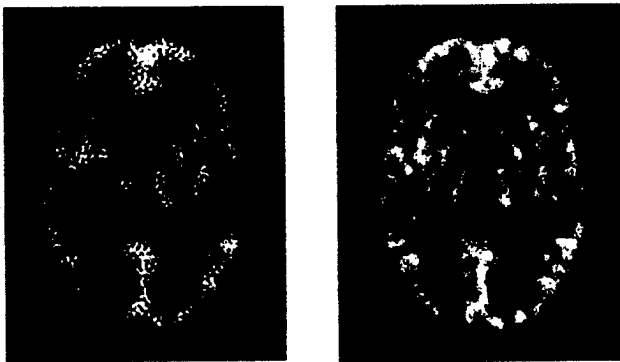


Fig. 17. The same slice of the Hoffman brain phantom shown in the previous figure when reconstructed with the Hann smoothing function and a cutoff frequency of (left) 0.3 and (right) 0.6.

IV. CONCLUSION

We evaluated the effect of filter apodization for the 3-D PET imaging using the 3-D RP algorithm. We investigated three low-pass apodization functions: Butterworth, Hann, and Hamming. For this work, we mainly studied the central slices which are less affected by the incompleteness of the 3-D data. For these slices the Butterworth filter offered a slightly better contrast noise performance over the Hann and Hamming filters. The Hann and Hamming windows showed similar behaviors. The choice of the cutoff frequency depended on the

data statistics and we found that for our high statistics data the best images were obtained with a cutoff frequency in the range of 0.6 to 0.8 for the Hann and in the range of 0.4 to 0.6 for the Butterworth windows. For the lower counts data using lower cutoff frequencies were more appropriate. We also found that the use of smoothing function in the reconstruction of the initial-2-D first-pass images mainly affected the edge slices.

REFERENCES

- [1] L. A. Shepp and B. F. Logan, "The Fourier reconstruction of a head section," *IEEE Trans. Nucl. Sci.*, vol. NS-21, pp. 21-43, Feb. 1974.
- [2] D. R. Gilland, B. M. W. Tsui, W. H. McCartney, J. R. Perry, and J. Berg, "Determination of the optimum filter function for SPECT imaging," *J. Nucl. Med.*, vol. 29, pp. 643-650, 1988.
- [3] J. S. Beis, A. Celler, and J. S. Barney, "An automatic method to determine cutoff frequency based on image power spectrum," *IEEE Trans. Nucl. Sci.*, vol. 42, pp. 2250-2254, Dec. 1995.
- [4] T. H. Farquhar, A. Chatziioannou, G. Chinn, M. Dahlbom, and E. J. Hoffman, "An investigation of filter choice for filtered back-projection reconstruction in PET," *IEEE Trans. Nucl. Sci.*, vol. 45, pp. 1133-1137, June 1998.
- [5] P. E. Kinahan and J. G. Rogers, "Analytic 3-D image reconstruction using all detected events," *IEEE Trans. Nucl. Sci.*, vol. 36, pp. 964-968, Feb. 1989.
- [6] S. R. Cherry, M. Dahlbom, and E. J. Hoffman, "Evaluation of a 3D reconstruction algorithm for multi-slice PET scanners," *Phys. Med. Biol.*, vol. 37, pp. 779-790, 1992.
- [7] E. J. Hoffman, P. D. Cutler, W. M. Digby, and J. C. Mazziotta, "3-D phantom to simulate cerebral blood flow and metabolic images for PET," *IEEE Trans. Nucl. Sci.*, vol. 37, pp. 616-620, Apr. 1990.
- [8] J. G. Colsher, "Fully three-dimensional positron emission tomography," *Phys. Med. Biol.*, vol. 25, pp. 103-115, 1980.
- [9] C. W. Stearns, C. R. Crawford, and H. Hu, "Oversampled filters for quantitative volumetric PET reconstruction," *Phys. Med. Biol.*, vol. 39, pp. 381-388, 1994.
- [10] D. A. Chesler and S. J. Riederer, "Ripple suppression during reconstruction in transverse tomography," *Phys. Med. Biol.*, vol. 20, pp. 632-636, 1995.
- [11] R. H. Huesman, G. T. Gullberg, W. L. Greenberg, and T. F. Budinger, *RECLBL Library Users Manual: Donner Algorithms for Reconstruction Tomography*. Berkeley, CA: Lawrence Berkeley Lab., Univ. California, 1977, pp. 49-58.
- [12] W.-H. Wong, "A positron camera detector design with cross-coupled scintillators and quadrant sharing photomultipliers," *IEEE Trans. Nucl. Sci.*, vol. 40, pp. 962-966, Aug. 1993.
- [13] W.-H. Wong, J. Uribe, W. Lu, and K. Hicks, "Design of a variable field prototype PET camera," *IEEE Trans. Nucl. Sci.*, vol. 43, pp. 1915-1920, June 1996.
- [14] W.-H. Wong, J. Uribe, K. Hicks, and M. Zambelli, "A 2-dimensional detector decoding study on BGO arrays with quadrant sharing photomultipliers," *IEEE Trans. Nucl. Sci.*, vol. 41, pp. 1453-1457, June 1994.
- [15] W.-H. Wong, G. Hu, N. Zhang, J. Uribe, J. Wang, H. Li, H. Baghaei, and S. Yokoyama, "Front end electronics for a variable field PET camera using the PMT-quadrant-sharing detector array design," *IEEE Trans. Nucl. Sci.*, vol. 44, pp. 1266-1270, June 1997.
- [16] R. H. Li, W.-H. Wong, N. Zhang, J. Wang, J. Uribe, H. Baghaei, and S. Yokoyama, "Prototype electronics for a variable field of view PET camera using the PMT-quadrant-sharing detector array," *IEEE Trans. Nucl. Sci.*, vol. 46, pp. 546-550, June 1999.
- [17] J. Uribe, H. Baghaei, H. Li, S. Yokoyama, N. Zhang, J. Wang, F. Dobbs, and W.-H. Wong, "Basic imaging characteristics of a variable field of view PET camera using quadrant sharing detector design," *IEEE Trans. Nucl. Sci.*, vol. 46, pp. 491-497, June 1999.
- [18] H. Baghaei, W.-H. Wong, J. Uribe, H. Li, N. Zhang, and Y. Wang, "Breast cancer studies with a variable field of view PET camera," *IEEE Trans. Nucl. Sci.*, vol. 47, pp. 1080-1084, June 2000.
- [19] H. Baghaei, W.-H. Wong, J. Uribe, H. Li, N. Zhang, and J. Wang, "The correction factors for a high resolution variable field of view PET camera," *J. Nucl. Med.*, vol. 40, p. 279P, May 1999.
- [20] S. Pajevic, M. E. Daube-Witherspoon, S. L. Bacharach, and R. E. Carson, "Noise characteristics of 3-D and 2-D PET images," *IEEE Trans. Med. Imaging*, vol. 17, pp. 9-23, Feb. 1998.

Effects of Attenuation Correction and 3D-Reconstruction Algorithms on Brain Lesion Detectability

Hossain Baghaei, *Member, IEEE*, Jorge Uribe, *Member, IEEE*, Hongdi Li, *Member, IEEE*, Yu Wang, Yaqiang Liu, Tao Xing, Rocio Farrell, and Wai-Hoi Wong, *Member, IEEE*

Abstract— We compared lesion detectability in brain phantom images obtained with a high resolution positron emission tomography (PET) camera in 4 ways: images were reconstructed with the three-dimensional reprojection algorithm (3DRP) with and without attenuation correction, and with the three-dimensional ordered subsets expectation maximization (3D-OSEM) algorithm with and without post-filtering. For this purpose, three small lesion phantoms with diameters of 3, 5, and 8.6 mm were embedded into the 3D Hoffman brain phantom. The approximate ratio of the activity concentration in the lesions to the surrounding brain gray matter ranged from 1.5 to 10. To scan the phantoms, we used the high-resolution MDA PET, a prototype 3D-PET camera. This camera is a multi-ring scanner with an intrinsic transaxial resolution of 2.8 mm. To minimize the number of imaging sessions, we took data for the hot lesion phantoms and the normal warm Hoffman brain phantom separately. Then, before performing any data corrections, we selectively combined two sets of the sinogram data to generate the sinogram data for the desired standard uptake values. When the lesions data were taken, the lesions were placed inside the Hoffman brain phantom filled only with water to provide the attenuation and scatter effects. We observed a slight improvement in lesion detectability for the 5 mm lesion located near the center of the image for attenuation corrected over un-corrected sinograms. In addition, images reconstructed from attenuation corrected sinograms visually looked better and the Hoffman brain phantom's structures were better observable. Images reconstructed with the 3D-OSEM algorithm followed by post-filtering showed a slight improvement in lesion detection over images reconstructed with the 3DRP algorithm.

I. INTRODUCTION

MANY researchers have investigated different techniques for improving the quality of reconstructed images in PET studies. Some of these investigators have studied the effects of attenuation correction on the quality of images. The

Manuscript received November 18, 2002. This work was supported in part by the NIH Grant RO1 CA58980, NIH Grant RO1 CA61880, NIH Grant RO1 CA76246, NIH Grant RO1 EB00217, NIH Grant RO1 EB001038, US Army Breast Cancer Grant, Texas Higher Education Grant, John S. Dunn Foundation Research Grant, and by the Cobb Foundation for Cancer Research.

Hossain Baghaei, Jorge Uribe, Hongdi Li, Yu Wang, Mehmet Aykac, Yaqiang Liu, Tao Xing and Wai-Hoi Wong are with the University of Texas M. D. Anderson Cancer Center, Houston, TX 77030 USA (H. Baghaei's telephone: 713-794-5270, e-mail: hbaghaei@di.mdacc.tmc.edu).

main advantages of attenuation correction are an improved anatomic orientation, improved image quality and increased image contrast and, in addition, images may be evaluated semi-quantitatively. However, the usefulness of attenuation correction for lesion detection is controversial [1]-[4]. Some researchers have evaluated iterative methods as an alternative to filtered back projection for reconstruction of PET images. It has been demonstrated that iterative reconstruction algorithms could improve the image quality over filtered back projection techniques [5]-[7].

The purpose of the work presented here was to compare lesion detectability (a) on images reconstructed with and without attenuation correction, and (b) on images reconstructed with filtered back projection versus those reconstructed with an iterative reconstruction algorithm. Data were obtained from scan of three small lesion phantoms embedded into a brain phantom. The attenuation correction factors were calculated assuming a uniform attenuation. The calculated attenuation, in contrast to measured attenuation, does not increase noise within reconstructed images. For image reconstruction we used the 3D ordered subsets expectation maximization (3D-OSEM) [7] and the 3D-reprojection (3DRP) [8] algorithms.

II. MATERIALS AND METHODS

For this study, three small lesion phantoms were embedded into the 3D Hoffman brain phantom [9]. The inner diameters of the embedded lesion phantoms were 3 mm, 5 mm, and 8.6 mm, and all have the same standard uptake values (SUVs). The approximate ratio of the activity concentration in the lesions to the background brain gray matter regions ranged from 1.5 to 10. The lesions were placed into the brain phantom white matter regions. The 5 mm lesion was placed near the center of the brain phantom and the other two lesions were placed near the peripheral of the brain phantom.

To scan the phantoms, we used the high-resolution MDA PET, a prototype PET camera. This camera is a multi-ring scanner with an intrinsic transaxial resolution of 2.8 mm. Each ring contains 448 bismuth germanate (BGO) crystals having an in-plane and axial crystal pitch of 2.66 and 2.80 mm, respectively. The detectors are grouped into blocks of 7X7 crystals. The camera detection system is divided into eight independent, movable modules. Each module can be

translated radially to alter the size of the patient opening, optimizing the detection sensitivity for different body cross-sections. Also the gantry can be rotated during data acquisition in 0.10° steps up to 45° . The gantry rotation is necessary to fill the gaps in the sinograms caused by the empty space between modules. The standard procedure for this camera is to acquire data in 1° steps. The detector module design, which is based on the quadrant-sharing technique, and electronics of the MDAPET camera have been described previously [10]-[14]. The imaging performance characteristics of the camera have also been discussed previously [15], [16].

The MDAPET camera has several modes of operation. We took data in the brain mode. In this mode, the camera has a ring diameter (the distance between two facing detector modules) of 44 cm and patient opening of 32 cm. The camera has 14 detector rings covering an axial field-of-view (FOV) of 3.85 cm. To compensate for the lower sensitivity of the MDAPET camera, that results from its small axial FOV, the 3D Hoffman brain phantom was scanned longer than in the typical clinical situation and at relatively higher activity and repeated several times. Then, the data were summed to obtain the equivalent number of true coincidence events as that a clinical version of the camera would have collected following a typical injected dose of 10 mCi ^{18}F -fluorodeoxyglucose (FDG) in a 20 minutes scan. All measurements were done in 3D mode (no-septa).

To minimize the number of imaging sessions, we acquired two separate data sets. We first acquired data for the hot lesion phantoms and then acquired data for the warm (normal) Hoffman brain phantom. When the lesions data were acquired, the lesions were placed inside the Hoffman brain phantom filled only with water (cold background) to provide the attenuation and scatter effects. Before applying different corrections, we selectively combined the two sets of sinogram data were to generate the sinogram data for the desired SUVs. This combination method greatly reduced the number of required measurements for different lesion uptake and also eliminated the effect of the 'cold' walls of the lesion phantoms that exists when hot lesions and the warm background are measured simultaneously [15], [16]. However, this technique requires the phantom to be positioned precisely, the concentration ratio of the tissue and background be known, the accidental coincidence be known and the effect of the dead time also becomes more important. This sinogram summing method allows all the different SUVs data for lesions to be taken in one experimental period by collecting the different SUVs data as the activity decays.

Prior to image reconstruction, the projection data were corrected. These corrections included random coincidence subtraction, geometric and detector-pair efficiency corrections [17]. When attenuation correction was performed, it was calculated by estimating the attenuation length from the shape of the Hoffman brain phantom and assuming a uniform attenuation coefficient. No scatter correction was performed.

All data were acquired in 3D mode with an axial acceptance of 13 rings, which produced 196 sinograms. In the present study, each sinogram had 239 radial bins and 180 azimuthal views and no axial or transaxial compression was performed on projection data. The radial sampling was 1.385 mm. The camera allows simultaneous imaging of 27 transaxial slices with 1.4-mm thickness. Each reconstructed image had 239 X 239 pixels.

III. RESULTS

A. Attenuation Study

Figure 1 shows two reconstructed slice images of the normal (without lesions) Hoffman brain phantom as they are compared to the phantom's pattern, which indicates how well the phantom structures are reproduced. These results, which are for a high-statistics acquisition (200 million true coincidence events in all sinograms), were reconstructed with the 3DRP algorithm. Attenuation correction factors were calculated and were applied to the sinogram data.

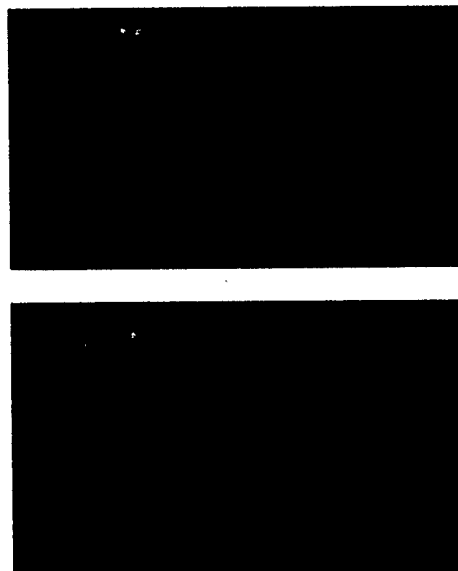


Fig. 1. Two image slices of the Hoffman brain phantom (without any lesions) reconstructed with the 3DRP algorithm compared to the true phantom's pattern on the right side.

Figure 2 shows two transaxial slices of the Hoffman brain phantom with three embedded lesion phantoms when the ratio of the activity concentration in the lesions to the surrounding background tissue (gray matter) was about 5. Figure 3 show two image slices when lesion-to-surrounding tissue density ratio was 2.2. The top-row images were reconstructed from attenuation-corrected sinograms and the bottom-row images were obtained from the non-attenuation corrected sinograms.

In both Figs. 2 and 3 the phantom's structures are better observable when data are corrected for attenuation effects. The 5 mm lesion which is located near the center of the brain phantom can be clearly seen in both Figs. 2 and 3 when

attenuation correction is applied. However, the 5 mm lesion can barely be observed in Fig. 3 for un-corrected data. The 8.6 mm lesion is located near the top of the image and 3 mm lesion located on the left side of the image. The 3 mm and 8.6 mm lesion can only be seen in Fig. 2. In order to improve detectability of the lesion images, the 8.6 mm lesion phantom was placed such that its brightness did not peak in the same slices as for the other two; this made the 8.6 mm lesion less visible than the 5 mm lesion in these particular slices. There were not any observable differences for the 3 and 8.6 mm lesions between images obtained with and without attenuation correction.

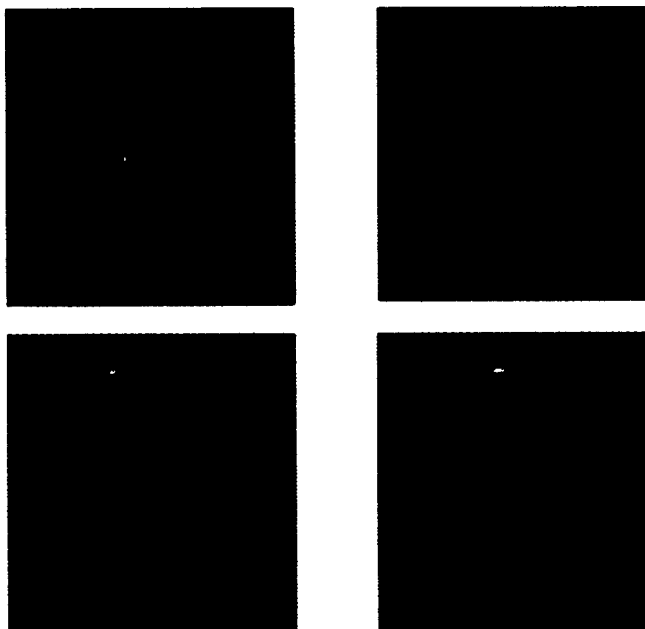


Fig. 2. Two image slices of the Hoffman brain phantom with three embedded lesions reconstructed with 3DRP algorithm: (top row) sinogram data were attenuation corrected; (bottom row) data were not attenuation corrected. The ratio of the activity density of lesions to the surrounding tissue (gray matter) was 5.

B. Reconstruction Algorithm Study

For comparison of the 3DRP and 3D-OSEM reconstruction algorithms, the projection data were corrected for attenuation. Fig. 4 shows two reconstructed image slices with three lesions when the ratio of the activity concentration in the lesions to the background was about 2.2. Top row images were reconstructed with the 3DRP algorithm, the middle row images were reconstructed with 3D-OSEM after the 40th sub-iteration and the ones in the bottom row reconstructed by 3D-OSEM followed by post-filtering after the 40th sub-iteration with a Metz filter. The Metz power parameter was set to 1 and the full width at maximum was 4 [19] for all calculations presented in this work. The activity ratio of 2.2 was the lowest activity at which the 5 mm lesion was clearly observable.

Fig. 5 shows two image slices with the 3 mm and 5 mm lesions reconstructed with 3DRP algorithm and 3D-OSEM

algorithm followed by post-filtering when lesion-to-surrounding tissue activity density ratio was 5.8. The activity ratio of 5.4 was the lowest activity at which the 3 mm lesion was clearly observable.

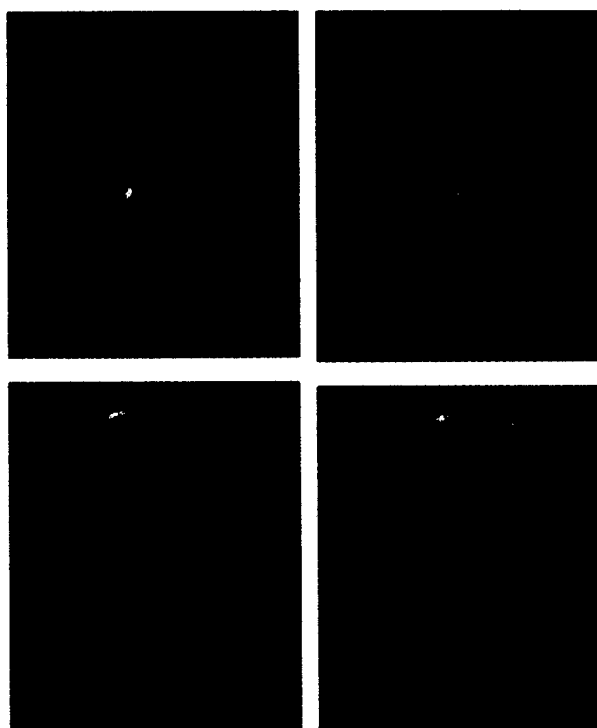


Fig. 3. Two image slices of the Hoffman brain phantom with three embedded lesions reconstructed with 3DRP algorithm: (top row) sinogram data were attenuation corrected; (bottom row) data were not attenuation corrected. The ratio of the activity density of the lesions to surrounding tissue was 2.2.

Visual comparison of the reconstructed images did not show any significant differences between the two reconstruction methods. Figure 6 shows a horizontal profile running through the middle of the 5 mm lesion image at the activity ratio of 5.8. Figure 7 shows a horizontal profile running through the middle of the 5 mm lesion image at the activity ratio of 2.2. In both Figs. 6 and 7 the 3D-OSEM results were post-filtered with the Metz filter after the 40th iteration. The profile data for each image was normalized according to the average count in the background for each case. Figs. 6 and 7 demonstrated that the OSEM algorithm has a slight advantage over the 3DRP algorithm.

IV. CONCLUSIONS

Images reconstructed with the 3DRP algorithm from attenuation-corrected data visually "looked" better than the images reconstructed from the non-attenuation corrected data: the structures of the Hoffman brain phantom were better observable for attenuation-corrected data. In terms of lesion detectability, for the 3 mm and 8.6 mm lesions, which were located near the peripheral of the Hoffman brain phantom, by visually inspecting images, we did not observe any

significant differences between the attenuation corrected and un-corrected methods. For the 5 mm lesion placed near the center of the images, attenuation correction produced a slightly better image (higher contrast) than the un-corrected.

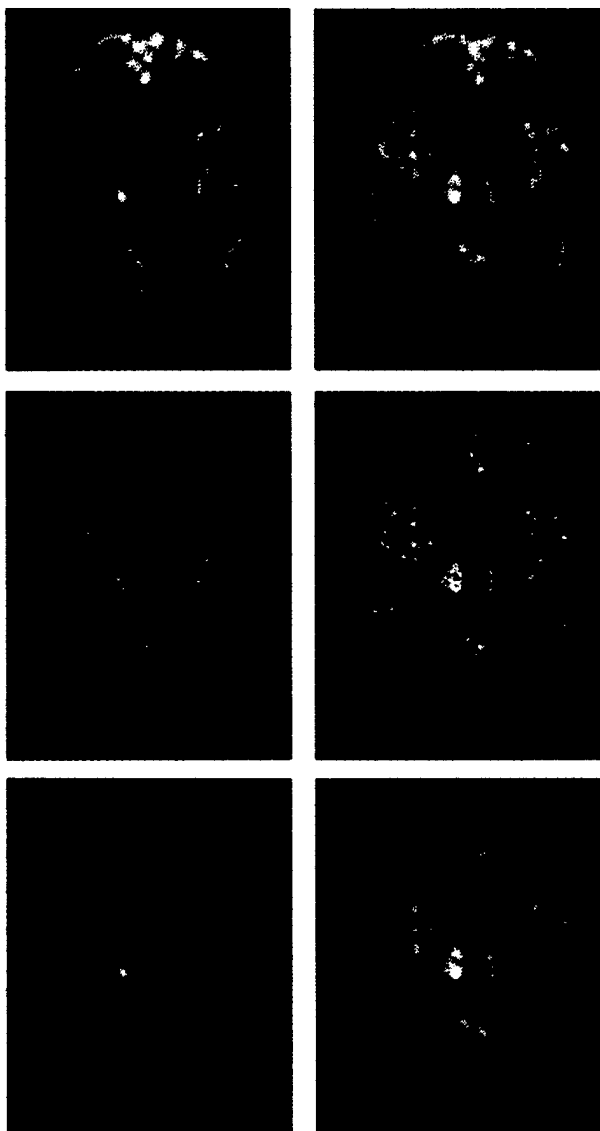


Fig. 4. Two images slices of the Hoffman brain phantom with 3 lesion phantoms: (top) reconstructed with the 3DRP algorithm, (middle) reconstructed with the 3D OSEM algorithm, and (bottom) reconstructed with 3D-OSEM followed by post-filtering using a Metz filter. The ratio of the activity density of the lesions to surrounding tissue was 2.2.

Both the 3DRP and 3D-OSEM algorithms reasonably reproduced the detailed structures of the Hoffman brain phantom. The images reconstructed by the 3D-OSEM algorithm "looked" better if post-filtering was performed. In terms of lesion detectability, by visually inspecting the images constructed by two different reconstruction algorithms, we did not observe any significant differences between them. However, by studying the horizontal profiles running along the middle of lesions, the OSEM algorithm, followed by post-filtering, showed a slight improvement in lesion detection over images reconstructed with the 3DRP

algorithm. This slight improvement may become important when the lesion detection is marginal at the cost of higher reconstruction time.

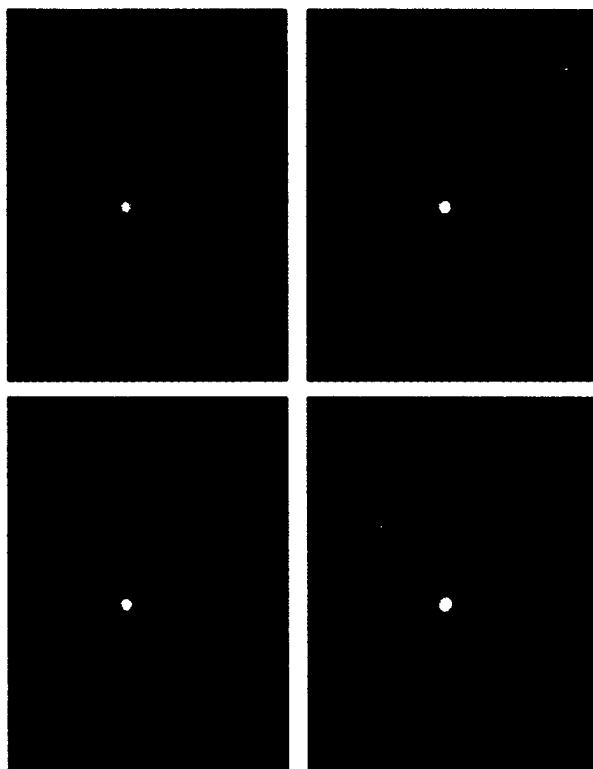


Fig. 5. Two images slices of the Hoffman brain phantom with 3 lesion phantoms: (top) reconstructed with the 3DRP algorithm, (bottom) reconstructed with 3D-OSEM followed by post-filtering. Ratio of the activity density of the lesions to surrounding tissue was 5.8.

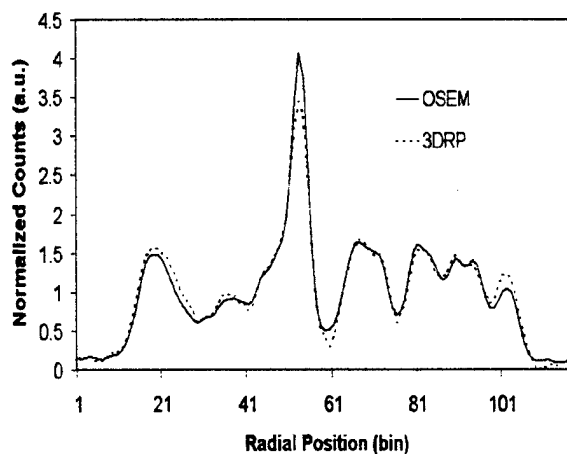


Fig. 6. A horizontal profile running through the middle of the 5 mm lesion images shown in Fig. 5 for the 3D-reprojection method and the 3D-OSEM algorithm followed by post-filtering. Ratio of the activity density of the lesions to surrounding tissue was 5.8

V. ACKNOWLEDGMENT

The authors would like to thank the personnel of the clinical PET center of the University of Texas M. D.

Anderson Cancer Center for their support in providing the FDG used for this work.

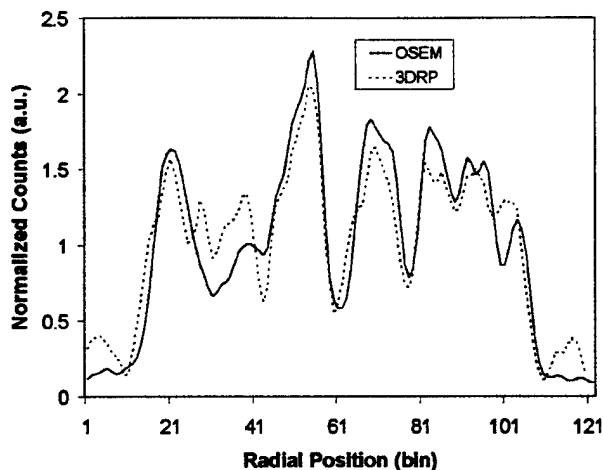


Fig. 7. A horizontal profile running through the middle of the 5 mm lesion images shown in Fig. 4 for the 3D-reprojection method and the 3D-OSEM algorithm with post-filtering. Lesion to surrounding tissue activity density ratio was 2.2.

VI. REFERENCES

- [1] C. Bleckmann, J. Dose, K. H. Bohuslavizki, R. Buchert, S. Klutmann, J. Mester, F. Janicke, and M. Clausen, "Effect of attenuation correction on lesion detectability in FDG PET of breast cancer," *J. Nucl. Med.*, vol. 40, no. 12, pp. 2021-2024, December 1999.
- [2] R. L. Wahl, "To AC or not to AC: That is the question," *J. Nucl. Med.*, vol. 40, no. 12, pp. 2025-2028, December 1999.
- [3] F. M. Bengel, S. I. Zeigler, N. Avril, W. Weber, C. Laubenbacher, and M. Schwaiger, "Whole-body positron emission tomography in clinical oncology: comparison between attenuation-corrected and uncorrected images," *Eur. J. Nucl. Med.*, vol. 24, pp. 1091-1098, 1997.
- [4] D. Delbeke, W. H. Martin, J. A. Patton, and M. P. Sandler, "Value of iterative reconstruction, attenuation correction, and image fusion in the interpretation of FDG PET images with an integrated dual-head coincidence camera and x-ray-based attenuation maps," *Radiology*, vol. 218, no. 1, pp. 163-171, Jan. 2001.
- [5] H. M. Hudson, and R. S. Larkin, "Accelerated image reconstruction using ordered subsets of projection data," *IEEE Trans. Nucl. Sci.*, vol. 13, no. 4, pp. 601-609, Dec. 1994.
- [6] A. J. Reader, D. Visvikis, K. Erlandsson, R. J. Ott, and M. A. Flower, "Intercomparison of four reconstruction techniques for positron volume imaging with rotating planar detectors," *Phys. Med. Biol.*, vol. 43, pp. 823-834, 1998.
- [7] M. Jacobson, R. Levkowitz, A. Ben-Tal, K. Thielemans, T. Spinks, D. Belluzzo, E. Pagani, V. Bettiardi, M. C. Gilardi, A. Zverovich, and G. Mitrai, "Enhanced 3D PET OSEM reconstruction using inter-update Metz filtering," *Phys. Med. Biol.*, vol. 45, pp. 2417-2439, 2000.
- [8] P. E. Kinahan, J. G. Rogers, "Analytic 3D Image Reconstruction Using all Detected Events," *IEEE Transaction on Nuclear Science*, vol. 46 pp.964-968, 1989.
- [9] E. J. Hoffman, P. D. Cutler, W. M. Digby, and J. C. Mazziotta, "3-D phantom to simulate cerebral blood flow and metabolic images for PET," *IEEE Trans. Nucl. Sci.*, vol. 37, no. 2, pp. 616-620, April 1990.
- [10] W.-H. Wong, "A positron camera detector design with cross-coupled scintillators and quadrant sharing photomultipliers," *IEEE Trans. Nucl. Sci.*, vol. 40, pp.962-966, August 1993; and *Conference Record of the 1992 IEEE Nuclear Science Symposium and Medical Imaging Conference (Orlando, FL)*, 1992.
- [11] W.-H. Wong, J. Uribe, W. Lu, and K. Hicks, "Design of a variable field prototype PET Camera," *IEEE Trans. Nucl. Sci.*, vol. 43, pp. 1915-1920, June 1996.
- [12] W.-H. Wong, J. Uribe, K. Hicks, and M. Zambelli, "A 2-dimensional detector decoding study on BGO arrays with quadrant sharing photomultipliers," *IEEE Trans. Nucl. Sci.*, vol. 41, pp. 1453-1457, June 1994.
- [13] W.-H. Wong, G. Hu, N. Zhang, J. Uribe, J. Wang, H. Li, H. Baghaei, and S. Yokoyama, "Front end electronics for a variable field PET camera using the PMT-quadrant-sharing detector array design," *IEEE Trans. Nucl. Sci.*, vol. 44, pp. 1266-1270, June 1997.
- [14] R. H. Li, W.-H. Wong, N. Zhang, J. Wang, J. Uribe, H. Baghaei, and S. Yokoyama, "Prototype electronics for a variable field of view PET camera using the PMT-quadrant-sharing detector array," *IEEE Trans. Nucl. Sci.*, vol. 46, pp. 546-550, June 1999.
- [15] J. Uribe, H. Baghaei, H. Li, S. Yokoyama, N. Zhang, J. Wang, F. Dobbs, and W.-H. Wong, "Basic imaging characteristics of a variable field of view PET camera using quadrant sharing detector design," *IEEE Trans. Nucl. Sci.*, vol. 46, pp. 491-497, June 1999.
- [16] H. Baghaei, W.-H. Wong, J. Uribe, H. Li, N. Zhang, and Y. Wang, "Breast cancer studies with a variable field of view PET camera," *IEEE Trans. Nucl. Sci.*, vol. 47, pp. 1080-1084, June 2000.
- [17] R.S. Miyaoka, S.G. Kohlmyer, T.K. Lewellen, "Hot Sphere Detection Limits for a Dual Head Coincidence Imaging System," *IEEE Trans. Nucl. Sci.*, vol. 46, pp.2185-2191, December 1999.
- [18] H. Baghaei, W.-H. Wong, J. Uribe, H. Li, N. Zhang, and J. Wang, "The correction factors for a high resolution variable field of view PET camera," *J. Nucl. Med.*, vol. 40, p.279P, May 1999.
- [19] H. Baghaei, J. Uribe, H. Li, Y. Wang, M. Aykac, Y. Liu, T. Xing, and W.-H. Wong, "An evaluation of the effect of filtering in 3-D OSEM reconstruction by using data from a high-resolution PET scanner," *IEEE Trans. Nucl. Sci.*, vol. 49, no. 5, pp. 2381-2386, October 2002.

Brain Lesion Detectability Studies with a High Resolution PET Operating in No-Septa and Partial-Septa Configurations

Hossain Baghaei, *Member, IEEE*, Wai-Hoi Wong, *Member, IEEE*, Jorge Uribe, *Member, IEEE*, Hongdi Li, *Member, IEEE*, Mehmet Aykac, Yu Wang, Yaqiang Liu, Tao Xing, and Rocio Farrell

Abstract—We investigated the effect of partial-septa configuration on the noise equivalent sensitivity and lesion detectability for a high-resolution PET camera. For this purpose we used the MDAPET camera to detect small lesions in brain images obtained from scan of the Hoffman brain phantom. Three-dimensional (3-D) positron emission tomography (PET) acquisition in comparison to two-dimensional (2-D) PET acquisition improves the sensitivity of the system at the cost of higher scatter and accidental coincidence contributions. A partial-septa system allowing 3-D acquisition may provide a better alternative to the 2-D acquisition and full 3-D acquisition. For this work, three small lesion phantoms with diameters of 3, 5, and 8.6 mm were embedded into the 3-D Hoffman brain phantom. The approximate activity concentration ratio of the lesions to the brain gray matter ranged from 1.5 to 10. Data for the hot lesion phantoms and the normal 3-D Hoffman brain phantom were taken separately. Then, the two sets of the sinogram data were selectively combined to generate the sinogram data for the desired SUVs. In the reconstructed images, we could clearly see the 8.6 mm lesion, with or without septa, at even the lowest activity ratio that we measured. The 5 mm and 3 mm lesions were observable at activity ratios of 2.2 and 5.4, respectively. We found that even though the use of septa increased the noise equivalent count rate and lowered the image noise, it did not necessarily improve lesion detectability. We also found that with partial-septa configurations the white matter regions of the brain had lower counts and the brain images visually look better; however, images taken in the no-septa configuration had slightly higher contrast.

I. INTRODUCTION

THE three-dimensional (3-D) positron emission tomography (PET) acquisition in comparison to two-dimensional (2-D) PET acquisition improves the sensitivity of the system at the cost of higher scatter and accidental coincidence. 3-D PET

Manuscript received November 18, 2002. This work was supported in part by the NIH Grant RO1 CA58980, NIH Grant RO1 CA61880, NIH Grant RO1 CA76246, NIH Grant RO1 EB00217, NIH Grant RO1 EB001038, US Army Breast Cancer Grant, Texas Higher Education Grant, John S. Dunn Foundation Research Grant, and by the Cobb Foundation for Cancer Research.

The authors are with the University of Texas M. D. Anderson Cancer Center, Houston, TX 77030 USA (H. Baghaei's telephone: 713-794-5270, e-mail: hbaghaei@di.mdacc.tmc.edu)

also has the potential to reduce data acquisition time compared to 2-D PET. Currently, commercial PET cameras operate in two extreme modes of no-septa (3-D acquisition mode) and all-septa-in (2-D acquisition mode) configurations. Several investigators have studied the effect of all-septa and no-septa configurations on lesion detectability and noise characteristics of the images and have found that 3-D acquisition mode may have advantages in imaging brain, small patients and animals and especially at low activity levels they report that it can outperform 2-D mode acquisition [1]-[4]. Recently, a hybrid PET design was proposed to acquire projection data in both 2-D and 3-D modes simultaneously by using rotating partial septa [5]. Several investigators have studied optimal septa spacing in gamma cameras for PET imaging [6], [7].

A partial-septa system, allowing 3-D acquisition, may provide a better alternative than the 2-D acquisition and full (no-septa) 3-D acquisition. In this study, intermediate septa designs were used to reduce the scatter and accidental coincidence with an acceptable sensitivity loss by using a 3-D PET camera that could operate in no-septa mode or with a partial-septa system. In our previous work, a Monte Carlo simulation was performed to evaluate possible septa designs, and for several septa configurations the noise equivalent count (NEC) rate was measured and compared [8]. In this work, we studied the effect of partial-septa on lesion detectability for brain cancer imaging.

II. MATERIALS AND METHODS

For this study, three small lesion phantoms were embedded into the 3D Hoffman brain phantom [9]. The inner diameters of the embedded lesion phantoms were 3 mm, 5 mm, and 8.6 mm, and all have the same standard uptake values (SUVs). The approximate ratio of the activity concentration in the lesions to the background brain gray matter regions ranged from 1.5 to 10. The lesions were placed into the brain phantom white matter regions. The 5 mm lesion was placed near the center of the brain phantom and the other two lesions were placed near the peripheral of the brain phantom.

To scan the phantoms, we used the high-resolution MDAPET, a prototype PET camera. This camera is a multi-ring scanner with an intrinsic transaxial resolution of 2.8 mm. Each ring contains 448 bismuth germanate (BGO) crystals having an in-plane and axial crystal pitch of 2.66 and 2.80 mm, respectively. The detectors are grouped into blocks of 7X7 crystals. The camera detection system is divided into eight independent, movable modules. Each module can be translated radially to alter the size of the patient opening, optimizing the detection sensitivity for different body cross-sections. Also the gantry can be rotated during data acquisition in 0.10° steps up to 45° . For this study the gantry was rotated during the data acquisition in 1° steps to fill the gaps in the sinograms caused by the empty space between modules. The detector module design, which is based on quadrant-sharing technique, and electronics of the PET camera were described previously [10]-[14]. The imaging performance characteristics of the camera were also discussed previously [15], [16].

MDAPET camera has 14 detector rings covering an axial field-of-view of 38.5 mm, as shown in Fig 1a, which is much smaller than a clinical camera. In order to simulate more closely the performance of a clinical size camera, the detector modules were modified axially to extend from 38.5 mm to 131 mm by placing the side shields farther apart as shown in Fig. 1b. Extensions added to each side of each detector modules were consisting of three layers of lead and aluminum as a BGO substitute to take into account for inter-crystal scattering. Each lead foil (3mm thick) was sandwiched between two 1.5 mm thick aluminum foils. Each side shield was extended from 60 mm to 85 mm to reduce the radiation coming from out of field-of-view (FOV).

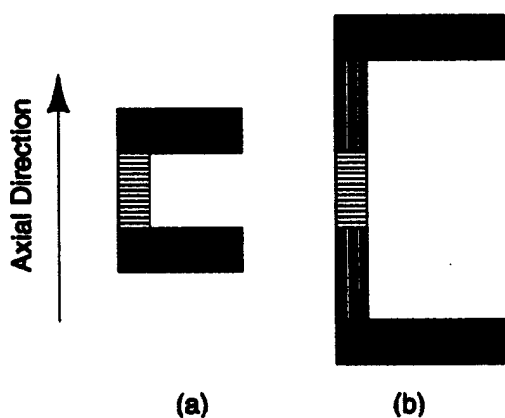


Fig. 1. (a) Original axial view of a detector module in MDAPET camera, (b) axial view of a modified detector module.

Fig.2 shows an axial view of the modified version of the MDAPET detector module for three septa configurations: (a) no-septa, (b) partial 5-septa with inter-gap separation between septa of 1.46 cm, and (c) partial 7-septa with inter-

gap separation between septa of 2.01 cm. Septa consisted of 2 mm lead in all designs.

We took data in the brain mode, one of several modes of operation of the MDAPET camera. In this mode, the camera has a ring diameter (the distance between two facing detector modules) of 44 cm. To compensate for the lower sensitivity of the MDAPET camera, due to its small "real" axial field of view, the brain phantom was scanned longer than a clinical study. In addition, the measurement was done at relatively higher activity and scanning was repeated several times. Then the data were summed to obtain an equivalent number of true events as a clinical version of the camera would collect in a typical injected dose of 10 mCi ^{18}F -fluorodeoxyglucose (FDG) in a 20 minutes scan.

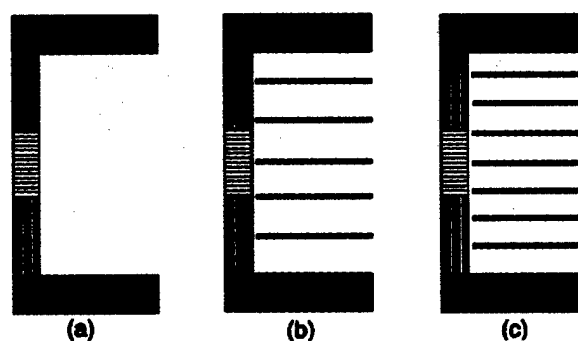


Fig. 2. Axial view of a modified MDAPET module with three different septa configurations: (a) no-septa, (b) partial 5-septa, and (c) partial 7-septa.

To minimize the number of imaging sessions, we acquired two separate data sets. We first acquired data for the hot lesion phantoms and then acquired data for the warm (normal) Hoffman brain phantom. When the lesions data were acquired, the lesions were placed inside the Hoffman brain phantom filled only with water (cold background) to provide the attenuation and scatter effects. Before applying different corrections, we selectively combined the two sets of sinogram data were to generate the sinogram data for the desired SUVs. This combination method greatly reduced the number of required measurements for different lesion uptake and also eliminated the effect of the 'cold' walls of the lesion phantoms that exists when hot lesions and the warm background are measured simultaneously [16], [17]. However, this technique requires the phantom to be positioned precisely, the concentration ratio of the tissue and background be known, the accidental coincidence be known and the effect of the dead time also becomes more important. This sinogram summing method allows all the different SUVs data for lesions to be taken in one experimental period by collecting the different SUVs data as the activity decays.

Prior to image reconstruction, the projection data were corrected. These corrections included random coincidence subtraction, attenuation correction, geometric and detector-

pair efficiency corrections [18]. The attenuation correction was performed by calculating the attenuation length from the shape of the phantom (cylinder) and assuming uniform attenuation. All data were acquired with the FDG tracer. For image reconstruction we used the 3DRP algorithm with a Butterworth filter [19], [20].

All data were acquired in 3-D mode with an axial acceptance of 13 rings, which produced 196 sinograms. In the present study, each sinogram had 239 radial bins and 180 azimuthal views and no axial or transaxial compression was performed on projection data. The radial sampling was 1.385 mm. The camera allows simultaneous imaging of 27 transaxial slices with 1.4-mm thickness. Each reconstructed image had 239 X 239 pixels.

III. RESULTS

A. NEC Study

The NEC was measured for a standard uniform NEMA (National Electrical Manufacturers Association) phantom 21 cm in diameter and 18 cm high. For these measurements 1.5 mCi, 2.9 mCi and 3.5 mCi of FDG was added to the water phantom for no-septa, 5-septa, and 7-septa configurations, respectively. True (un-scattered and scattered) and accidental coincidence count rates were measured in full 3-D acquisition mode as the activity decayed for each configuration. The true count rates for three configurations are compared in Fig. 3. The scatter fraction values used for NEC calculation were 37.9% for no-septa, 27% for 5-septa and 24.5% for 7-septa configurations. The NEC for three configurations is shown in Fig. 4. It is clear that, in terms of NEC, for activity of 0.07 $\mu\text{Ci/cc}$ or higher the MDAPET scanner in brain mode performed much better for 5-septa, and 7-septa configurations than for the no-septa configuration.

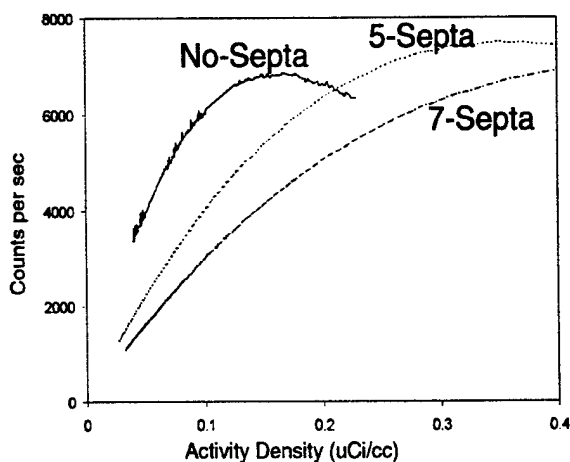


Fig. 3. Comparison of true count rates for three detector configurations: no-septa, 5-septa, and 7-septa.

In the brain studies, typical activity concentration value ranges between 0.15 $\mu\text{Ci/cc}$ and 0.30 $\mu\text{Ci/cc}$ for 10 μCi FDG injection. In this range, such intermediate septa configurations as the partial 5-septa or 7-septa configurations may be more appropriate. The no-septa configuration reached its NEC peak rate around 0.07 $\mu\text{Ci/cc}$. As a result, in no-septa configuration less amount of activity (e.g. 5 mCi) may be more appropriate.

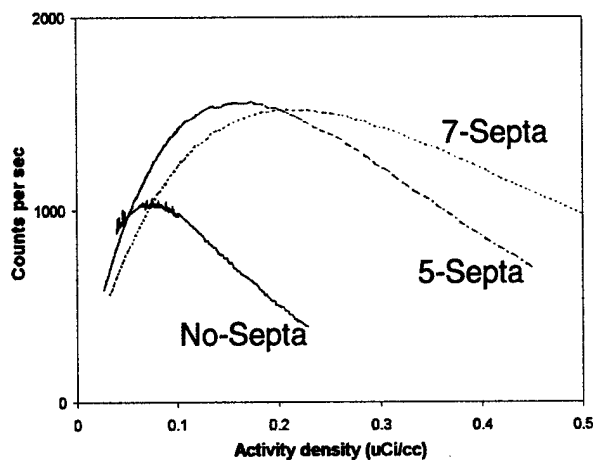


Fig. 4. Comparison of NEC rates for three detector configurations: no-septa, partial 5-septa, and 7-septa.

B. Lesion Detectability Study

Figure 5 shows two reconstructed image slices of the Hoffman brain phantom without embedded lesion phantoms for no-septa (top), 5-septa (middle), and 7-septa (bottom) configurations. The images show that, as the number of septa increased, the white matter (background) contribution became less observable, the gray matter contribution became more pronounced and image quality visually improved. The total true coincidence events collected were 76 million, 57 million, and 33 million for no-septa, 5-septa, and 7-septa configurations, respectively. The scatter fraction from Hoffman brain phantom studies was estimated to be 31.3%, 20.5% and 14% for the no-septa, 5-septa and 7-septa cases. The ratio of NEC for the 5-septa to no-septa case was calculated to be about 1.25.

Fig. 6 shows two reconstructed image slices with 3 mm and 5 mm embedded lesion phantoms when the ratio of the activity concentration in the lesions to background (gray matter) was 5.4. In order to improve visualization of smaller lesions, the 8.6 mm lesion phantom was placed such that it did not appear at the same slices with the others. The activity ratio of 5.4 was the lowest activity ratio at which the 3 mm lesion was observable.

Fig. 7 shows two reconstructed image slices with 5 mm embedded lesion phantom when the ratio of the activity concentration in the lesions to background (gray matter) was

2.2. The activity ratio of 2.2 was the lowest activity at which this lesion was clearly observable.

Fig. 8 shows two reconstructed image slices with 8.6 mm lesion when the activity concentration in the lesions to the background was 1.5. This was the lowest activity ratio that we measured, and the 8.6 mm lesion was still clearly observable.

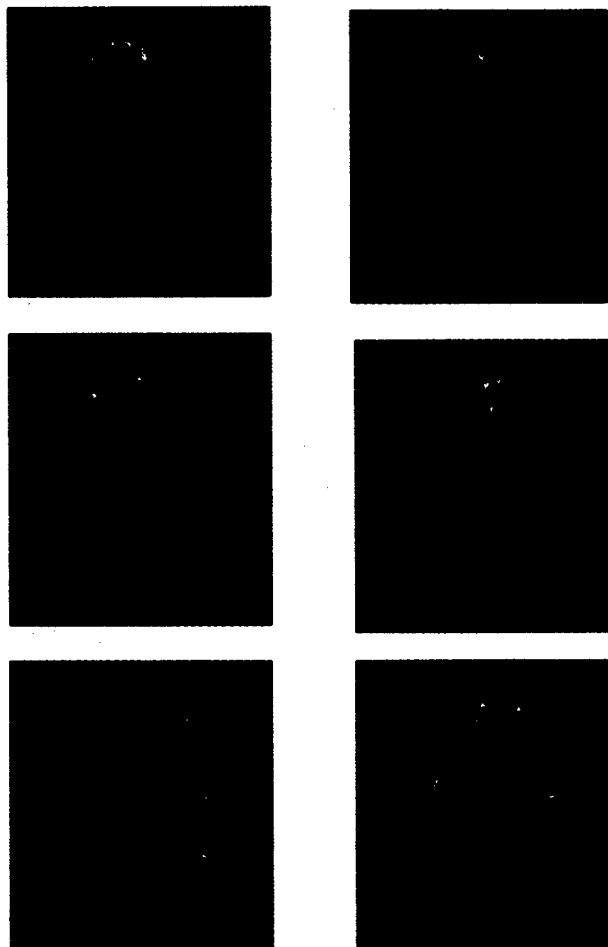


Fig. 5. Two image slices of the Hoffman brain phantom reconstructed with the 3DRP algorithm for three different septa configurations: (top) no-septa, (middle) 5-septa, and (bottom) 7-septa.

Visual comparison of the images did not show any significant differences between the two septa configurations in terms of lesion detectability; however 5-septa images had less noise background. Figs. 9 and 10 show the horizontal profiles running along the middle of the 3 mm lesion image at activity ratios of 5.4 and 7.4, respectively. Figs. 11 and 12 show the horizontal profiles running along the middle of the 5 mm lesion image at activity ratios of 2.2 and 7.4 respectively. Figs. 13 and 14 show the horizontal profiles running along the middle of the 8.6 mm lesion image at activity ratios of 2.2 and 7.4, respectively. The profile data

for each image was normalized according to the average count in the background for each case.

Figs. 9-14 show that the ratio of the peak (lesion activity) to the background (gray matter) was slightly higher for the no-septa configuration, especially for the largest lesion.

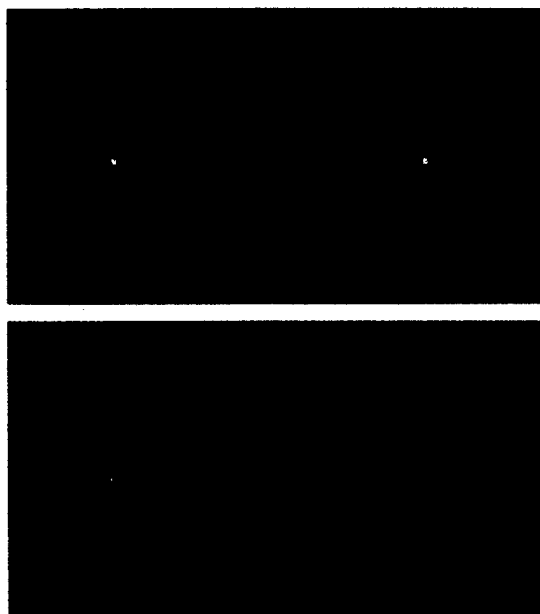


Fig. 6. Two image slices of the Hoffman brain phantom with 3 mm and 5 mm lesions for two different septa configurations: (top) no-septa and (bottom) 5-septa. The ratio of activity concentration of the lesions to gray matter was 5.4.

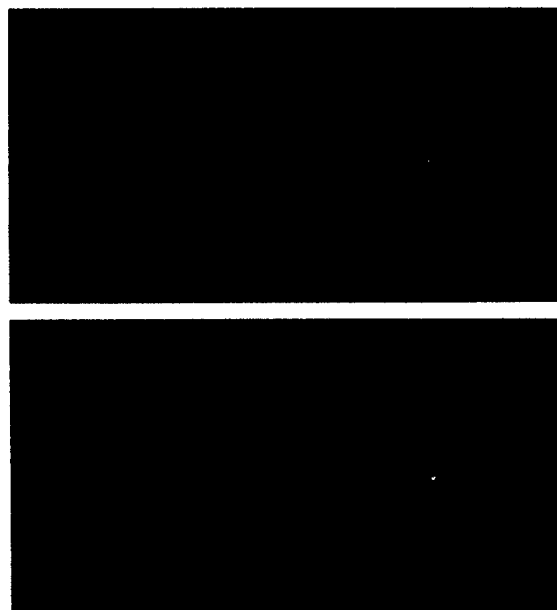


Fig. 7. Two image slices of the Hoffman brain phantom with 5 mm lesions for two different septa configurations: (top) no-septa and (bottom) 5-septa. The ratio of activity concentration of the lesions to gray matter was 2.2.

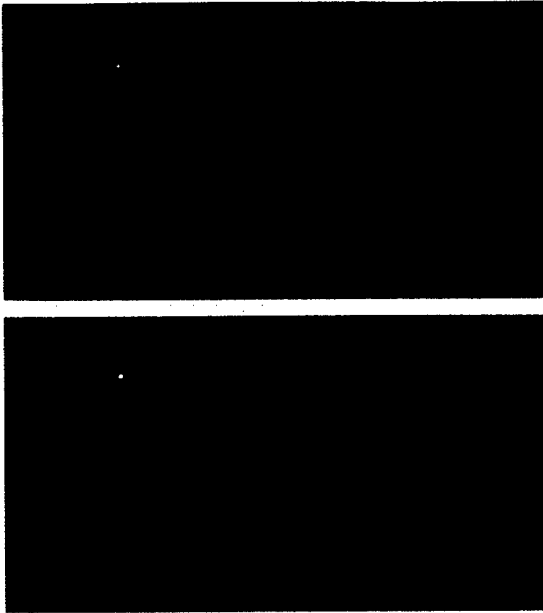


Fig. 8. Two image slices of the Hoffman brain phantom with 8 mm lesions for two different configurations: (top) no-septa and (bottom) 5-septa. The ratio of activity concentration of the lesions to gray matter was 1.5.

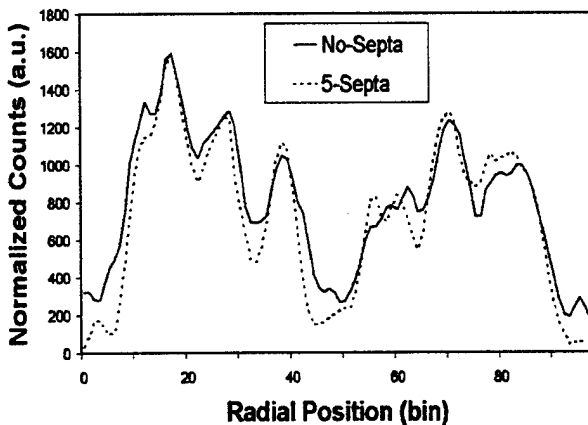


Fig. 9. A horizontal profile running through the middle of the 3 mm lesion image slices shown in figure 6 for no-septa and partial 5-septa configurations. Ratio of activity concentration of the lesions to gray matter was 5.4.

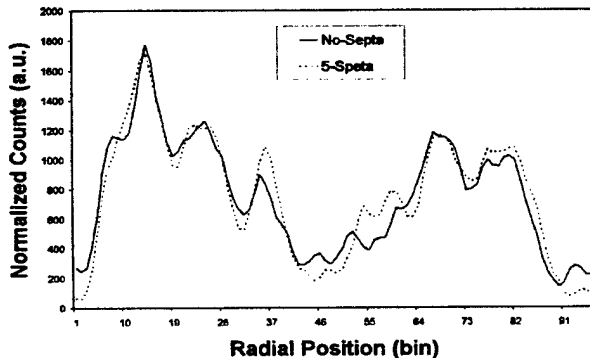


Fig. 10. A horizontal profile running through the middle of the 3 mm lesion images for no-septa and partial 5-septa configurations. Ratio of activity concentration of the lesions to gray matter was 7.4.

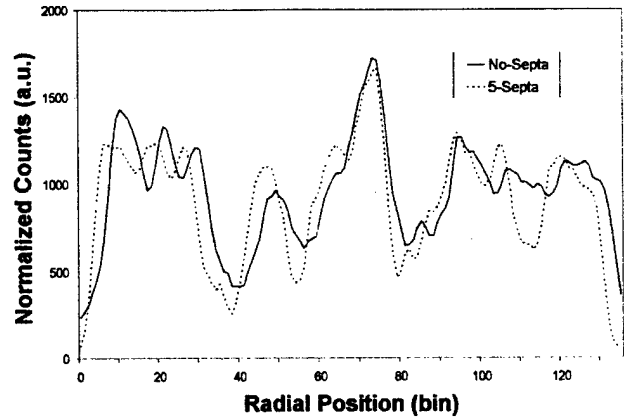


Fig. 11. A horizontal profile running through the middle of the 5 mm lesion image slices shown in figure 7 for no-septa and partial 5-septa configurations. Ratio of activity concentration of the lesions to gray matter was 2.2.

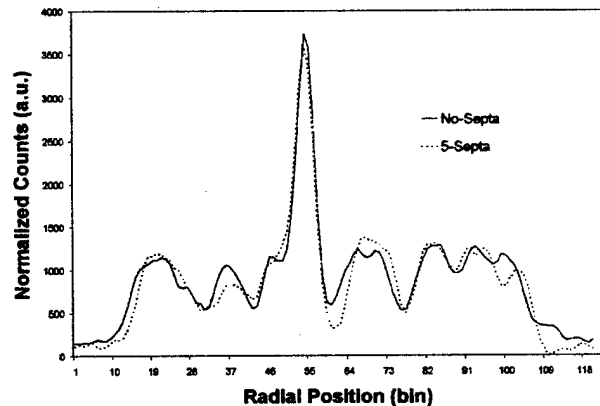


Fig. 12. A horizontal profile running through the middle of the 5 mm lesion images for no-septa and partial 5-septa configurations. Ratio of activity concentration of the lesions to gray matter was 7.4.

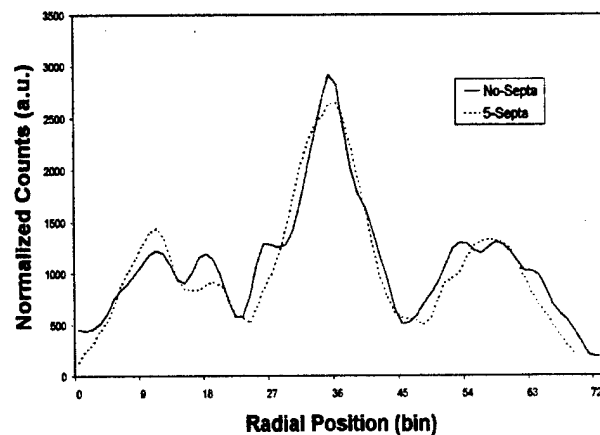


Fig. 13. A horizontal profile running through the middle of the 8.6 mm lesion images for no-septa and partial 5-septa configurations. Ratio of activity concentration of the lesions to gray matter was 2.2.

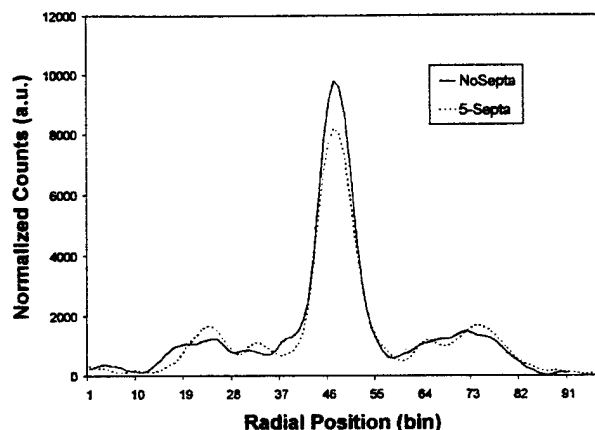


Fig. 14. A horizontal profile running through the middle of the 8.6 mm lesion images for no-septa and partial 5-septa configurations. Ratio of activity concentration of the lesions to gray matter was 7.4.

IV. CONCLUSIONS

The MDAPET camera operating in partial 5-septa and 7-septa configurations performed better than no-septa case in terms of NEC. For the 5-septa configuration the NEC peaked around 0.18 mCi/cc with ~ 1.6 Kcps value, and the camera sensitivity was estimated to be 53% compared to the no-septa case. For 7-septa NEC peaked around 0.22 mCi/cc with ~ 1.5 Kcps value and the camera sensitivity was estimated to be 35% compared to the no-septa case.

The visual inspection of the lesion images showed that the 3 mm lesion phantom embedded in the 3-D Hoffman brain phantom could be clearly observed, with or without partial 5-septa, when the activity concentration ratio between the lesion and the background (gray matter) was greater than 5.4. The 5 mm lesion could be seen at an activity ratio greater than 2.2. The 8.6 mm lesion was observable even at the lowest activity ratio (1.5) that we measured. We found that even though the use of septa increased the NEC rate, that increase not translated into improvement of the lesion detectability. We found that with septa the white matter regions of brain had less count and the brain images had less noise and images looked better; however, images without septa had slightly higher contrast. We are currently completing our measurement with 7-septa configuration for lesion imaging.

The NEC measurement was done with a cylindrical phantom, which was larger than the Hoffman brain phantom. Since both scattered and accidental coincidence contributions are larger in NEMA phantom than the brain phantom, partial septa would have greater effect on NEC. In brain lesion measurements we had little contribution from activity outside the FOV of the camera. In a more realistic condition, when there are activities outside of FOV, the effect of partial-septa system could become more important.

V. ACKNOWLEDGMENT

The authors would like to thank the personnel of the clinical PET center of the University of Texas M. D. Anderson Cancer Center for their support in providing the FDG used for this work.

VI. REFERENCES

- [1] D. J. Kadmas, P. E. Christian, S. D. Wollenweber, S. G. Kohlmyer, C. W. Stearns, "Comparative evaluation of 2D and 3D lesion detectability on a full-ring BGO PET scanner," *J. Nucl. Med.*, vol. 43, no. 5, p. 56P, May 2002.
- [2] S. Pajevic, M.E. Dauve-Witherspoon, S. L. Bacharach, and R. E. Carson, "Noise characteristics of 3-D and 2-D PET images," *IEEE Trans. Med. Imag.*, vol. 17, pp. 9-23, February 1998.
- [3] D. L. Baily, T. Jones, T. J. Spinks, M. C. Gilardi, and D. W. Townsend, "Noise equivalent count measurements in a neuro-PET scanner with retractable septa," *IEEE Trans. Med. Imag.*, vol. 10, pp. 256-260, 1991.
- [4] C. W. Stearns, S. R. Cherry, C. J. Thompson, "NECR analysis of 3D brain PET scanner designs," *IEEE Trans. Nucl. Sci.*, vol. 42, no. 4, pp. 1075-1079, xxx, 1995.
- [5] J. E. Tanaka, T. Hasegawa, T. Yamashita, H. Okada and H. Murayama "A 2D/3D hybrid PET scanner with rotating partial slice-septa and its quantitative procedures", *Phys. Med. and Biol.*, vol. 45, pp. 2821-2841, 2000.
- [6] Turkington, T.G., Sampson, W.H., "Optimizing septal spacing for gamma camera PET imaging", *IEEE Medical Imaging Conference Record*, vol. 3 pp. 1767, 2000.
- [7] S.J. Glick, C.J. Groiselle, J.A. Kolthammer, R.Z. Stodilka, "Optimization of septal spacing in hybrid PET using estimation task performance", *IEEE Medical Imaging Conference Record*, 2001.
- [8] M. Aykac, J. Uribe, H. Baghaei, H. Li, Y. Wang, Y. Liu, T. Xing and W-H. Wong, "Septa design study for volumetric imaging in positron emission tomography," *IEEE Trans. Nucl. Sci.*, vol. 49, no. 5, pp. 2097-2102, October 2002.
- [9] E. J. Hoffman, P. D. Cutler, W. M. Digby, and J. C. Mazziotta, "3-D phantom to simulate cerebral blood flow and metabolic images for PET," *IEEE Trans. Nucl. Sci.*, vol. 37, no. 2, pp. 616-620, April 1990.
- [10] W-H. Wong, "A positron camera detector design with cross-coupled scintillators and quadrant sharing photomultipliers," *IEEE Trans. Nucl. Sci.*, vol. 40, pp. 962-966, August 1993; and *Conference Record of the 1992 IEEE Nuclear Science Symposium and Medical Imaging Conference (Orlando, FL)*, 1992.
- [11] W-H. Wong, J. Uribe, W. Lu, and K. Hicks, "Design of a variable field prototype PET Camera," *IEEE Trans. Nucl. Sci.*, vol. 43, pp. 1915-1920, June 1996.
- [12] W-H. Wong, J. Uribe, K. Hicks, and M. Zambelli, "A 2-dimensional detector decoding study on BGO arrays with quadrant sharing photomultipliers," *IEEE Trans. Nucl. Sci.*, vol. 41, pp. 1453-1457, June 1994.
- [13] W-H. Wong, G. Hu, N. Zhang, J. Uribe, J. Wang, H. Li, H. Baghaei, and S. Yokoyama, "Front end electronics for a variable field PET camera using the PMT-quadrant-sharing detector array design," *IEEE Trans. Nucl. Sci.*, vol. 44, pp. 1266-1270, June 1997.
- [14] R. H. Li, W-H Wong, N. Zhang, J. Wang, J. Uribe, H. Baghaei, and S. Yokoyama, "Prototype electronics for a variable field of view PET camera using the PMT-quadrant-sharing detector array," *IEEE Trans. Nucl. Sci.*, vol. 46, pp. 546-550, June 1999.
- [15] J. Uribe, H. Baghaei, H. Li, S. Yokoyama, N. Zhang, J. Wang, F. Dobbs, and W-H. Wong, "Basic imaging characteristics of a variable field of view PET camera using quadrant sharing detector design," *IEEE Trans. Nucl. Sci.*, vol. 46, pp. 491-497, June 1999.
- [16] H. Baghaei, W-H. Wong, J. Uribe, H. Li, N. Zhang, and Y. Wang, "Breast cancer studies with a variable field of view PET camera," *IEEE Trans. Nucl. Sci.*, vol. 47, pp. 1080-1084, June 2000.

- [17] R.S. Miyaoka, S.G. Kohlmyer, T.K. Lewellen, "Hot Sphere Detection Limits for a Dual Head Coincidence Imaging System," *IEEE Trans. Nucl. Sci.*, vol. 46, pp.2185-2191, December 1999.
- [18] H. Baghaei, W-H. Wong, J. Uribe, H. Li, N. Zhang, and J. Wang, "The correction factors for a high resolution variable field of view PET camera," *J. Nucl. Med.*, vol. 40, p.279P, May 1999.
- [19] P. E Kinahan, J. G. Rogers, "Analytic 3D Image Reconstruction Using all Detected Events," *IEEE Transaction on Nuclear Science*, vol. 46 pp.964-968, 1989.
- [20] H. Baghaei, W-H. Wong, H. Li, J. Uribe, Y. Wang, M. Aykac, Y. Liu, T. Xing, and, "Evaluation of the effect of filtering apodization for volume PET imaging using the 3DRP algorithm," *IEEE Trans. Nucl. Sci.*, to be published in February 2003.